Lecture Notes in Mechanical Engineering

Taoufik Boukharouba
Fakher Chaari
Mounir Ben Amar
Krimo Azouaoui
Nourdine Ouali
Mohamed Haddar *Editors*

# Computational Methods and Experimental Testing In Mechanical Engineering

## Selected Papers from the 6th Algerian Congress on Mechanics, CAM 2017, November 26–30, 2017, Constantine, Algeria

Springer

# Lecture Notes in Mechanical Engineering

**Lecture Notes in Mechanical Engineering (LNME)** publishes the latest developments in Mechanical Engineering—quickly, informally and with high quality. Original research reported in proceedings and post-proceedings represents the core of LNME. Volumes published in LNME embrace all aspects, subfields and new challenges of mechanical engineering. Topics in the series include:

- Engineering Design
- Machinery and Machine Elements
- Mechanical Structures and Stress Analysis
- Engine Technology
- Aerospace Technology and Astronautics
- Nanotechnology and Microengineering
- Control, Robotics, Mechatronics
- Theoretical and Applied Mechanics
- Dynamical Systems, Control
- Fluid Mechanics
- Engineering Thermodynamics, Heat and Mass Transfer
- Precision Engineering, Instrumentation, Measurement
- Materials Engineering
- Tribology and Surface Technology

To submit a proposal or request further information, please contact the appropriate Springer Editor:

Li Shen at li.shen@springer.com (China)
Dr. Akash Chakraborty at akash.chakraborty@springernature.com (India)
Dr. Leontina Di Cecco at Leontina.dicecco@springer.com (all other Countries)
Please check the Springer Tracts in Mechanical Engineering at http://www.springer.com/series/11693 if you are interested in monographs, textbooks or edited books. To submit a proposal, please contact Leontina.dicecco@springer.com and Li.shen@springer.com.

**Indexed by SCOPUS. The books of the series are submitted for indexing to Web of Science.**

More information about this series at http://www.springer.com/series/11236

Taoufik Boukharouba · Fakher Chaari ·
Mounir Ben Amar · Krimo Azouaoui ·
Nourdine Ouali · Mohamed Haddar
Editors

# Computational Methods and Experimental Testing In Mechanical Engineering

## Selected Papers from the 6th Algerian Congress on Mechanics, CAM 2017, November 26–30, 2017, Constantine, Algeria

Springer

*Editors*
Taoufik Boukharouba
Laboratory for Advanced Mechanics
University of Science and Technology
Houari Boumediene (USTHB)
Bab-Ezzouar, Algeria

Fakher Chaari
Department of Mechanical Engineering
National School of Engineers
of Sfax
Sfax, Tunisia

Mounir Ben Amar
Laboratory of Materials Science
and Process
University of Paris 13
Villetaneuse, France

Krimo Azouaoui
Laboratory for Advanced Mechanics
University of Science and Technology
Houari Boumediene (USTHB)
Bab-Ezzouar, Algeria

Nourdine Ouali
Department of Mechanical Engineering
University of Science and Technology
Houari Boumediene (USTHB)
Bab-Ezzouar, Algeria

Mohamed Haddar
National School of Engineers of Sfax
Sfax, Tunisia

ISSN 2195-4356 ISSN 2195-4364 (electronic)
Lecture Notes in Mechanical Engineering
ISBN 978-3-030-11826-6 ISBN 978-3-030-11827-3 (eBook)
https://doi.org/10.1007/978-3-030-11827-3

Library of Congress Control Number: 2019931532

© Springer Nature Switzerland AG 2019
This work is subject to copyright. All rights are solely and exclusively licensed by the Publisher, whether the whole or part of the material is concerned, specifically the rights of translation, reprinting, reuse of illustrations, recitation, broadcasting, reproduction on microfilms or in any other physical way, and transmission or information storage and retrieval, electronic adaptation, computer software, or by similar or dissimilar methodology now known or hereafter developed.
The use of general descriptive names, registered names, trademarks, service marks, etc. in this publication does not imply, even in the absence of a specific statement, that such names are exempt from the relevant protective laws and regulations and therefore free for general use.
The publisher, the authors and the editors are safe to assume that the advice and information in this book are believed to be true and accurate at the date of publication. Neither the publisher nor the authors or the editors give a warranty, express or implied, with respect to the material contained herein or for any errors or omissions that may have been made. The publisher remains neutral with regard to jurisdictional claims in published maps and institutional affiliations.

This Springer imprint is published by the registered company Springer Nature Switzerland AG
The registered company address is: Gewerbestrasse 11, 6330 Cham, Switzerland

# Foreword

This book gathers contributions presented at the Algerian Congress of Mechanics "*Congrès Algérien de Mécanique CAM*", www.cam-dz.org, held on 26–30 November 2017, in the beautiful city of Constantine, in eastern Algeria. The congress brought together eminent scientists working in the field of mechanics of materials and structures, as well as on fluid mechanics, heat transfer, reactive flows and transport phenomena, with a close connection with renewable energies and sustainable development.

Two workshops were organized during the conference. The first one was about *Crack Propagation and Damage in Structures for Aeronautics*. The second one was on *Biomechanics and Biomaterials for Health*. The CSPBAT laboratory from Paris 13 University was very much involved in the latter, which was intended to stimulate the interest of participants towards public health issues. The conference also counted a special session dedicated to the field of fatigue, which was organized in close collaboration with the French Association of Mechanics (AFM), and was very successful in terms of number and quality of the selected contributions.

After 313 peer-reviewed contributions, 268 papers were accepted for presentations from 10 countries, which lead to an acceptation rate of 85.6%. 151 speakers were present at the conference, and 16 plenary lectures, 13 introductive lectures, 79 oral presentations and 43 posters were held. Moreover, the Workshop on *Biomechanics and Biomaterials for Health* was animated by six eminent professors.

A major objective of the Algerian Congress of Mechanics is to develop connections between academic and applied researchers. For that, the Algerian Congress of Mechanics received its essential help from the Algerian Association for Technology Transfer "a2t2" that has been working for more than a decade with the organizers of this scientific meeting. A special feature of CAM is to be itinerant upon the Algerian territory, friendly and informal.

Recently, a College of Experts, Monitoring and Ethics (CESD) was set up in order to oversee future editions of Algerian Congress of Mechanics at both scientific and organizational levels as well as to define the topics, coordinators and the host university for this biannual meeting, based on a tender.

We believe that the Algerian Congress of Mechanics meeting represents a major scientific event in North Africa. The current book presents recent advances and brings new materials for students and scientists. The next Algerian Congress of Mechanics will come in a new format in 2019. It will be articulated around three predominantly mechanical sectors: *Mechanics of solid materials, fluids and structures*, *Mechanical engineering and manufacturing* and *Materials and structures in civil engineering*.

Villetaneuse, France

Ramtani Salah
Paris 13 University

# Contents

# Mixing-Time in T-Mixer Reactor

**Khaled Oualha, Mounir Ben Amar and Andrei Kanaev**

## 1 Introduction

The design of T-mixer (Fig. 1) in general is a trade-off between several parameters, such as: pressure variation, mixing time, volume, and velocity field. In particular, the design of the T-mixer is very important in the development of monodisperse nanoparticles because it necessary that the two reagents are completely mixed before the chemical reaction processes established. This is required in the chemical process engineering in general (Bałdyga and Pohorecki 1995) and for kinetics reaction studies of chemical and biological substances, as for example in sol-gel process (Azouani et al. 2010; Labidi et al. 2015; Azouani et al. 2007) and protein folding studies (Schönfelder et al. 2016; Roder and Shastry 1999). So the mixing time in order of some millisecond is required in order to produce monodisperse and reactive nanoparticles.

In present paper, we report on the influence of the T-mixer geometry on the flow regime (Beebe et al. 2002) and we aim to validate the mixing process experimentally and numerically by measuring the length ($Z_i$) for obtaining the micro-mixing. The mixing, in T-mixer with non-aligned inputs, is studied using Computational Fluid Dynamics (*CFD*). The discretization of the main circular outlet and inlet microchannel were done using finite element method. This model allowed us to determine mixing times and to visualize mixing and reaction zones in the T-mixer. This study served as a basis for optimizing the limiting conditions of preparation of micro-mixing in the T-mixer (Oualha et al. 2017).

---

K. Oualha · M. Ben Amar (✉) · A. Kanaev
Laboratoire des Sciences des Procédés et des Matériaux, CNRS, Université Paris 13, Sorbonne Paris Cité, 93430 Villetaneuse, France
e-mail: mounir.benamar@lspm.cnrs.fr

T. Boukharouba et al. (eds.), *Computational Methods and Experimental Testing In Mechanical Engineering*, Lecture Notes in Mechanical Engineering,
https://doi.org/10.1007/978-3-030-11827-3_1

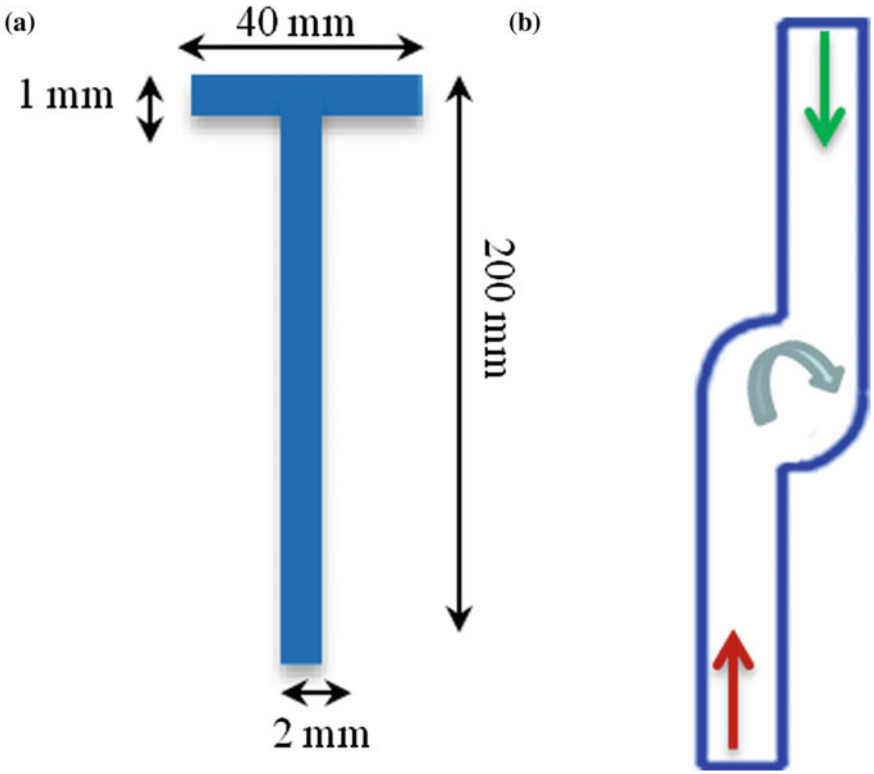

Fig. 1 Front view (a) and top view (b) of the micro T-mixer

# 2 Experimental Setup

## 2.1 Experimental Device

To estimate the mixing height in our T-mixer, we used the bleaching method of a colored indicator. The neutralization of a strong acid with a strong base is visually followed by a colored indicator (phenolphthalein). Moreover, these viewing experiences are very simple to make. So we prepared two solutions:

- Solution of NaOH (sodium hydroxide), 0.040 N (0.040 M) with the color indicator (phenolphthalein).
- Solution of $H_2SO_4$ (sulfuric acid), 0.042 N (0.021 M).

The experimental setup used for characterization of the height of the mixture in the outlet leg is illustrated in Fig. 2.

- 50 mL of solution of $H_2SO_4$ 0.042 N in $R_1$ (thermostated tank).
- 50 mL of solution of NaOH + phenolphthalein in $R_2$.

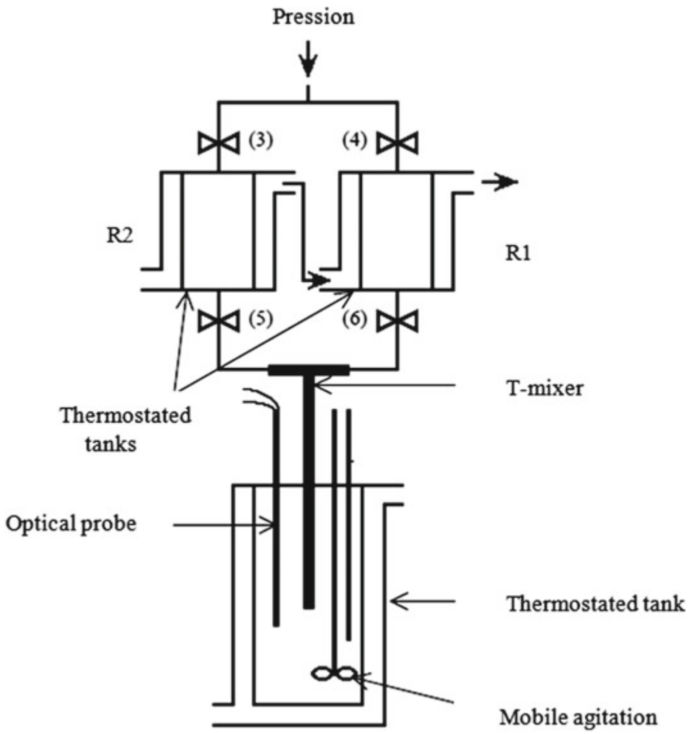

**Fig. 2** Experimental device

- Opening valves (3) and (4) valves and making pressure $P$.
- Opening valves (5) and (6).

And finally we visualize the height of the mixing point in the T-mixer (length where the color changes from pink to colorless) using a high speed camera.

In fact, the transit of the coloring from pink to transparent is due to the neutralization of the strong acid by a strong base, once this reaction (1) has been established, we will have a neutral solution (a neutral pH value $6.5 < \mathrm{pH} < 7$) and disappearance of the pink color which allows us to measure ($Z_i$) and thereafter the mixing time $t_m$ (Eq. 2) by knowing the mean velocity of the flow:

$$2\mathrm{Na}^+ + 2\mathrm{OH} + \mathrm{SO}_4 + 2\mathrm{H}_3\mathrm{O} = \mathrm{Na}_2\mathrm{SO}_4 + 4\mathrm{H}_2\mathrm{O} \tag{1}$$

$$t_m = \frac{\pi l d^2}{4Q} \tag{2}$$

$t_m$: mixing time, $d$: Diameter of the pipeline, $l$: length of disappearance of the pink color and $Q$: Flow rate in the mixer.

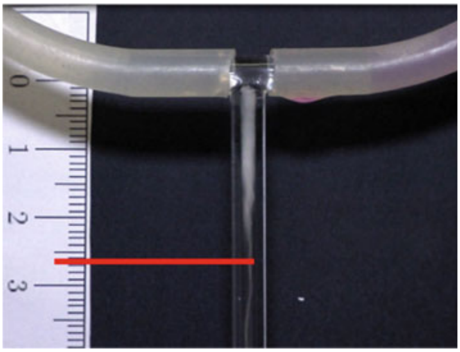

**Fig. 3** Mixture formation for pressure P = 5 bars

### 2.2 *Results and Discussions*

To estimate the mixing height in our T-mixer, we used the bleaching method of a colored indicator. The neutralization (discoloration) of a strong acid with a strong base is visually followed by a colored indicator, who is the phenolphthalein. And we use a hight speed camera to visualize the mixing point $Z_i$ in the T-mixer (height where the color changes from pink to colorless).

Figure 3 shows that the discoloration is indicated between 22 and 24 mm. These results show that the mixture become homogenous at almost 100% for a length $Z_i$= (23 ± 1) mm, which allows us to have mixing time in order of 8 ms. In order to validate our experimental result, we have set up numerical model which allows us to calculate the lengths of obtaining micro-mixture and to compare them to experimental result.

## 3 Numerical Setup

### 3.1 *Geometry and Meshing*

The micro T-mixer, shown in Fig. 1, comprises two cylindrical inlet channels of diameter $d = 1$ mm and length $l = 2$ cm, connected to the main outlet channel of diameter $D = 2$ mm and length $L = 20$ cm. The Reynolds number of the fluids is conserved in this geometry. The right-handed rectangular coordinate frame is positioned with the z-axis along the main outlet tube, x-axis in the plane of the inlet and out-let tubes and y-axis perpendicular to the x-z plane. Elementary volumes of the finite element model used in the present numerical calculations are depicted in Fig. 4.

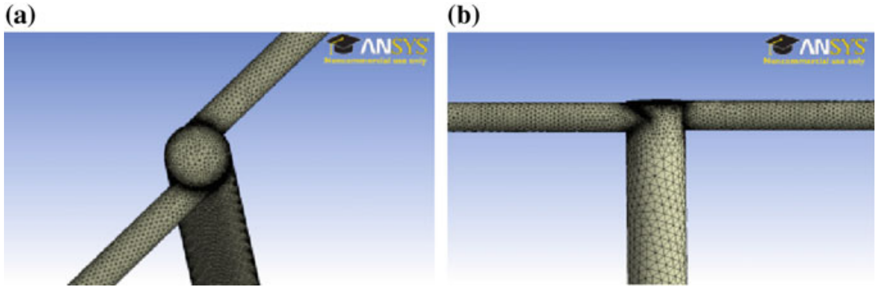

**Fig. 4** **a** Top and **b** frontal views of the finite element model of the T-mixer

## 3.2 *Theory*

The flow of an incompressible Newtonian liquid in microchannels can generally be described by the averaged Navier-Stokes equation (Wong et al. 2004; Judy et al. 2002) and continuity equation. Each instantaneous quantity can be split into time-averaged and fluctuating components and the resulting equation time averaged to yield:

$$\begin{cases} \frac{\partial \langle u_i \rangle}{\partial t} + \frac{\partial \left\langle u'_j u'_i \right\rangle}{\partial x_j} + \frac{\partial \left\langle u_j u_i \right\rangle}{\partial x_j} = -\frac{1}{\rho} \frac{\partial \langle P \rangle}{\partial x_i} + \upsilon \frac{\partial^2 \langle u_i \rangle}{\partial x_j \partial x_i} \\ \frac{\partial \langle u_i \rangle}{\partial x_i} = 0 \end{cases} \tag{3}$$

The Reynolds stress tensor can be expressed as:

$$\tau_{ij} = \left\langle u'_j u'_i \right\rangle \tag{4}$$

The closure used on the Reynolds stress is based on the viscosity. It is to express the fact that the Reynolds stress behaves with all viscous stresses:

$$\left\langle u'_j u'_i \right\rangle = -\upsilon \left( \frac{\partial \langle u_i \rangle}{\partial x_j} + \frac{\partial \left\langle u_j \right\rangle}{\partial x_i} \right) + \frac{2}{3} \delta_{ij} k \tag{5}$$

$\upsilon_t$ is the fluid viscosity and $k$ is the instant turbulent kinetic energy, it can be written as:

$$k = \frac{1}{2} \left\langle u'_i \right\rangle^2 \tag{6}$$

In the implementation of this model the Kolmogorov-Prandtl expression for the turbulent viscosity is used:

**Table 1** Constants of k-ε model

| $C_\mu$ | $C_{\varepsilon 1}$ | $C_{\varepsilon 2}$ | $\sigma_k$ | $\sigma_\varepsilon$ |
|---|---|---|---|---|
| 0.09 | 1.44 | 1.92 | 1.0 | 1.3 |

$$\upsilon_t = c_\mu \frac{k^2}{\varepsilon} \tag{5}$$

And:

$$\varepsilon = \upsilon \frac{\partial u_i'}{\partial x_j} \frac{\partial u_i'}{\partial x_j} \tag{6}$$

Of all the turbulence models, the k-ε model (Okaze et al. 2015) is the most used in the literature and in commercial codes such as FLUENT (ANSYS Fluent 2013). For an incompressible Newtonian fluid, two transport equations are solved: k (the turbulence kinetic energy) and $\varepsilon$ (the turbulence dissipation). It remains to determine $k$ and $\varepsilon$ with the two respective transport equations:

$$\frac{\partial k}{\partial t} + u_j \frac{\partial k}{\partial x_j} = -\langle u_i' u_j' \rangle \frac{\partial u_j}{\partial x_j} - \varepsilon + \frac{\partial}{\partial x_j} (\upsilon + \sigma_k \upsilon_k) \cdot \frac{\partial k}{\partial x_j} \tag{7}$$

$$\frac{\partial \varepsilon}{\partial t} + u_j \frac{\partial k}{\partial x_j} = -\, \mathrm{C}_{\varepsilon 1} \langle u_i' u_j' \rangle S_{ij} \frac{\varepsilon}{k} - C_{\varepsilon 2} \frac{\varepsilon^2}{k} + \frac{\partial}{\partial x_j} \left( (\upsilon + \sigma_\varepsilon \upsilon_t) \cdot \frac{\partial \varepsilon}{\partial x_j} \right) \tag{8}$$

where: $S_{ij} = \frac{1}{2}\left( \frac{\partial \langle u_i \rangle}{\partial x_j} + \frac{\partial \langle u_j \rangle}{\partial x_i} \right)$ is the mean rate of strain tensor.

$C\mu$, $\mathrm{C}\varepsilon_1$, $\mathrm{C}\varepsilon_2$, $\sigma_\mathrm{k}$, $\sigma_\varepsilon$ are adjusted constants. They are determined through experiments on fundamental flows (turbulence grids, sheared flow…) and summarized in Table 1.

## 3.3 Results and Discussions

In this section, we evaluate the length ($Z_i$) for obtaining the micro-mixing along the z-axis of the outlet channel of T-mixer. In the numerical simulation, we accept typical experimental conditions reported for the sol-gel $TiO_2$ nanoparticles production used by Rivallin et al. (2005):

- Channel 1: Solution of NaOH (sodium hydroxide), 0.040 N (0.040 M) with the color indicator (phenolphthalein).
- Channel 2: Solution of $H_2SO_4$ (sulfuric acid), 0.042 N (0.021 M).

The molar fractions of different quantities are computed and introduced. The micromixing criterion is the achievement of a homogeneous mixture of the two reagents. Figure 5 shows the molar fractions of NaOH.

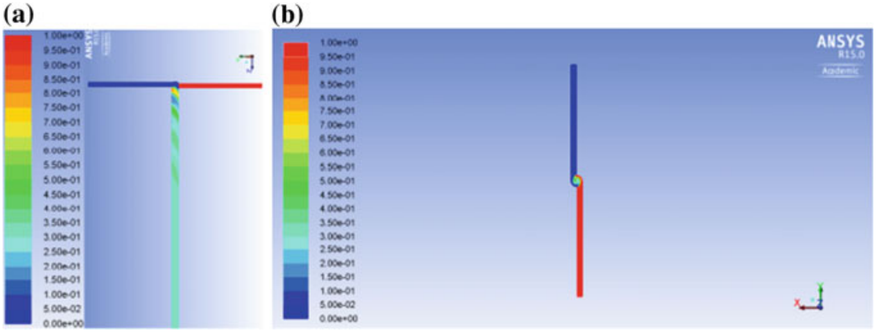

**Fig. 5** **a** Front and **b** top views Molar fraction of NaOH

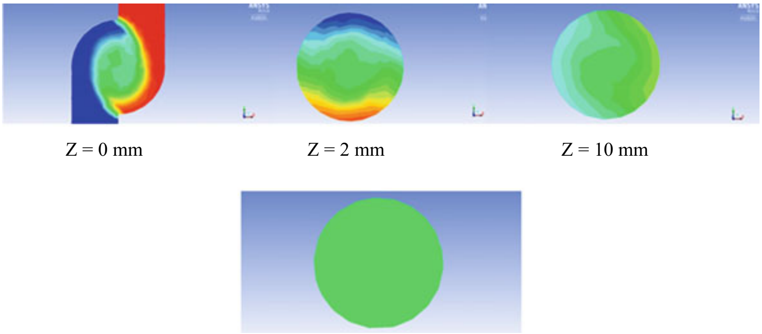
Z = 0 mm
Z = 2 mm
Z = 10 mm
Z = 24 mm

**Fig. 6** Molar fractions of the mixed fluids in different cross-sections along z-axis of T-mixer

To evaluate the height ($Z_i$) for obtaining the micro-mixing, one is interested on the molar fraction of NaOH along the $Z$ axis. The mixture is considered as perfect when the molar fraction becomes a constant. These molar fractions, calculated in different cross-sections ($x$, $y$) of the main outlet tube along $Z$-axis, are shown in Fig. 6.

These results have allowed us to determine the position on the $Z$ axis, of the formation of micro-mixing $Z = 24$ mm.

## 4 Conclusions

In this paper we study, numerical and experimental height ($Z_i$) for obtaining the micro-mixing in our T-mixer. These results allowed us, to calculate the mixing time which is in the order of some milliseconds, between 4 and 8, ms which gives us more safety with the reaction time, to check and respect the condition of Damköhler to produce monodisperse nanoparticles and finally to validate our numerical model for T-mixer. The turbulence model k-ε by using FLUENT Software has well predicted the evolution of the flow along the outlet leg of our T-mixer along Z axis.

## References

ANSYS Fluent Theory Guide (2013) V.15

Azouani R, Soloviev A, Benmami M, Chhor K, Bocquet JF, Kanaev A (2007) Stability and growth of titanium-oxo-alcoxy TixOy(OiPr)z clusters. J Phys Chem C 111:16243–16248

Azouani R, Michau A, Hassouni K, Chhor K, Bocquet JF, Vignes JL, Kanaev A (2010) Elaboration of pure and doped $TiO_2$ nanoparticles in sol-gel reactor with turbulent micromixing: application to nanocoatings and photocatalysis. Chem Eng Res Design 88:1123–1130

Bałdyga J, Pohorecki R (1995) Turbulent micromixing in chemical reactors. Chem Eng J 58:183–195

Beebe DJ, Mensing GA, Walker GM (2002) Physics and applications of microfluidics in biology. Ann Rev Biomed Eng 4:261–286

Judy J, Maynes D, Webb BW (2002) Characterization of frictional pressure drop for liquid flows through microchannels. Int J Heat Mass Transfer 45:3477–3489

Labidi S, Jia Z, Ben Amar M, Chhor K, Kanaev A (2015) Nucleation and growth kinetics of zirconium-oxo-alkoxy nanopparticles. Phys Chem Chem Phys 17:2651–2659

Okaze T, Takano Y, Mochida A, Tominaga Y (2015) Development of a new k–ε model to reproduce the aerodynamic effects of snow particles on a flow field. J Wind Eng Ind Aerodyn 144:118–124

Oualha K, Ben Amar M, Michau A, Kanaev A (2017) Observation of cavitation in exocentric T-mixer. Chem Eng J 321:146–150

Rivallin M, Benmami M, Kanaev A, Gaunand A (2005) Sol–gel reactor with rapid micromixing: modelling and measurements of titanium oxide nano-particle growth. Chem Eng Res Des 83(1):67–74

Roder H, Shastry M (1999) Methods for exploring early events in protein folding Curr. Opin Struct Biol 9:620–626

Schönfelder J, De Sancho D, Perez-Jimenez R (2016) The power of force: insights into the protein folding process using single-molecule force spectroscopy. J Molecular Biology 428(21):4245–4257

Wong SH, Ward MCL, Wharton CW (2004) Micro T-mixer as a rapid mixing micromixer. Sens Actuators 100:359

# Thermal Hydraulic Modeling of a Nuclear Reactor Core Channel Using CFD; Application for an EPR

**Kamel Sidi-Ali, Djaber Ailem, El Moundir Medouri and Toufik Belmrabet**

## 1 Introduction

EPR is a nuclear reactor of about 1650 MW of electric power, using pressurized water as coolant, in high nuclear safety conditions. *EPR* more broadly refers to the global system integrating in particular the protective envelope made of concrete, the safety systems and the turbo-alternator group which ensures the production as mentioned by Bernard (2008). The French Atomic Energy Commission ranks EPR as a third generation reactor. *EPR* operates according to the same general principles as its predecessors, the second generation Pressurized Water Reactors (*PWRs*) operating today, as reported by FEACE (2011). The thermalhydraulic analysis of a nuclear reactor core channel is approached by studying the flow and heat transfer in a single channel of this core. This channel summarizes the thermalhydraulic behavior of the fuel clad, which is the first nuclear safety barrier, to be preserved in any normal or accidental operating situation, Delhaye (2008). This behavior is dependent on the fluid flow to ensure the best cooling of this clad and of the operating pressure which maintains the boiling temperature of the cooling fluid at a high value. The *CFD* approach, Salama and El-Morshedy (2011), for the study of such situations is increasingly used because it allows a minitious investigation of the phenomenon and gives results in *3D*, immediately exploitable, Kaddour et al. (2016). It is this numerical experimentation that will be used in this work to verify that the results obtained by *CFD* are physically correct and very more conservative with respect to nuclear safety.

---

K. Sidi-Ali (✉)
Nuclear Research Center of Draria, Sebala Draria, Algiers, Algeria
e-mail: k-sidiali@crnd.dz; kamelsidiali@gmail.com

D. Ailem · E. M. Medouri · T. Belmrabet
E.M. Polytechnic, Bordj El Bahri, Algiers, Algeria

T. Boukharouba et al. (eds.), *Computational Methods and Experimental Testing In Mechanical Engineering*, Lecture Notes in Mechanical Engineering,
https://doi.org/10.1007/978-3-030-11827-3_2

## 2 Equation Set-Up

The equation set-up is established for the flow described in Fig. 1. The flow is considered in steady-state and the cooling fluid incompressible.

On Fig. 1, the calculation domain is presented. This domain is constituted by four fuel rods in an inline disposition. Cooling fluid, in the cross-section, is flowing from the bottom to the top of the domain in the opposite direction of gravity. Heat is transferred from the quarter part of each fuel rod to the cooling fluid.

The conservation equations at steady state for continuity, momentum and energy are given respectively by Eqs. (1, 2 and 3):

$$\nabla\left(\rho\vec{U}\right)=0 \tag{1}$$

$$\nabla\left(\rho\vec{U}\vec{U}\right)=-\nabla p+\rho\vec{g}+\nabla\left[\mu\left(\nabla\vec{U}+\left(\nabla\vec{U}\right)^{T}\right)\right] \tag{2}$$

$$\nabla\left[(\rho E+P)\vec{U}\right]=\nabla\left[(k\nabla T)-\sum\nolimits_{j}h_j\vec{J}_j+\left(\bar{\bar{\tau}}\,.\,\vec{U}\right)\right]+S \tag{3}$$

where $\rho$ is the air density, $\vec{U}$ the velocity vector of air, $p$ the pressure, $\mu$ the shear viscosity of air, $\vec{g}$ the gravity vector, $k$ the thermal conductivity, $E$ the total energy, $\bar{\bar{\tau}}$ the viscous stress tensor, $S$ the source term, $h_j$ the convective heat transfer coefficient, $\vec{J}_j$ the velocity of each species and $T$ the air temperature at the entry of the channel.

For turbulence, the $k-\omega\,SST$ (Shear-Stress Transport) model of Menter (1994) is used. The transport equations of this model are:

$$\frac{\partial}{\partial x_i}(\rho k U_i)=\frac{\partial}{\partial x_j}\left[\left(\mu+\frac{\mu_t}{\sigma_k}\right)\frac{\partial k}{\partial x_j}\right]+G_k-Y_k \tag{4}$$

$$\frac{\partial}{\partial x_i}(\rho\omega U_i)=\frac{\partial}{\partial x_j}\left[\left(\mu+\frac{\mu_t}{\sigma_\omega}\right)\frac{\partial\omega}{\partial x_j}\right]+G_\omega-Y_\omega+D_\omega \tag{5}$$

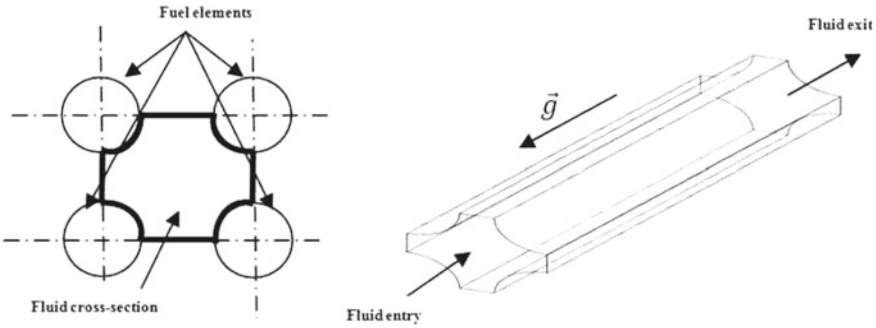

**Fig. 1** Thermal-hydraulic domain

where: $\sigma_k = \frac{1}{F_1\sigma_{k,1}+(1-F_1)\sigma_{k,2}}$; $\sigma_{k,1} = 1.176$, $\sigma_{k,2} = 1.0$ $\sigma_\omega = \frac{1}{F_1\sigma_{\omega,1}+(1-F_1)\sigma_{\omega,2}}$; $\sigma_{\omega,1} = 2.0$, $\sigma_{\omega,2} = 1.168$, $F_1$ and $F_2$ are the blending functions.

The heat flux distribution is given by:

$$Q(z) = Q_0 \cos\left(\frac{\pi z}{\ell_e}\right) \tag{6}$$

where, $Q_0$ is the heat flux per square meter, $\ell_e$ is the active length of the channel and $z$ the channel length.

The User Defined Function (*UDF*) available in FLUENT is used to introduce this heat generation law.

For boundary conditions, a velocity inlet is taken at the inlet of the channel, and a pressure outlet condition at its exit. A wall condition is applied to the walls of the channel. At the entry of the calculation domain, a uniform velocity profile is taken:

$$U = U_0 \tag{7}$$

The profile of the velocity, in the channel, is determined by the universal velocity profile introduced by Prandtl and written in the following form:

$$\frac{U}{U^*} = \left\{ \begin{array}{c} y^+,\ y^+ \le y_v^+ \\ \frac{1}{k_{vk}} \ln(E_c y^+),\ y^+ \ge y_v^+ \end{array} \right\} \tag{8}$$

where $U^*$ is the local friction velocity, $y^+$ the dimensionless position of $y$, $y_v^+$ the dimensionless thickness of the viscous sub-layer equal to 11.225, $E_c$ a constant equal to 9.793 and $k_{vk}$ the Von Karman constant equal to 0.4187.

The calculations are stopped when diffusion fluxes, for all quantities in the exit direction, are zero.

$$\frac{\partial U}{\partial n} = 0 \quad ; \quad \frac{\partial k}{\partial n} = 0 \quad ; \quad \frac{\partial \omega}{\partial n} = 0 \tag{9}$$

where $(\partial/\partial n)$ is the derivative with respect to the normal direction to the exit surface.

The numerical domain presented in Fig. 1 is meshed with *GAMBIT*. The mesh done is a structured one; it is presented in Fig. 2. The meshed numerical domain is then divided in four quarters. Only one quarter mesh is used for calculations in FLUENT.

The aim of the mesh sensitivity is to minimize the number of the mesh cells without influencing the reliability and the accuracy of the results. In other words, to guarantee that obtained results are not dependent to the used mesh. To ensure this condition, ten meshes were tested. The profile of the maximal temperature is drawn out at the exit of the channel for the ten meshes. The cells number was varied from 2.7 to 4.5 million. The choice of the mesh is the one that the temperature profile is no longer changing. The obtained results are given in Fig. 3. One can see that the mesh with 3.6 million cells is the one where the maximal temperature stays constant, so this is the mesh which will be used in this study.

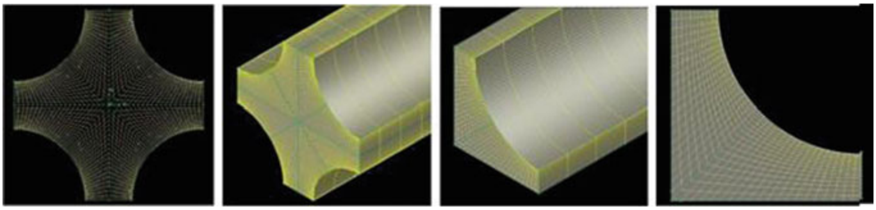

**Fig. 2** Channel meshing

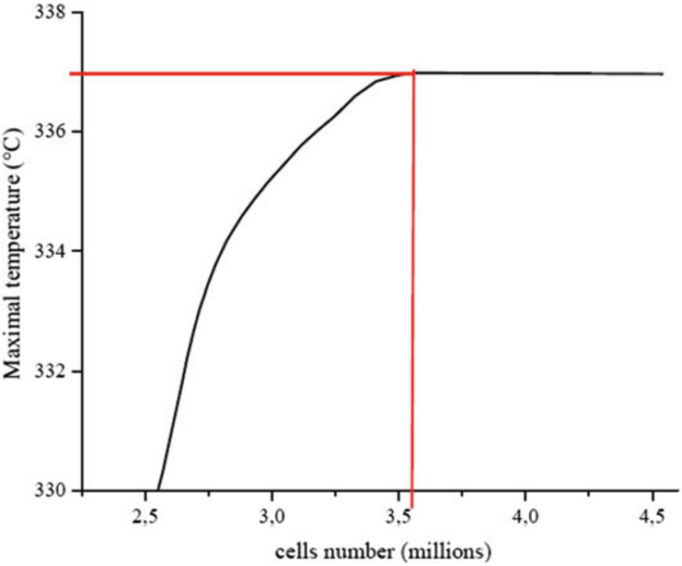

**Fig. 3** Mesh sensitivity

## 3 Essential Core and Thermal-Hydraulic Parameters of EPR

*EPR* is a pressurized nuclear reactor using water as a cooling fluid and moderator. The *EPR*'s contains a set of 241 fuel assemblies, disposed in an inline disposition; each fuel assembly contains 264 fuel rods. Fuel assemblies are 4.85 m height. The fuel rod diameter is 0.95 cm and the clad thickness of zircaloy is 0.625 cm. The fuel rod pitch is 1.26 cm. The EPR's core has an equivalent diameter of about 3767 mm and a core average active fuel height of about 4200 mm, thus a height-to-diameter ratio of 1.115. The total cross-section area of the active core is about 111,450 cm$^2$. More thermal-hydraulic data of the EPR is given in Table 1.

**Table 1** Thermal-hydraulic design data of EPR (Sengler et al. 1999)

| Characteristics | Value |
|---|---|
| Total core heat output (MW$_{th}$) | 4250 |
| Number of loops | 4 |
| Nominal system pressure (absolute)(MPa) | 15.5 |
| *Coolant flow* | |
| Core flow area (m$^2$) | 5.9 |
| Core average coolant velocity (m s$^1$) | 5.0 |
| Core average mass velocity (g cm$^2$ s$^1$) | 331.5 |
| Total mass flow rate/loop (kg s$^1$) | 21,035 |
| Thermal design flow/loop (m$^3$ h$^1$) | 26,520 |
| Mechanical design flow/loop (m$^3$) | 27,581 |
| *Coolant temperature* °C | |
| Nominal inlet | 291.5 |
| Mean coolant nominal core outlet temperature | 328.8 |
| Mean coolant nominal vessel outlet temperature | 326.5 |
| Average rise in core | 37.3 |
| Average in core | 310.15 |
| *Heat transfer* | |
| Heat transfer surface area (m$^2$) | 7975 |
| Average core heat flux (W cm$^1$) | 51.9 |
| Maximum core heat flux (nominal operation) (W cm$^2$) | 146.9 |
| Average linear power density (W cm$^1$) | 154.9 |
| Peak linear power for normal operating conditions (F Q = 2:93), (W cm$^1$) | 450 |
| Hot spot pellet center temperature (C) | 1770 |
| Peak linear power protection threshold (W = cm) | 590 |
| Hot spot pellet center temperature (C) | 2200 |
| DNB ratio: minimum DNBR under nominal operating conditions with | |
| F H = 1.75–Cos 1.45 | 2.33 |
| F H = 1.60–Cos 1.45 | 2.77 |
| *Fuel assembly* | |
| Number of fuel assemblies | 241 |
| Fuel assembly pitch (cm) | 21.504 |
| Active fuel height (cm) | 420 |
| Lattice pitch (cm) | 1.26 |

(continued)

**Table 1** (continued)

| Characteristics | Value |
|---|---|
| Number of fuel rods per assembly | 264 |
| Number of control rod assembly or instrumentation guide thimbles per assembly | 25 |
| Cladding material | Zircaloy |
| Outside fuel rod diameter (cm) | 0.95 |
| *Core performance characteristics* | |
| Power density in hot conditions [KW (core liter)$^{-1}$] | 89.3 |
| Power density in hot conditions [KW (fuel liter)$^{-1}$] | 99.3 |

## 4 Results and Discussion

The results obtained in *3D* are averaged according to the volume of the studied channel. The length of the channel is divided into 12 equal volumes and all the physical quantities were averaged according to these 12 volumes.

A set of results is obtained and presented. The first results are obtained for a normal operation of the *EPR* with a cooling fluid velocity of 5 m/s. The profiles of pressure, cooling fluid temperature and clad temperature along the channel were plotted. The temperature of the cooling fluid at the exit of nuclear reactor core, which is 328.8 °C, is compared to the one calculated which is equal to 340 °C. The relative difference being 3.3%, the results are considered satisfactory and a parametric study is made.

For the parametric study, the cooling fluid velocity is varied from 5 to 6 m/s by steps of 0.2 m/s. The obtained results are presented in Figs. 4, 5 and 6. In Fig. 4, one can see that the pressure does not vary too much, along the channel, with respect to the increase of the cooling fluid velocity. The pressure increases by only 0.1% when the cooling fluid velocity increases from 5 to 6 m/s. The evolution of pressure, along the channel, is linear in agreement with the physics of the phenomenon.

In Fig. 5, the parametric study shows that the profiles of the cooling fluid temperature have the same behavior except at the exit of the channel. One notices the correct physical behavior of the flow, when the cooling fluid velocity increases therefore the fluid flow, increases so the cooling process is more efficient. This behavior is confirmed by the temperature drop of the cooling fluid from 340 to 332 °C.

In Fig. 6, the different obtained profiles for the clad temperature show a similar behavior except at the peaks and the exit of the channel for the six values of the cooling fluid velocity used. All profiles have a peak located not in the middle of the channel but located at nearly 70% of the total height of the channel. This is the place where the temperature is the most important and therefore it is the critical zone of the channel. This result is valid when knowing that a sinusoidal heat flux profile was considered.

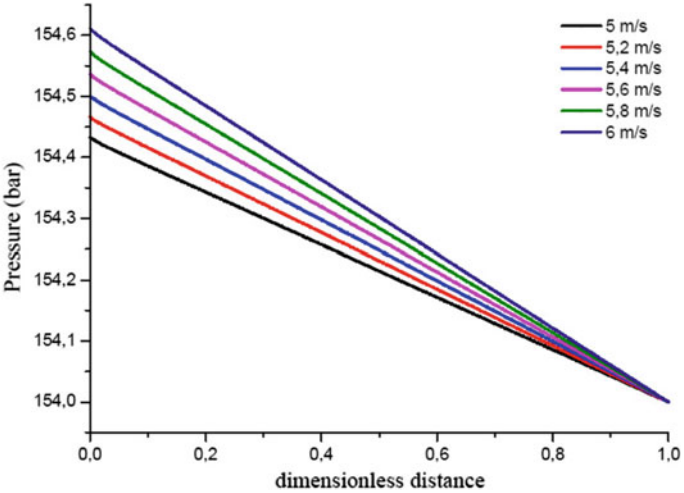

**Fig. 4** Pressure evolution in the channel

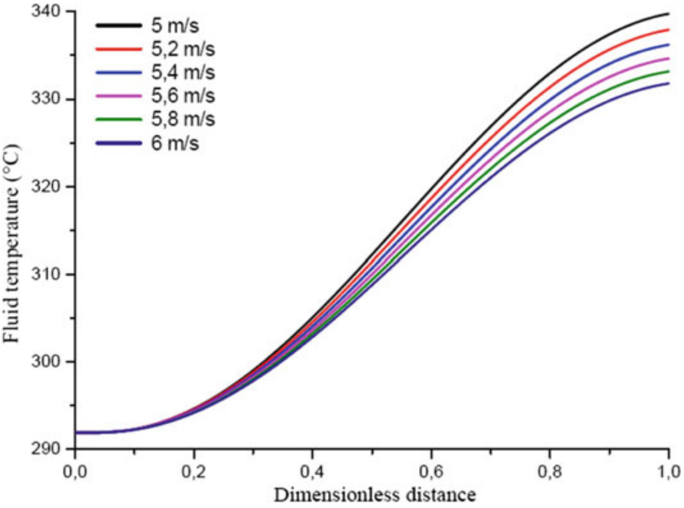

**Fig. 5** Fluid temperature evolution

## 5 Conclusions

In this work, *CFD* were used to investigate the behavior of the pressure, the temperature of the cooling fluid and the temperature of the fuel clad in the channel of the nuclear reactor core of an *EPR*. When analyzing different obtained profiles, one can say that their behaviors are physically correct. A relative difference calculation was done showing that results obtained by *CFD* are very acceptable. The cooling

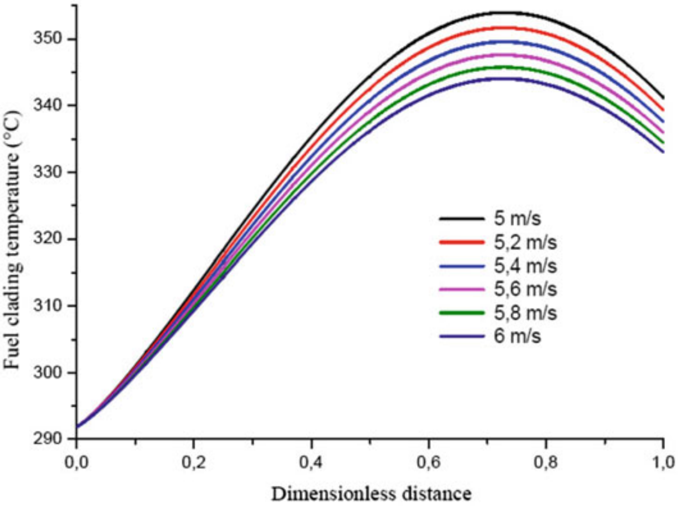

**Fig. 6** Clad temperature evolution

fluid temperature at the exit of the nuclear reactor core obtained by *CFD* is more important than that given by the design data of the *EPR*. The margin is close to 12 degrees. This shows that the results obtained by *CFD* are more conservative.

## References

Bernard J (2008) Energie nucléaire\les réacteurs nucléaires électrogènes. (Nuclear energy/power nuclear reactors) INSA Course, Toulouse

Delhaye JM (2008) Thermo-hydraulique des réacteurs. (Reactors thermalhaydraulics) INSTN, Paris

FEACE (2011) Fondation d'entreprise ALCEN pour la connaissance des énergies: Un réacteur à la pointe du progrès. Areva

Kaddour-Hoceine B, Gasmi A, Sidi-Ali K (2016) Analyse thermo-hydraulique d'un canal de réacteur nucléaire de puissance type AP1000 en utilisant les approches CFD, CFD & Tech Conference, CRND Draria. Algiers

Menter FR (1994) Two-equation eddy-viscosity turbulence models for engineering applications. AIAA J 32:269–289

Salama A, El-Morshedy S (2011) CFD simulation of the IAEA 10 MW generic MTR reactor under loss of flow transient. Ann Nucl Energy 38:564–577

Sengler G, Foret F, Schlosse G, Lisdat R, Stelletta S (1999) EPR core design. Nucl Eng Des 187:79–119

# Thermochemical Modeling in Hypersonic Reactive Flow Behind Strong Shock Wave

**Youcef Ghezali, Rabah Haoui and Amer Chpoun**

## 1 Introduction

The entry of space vehicles into a planetary atmosphere from outer space occurs at hypersonic speeds which lead to the formation of a strong shock wave. The high kinetic energy is converted to the thermal energy caused a chemical and thermal non-equilibrium flow around the body. As the temperature of a gas is increased above a certain value, the vibrational motion of molecules will become important, absorbing some of the energy which otherwise would go into the translational and rotational molecular motions. As the gas temperature is further increased, the molecules will begin to dissociate and even ionize. Under these conditions, the gas becomes vibrational excited and chemically reacting. The flow is modeled assuming that the continuum approximation is valid. It is assumed that the rotational and translational energy modes of all species can be described by a single temperature $T$ because the rotational energy equilibrates with the translational energy in just a few collisions. Furthermore, it is assumed that the vibrational and electronic energy modes of all species and the electron translational energy mode can be described by a single temperature $T_v = T_e = T_{el}$, this model called Two-temperature model $T.T_v$ (translational-rotational, vibrational-electronic-electron) proposed by park and the

---

Y. Ghezali (✉) · R. Haoui
LMESC, Department of Mechanical Engineering, University of Sciences and Technology
Houari Boumediene, 16111 Algiers, Algeria
e-mail: ghezali_youcef@yahoo.fr

R. Haoui
e-mail: haoui_rabah@yahoo.fr

A. Chpoun
LMEE, University of Paris-Saclay, 91000 Evry, France
e-mail: A.Chpoun@iut.univ-evry.fr

T. Boukharouba et al. (eds.), *Computational Methods and Experimental Testing In Mechanical Engineering*, Lecture Notes in Mechanical Engineering,
https://doi.org/10.1007/978-3-030-11827-3_3

temperatures of free electrons and electronic excitation are supposed to be identical and equal to the vibrational temperature of nitrogen $T_e = T_{el} = T_{vN_2}$ according to Park (1989) observation.

The air was considered as a reactive mixture of the eleven species $O_2$, $N_2$, NO, $O_2{}^+$, $N_2{}^+$, $NO^+$, $O^+$, $N^+$, $e^-$ in which the diatomic species $O_2$, $N_2$ and NO are considered in vibrational non-equilibrium. The vibrational energy of the molecular ions $N_2{}^+$, $O_2{}^+$ and $NO^+$ are assumed to be controlled by the vibrational temperatures of $T_{vO_2}$, $T_{vN_2}$, $T_{vNO}$, respectively. The reactions can be classified as (Park 1993) a dissociation reactions, exchange reactions including Zel'dovich's reactions, charge exchange reactions, associative ionization reactions and electron impact ionization reactions.

## 2 System of Equations

An arbitrary chemical reaction can be written as:

$$\sum_{s=1}^{ns} \upsilon_s^{\prime(r)} A_s^{(r)} \Leftrightarrow \sum_{s=1}^{ns} \upsilon_s^{\prime\prime(r)} A_s^{(r)} \tag{1}$$

$\upsilon_s^{\prime(r)}$ and $\upsilon_s^{\prime\prime(r)}$ are the stoichiometric mole numbers of the reactants and products of species $A_s^{(r)}$, the source term of the chemical equation of evolution of the species s is given provided through:

$$\dot{\omega} = M_s \sum_{(r)} (\upsilon_s^{\prime\prime\prime(r)} - \upsilon_s^{\prime(r)}) \left[ k_f^{(r)} \prod_{(r)} \left( \frac{\rho_r}{M_r} \right)^{\upsilon_s^{\prime(r)}} - k_b^{(r)} \prod_{(r)} \left( \frac{\rho_r}{M_r} \right)^{\upsilon_s^{\prime\prime(r)}} \right] \tag{2}$$

Both forward and backward reaction rates are represented by $k_f^{(r)}$ and $k_b^{(r)}$. The forward rate constant, $k_f$ is assumed to follow the Arrhenius law:

$$k_f = A_f T^{b_f} \mathrm{e}^{-\frac{\theta_{d,f}}{T}} \tag{3}$$

where $A_f$ a pre-exponential factor $b_f$ is the temperature exponent and $\theta_{d,f}$ is the temperature of activation derived from the activation energy. Park (1993) suggested a geometrically average rate controlling temperature $T_a$ for dissociation reactions. $T_a$ is defined as:

$$T_a = T^q T_{v,m}^{1-q} \tag{4}$$

With $q = 0.5$ in the original formulation proposed by Park. Sharma et al. (1992) suggested that the value of $q$ varied from 0.6 to 0.7 might be more realistic for high enthalpy flow and consequently, a value of 0.7 is used in the present study.

$$k_b = \frac{k_f}{k_{eq}} \tag{5}$$

The backward reaction rate is calculated from forward reaction rate and equilibrium reaction rate coefficient $k_{eq}$ which is given as a separate polynomial curve fit form stated by Park (1990) as given below:

$$k_{eq} = exp(A_1 Z^{-1} + A_2 + A_3 \ln Z + A_4 Z + A_5 Z^2) \tag{6}$$

where:

$$Z = \frac{10000}{T} \tag{7}$$

The Euler equations for the mixture in non-equilibrium contains in addition for mass, momentum and energy conservation, equations of the evolution of chemical species and the energy of vibration of the molecules. The conservation equations of the flow are:

$$\frac{d(\rho u)}{dx} = 0 \tag{8}$$

$$\frac{d(\rho u^2 + p)}{dx} = 0 \tag{9}$$

$$\frac{d(p + \rho e)u}{dx} = 0 \tag{10}$$

The equation of relaxation of the chemical species is written:

$$\frac{d(\rho_s u)}{dx} = \omega_{cs} \tag{11}$$

$e$ is the total energy per unit mass which include translational-rotational and vibrational energies, the enthalpies of formation of the species, the species electronic energy, the electron energy and the kinetic energy (Candler and Park 1988) which yields:

$$e = \sum_{s \neq e}^{10} c_{vtr,s} T + \sum_{m=1}^{6} Y_s e_{vm} + \sum_{s=1}^{11} Y_s h_{fs}^0 + \sum_{s=1}^{11} Y_s e_{el,s} + \frac{1}{2} \sum_{s=1}^{11} Y_s u_s^2 + E_e \tag{12}$$

where $c_{vtr,s}$ is the translational-rotational specific heat of species $s$, given by:

$$c_{vtr,s} = c_{vtranslation,s} + c_{vrotation,m} \tag{13}$$

where the translational and rotational specific heat at a constant volume is assumed constant and is given by:

$$c_{vtranslation,s} = \frac{3}{2}\frac{R}{M_s} \tag{14}$$

$$c_{vrotation,m} = \frac{R}{M_m} \tag{15}$$

where $M_s$ and $M_m$ represent a species and molecules molecular weight, respectively.

The species vibrational energy per unit mass $e_{v,m}$ is modelled using a harmonic oscillator as:

$$e_{v,m} = \frac{R}{M_m}\frac{\theta_{v,m}}{\exp(\frac{\theta_{v,m}}{T_{v,m}}) - 1} \tag{16}$$

where $R$ is the universal gas constant and $\theta_{v,m}$ is the characteristic temperature of vibration of the molecule $m$, the vibrational mode becomes excited at the characteristic vibrational temperature $\theta_{v,m}$, typically $\theta_{v,\mathrm{N}_2}$= 3392.7 K for the ground electronic state of $\mathrm{N}_2$ and $\theta_{v,\mathrm{O}_2}$= 2240 K for $\mathrm{O}_2$.

The characteristic temperature of vibration $\theta_{v,m}$ for the diatomic molecules and the enthalpies of formation for all species $h^0_{fs}$ are shown in (Allouche et al. 2014). The species electronic energy is assumed to follow a Boltzmann distribution at the excitation temperature $T_{el}$ where $T_e = T_{el} = T_{v\mathrm{N}_2}$ according to the Two-Temperature model (Park 1989), $e_{el}$ (Candler and Park 1988) is modelled by:

$$e_{el}(T_{el}) = \frac{R}{M_s}\frac{\sum_i g_{i,s}\theta_{ei,s}e^{-\theta_{ei,s}/T_{el}}}{\sum_i g_{i,s}e^{-\theta_{ei,s}/T_{el}}} \tag{17}$$

where $\theta_{ei,s}$ and are the characteristic electronic temperature and the degeneracy of a given electronic state $i$ for species $s$, respectively. $\theta_{ei,s}$ and $g_{i,s}$ are shown in (Casseau et al. 2016).

The electron energy per unit mass $E_e$ (Candler and Park 1988) is given by:

$$E_e = Y_e c_{ve} T_e + \frac{1}{2} Y_e u_e^2 \tag{18}$$

where the electron specific heat at a constant volume is expressed by:

$$c_{ve} = \frac{3}{2}\frac{R}{M_e} \tag{19}$$

The pressure is calculated assuming that each species can be modeled using a perfect gas relation and Dalton's law of partial pressures so that:

$$p = \sum_{s \neq e}^{11} p_s + p_e = \sum_{s \neq e}^{11} \rho_s \frac{R}{M_s} T + \rho_e \frac{R}{M_e} T_e \tag{20}$$

The model used for calculating the energy exchange between translational and vibrational modes has the Landau Teller form (Park 1993):

$$\frac{de_{v,m}}{dt} = \frac{e_{v,m}(T) - e_{v,m}}{\tau_m} \tag{21}$$

$e_{v,m}(T)$ is the equilibrium energy of vibration at the temperature of translation-rotation expressed as:

$$e_{v,m}(T) = \frac{R}{M_m} \frac{\theta_{v,m}}{\exp(\frac{\theta_{v,m}}{T}) - 1} \tag{22}$$

$\tau_m$ is the relaxation time expressed as (Park 1993):

$$\tau_m = \tau_{MW,m} + \tau_{p,m} \tag{23}$$

The relaxation time of species m $\tau_{MW,m}$ is calculated using the molar averaged correlation developed by Millikan and White (Park 1993):

$$\frac{1}{\tau_{MW,m}} = \sum \frac{x_s}{\tau_{MWm,s}} \tag{24}$$

Here $x_s$ is the molar fraction of species $s$ and $\tau_{MWm,s}$ the vibrational relaxation time of $m$ due to the collision with species $s$. Millikan and White present semi-empirical correlations between observed vibrational relaxation times over a temperature range of 300–8000 K and the relevant molecular constants. These correlations permit an estimation of $\tau_{MWm,s}$, the vibrational relaxation time for species $m$ due to inelastic collisions. The correlation (Park 1993) is expressed as:

$$\tau_{MWm,s} = \frac{1}{p} \exp\left[A_{m,s}\left(T^{\frac{1}{3}} - 0.015\mu_{m,s}^{\frac{1}{4}}\right) - 18.42\right] \tag{25}$$

where $p$ must be given in atmospheres.

$$A_{m,s} = 1.16 \times 10^{-3} \mu_{m,s} \theta_{v,m}^{\frac{4}{3}} \tag{26}$$

$\mu_{m,s}$ is the reduced molecular weight in g/mole and computed as:

$$\mu_{m,s} = \frac{M_m M_s}{M_m + M_s} \tag{27}$$

Park (1989) proposed a second relaxation time to be added to the Landau–Teller relaxation time which takes account of the limited collision cross section. For temperatures above 8000 K, Park's high temperature correction is adopted as:

$$\tau_{p,m} = \frac{1}{N_m c_m \sigma_m} \tag{28}$$

$$c_m = \sqrt{\frac{8RT}{\pi M_m}} \tag{29}$$

where $c_m$ is the average molecular speed or the thermal speed of species $s$ and $N_m$ is the number density of the colliding particles. The empirically found formula for the limiting collision cross section $\sigma_m$ following Park (1989) is:

$$\sigma_m = 10^{-21}\left(\frac{50000}{T}\right)^2 \tag{30}$$

Park (1989) proposes an empirical link function between the Landau–Teller and diffusive rates of the form:

$$\frac{de_{v,m}}{dt} = \frac{e_{v,m}(T) - e_{v,m}}{\tau_m}\left(\frac{T_{ch} - T_{vm}}{T_{ch} - T_{vm,ch}}\right)^{S-1} \tag{31}$$

$$S = 3.5\exp\left(-\frac{\theta_{v,m}}{T_{ch}}\right) \tag{32}$$

where the expressions $T_{ch}$ and $T_{vm,ch}$ are translational rotational and the species vibrational temperatures evaluated just behind the shock wave.

For the vibrational-vibrational exchange, we employ the expression by Candler (Furudate et al. 2000):

$$\omega_{VV,m} = \sum_{r\neq m}\sqrt{\frac{8RT}{\pi\mu_{mr}}}\sigma_{mr}N_a P_{mr}\left(\frac{\rho_m}{M_m}E_{vr} - \frac{\rho_r}{M_r}E_{vm}\right) \tag{33}$$

Symbol $\mu_{mr}$ denotes the reduced molar mass and $N_a$, the Avogadro's number. The energy transfer probability $P_{mr}$ and the collision cross-sections $\sigma_{mr}$ are given by the following form proposed by Park and Lee (1995):

$$p_{\mathrm{N_2-NO}} = 5.5\times10^{-5}\left(\frac{T}{1000}\right)^{2.32} \tag{34}$$

$$p_{\mathrm{N_2-O_2}} = 3.0\times10^{-5}\left(\frac{T}{1000}\right)^{2.32} \tag{35}$$

$$p_{\mathrm{O_2-N}O} = 5.5\times10^{-5}\left(\frac{T}{1000}\right)^{2.32} \tag{36}$$

$$\sigma_{mr} = 10^{-19} p_{mr} \tag{37}$$

## 3 Results and Discussion

In this work, two points of the Fire II re-entry trajectory are selected as test cases. The flow conditions are listed in Table 1 (Panesi et al. 2009). The classical Rankine-Hugoniot jump relations are used in order to calculate the flow parameters just behind the shock.

Figure 1 shows the evolution of the translational-rotational and vibrational temperatures just behind the shock wave for the 1634 s case (elapsed time from the launch) (Panesi et al. 2009). Just after the shock, the translational-rotational temperature falls from a value of 62,700 K to almost 10,600 K in a relaxation range of 1 cm which agrees well with the results obtained by Panesi et al. (2009). This decrease is mostly the result of the vibrational and electronic excitation and also by the chemical reactions such as dissociation and ionization which are endothermic reactions. We observe that the vibrational temperature of $T_{vO_2}$, $T_{vN_2}$, $T_{vNO}$ are lower than those obtained by Panesi et al. (2009) in which the vibrational state populations of the $N_2$, $O_2$, and NO molecules are assumed to follow Boltzmann distributions respectively at $T_{vO_2}$, $T_{vN_2}$, $T_{vNO}$. In our study the vibrational temperature are determined directly from the vibrational energy Eq. (16) in which the vibrational energies of the diatomic species are based on the harmonic oscillator assumption.

**Table 1** Title of the table

| Trajectory point | t = 1634 s | t = 1643 s |
|---|---|---|
| H (km) | 76.42 | 53.04 |
| Pressure, $P_1$(pa) | 2 | 21.3 |
| Temperature, $T_1$(K) | 195 | 276 |
| Velocity, $U_1$(m/s) | 11,360 | 10,480 |

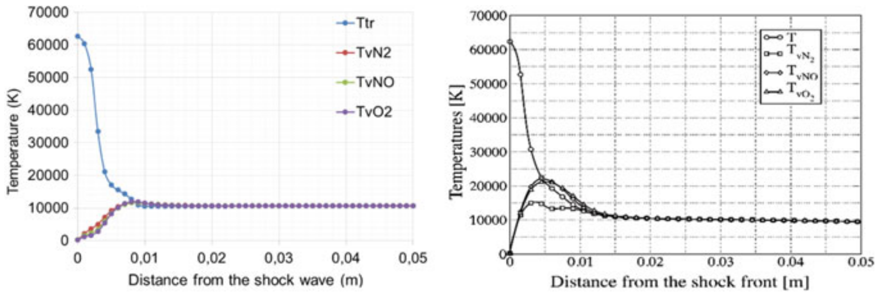

**Fig. 1** 1634 s case, evolution of translational and vibrational temperatures behind the shock wave compared to Panesi's results (right) (Panesi et al. 2009)

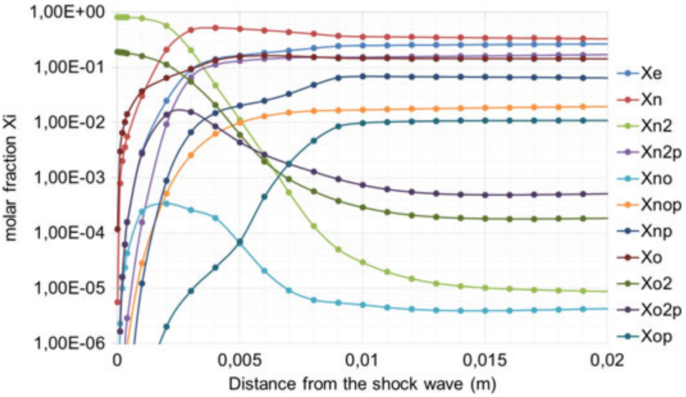

**Fig. 2** 1634 s case, evolution of species mole fractions behind the shock wave

The Fig. 2 shows the evolution of species mole fractions behind the shock wave for the 1634 s case. After the shock, the oxygen $O_2$ and the nitrogen $N_2$ molecules begin to dissociate and their dissociation allows the formation of other species such as O, N and NO, which is produced by the Zel'dovich reactions. Due to the high temperature, ionization occurs by the formation of ions such as $O_2^+$, $N_2^+$, $NO^+$, $O^+$, $N^+$ and $e^-$. Their values at the equilibrium region are presented by $O_2 = 3\ 10^{-2}$ %, $N_2 = 5.8\ 10^{-4}$%, NO = 6 $10^{-4}$ %, O = 14.4 %, N = 26 %, $O_2^+ = 0.07$ %, $N_2^+ = 21.6$ %, $NO^+ = 2.08$ %, $O^+ = 1.05$ %, $N^+ = 4.95$ % and $e^- = 29.8$ %.

Figure 3 shows the evolution of the translational-rotational and vibrational temperature behind the shock wave for the 1643 s case where the initial conditions before the shock for the velocity, temperature and pressure are 10.48 km/s, 276 K and 21.3 pa respectively. It is observed that the behavior of the temperatures follows the same evolutions as those found in the first case. In this case, the relaxation zone is much smaller and this is due to the fact that the increase in pressure increases collisions between particles. Consequently, the dissociation and ionization occur rapidly and the equilibrium state is reached quickly. As a result, the relaxation zone diminishes.

## 4 Conclusion

This study focuses on a reactive and ionized flow in a vibrational non equilibrium behind an intense shock wave. A computer code was developed to solve the system of equations where the finite differences method was selected with a convergence criterion of $10^{-6}$. The finite-rate chemistry model and the energy relaxation model used to describe the chemical and thermal non-equilibrium of the flowfield are also presented according to Park's work. The results were compared with other recently published studies in literature. Among the physical and chemical phenomena that occur behind a strong shock, it was noticed that the flow temperature is strongly

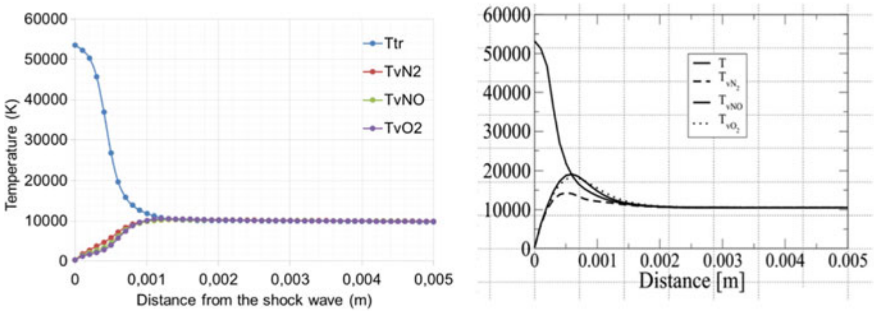

**Fig. 3** 1643 s case, evolution of translational and vibrational temperatures behind the shock wave compared to the Panesi's results (right) (Panesi et al. 2009)

decreasing in the beginning because the reactions rates are rapid; most of the thermal energy is used to provoke the dissociation and ionization. Then, given that the temperatures is diminishing, reactions rates are slower, consequently we tend to an equilibrium state. In contrary, vibrational temperature takes a time to be excited before reaching its equilibrium value.

## References

Allouche R, Haoui R, Renane R (2014) Numerical simulation of reactive flow in non-equilibrium behind a strong shock wave during re-entry into earth's atmosphere. J Mech Ind 15:81–87. https://doi.org/10.1051/meca/2014002

Candler GV, Park C. (1988) The computation of radiation from nonequilibrium hypersonic flows, AIAA 1988-2678. https://doi.org/10.2514/6.1988-2678

Casseau V, Palharini R, Scanlon T, Brown R (2016) A two-temperature open-source cfd model for hypersonic reacting flows, part one: zero-dimensional analysis. Aerospace 3(4):34. https://doi.org/10.3390/aerospace3040034

Furudate M, Suzuki T, Sawada K, (2000) Calculation of intermediate hypersonic flow using multi-temperature model, AIAA 2000–0343. https://doi.org/10.2514/6.2000-343

Panesi M, Magin T, Bourdon A, Bultel A, Chazot O (2009) Analysis of the FIRE II flight experiment by means of a collisional radiative model. J Thermophys Heat Transfer 23:236–248. https://doi.org/10.2514/1.39034

Park C (1989) Assessment of two-temperature kinetic model for ionizing air. J Thermophys Heat Transfer 3:233–244. https://doi.org/10.2514/3.28771

Park C (1990) Nonequilibrium hypersonic aerothermodynamics. Wiley, New York

Park C (1993) Review of chemical-kinetic problems of future NASA missions. I—earth entries. J Thermophys Heat Transfer 7:385–398. https://doi.org/10.2514/3.431

Park C, Lee SH (1995) Validation of multi-temperature nozzle flow code. J Thermophys Heat Transfer 9:9–16. https://doi.org/10.2514/3.622

Sharma SP, Hou WM, Park C (1992) Rate parameters for coupled vibration-dissociation in a generalized SSH approximation. J Thermophys Heat Transfer 6:9–21. https://doi.org/10.2514/3.312

# Kinematic and Dynamic Modeling and Simulation Analysis of a Cable-Driven Continuum Robot

**Ammar Amouri, Chawki Mahfoudi and Selman Djeffal**

## 1 Introduction

Continuum robots are a category of robotic systems inspired by many similar biological structures, which can bend at any point along their central axis. They imitate morphologies and movements of some animals like elephant trunks, tentacles and snakes (Immega and Antonelli 1995; Falkenhahn et al. 2015; Walker and Hannan 1999; Buckingham and Graham 2003; McMahan et al. 2005; McMahan and Walker 2009). These robots differ fundamentally from the traditional robots by having an unconventional structure (Robinson and Davies 1999). Their actuators are incorporated into the structure, such as cables and bellows instead of mechanical actuators. Compared with rigid robots, continuum robots have provided a number of advantages in terms of maneuverability, handling, grasping and locomotion (Webster and Jones 2010).

Research activities in the field of this category have evolved in two main directions: hard or soft structures, depending on the material of their parts. The first class handles manipulators construct by a serial concatenation of rigid bodies or parallel structures (Walker and Hannan 1999; Buckingham and Graham 2003), and the second one process manipulators with multiple bending sections (Webster and Jones

---

A. Amouri (✉)
Department of Mechanical Engineering, University of Brothers Mentouri,
Constantine, Algeria
e-mail: ammar_amouri@yahoo.fr

C. Mahfoudi · S. Djeffal
Department of Mechanical Engineering, University Labri Ben M'Hidi,
Oum El Bouaghi, Algeria
e-mail: c_mahfoudi_dz@yahoo.fr

S. Djeffal
e-mail: selmanleer@gmail.com

T. Boukharouba et al. (eds.), *Computational Methods and Experimental Testing In Mechanical Engineering*, Lecture Notes in Mechanical Engineering,
https://doi.org/10.1007/978-3-030-11827-3_4

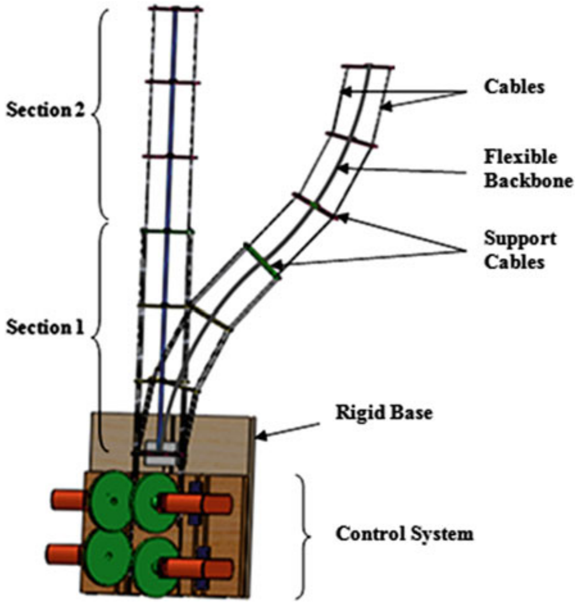

**Fig. 1** Planar Cable-driven continuum robot design

2010; Amouri et al. 2017). One of these structures is called cable-driven continuum robot that interested in this work.

The fundamental problem in continuum robots is kinematics modeling. However, based on constant curvature assumption, tens of kinematic models are developed and explored in details in the literature such as (Webster and Jones 2010; Amouri et al. 2017; Amouri et al. 2014; Bailly and Amirat 2005; Mahl et al. 2014; Lakhal et al. 2014). On the other hand, computing dynamic modeling of continuum manipulators remains a difficult task. Several methods and theories exist such as: Euler-Lagrange method, Cosserat rod theory, virtual power principle and so on. Despite that, there are only a very few contributions about the dynamic modeling, in particular, for the class of continuum robot under consideration (Amouri et al. 2018; Rone and Ben-Tzvi 2014; He et al. 2013) and this due to the difficulty of solving the complex resulting partial differential equations.

In this paper a Planar Cable-Driven Continuum Robot is designed and developed using Solidworks software as shown in Fig. 1. Then, the mathematical formulations of the considered robot are given providing the calculation of velocities. Followed by developing equations of motion using Euler-Lagrange method. To emphasize the obtained results in Matlab/Simulink software for the resulted dynamic model, simulation by using Solidworks is carried out. The results of both software are presented and discussed.

The paper is organized as follows: Sect. 2 describes the Planar Cable-Driven Continuum Robot. Kinematic models are derived in Sect. 3. By using the Lagrange method, the dynamic model of the *P-CDCR* is obtained in Sect. 4. Numerical

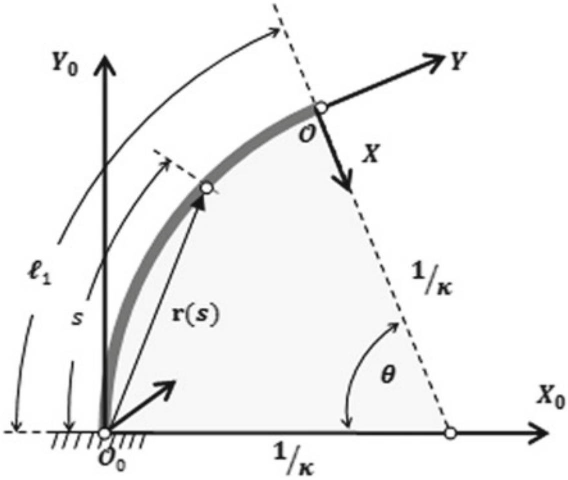

**Fig. 2** Kinematics of the flexible backbone

examples simulating the dynamic model are presented and discussed in Sect. 5. Besides, the verification of the obtained results is made up in Solidworks software.

## 2 Planar Cable-Driven Continuum Robot and Description

The design scheme of *P-CDCR* consists of two sections which are presented in Fig. 1. Each section is composed of three basic elements: flexible backbone, support cables and two inextensible cables. The principal of functioning of the *P-CDCR* consists of applying adequate electrical voltages to the motors in order to generate tensions on the cables. The resulting applied force at the end-point leads to displacement towards a corresponding position on its workspace presenting by deflections of flexible backbone. In this work, only the first section is considered.

In order to describe the first section of *P-CDCR* in accordance with the structural design presented in Fig. 1, two reference frames are defined. The first one is the absolute frame $\Re_0(O_0, X_0, Y_0)$, commonly called reference workshop. Then, the frame $\Re(O, X, Y)$ is assigned to the end-point of the flexible backbone. This section is parameterized by: arc length $l$, curvature $\kappa$ and bending angle $\theta$ (see Fig. 2).

## 3 Kinematic Modeling

This section defines the kinematic model of the *P-CDCR* under consideration. The modeling assumptions used in this paper are introduced firstly; then, position vectors and orientation matrices are derived thereafter.

### 3.1 Modeling Assumptions

- Without loss of generality, the developments of kinematic and dynamic models are based on the following assumptions:
  - the central axis of flexible backbone is modeled by an inextensible arc of circle (Webster and Jones 2010),
  - the section has one degree of freedom (*DoF*) for planar bending;
  - no external forces, except driving forces,
  - the flexible backbone has a uniform mass distribution along its length, and possesses a high stiffness that permits the torsion avoiding,
  - the flexible backbone is assumed to have linear relation between strain and stress (Fertis 1996).

### 3.2 Kinematics Modeling

To derive kinematics variables namely linear position, orientation, linear velocity and angular velocity, exploiting our previous work developed in reference (Amouri et al. 2018); accordingly, the position vector $r$ of the any point on the flexible backbone with respect to its reference frame $\Re_0$ can be expressed as :

$$r = \begin{cases} X = \frac{l}{\theta}(1 - \cos(\theta_s)) \\ Y = \frac{l}{\theta}\sin(\theta_s) \end{cases} \tag{1}$$

With:

$$\theta_s = \frac{s \cdot \theta}{l} \tag{2}$$

At each point of flexible backbone, the orientation can be determined by a rotation matrix $R$ given as follows:

$$R = \begin{bmatrix} \cos(\theta_s) & \sin(\theta_s) \\ -\sin(\theta_s) & \cos(\theta_s) \end{bmatrix} \tag{3}$$

The linear velocity of any point at $s$ can be determined by derivation of Eq. (1) with respect to time as follows:

$$\dot{r} = \begin{cases} \frac{dX}{dt} = \frac{1}{\theta}\big[s \cdot \sin(\theta_s) - \frac{l}{\theta}(1 - \cos(\theta_s))\big]\dot{\theta} \\ \frac{dY}{dt} = \frac{1}{\theta}\big[s \cdot \cos(\theta_s) - \frac{l}{\theta}\sin(\theta_s)\big]\dot{\theta} \end{cases} \tag{4}$$

## 4 Dynamic Modeling

The structure of *P-CDCR* consists of one flexible backbone, two cables and a number of support cables (platelets). In this study, we focus only on the flexible backbone. Thus, to derive the dynamic model using the Euler-Lagrange method, terms namely kinetic and potential energies should be calculated firstly. We start with the calculation of the kinetic energy, the potential energy and the coupled second-order differential equations are obtained thereafter.

### *4.1 Kinetic Energy of the P-CDCR*

Following what was mentioned before; the kinetic energy of the *P-CDCR* is exactly the flexible backbone's kinetic energy $T$. Because the flexible backbone radius is very small compared to its length, the rotational kinetic energy can be ignored. Consequently, the kinetic energy can be expressed with the translational energy as follows:

$$T = \frac{m_b}{2} \int_0^l \dot{r}^2 ds \tag{5}$$

where: $m_b$ is the flexible backbone mass and $s$ is curvilinear coordinate.

Developing Eq. (5), gives:

$$T = \frac{1}{2} l^3 m_b \left( -\frac{4}{\theta^5} \sin\theta + \frac{2}{\theta^4} \cos\theta + \frac{2}{\theta^4} + \frac{\theta^2}{3} \right) \dot{\theta}^2 \tag{6}$$

### *4.2 Kinetic Energy of the P-CDCR*

Due to low weight of flexible backbone, the gravitational energy can be ignored relative to elastic potential energy where the maximum ratio between them is less than 0.9% (see Fig. 3). Thus, the potential energy of *P-CDCR* can be expressed as (Fertis 1996):

$$U = \frac{E I_b}{2l} \theta^2 \tag{7}$$

where: $E$ is the module of elasticity, $I_b$ and $l$ are, respectively, the second moment of cross-sectional area and the length of each flexible backbone.

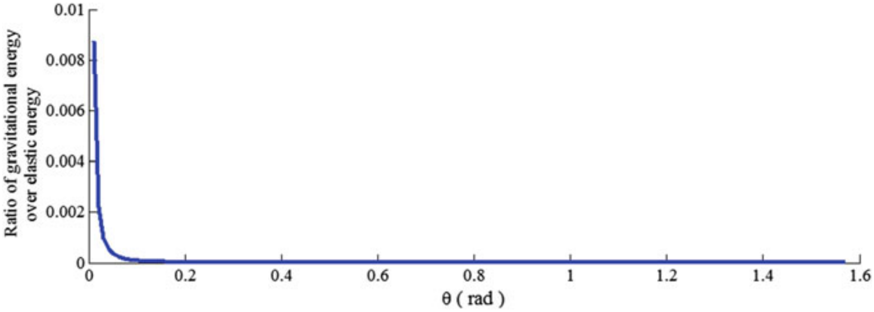

**Fig. 3** Ratio between gravitational energy over elastic energy of the flexible backbone calculated as function of the bending angle

### 4.3 *Dynamical Model of the P-CDCR*

For generalized coordinate θ, the obtained dynamic model from the application of Euler-Lagrange's method can be represented in the compact form as:

$$M\ddot{\theta} + C\dot{\theta} + K\theta = F(t) \tag{8}$$

where: $M$, C and K are given as follows:

$$M = m_b l^2 \left( -\frac{4}{\theta^5} \sin\theta + \frac{2}{\theta^4} \cos\theta + \frac{2}{\theta^4} + \frac{\theta^2}{3} \right) \tag{9}$$

$$C = m_b l^3 \left( -\frac{18}{\theta^5} \cos\theta + \frac{3}{\theta^4} \sin\theta + \frac{36}{\theta^6} \sin\theta - \frac{1}{\theta^3} + \frac{8}{\theta^5} \right) \tag{10}$$

$$K = \frac{EI_b}{l} \tag{11}$$

## 5 Simulation Studies

To underline the validity of the proposed dynamic model, some numerical examples are performed using Matlab software. Moreover, to confirm the obtained results, simulation studies using Solidworks software are carried out. The estimated parameters and geometric properties of the *P-CDCR* under consideration are given in Table 1. We notice that the mass and modulus of elasticity of flexible backbone are taken from Solidworks library according to structure design.

**Table 1** Parameters of the P-CDCR

| Parameters | Designation | Value |
|---|---|---|
| $l$ | Flexible backbone length | 300 mm |
| $d$ | Flexible backbone diameter | 5 mm |
| $m_b$ | Flexible backbone mass | 6 g |
| E | Modulus of elasticity | 2 GPa |

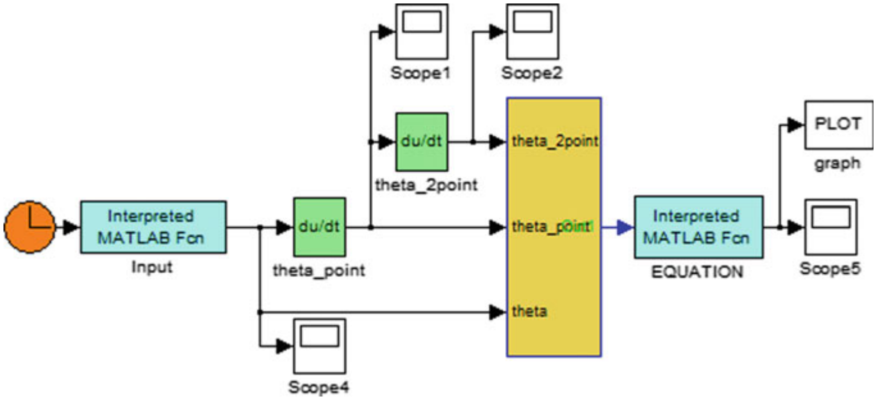

**Fig. 4** P-CDCR modeled in Matlab/Simulink

## 5.1 Matlab Simulation Run

The dynamic model has been implemented in Matlab/Simulink including the numerical derivatives of velocities and accelerations, as shown in Fig. 4. In this example, we have estimated the actuated force on cable 1 required for the end-point of *P-CDCR* to track the desired trajectory in its workspace. Figure 5 shows the obtained simulation results of dynamic responses for tracking a circular path. Some configurations of the considered *P-CDCR* behavior, which are performed after stabilization of the dynamic model simulation, are shown in Fig. 6.

## 5.2 Solidworks Simulation Run

Solidworks environment is a *3D* mechanical computer-aided design used to create models, assemblies and modeling it. Among its advantages is to evaluate the research results within a small amount of time, reduce the errors and so on. Various cases can be treated by Solidworks software such as: static study and linear and nonlinear

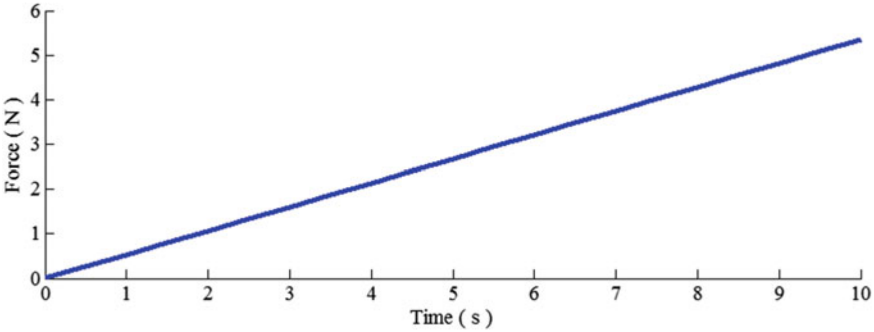

**Fig. 5** Temporal evolutions of force on the cable 1

**Fig. 6** Some configurations of the P-CDCR (Matlab)

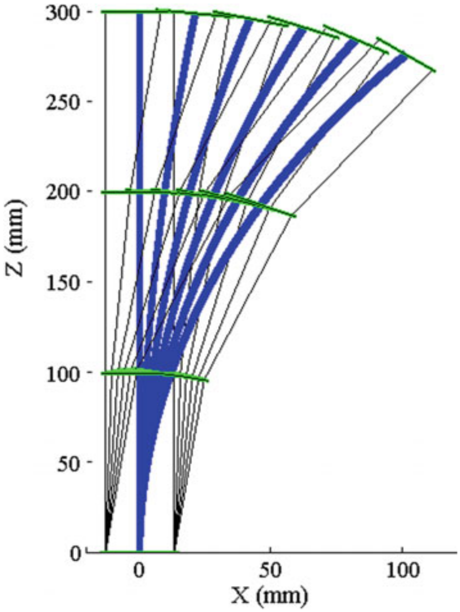

dynamic studies, etc. in this work, two examples on static and nonlinear dynamic cases are presented and discussed in the following.

### a. **Nonlinear dynamic case**

In this simulation, we have estimated the motions of *P-CDCR*. Thus, the resulted dynamic responses of the first example (e.g. Matlab simulation run) are used as step inputs. The simulation has been accomplished within 24 min 20 s, corresponding to 100 position captures. Figure 7 shows some configurations of the flexible backbone. Cartesian trajectory tracked by the end-point of the *P-CDCR* as well as Cartesian velocities and accelerations along *X* and *Z* axis are presented in Fig. 8.

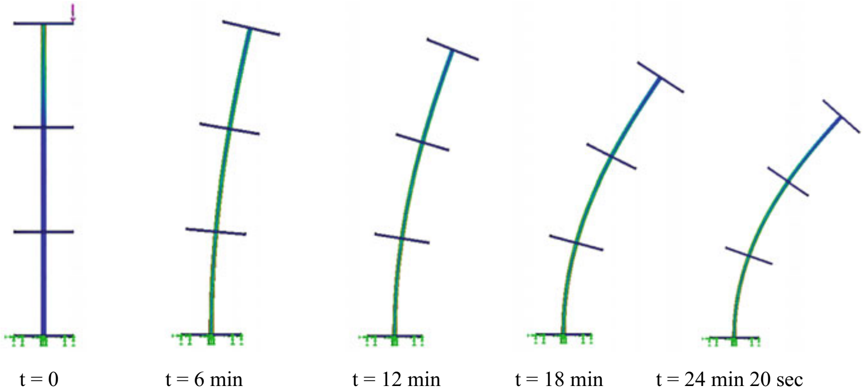

**Fig. 7** Some configurations of the P-CDCR (Solidworks)

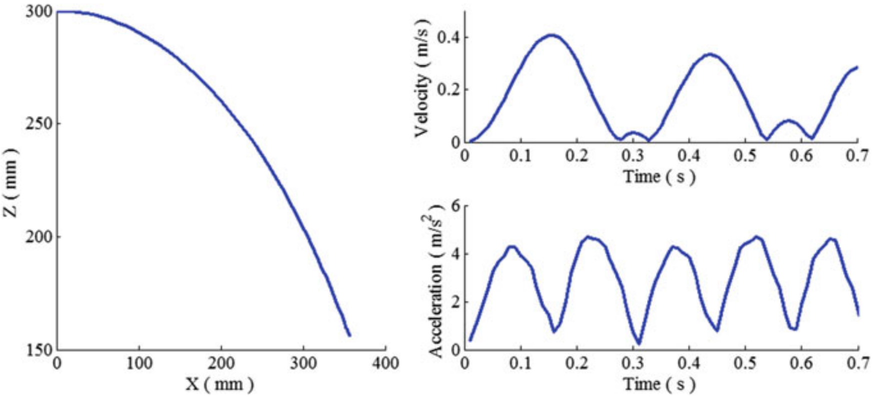

**Fig. 8** End-point trajectory and its velocity and acceleration (Solidworks)

### b. Nonlinear dynamic case with gravitational effect

The same inputs used previously are applied in this example by adding the gravitational effect of the flexible backbone. Figure 9 shows the length profiles determinate by using Solid works software and those obtained by the proposed model, where the Euclidean errors are deduced. The displayed curves show that there is a significant convergence between them, where Euclidian errors along $X$ and $Y$ axis is very smaller that validate our ignoring of gravitational energy over elastic one.

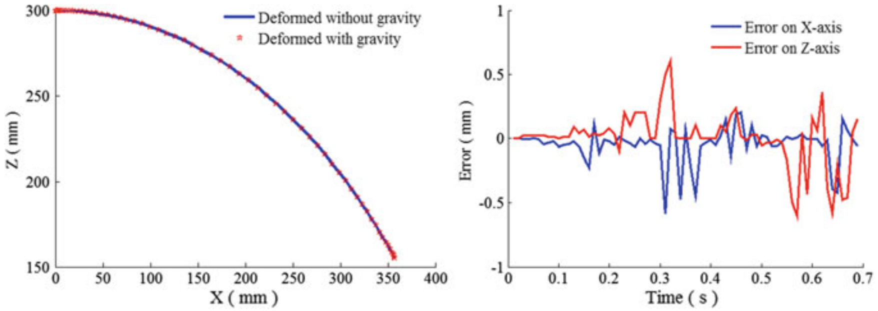

**Fig. 9** End-point trajectory of flexible backbone from Solidworks software and errors between them

## 6 Conclusion

The objective of this work is modeling and simulation of planar cable-driven continuum robot, precisely its flexible backbone, by using Matlab/Simulink and Solidworks software. Mathematical expressions of kinematical models are developed on the basis of constant curvature assumption and the dynamical model is derived by using the Euler-Lagrange method. The obtained results from both software are compared and discussed. From this analysis, it was found that the displayed trajectories are similar to the validating proposed models. On the other hand, by increasing additional forces (i.e. gravitational effects), the deformed of flexible backbone is not a circular arc.

## References

Amouri A, Mahfoudi C, Zaatri A et al (2014) A new approach to solve inverse kinematics of flexible continuum planar robot. AIP Conf Proc 1618:643–646

Amouri A, Mahfoudi C, Zaatri A et al (2017) A metaheuristic approach to solve inverse kinematics of continuum manipulators. J Syst Control Eng 231(5):380–394

Amouri A, Zaatri A, Mahfoudi C (2018) Dynamic modeling of a class of continuum manipulators in fixed orientation. J Intelligent and Rob Syst 91(3–4):413–424

Bailly Y, Amirat Y (2005) Modeling and control of a hybrid continuum active catheter for aortic aneurysm treatment. In: 2005 IEEE international conference on robotic and automation, Barcelona, Spain, pp 924–929

Buckingham R, Graham A (2003) Reaching the unreachable—snake arm robots. In: 2003 International Symposium of Robotics, Chicago

Falkenhahn V, Mahl T, Hildebrandt A et al (2015) Dynamic modeling of bellows-actuated continuum robots using the Euler-Lagrange formalism. IEEE Trans Rob 31(6):1–13

Fertis DG (1996) Advanced mechanics of structure. Marcel Dekker, Inc., New York City

He B, Wang Z, Li Q, Xie H, Shen R (2013) An analytic method for the kinematics and dynamics of a multiple-backbone continuum robot. Int J Adv Rob Syst 10:1–13

Immega G, Antonelli K (1995) The KSI tentacle manipulator. In: 1995 IEEE International Conference on Robotics and Automation, pp 3149–3154

Lakhal O, Melingui A, Chibani A, et al (2014) Inverse kinematic modeling of a class of continuum bionic handling arm. In: 2014 ASME/IEEE international conference on advanced intelligent mechatronics, Besançon, France, pp 1337–1342

Mahl T, Hildebrandt A, Sawodny O (2014) A variable curvature continuum kinematics for kinematic control of the bionic handling assistant. IEEE Trans Rob 30(4):935–949

McMahan W, Walker ID (2009) Octopus-inspired grasp-synergies for continuum manipulators. In: 2009 IEEE international conference on robotics and biomimetics, ROBIO, pp 945–950

McMahan W, Jones BA, Walker ID (2005) Design and implementation of a multi-section continuum robot: air-Octor. In: 2005 IEEE/RSJ international conference on intelligent robots and systems, pp 2578–2585

Robinson G, Davies JBC (1999) Continuum robots—a state of the art. In: 1999 IEEE international conference on robotics and automation, Detroit, Michigan, pp 2849–2854

Rone W, Ben-Tzvi P (2014) Mechanics modeling of multi-segment rod-driven continuum robots. J Mech Rob 6

Walker ID, Hannan MW (1999) A novel elephant's trunk' robot. In: 1999 IEEE/ASME, International Conference on Advanced Intelligent Mechatronics, pp 410–415

Webster RJ, Jones BA (2010) Design and kinematic modeling of constant curvature continuum robots: a review. Int J Robot Res 29(13):1661–1683

# A Novel Constitutive Modelling for Spring Back Prediction in Sheet Metal Forming Processes

**Ahmed Maati, Laurent Tabourot, Pascale Balland, El Hadj Ouakdi and Salim Belaid**

## 1 Introduction

The finite element method is more used to predict complex phenomena may be produced by plastic deformation of metals. *SB* is generally referred to as the change of part shape that occurs upon removal of constraints after forming (Xia and Cao 2014). After *SB*, the part reaches an internal equilibrium in the absence of external forces. Residual stresses still exist within the part; however, they are self-balanced (Xia 2007).

In recent years, much research has been devoted to find techniques and methods to reduce *SB*.

The study of the influence of material properties and processing parameters on *SB* is very important to design the forming tools. In literature, several experimental and numerical studies were conducted to characterize the influence of these parameters on *SB* during the bending operation. Wang et al. (1993) developed models for plane strain sheet bending to predict *SB*, minimum bending ratio, strain and residual stress distributions, etc. The results obtained by Jiang et al. (2015) show that the hardening exponent, bending radius and thickness ratio, friction coefficient, and blank holder force have great influences on the springback angle and stress level.

Knowing that the amount of *SB* that occurs after the bending operation is an intrinsic property of metals, an accurate experimental characterization of sheet metal

---

A. Maati (✉) · S. Belaid
Mechanical Laboratory, Amar Telidji University, Laghouat 03000, Algeria
e-mail: a.maati@lagh-univ.dz

A. Maati · E. H. Ouakdi
Laboratory of Physics and Mechanics of Metallic Materials, Setif 1 University, Setif 19000, Algeria

L. Tabourot · P. Balland
SYMME Laboratory, Savoie Mont Blanc University, 74940 Annecy-le-Vieux, France

T. Boukharouba et al. (eds.), *Computational Methods and Experimental Testing In Mechanical Engineering*, Lecture Notes in Mechanical Engineering,
https://doi.org/10.1007/978-3-030-11827-3_5

is unavoidable towards more accurate prediction of *SB*. So, *modelling* mechanical behaviour of metal is crucial to improve simulation reliability. The models obtained, for example, by integrating selected physical phenomena seem a more intricate alternative, but they allow a general description without multiplying parameters and costly identifications (Tabourot et al. 2012). Most works in the field make use of classic phenomenological models while this type of models should include some simplifications by considering the material is homogeneous at the microscopic level, also every model corresponds a well-defined situation (Tabourot et al. 2014, Maati et al. 2015). Indeed, metallic alloys are discrete and heterogeneous (polycristals). There are several possible sources *of* heterogeneity such as grain size, crystallographic grain orientation, precipitates, dislocations, etc. Thus, taking into account the heterogeneities of the metallic structure makes the model more consistent to achieve specific numerical results. To this end, Tabourot et al. (2015) proposed a *CM* to investigate the localization phenomenon in the case of a tensile test on *C68* grade steel. This paper is mainly devoted to the influence of the local heterogeneities on *SB* phenomenon through case study. By way of comparison, two types of simulations (with and without considering the material heterogeneities) were performed for predicting *SB* in L-bending operation. Tests have been carried out on commercially pure titanium sheets.

## 2 Experimental Traction Data

The true Stress-Strain curve for titanium *T40* was obtained via the digital image correlation (Vacher et al. 1999). Figure 1 shows the deformation field on the surface of the specimen oriented in the *RD*. The acquisition frequency was 2 images per second and the total number of images acquired is limited to 120 images over a test time equal to 60 s. The tensile tests are performed at a constant crosshead speed $V =$ 10 mm/min on titanium specimens with a rectangular cross-section ($1.6 \times 10$ mm$^2$).

The true Stress-Strain curve is illustrated in Fig. 2. The Young's modulus was determined using the linear regression method on extensometer data in the elastic range. In this study, the Poisson's ratio has not been identified, it is assumed to be equal to its usual experimental value ($\upsilon = 0.34$).

## 3 Numerical Simulation of Tensile Test Experienced by Sheet Specimens of Titanium T40 Alloy

### 3.1 Without Considering the Material Heterogeneity

The mechanical behaviour of Titanium *T40* was initially modeled by a Young's modulus and a Poisson's ratio in the elastic range of the traction curve; and by a

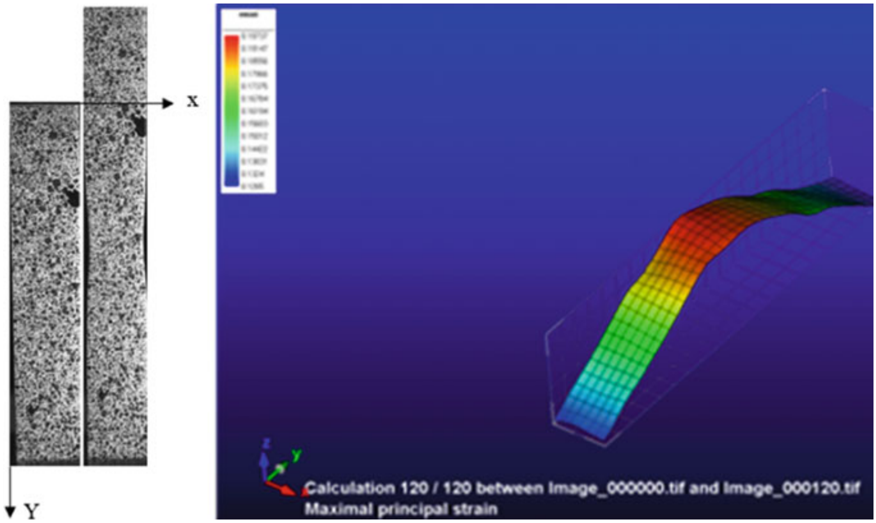

**Fig. 1** Deformation $\varepsilon_{yy}$ field obtained via digital image correlation (DIC)

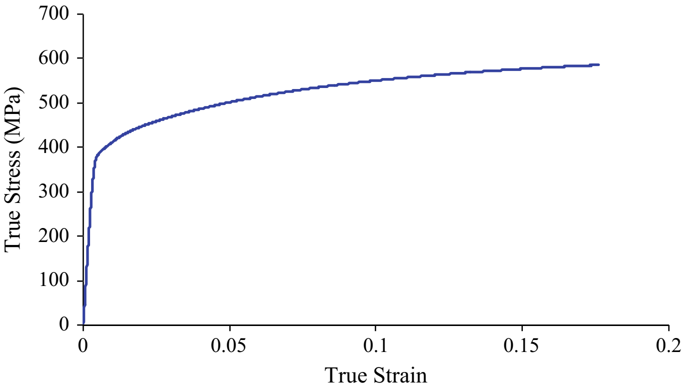

**Fig. 2** True Stress-Strain curve obtained via DIC in the RD

reference curve $\sigma(\varepsilon_p)$ in the plastic range of the traction curve as shown in Fig. 3, $\sigma_y$ is the yield stress, typically equal to the elastic limit of the material. The numerical simulation of tensile test without considering the material heterogeneity shows the symmetry of stress and strain relative to the center of the sample as illustrated in Fig. 4. Furthermore, the Fig. 5 shows the evolution of the equivalent plastic strain along path oriented towards the center of the sample (12 selected nodes).

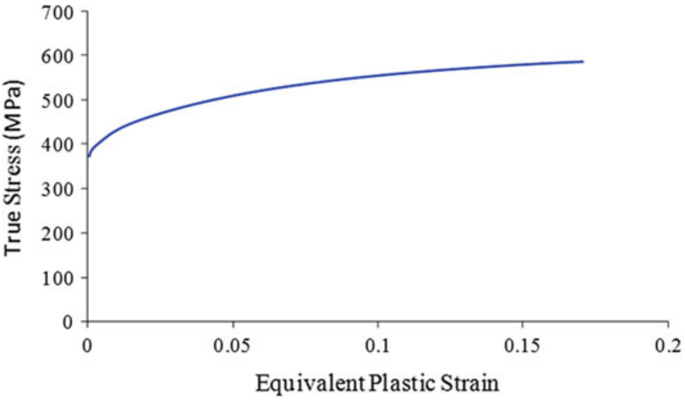

**Fig. 3** Schematic reference curve obtained via DIC in the RD

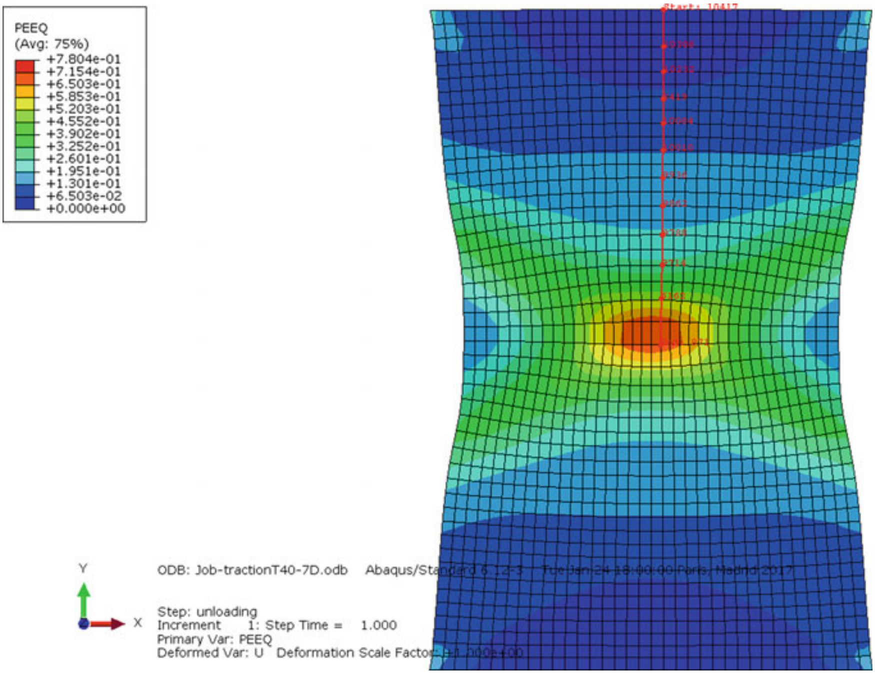

**Fig. 4** Symmetry of strain distribution with respect to the centre of the test piece

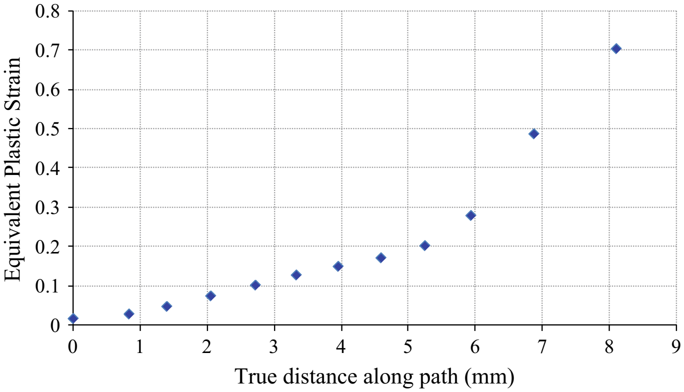

**Fig. 5** Evolution of the plastic strain along path oriented towards the centre of the sample

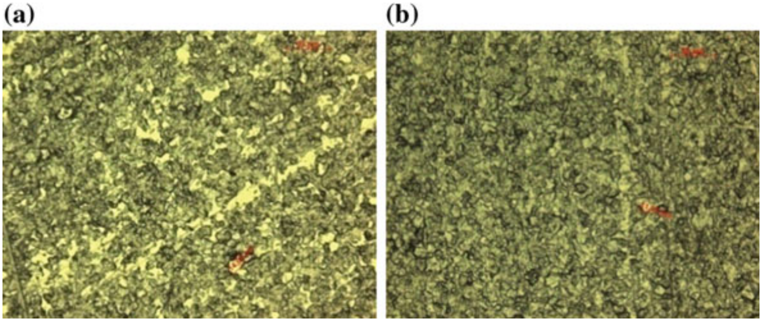

**Fig. 6** Highlighting the microstructure of titanium T40 using an optical microscope (G20), **a** without chemical attack, **b** with chemical attack (t = 30 s)

### *3.2 By Considering the Material Heterogeneity*

At a microscopic level, the metal alloys are discrete and heterogeneous materials. There are many top causes that are responsible for these material heterogeneities such as grain and sub grain structuration, crystallographic orientation of the grains, presence of precipitates and gaps, etc. As mentioned above, it has appeared interesting to introduce such spatial distributions in order to model the elastoplastic behaviour of metallic material. An image showing the microstructure of titanium *T40* was taken using an optical microscope (Fig. 6).

To render the physical effect due to such properties, it is proposed to quantify and distribute pertinent mechanical properties spatially throughout the material. For example, highlighting the Bauschinger effect is numerically possible using a *CM* without making use of experimental tests which are often costlier.

The *CM* proposed in this study is based on the one hand on the modelling studies carried out by Tabourot et al. (2014), and on the other hand, on the heterogeneous

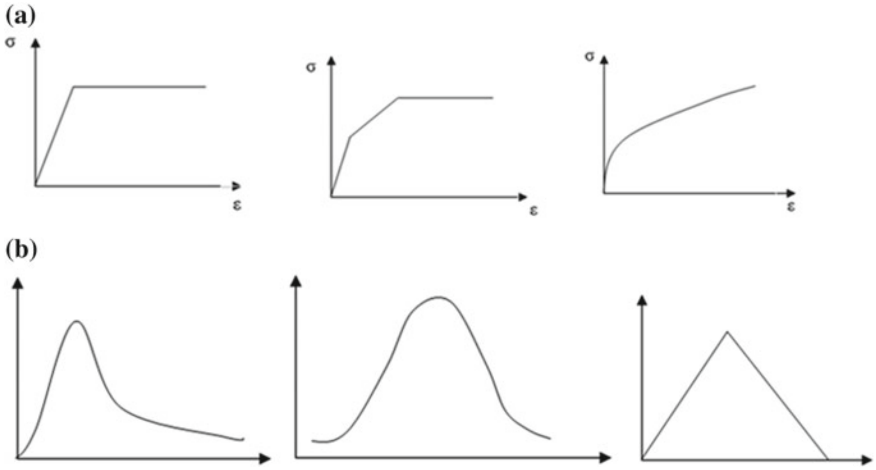

**Fig. 7** Examples of local behaviour laws and probability distribution functions (Bizet 2016)

finite element approach like the one proposed by Furushima et al. (2013). To predict the effect of a phenomenon sensitive to material heterogeneities (such as *SB*), the *CM* assigns to each grain size a local behaviour law by using a probability distribution function. Literature has a set of local behaviour laws and probability distribution functions such as those described in Fig. 7.

Assume that $\sigma_y$ is randomly distributed according to a Rayleigh distribution as given in the following equation (Bizet 2016):

$$f\left(\frac{x}{\sigma_{ym}}\right) = \frac{2x}{\sigma_{ym}^2}\exp\left(-\frac{x^2}{\sigma_{ym}^2}\right) \tag{1}$$

$x$ varies from 0 to $\infty$, $\sigma_{ym}$ is the average yield stress ($\sigma_{ymean}$) defining Rayleigh's distribution shape (see Fig. 8).

A saturation stress $\sigma_{sat}$ is used to delimit the random distribution of $\sigma_y$. By way of comparison; the numerical simulation used two elastoplastic constitutive laws as local laws. A bilinear elastoplastic constitutive law characterized by slop $n$, it is given by the following relation:

$$\sigma = n\varepsilon_p + \sigma_y \tag{2}$$

The Hollomon's law is used to model the plastic portion of true Stress—Strain curve. It is given by the following relation:

$$\bar{\sigma} = K\left(\bar{\varepsilon}_p\right)^n \tag{3}$$

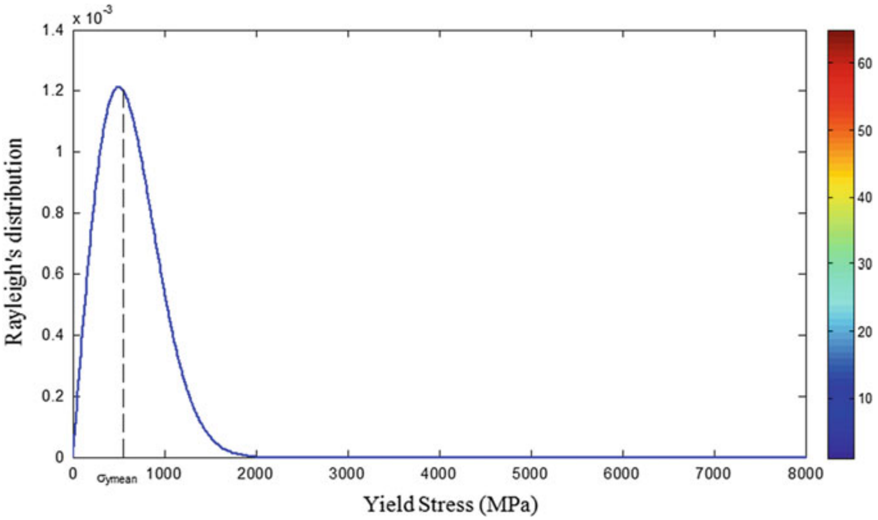

**Fig. 8** Rayleigh's distribution for the CM model for 10,000 elements

**Table 1** Numerical parameters introduced in the simulation

| Local law | Simulation field | Element type | Distribution law | Number of elements | CM parameters |
|---|---|---|---|---|---|
| Hollomon's law | 2D | CPE4R | Rayleigh | 1200 | $\sigma_{ym} =$ 185 MPa and $n = 0.18$ |
| Bilinear law | 3D | C3D8R | Rayleigh | 12,000 | $\sigma_{ym} =$ 500 MPa, $\sigma_{sat} =$ 1345 MPa *and* $N = 575$ |

A Coupled Abaqus/Python algorithm was used to optimize the parameters of both local laws proposed above by fitting numerical curve to experimental data. The true Stress-Strain curve obtained with optimized values (see Table 1) is given in Fig. 9.

The numerical simulation of tensile test by considering the material heterogeneity shows the asymmetry of stress and strain with respect to the centre of the test piece. I.e. the most loaded element can be located at any point in the test piece. The Fig. 10 shows the evolution of the equivalent plastic strain along path previously selected.

To highlight the kinematic hardening effect, a traction-compression test is simulated. Some cycles were presented before buckling deformation (Fig. 11).

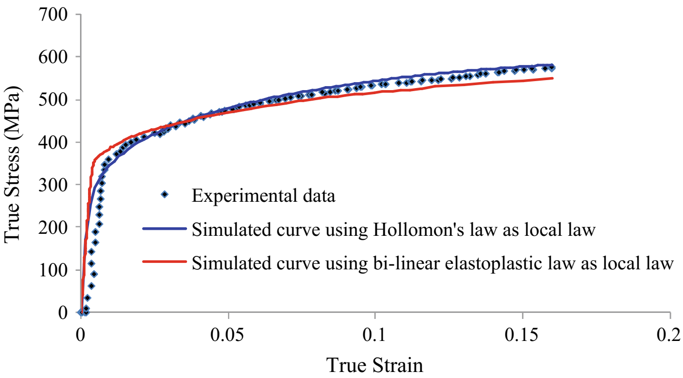

**Fig. 9** Experimental and numerical true Stress—Strain curves of T40 alloy

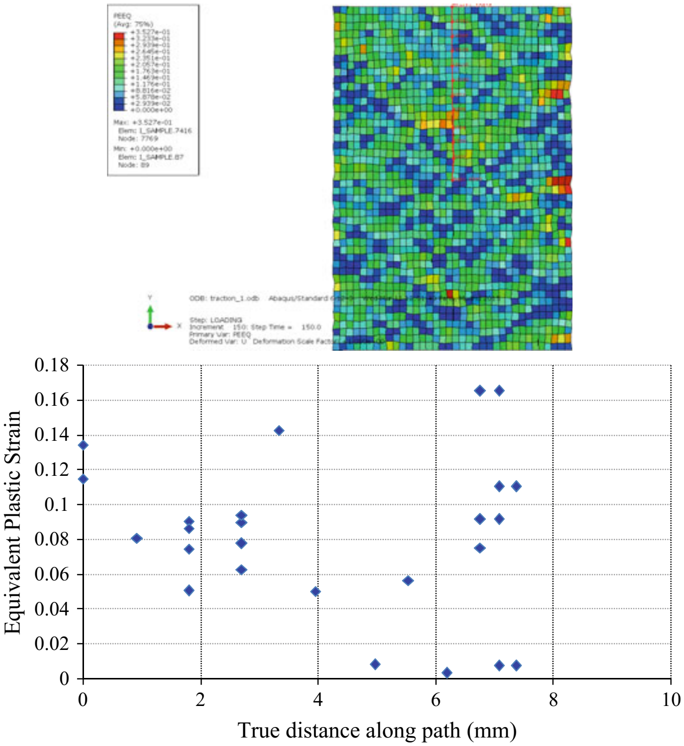

**Fig. 10** Evolution of the equivalent plastic strain along path by using the CM

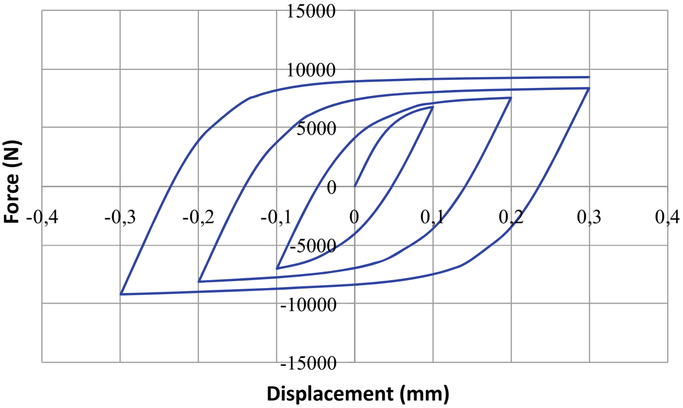

**Fig. 11** Numerical tension—compression test on titanium T40 alloy using CM

**Table 2** SB values of different methods

| *SB* | Material heterogeneities not included | Material heterogeneities included using Hollomon's approach (2D) | Experimental measure | Material heterogeneities included using bilinear approach (3D) |
|---|---|---|---|---|
| $\Delta\theta$ (°) | 4.5 | 3.6 | 3.7 | 4.2 |

## 4 Numerical Simulation of L-Bending Operation with *SB* Stage

The software ABAQUS/Standard has been used to setup the numerical model of L-bending operation with SB stage. The tools were assumed to be perfectly rigid. Two mesh element types were used, on the one hand, the part mesh which consisted of 12,000 volume elements, is obtained using *C3D8R*, and on the other hand, the part mesh which consisted of 1200 shell surface elements, is obtained using *CPE4R*. In order to take the different interactions between the rigid tools and the blank into account, a friction coefficient ($\mu = 0.15$) is proposed. Once the punch has done the prescribed displacement ($U_2 = 18$ mm), the simulation removes the punch and the spring back will occur. The numerical description of the L-bending operation with *SB* stage is illustrated in Fig. 12. Other representative figures resulting from the simulation have been illustrated (Fig. 13a, b).

A comparison was done between results obtained; firstly, from numerical simulation with and without considering the material heterogeneities and secondly by measuring experimentally the spring back for bending a 90°. As shown in Table 2, the results for the three methods are presented. $\Delta\theta = \theta_1 - \theta_2$ denotes the variation in the bending angle of the test piece before and after spring back.

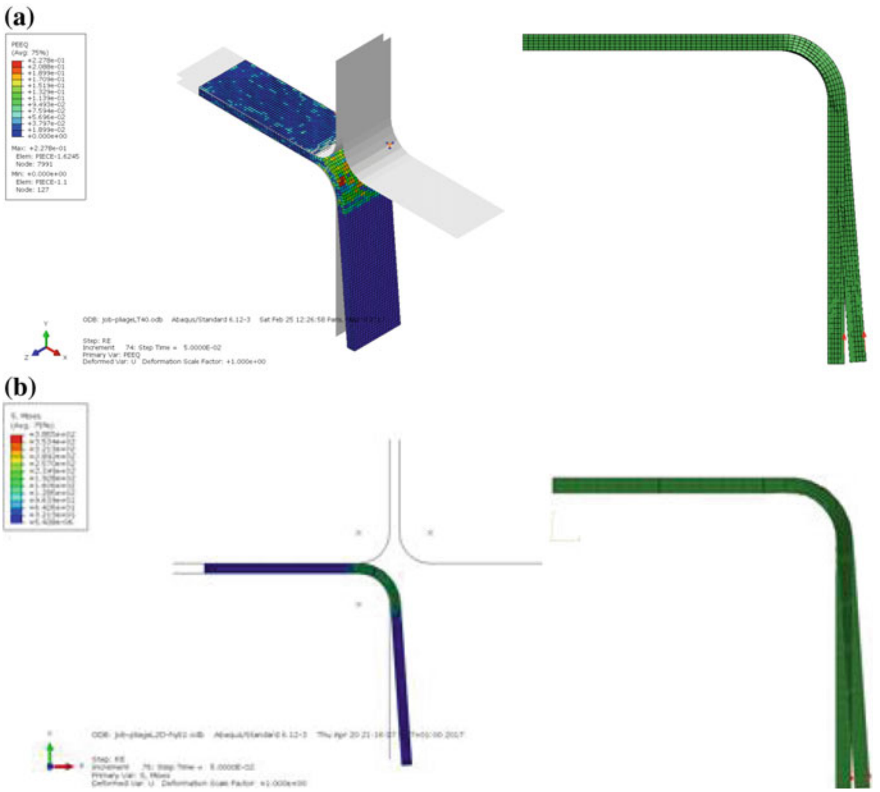

Fig. 12 **a** 3D L-bending numerical model with spring back stage, **b** 2D L-bending numerical model with springback stage

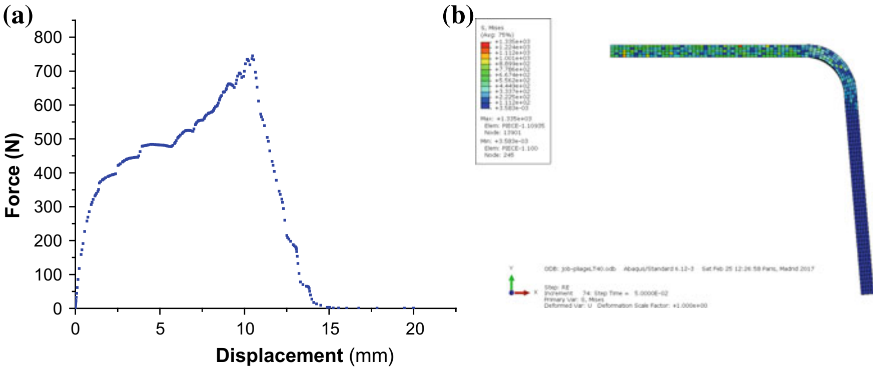

Fig. 13 **a** Force-displacement curve during the loading step, **b** a random variation of von Mises stress through the sheet thickness

According to the numerical simulation results, a good agreement in terms of *SB* amount is observed between simulation results using Hollomon's approach as a local law and experimental data. This comparison showed an average relative error of less than 3%, Furthermore, this error increases in the case using bilinear approach as a local law with an average value of 13%, and it increases more if the material heterogeneities is not included.

## 5 Conclusion

A *CM* that introduces the material heterogeneities to describe the mechanical behaviour of metals has been presented. An experimental characterization of the material response using plate specimens has been firstly performed in order to obtain the reference curve that will be used as input data in the *FEA* code.

A python script is used to identify the *CM* parameters. Numerical simulation of L-bending process with *SB* stage was performed using a *CM* which is a combination of a local law and a probability distribution function. An acceptable convergence is observed between the numerical results using Hollomon's approach as a local law and the measurements of *SB*, the error increases if the material heterogeneities is not included.

A numerical simulation of traction—compression test was carried out using a *CM* in order to reproduce the kinematic hardening effect due to cyclic loading; this effect is weakly observable for simple bends and creases.

Finally, this type of physically based models will certainly be more effective to predict complex phenomena generated by the plastic deformation and which are more sensitive to the material heterogeneities (spring back in deep-drawing process for example).

## References

Bizet L (2016) Caractérisation et modélisation du comportement thermomécanique des matériaux métalliques, vers la prise en compte des hétérogénéités microstructurales intrinsèques, Doctoral Thesis

Xia ZC (2007) Constitutive modeling of advanced high-strength steels for Springback simulation. Computational mechanics, pp 299–299, SpringerLink

Xia ZC, Cao J (2014) Springback, CIRP encyclopedia of production engineering

Furushima T, Tsunezaki H, Nakayama T, Manabe K, Alexsandrov S (2013) Prediction of surface roughening and necking behaviour for metal foils by inhomogeneous FE material modeling. Key Eng Mater 554(557):169–173

Jiang HJ, Hong-Liang D (2015) A novel model to predict U-bending springback and time-dependent springback for a HSLA steel plate. Int J Adv Manuf Technol 81(5–8):1055–1066

Maati A, Tabourot L, Balland P, Ouakdi EH, Vautrot M, Ksiksi N (2015) Constitutive modelling effect on the numerical prediction of springback due to a stretch-bending test applied on titanium T40 alloy. Arch Civ Mech Eng 15:836–846

Tabourot L, Balland P, Raujol-Veillé J, Vautrot M, Déprés C, Toussaint F (2012) Compartmentalized model for the mechanical behaviour of Titanium. Key Eng Mater 504(506):673–678

Tabourot L, Balland P, Ndèye AS, Vautrot M, Ksiksi N, Maati A (2014) Numerical study of the impact of constitutive modelling on the evolution of necking in the case of a tensile test on C68 grade steel. Key Eng Mater 611(612):521–528

Tabourot L, Maati A, Balland P, Vautrot M (2015) Influence of heterogeneities and of their distribution on the elastoplastic behaviour of metals. In: International symposium on plasticity, Montego Bay, Jamaica

Vacher P, Dumoulin S, Morestin F, Mguil-Touchal S (1999) Bidimensional strain measurement using digital images. J Mech Eng Sci 213(8):811–817

Wang C, Kinzel G, Altan T (1993) Mathematical modelling of plane-strain bending of sheet and plate. J Mater Proc Tech 39:279–304

# Microstructural Analysis of Nickel-Based Composite Coatings and Their Effect on Micro-hardness and Nano-indentation Behavior

**Rabah Azzoug, Fatah Hellal and Yamina Mebdoua**

## 1 Introduction

Besides the success that the cemented carbides have gained in various industrial sectors since their invention in the 1930s (Ren et al. 2013; Tarragó et al. 2014; Ettmayer et al. 2014), thermal spray coatings reinforced with tungsten carbides, are well considered as materials of future owing to their exceptional toughness, hardness, and strength combined with an excellent in-service wear resistance (Li and Yang 2013). Among them, those based on the nickel self-fluxing alloys are, nowadays, of a prime interest as these represent the most appropriate alternatives to the costly cobalt based coatings, which are well known for their environmental undesirable effect and toxicity (Iždinská et al. 2010, Škamat et al. 2015). They are widely used as hard coating materials to wear components and extend their lifetime in harsh environments. As metal matrix composites (*MMCs*), their structure mainly consists of an interpenetrating network of refractory, hard and brittle WC carbides embedded in a nickel metallic binder. Both the thermal stability down to (~2000 K) of the *WC* and the outstanding nickel passivity grant an excellent hot corrosion resistance to the running parts at temperatures exceeding 823 °C, a temperature that surpasses that allowed by Co-based alloys (~500 °C) (Islak and Buytoz 2013; Lin et al. 2006). Despite what the addition of the other hard components can impart to the composite hardness and its chemical stability (Garrido et al. 2017; Ozer et al. 2011), by varying

---

R. Azzoug (✉) · F. Hellal
Ecole Nationale Polytechnique, Département de Métallurgie, LSGM, 16200 Algiers, Algeria
e-mail: rabah.azzoug@g.enp.edu.dz

F. Hellal
e-mail: fatah.hellal@g.enp.edu.dz

Y. Mebdoua
Centre de Développement des Technologies Avancées, Baba Hassen, Algiers, Algeria
e-mail: ymebdoua@cdta.dz

T. Boukharouba et al. (eds.), *Computational Methods and Experimental Testing In Mechanical Engineering*, Lecture Notes in Mechanical Engineering,
https://doi.org/10.1007/978-3-030-11827-3_6

the elemental chemical composition of a nickel alloy, matrix properties may be varied in a wide range from the soft antifriction with excellent corrosion resistance (~300 HV) to the hard (~780 HV). Boron, chromium, and carbon are primarily added as strengthening elements in these alloys for producing the hard phases of borides and carbides which increase their aptitude to mitigate cavitation and wear (Škamat et al. 2015; Lin et al. 2006). As same as silicon does, boron has a self-fluxing effect that enables to reduce the alloys' melting point and can hence ameliorate the ductility, the creep resistance and increases the boundary strength and cohesivity (Kontis et al. 2016, 2017). Furthermore, the addition of chromium and aluminum considerably consolidates the resistance of the material against hot corrosion and oxidation. The rare earth elements like $L_a$, $C_e$, and $Y$ have shown their ability to make higher the anti-oxidation and anticorrosion behavior and promoted plasticity. Moreover, the addition of *Mo*, *Y*, and *Nb*, refine the coating microstructure and raise the hardness (Hu and Hou 2017).

High-temperature thermal spraying processes such as high-velocity oxy-fuel (*HVOF*), plasma spraying (*PS*), and spray fusion (*SF*) are conventionally applied to deposit these hard materials to produce more dense deposits by melting the binder phase (Lioma et al. 2015; Li and Yang 2013). However, the low cost and the simplicity of the flame spraying make practically the last the most useful process even though their coating porosity content (~10 to 20%) and adherence strength (~70 MPa for the self-fluxing ones) are comparatively mediocre. Trying to overcome somewhat these drawbacks by taking advantage of both prior and post-treatment processing was the point of recent investigations. For multicomponent chemical systems, when the coatings would be build up under a no equilibrium thermodynamic conditions, avoiding the inevitable microstructural changes promoting the formation of detrimental phases requires a full array of trial and error try-outs to determine the optimum processing parameters. The wise selection of these leads to get relatively consistent coatings more compliant with the required specifications and standards. An in-depth assimilation of the behavior of the developed coatings customarily help to predict the prominent mechanisms arisen before their failure and that, accordingly, allow to push the boundaries towards further enhancements.

Presently, the purpose of providing further foundations is to improve the current nickel-based coating performances, to be more efficient under the more severe and aggressive working conditions. The present paper is devoted to highlighting the influence of the grit blasting on the substrate hardness, the effect of the presence of the Ni-based bonding layer on the coating microstructure, and the way their mechanical features, namely the micro-hardness and the nano-indentation behavior, are affected.

## 2 Experimental Procedure

Spherotene wire consisting of NiCrBSi alloy reinforced with *WC* carbides were flame sprayed on cylindrical steel substrates (*X18*) with 30 mm in diameter and 5 mm in thickness, preheated to 150 °C after cleaning, grit blasting and bond layer deposition.

**Table 1** Flame spraying processing parameters

| Acetylene pressure | Oxygen pressure | Spray distance | Torch velocity |
|---|---|---|---|
| [bars] | [bars] | [mm] | [mm/s] |
| 0.2 | 4 | 120 | 1 |

**Table 2** The chemical composition of the powder used to perform the bonding layer

| Element | Ni | Mn | Cr | Si | Fe |
|---|---|---|---|---|---|
| %Wt | 72.46 | 10.79 | 8.34 | 4.95 | 3.46 |
| | 72.87 | 10.47 | 8.53 | 5.01 | 3.12 |

The coated samples were then cut into four pieces. Their surfaces were polished up to 3 μm of roughness with diamond slurries and then etched. The selected processing parameters are listed in Table 1.

The chemical composition of the feedstock powder that has been used to perform the bonding layer was determined by *EDAX* spectroscopy analysis using an accelerating voltage of 25 kV. The results of this analysis are tabulated in Table 2.

The micrograph showing the morphology of this powder (Fig. 1a) was obtained by the mean of a scanning electron microscope. The associated dispersive energy spectra are shown in Fig. 1b.

The metallographic observations of the coating microstructure were made with an optical microscope (*OPTIKA M-789*) equipped with a camera for image acquisition. The image processing software ImageJ has been used to enhance contrast after image acquisition. It then allowed us to evaluate the morphological parameters of our microstructure and, in particular, the phase ratios. Using Mytutoyo *HM100* micro-hardness instrument, a filiation of micro-hardness measurements was carried out on the transversal cross-section of a sample, under a constant charge of 0.1Kgf, starting from the substrate to the top sprayed coating surface while passing through the bonding layer. A step of 50 μm has been applied. Nano-indentation tests were performed with a nano-indenter Bruker AXS *BW/508/98/RÖ CSM* tester, according to Oliver-Pharr method. A Vickers indenter with a maximum load of 100 μN was used. The indentation velocity was fixed at 2500 nm/min and the dwell time to be maintained at the maximum load at 10 s. The charge/discharge velocity was equal to 200 μN/min.

## 3 Results and Discussion

The optical micrographs obtained from the inside of the coatings (Figs. 2 and 3) reveal a microstructure consisting of tungsten carbide particles of different sizes and shapes (spherical or irregular). These carbides are embedded in a matrix containing the nickel solid solution of $\gamma$ dendrites (67%) surrounded by $\gamma$-$Ni_3B$ eutectic (*30%*) and fine precipitates of various morphologies dispatched in inter and intradendritic

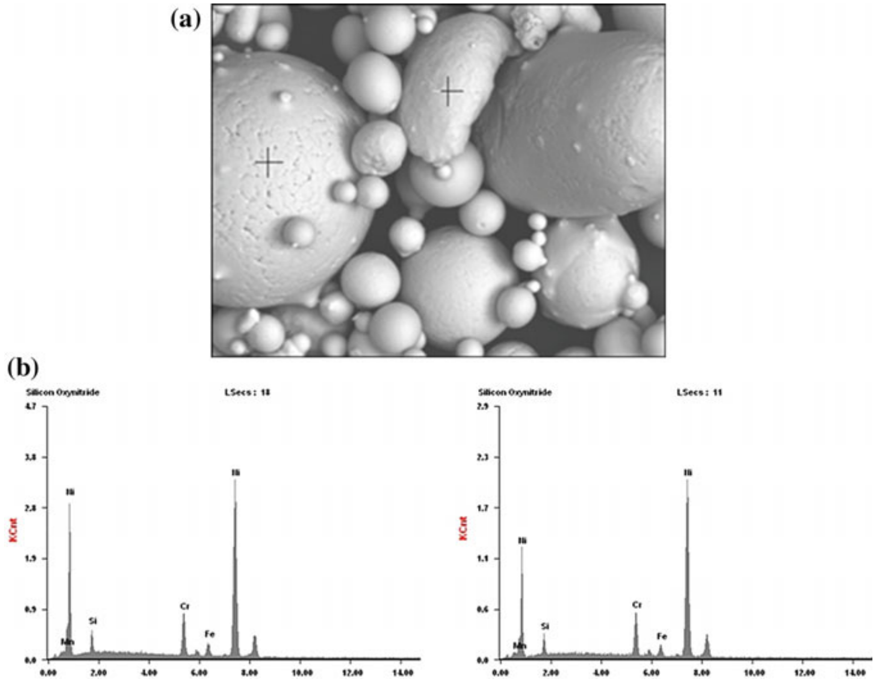

**Fig. 1** **a** Micrograph showing the morphology of the sprayed powder used to perform the bonding layer and the selected EDAX analysis spots; **b** Dispersive energy spectrum associated with each analysis

sites in a discontinuous manner. Since the spraying at a low distance from the prepared surfaces using low deposition velocity, provides an excess of heat energy during the deposition $\gamma$ dendrites were seemingly initiated and grown within the solidification pool at the first moment of deposition. Moreover, with the temperature decreasing, boron and carbon segregated from them towards their boundaries due to their limited solubility in the nickel phases to form the precipitates identified as carbides and borides elsewhere (Otsubo et al. 2000). During these sequences and under the successive impingement of the other in-flight molten particles, the amount of porosity ensued from the entrapped gas gradually decreased inside the coating. Following the cooling in super cooling conditions, when the equilibrium eutectic temperature was reached, the inter-dendritic melt then solidified to yield the eutectic mixture. It is important to note that after complete solidification, the *WC* borders have constituted favorable sites for the nucleation of dendrites wrapping them and the majority of carbides were preferably located in intra-granular dendritic sites while the borides were more concentrated on the grain boundaries. Further, the residual porosity can be distinguished from the formers after etching by their spherical like shape.

Moreover, Fig. 4 left illustrates the sensitivity of the used nickel alloy to cracking due to a generation of residual stresses as result of a high thermal expansion mismatch

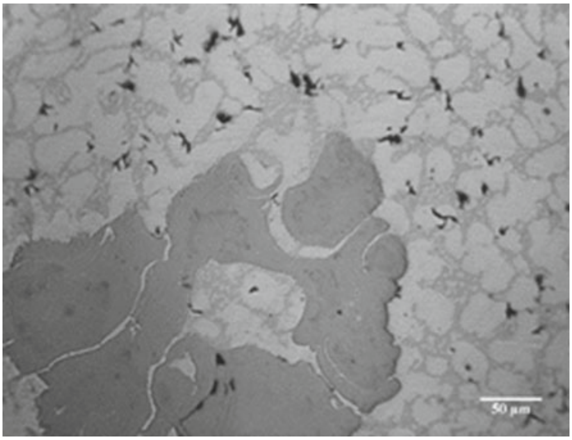

**Fig. 2** Micrograph shows the microstructure obtained from the inside of the coating

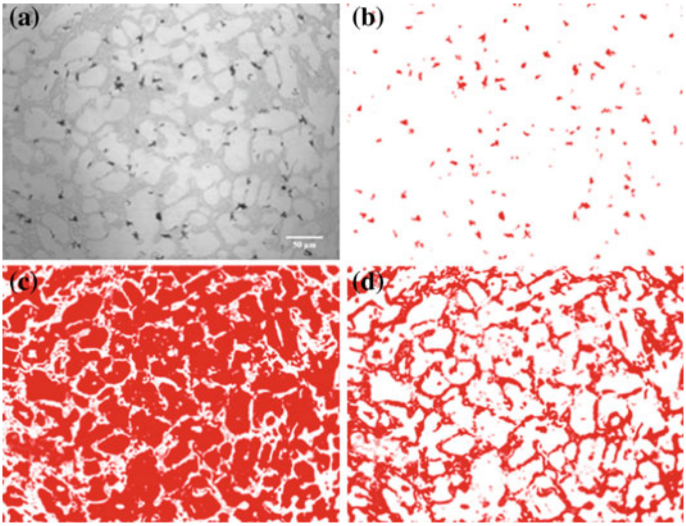

**Fig. 3** Micrograph show the matrix microstructure before (**a**) and after (**b**–**d**) image processing

and an unfit cooling mode. As seen in Fig. 4 right, several matrix regions showed a textured microstructure, within it, the dendrites are oriented in opposite directions as a consequence of an assorted directional heat transfer.

As depicted in Fig. 5, this composite mixture is mechanically adherent to the prepared substrate surface. *WC* superior density as compared with that of the melted Ni binder allows many *WC* particles to be localized on the bottom of the coatings rather than being on their top surface during the deposition. Thus, on the bottom of the coating, *WC* carbides are not too distant, and their amount at that region is higher

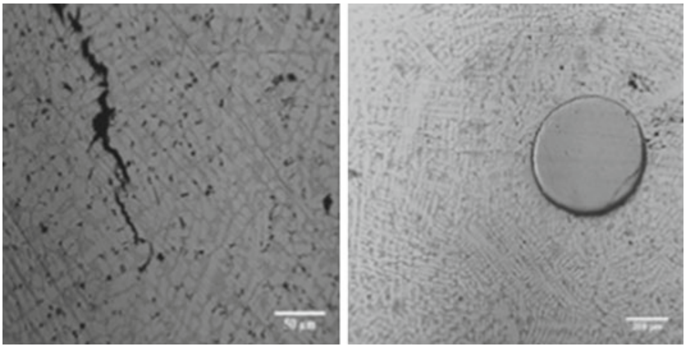

**Fig. 4** Micrographs obtained from the coating matrix show (left) an initiated micro-crack and (right) a textured microstructure within it

**Fig. 5** Optical image shows the cross-sectional coating microstructure

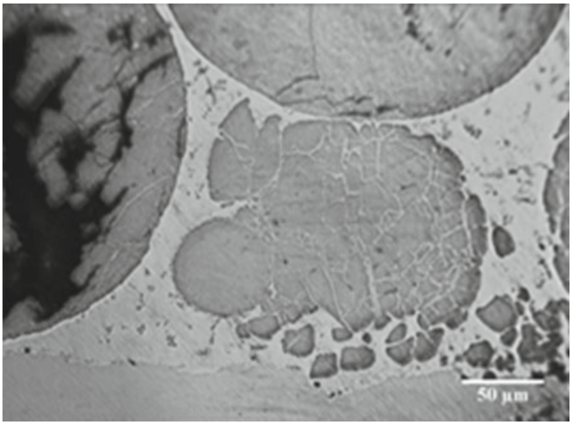

than that observed from the coating top surface micrographs. Additionally, all the previous micrographs confirm that no dissolution reaction of *WC* in the matrix takes place during the processing and the tungsten carbides remain in their unmuted form.

Despite the fact that the samples were preheated after bond layer deposition before applying the coatings until the temperature of the exposed surfaces reaches 150 °C, it can be seen that the microstructure of the top coating surface and that revealed just in the vicinity of the bond layer were comparatively alike. By contrast with Simunovica et al. results (Simunovic et al. 2017), no detection of any changes in this zone can hence confirm that the Ni-based bonding layer splayed over 35 µm of thickness had played the obstacle role against iron diffusion throughout the substrate/coating interface.

Therefore, the cross-sectional micro-hardness evolution profile (Fig. 6) demonstrate that the *XC18* carbon steel top surface has undergone a hardening due to a cold deformation occurred during the grit blasting treatment. On the affected volume and along 150 µm from the interface, the hardness seems to follow a linear-like evolution

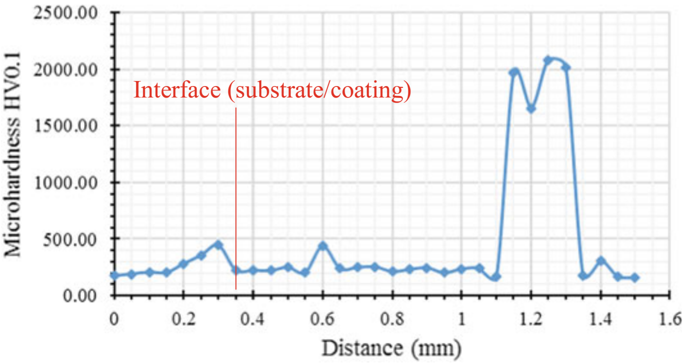

**Fig. 6** Cross sectional micro-hardness evolution profile

suggesting that the more the distance is closer to the interface, the more the surface is plastically deformed, and the more the hardness is high. This result is in agreement with Coddet et al. findings (Coddet et al. 1999).

While the mean hardness of the coating matrix and that of the steel substrates were slightly similar (~210 ± 15 HV), near the interface, the hardness has achieved its maximum value that was around 445 HV. In several matrix areas, the hardness rose sharply because of the presence of hard precipitates. As the residual impressions' sizes were almost bigger than the precipitates' mean size, the dissimilarity between these relatively high hardness values apparently depends on the type, the shape and the number of precipitates being indented. The *WC* surrounding zones were found to have a remarkable lower hardness attributed to the presence of $\gamma$ dendrites.

For figuring out the main contributable factors to the occasional increase and decrease in the matrix hardness, the nano-indentation tests were performed on various dendritic arm areas starting from the center towards the boundaries. Several tests were further carried out on eutectic regions around which the proportion of phases was not the same. By analyzing Fig. 7, displaying some micrographs captured from the indented surfaces after the nano-indentation tests, it appears that the pop-in event, both of matrix constituents were subjected to, is more pronounced in the eutectic phases comparatively with that emerged in the dendritic arms.

The obtained curves presenting the recorded variation of the applied charge P as a function of the depth of penetration h are shown in Figs. 8 and 9. From these results, it can be drawn that the first stage of the loading section in which the nano-indentation curves coincide, indicates that the material has experienced a pure elastic deformation. This stage was then followed by an elastoplastic transition preceding the plastic deformation. After maintaining the load at its maximum value, by unloading the indenter, a systematic elastic recovering goes on as a response from the material against penetration.

For the dendritic indented phases (Fig. 7), when the distance from the center is too small, it can be noticed that there is a little difference between the obtained nano-indentation graphs. When this distance becomes closer to the grain boundaries, the

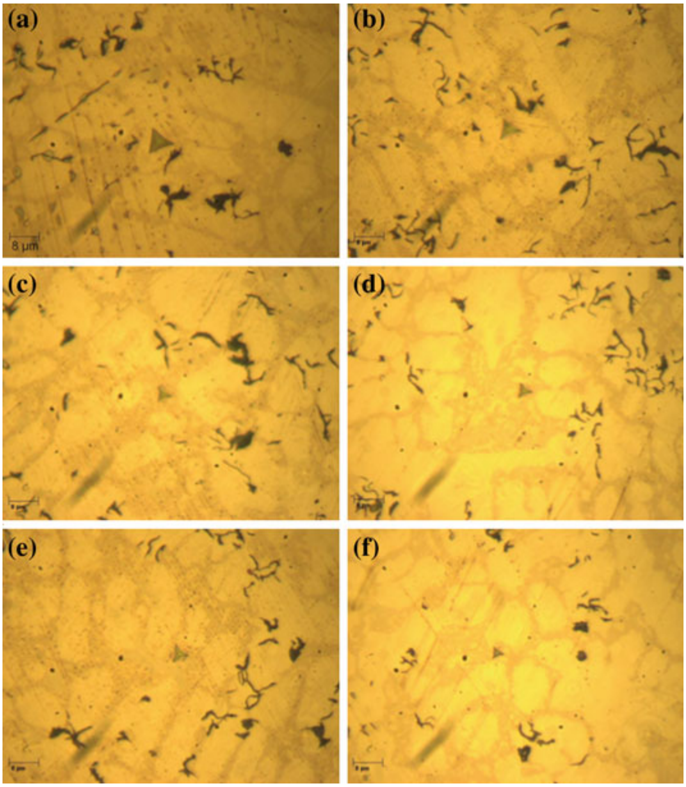

**Fig. 7** Optical micrographs show various nano-indented surfaces (**a**, **b**): nano-indented dendritic regions (**d**–**g**) nano-indented eutectic regions

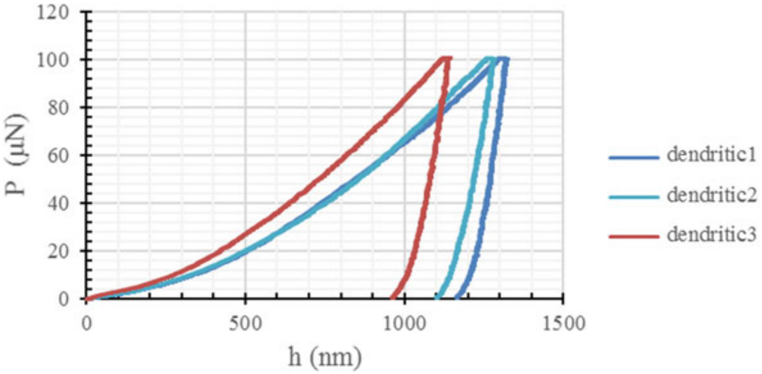

**Fig. 8** Load–displacement (P–h) curves obtained during nano-indentation experiments carried out on dendritic regions

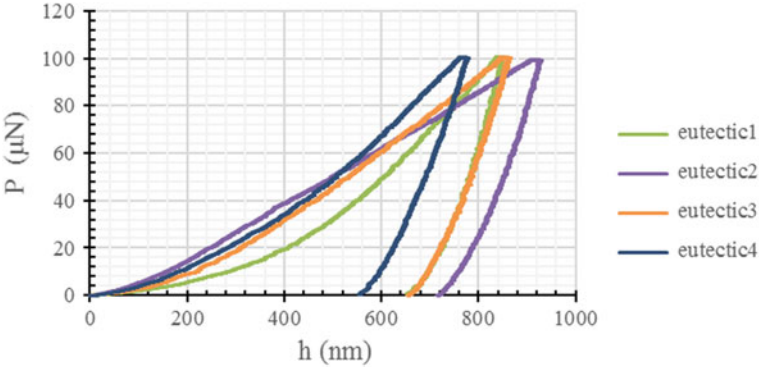

**Fig. 9** Load–displacement curves (P–h) obtained during nano-indentation experiments carried out on various eutectic regions

**Table 3** The obtained elastic moduli and hardness values after the nano-indentation tests

| | No. | E (GPa) | Hv10 |
|---|---|---|---|
| Dendritic | 1 | 196.03 | 311.63 |
| | 2 | 160.16 | 343.71 |
| | 3 | 200.35 | 444.22 |
| Eutectic | 4 | 190 | 746.74 |
| | 5 | 207.24 | 903.05 |
| | 6 | 248.71 | 904.33 |
| | 7 | 213.89 | 1217.4 |

associated graph bends sharply to the left. As a result, the elastic domain of that curve becomes less extended as compared with the others. Likewise, in the case of eutectic phases (Fig. 8), the curves become more inclined with the small inter-distance between the eutectic surrounding dendrites and the decreasing in the size of the nickel grains confined inside them.

Furthermore, after the loading stage, by keeping the loading charge constant at its maximum value, it can be mentioned that no discrepancy in the depth of penetration has been recorded. That confirms that in the indentation stress field, there was any movement of dislocations which prove in particular that the *NiCr* based matrix does not show a creep phenomenon, the Inconel arc sprayed coatings containing porosity and oxides have shown during Mebdoua et al. (2017) nano-indentation tests. Moreover, the elastic moduli and hardness of the indented phases are listed in Table 3. The extracted data from the unloading part of each graph were calculated and summarized in Table 4.

These results indicate that the dendrites' hearts have a mean hardness of 366 Hv and elastic modulus ($E$) of about 185 GPa which result in a low capacity to bear the plastic deformation as the ratio $H/E^2$ is the least. However, the great tendency of hardness to increase has been observed when approaching the grain boundaries. This has

**Table 4** The extracted data from the nano-indentation curves

| | No. | $h_m$ (nm) | $h_{rc}$ (nm) | $h_e$ (nm) | $h_r$ (nm) |
|---|---|---|---|---|---|
| Dendritic | 1 | 1317.52 | 1230.65 | 1253.37 | 1167.23 |
| | 2 | 1277.56 | 1169.09 | 1196.76 | 1104.66 |
| | 3 | 1135. 76 | 1033.78 | 1060.34 | 963.49 |
| Eutectic | 4 | 924.84 | 787.42 | 821.57 | 720.09 |
| | 5 | 859.68 | 718.51 | 752.60 | 659.78 |
| | 6 | 843.18 | 721.49 | 752.54 | 655.19 |
| | 7 | 772.10 | 612.39 | 650.12 | 556.12 |

been accompanied by a mutual decreasing of all the nanoindentation characterizing depths. That is to say, the depth from the original specimen surface at maximum load $P_m(h_m)$, the calculated depth of the residual impression for an equivalent punch ($h_{rc}$), the elastic displacement during unloading ($h_e$), and the depth of residual impression ($h_r$) (Table 4). Nevertheless, the dendritic hardness values remain inferior to those obtained by indenting the eutectic phases.

As compared with Bezborodov et al. investigation (Bezborodov and Yu 2016) and by relating the results to what was observed from the nano-indentation micrographs, the increase of the eutectic phases hardness may be attributed to both the smallest size of nickel grains present in the eutectic and the small inter-distance between eutectic surrounding dendrites. However, as many authors expected it (Fale et al. 2015; Pramanik et al. 2008), the results can be significantly affected by the presence of WC reinforcements beyond the indented surfaces since these can oppose to the indenter penetration and act as an opposing indenter. Therefore, from a metallurgical point of view, the *WC* carbides constitute great impediments to the motion of dislocations formed around them when the plastic deformation is produced leading to a particular strengthening commonly known as Orowan strengthening mechanism. This strengthening can be strictly enhanced by raising the volume fraction of reinforcement carbides and influenced by particles' shape, their typical morphology and their distribution inside the coatings as well. Hence, the thermal mismatch between the matrix and the *WC* carbides contribute separately to the increase of dislocation density within the matrix and consequently to its work hardening.

## 4 Conclusion

From the present investigation, we can infer that:

- The *Ni* based-*WC* coatings deposited by the flame spraying are characterized by a matrix of a dendritic structure surrounded by interdendritic eutectic phase and by precipitates.

- The local hardness increase within the coating matrix is ascribed to the presence of a heterogeneous distribution of fine-sized precipitates, while the relatively high hardness values observed on the micro-hardness profile is attributed to the grit blasting treatment near the interface.
- In our case, no dissolution reaction occurred during processing.
- The used Ni-based alloy is sensitive to cracking when cooling in air.
- The nano-indentation behavior may vary depending on the nature of the phases and their rate in the indented surface.

## References

Bezborodov VP, Yu NS (2016) Microstructure and mechanical properties of eutectic nickel alloy coatings. IOP Conf Ser: Mat Sci Eng 124(1):012119

Coddet C, Montavon G, Ayrault-Costil S, Freneaux O, Rigolet F, Barbezat G, Wazen P (1999) Surface preparation and thermal spray in a single step: The PROTAL process—example of application for an aluminum-base substrate. J Therm Spray Technol 8(2):235–242

Ettmayer P, Kolaska H, Ortner HM (2014) 1.01—history of hardmetals A2—Sarin, Vinod K. In: Comprehensive hard materials. Oxford, Elsevier, pp 3–27

Fale S, Likhite A, Bhatt J (2015) Nanoindentation, compressive and tensile deformation study of in-situ Al–AlN metal matrix composites. Trans Indian Inst Met 68(2):291–297

Garrido MA, Rico A, Gómez MT, Cadenas M, Fernández-Rico JE, Rodríguez J (2017) Tribological and oxidative behavior of thermally sprayed NiCrBSi coatings. J Thermal Spray Technol, pp 1–13

Hu C, Hou S (2017) Effects of rare earth elements on properties of Ni-base superalloy powders and coatings. Coatings 7(2):30

Islak S, Buytoz S (2013) Microstructure properties of HVOF-sprayed NiCrBSi/WCCo-based composite coatings on AISI 1040 steel. Optoelectron Adv Mat-Rapid Commun 7(11–12):900–903

Iždinská Z, Nasher A, Iždinský K (2010) The structure and properties of composite laser clad coatings with Ni based matrix with WC particles. Materials Eng. 17(2):1

Kontis P, Yusof HM, Pedrazzini S, Danaie M, Moore KL, Bagot PAJ, Reed RC (2016) On the effect of boron on grain boundary character in a new polycrystalline super-alloy. Acta Mater 103(Supplement C):688–699

Kontis P, Alabort E, Barba D, Collins DM, Wilkinson AJ, Reed RC (2017) On the role of boron on improving ductility in a new polycrystalline super-alloy. Acta Mater 124(Supplement C):489–500

Li C-J, Yang G-J (2013) Relationships between feedstock structure, particle parameter, coating deposition, microstructure and properties for thermally sprayed conventional and nanostructured WC–Co. Int J Refract Metal Hard Mater 39:2–17

Lin MC, Chang LS, Lin HC, Yang CH, Lin KM (2006) A study of high-speed slurry erosion of NiCrBSi thermal-sprayed coating. Surf Coat Technol 201(6):3193–3198

Lioma D, Sacks N, Botef I (2015) Cold gas dynamic spraying of WC–Ni cemented carbide coatings. Int J Refract Metal Hard Mater 49:365–373

Mebdoua Y, Fizi Y, Lahmar H (2017) Determination of elastic-plastic parameters of inconel arc sprayed coating. In: Boukharouba T, Pluvinage G, Azouaoui K (eds) Applied mechanics, behavior of materials, and engineering systems: selected contributions to the 5th Algerian congress of mechanics, CAM2015, El-Oued, Algeria, pp 193–203, 25–29 Oct 2017. Springer International Publishing, Cham

Ren X, Miao H, Peng Z (2013) A review of cemented carbides for rock drilling: an old but still tough challenge in geo-engineering. Int J Refract Metal Hard Mater 39:61–77

Simunovic K, Slokar L, Havrlisan S (2017) SEM/EDS investigation of one-step flame sprayed and fused Ni-based self-fluxing alloy coatings on steel substrates. Phil Mag 97(4):248–268

Škamat J, Cernasejus O, Valiulis AV, Lukauskaite R, Visniakov N (2015) Improving hardness of Ni-Cr-Si-B-Fe-C thermal sprayed coatings through grain refinement by vibratory treatment during refusion. Mat Sci/Medziagotyra 1(2)

Tarragó Cifre JM, Jiménez Piqué E, Turón Viñas M, Rivero L, Al-Dawery I, Schneider L, Llanes Pitarch LM (2014) Fracture and fatigue behavior of cemented carbides: 3D focused ion beam tomography of crack-microstructure interactions. Int J Powder Metall 50:1–10

Otsubo F, Era H, Kishitake K (2000) Structure and phases in nickel-base self-fluxing alloy coating containing high chromium and boron. J Therm Spray Technol 9(1):107–113

Ozer A, Kriven WM, Tur YK (2011) An experimental study on the effects of SiC on the sintering and mechanical properties of Cr3C2-NiCR cermets. In: Mechanical properties and performance of engineering ceramics and composites VI. 2011, pp 271–279. Wiley

Pramanik A, Zhang LC, Arsecularatne JA (2008) Deformation mechanisms of MMCs under indentation. Compos Sci Technol 68(6):1304–1312

# Effect of Slag and Natural Pozzolan on the Mechanical Behavior of Recycled Glass Mortars

**Zineb Douaissia and Mouloud Merzoud**

## 1 Introduction

Papers Glass is a material that can be recycled many times. However, the glass harvested is a mixed product and its reuse can become difficult. In this case, it is used for other applications such as abrasive road, glass wool, municipal filtrations. Previous work has shown that glass can be incorporated into concrete using two approaches. In the form of aggregates or as a cement additive. Incorporating glass as a granulate has the advantage of using large volumes of material and does not require fine crushing. But the main concern in such application is that the glass can react with the cement, it is the risk of the alkali-silica reaction (*ASR*) that cause swelling and cracking of the concrete (Idir et al. 2010; Carles-Gibergues et al. 2008).

To reduce the *ASR*, studies have suggested the combination of glass aggregate with pozzolans such as: silica fumes, fly ash or Meta Kaolin (Jin et al. 2000; Meyer and Baxter 1997; Yixin et al. 2000; Zhu et al. 2009). These pozzolans have shown their efficiency, they have the advantage of having a pozzolanic activity and, from an environmental and economic point of view, to limit the amount of cement consumed. Pozzolans do not have binding properties, but pozzolanic reactivity; the authors substitute it for cement in proportions of up to 30% by mass (Idir et al. 2011). In this case, the absolute volume of the mortar increases and the volume ratio (water/solid) decreases. These parameters can influence the properties of hardened mixtures and involve uncertainties in the evaluation of the different actions of mineral additions on the properties of cementations materials. But in the case of a volume substitution of cement, the absolute volume of the mortar and the volume ratio (water/solid) remains

---

Z. Douaissia (✉) · M. Merzoud
Civil Engineering Laboratory, Badji Mokhtar University, 23000 Annaba, Algeria
e-mail: douaissiazinebgc@gmail.com

M. Merzoud
e-mail: mouloudmerzoud@univ-annaba.org

T. Boukharouba et al. (eds.), *Computational Methods and Experimental Testing In Mechanical Engineering*, Lecture Notes in Mechanical Engineering,
https://doi.org/10.1007/978-3-030-11827-3_7

unchanged. In this case, the compactness of the granular structure and the porosity of the cementations matrix of the additive mixtures remain comparable to those of the mixture without additions and only the effects of the additive particles are taken into account in the cementations phase (Boudchicha et al. 2007). To evaluate the influence of additions on the mechanical behavior of recycled glass mortars; we propose to use this method based on gradual volume substitution (10, 20, 30%) of the cement by granulated blast furnace slag ($L_a$) and Beni-Saf's natural pozolan ($P_z$).

Granulated blast furnace slag is a by-product of the manufacture of cast iron suddenly cooled by water spraying; this quenching causes vitrification of the material. It is a latent hydraulic material (consisting mainly of 4 oxides: Cao, $SiO_2$, $Al_2O_3$ and MgO, that is to say it has hydraulic properties when undergoing a suitable activation. It is most often used in a mixture with Portland cement and it is the portlandite formed by hydration of the clinker which activates the hydration of the slag. The natural pozzolan of Beni-Saf ($P_z$), a rock from the Bouhamidi deposit at Béni-Saf in Algeria is used by cement factories as an active addition at rates of 15–20% in the manufacture of cement compounds. It is essentially composed of silica and alumina. The physico-mechanical properties of cements and mortars with pozzolan were studied by several authors (Boudchicha et al. 2007).

The use of mineral additions is interesting from a rheological point of view (helps increase the stability of the concrete, thus contributing to the reduction of the heat of hydration and the withdrawal of the concrete). Recent studies that have considered the influence of mineral additions on the properties of cement materials have shown that these additions by their fineness and a more or less significant reactivity with cement can in certain cases lead to significant changes in the mechanical properties. Some authors consider that the presence of mineral additions multiplies the possibilities of germination of hydrated cement products and thus facilitates the formation of a solid structure guaranteeing the first mechanical strengths (Manjit and Mridul 1999; Memon et al. 2002; Douaissia 2018). On the other hand, granulated blast furnace slag produced a decrease in compressive strength at 28 days and an improvement at 120 days (Demirboga 2003) and that the use of a 15% El Hadjar slag rate appeared optimal.

The replacement of cement with pozzolan from 10 to 30% results in an increase of the normal consistency, a reduction of the setting time, a decrease of the mechanical resistance to young aged and a conservation of these long-term resistance (Çolak 2003). The aim of this article is to study the mechanical behavior (stress-strain curves, strengths, strains, energy and elasticity modules) of recycled glass mortars by taking advantage of the pozzolanic reaction brought by the ternary association cement, supplementary cementations materials (*SCMs*) (Granulated slag, natural pozzolan) and recycled glass in order to achieve optimal valorization of glass waste.

## 2 Materials

The Portland cement used is of the CPJ-CEM II/A 52.5R type (NF EN 197-1. 2012) manufactured at the Lafarge cement plant in Hammam Dalaâ wilaya of M'sila, Algeria. The aggregate ($V$) used to make mortar mixtures is a recycled sand resulting from the grinding of glass windows known by their reactivity with ASR. This glass comes from the "SARL Vitre KHEZZANE" whose factory is located in the industrial zones Meboudja Chaiba, Sidi Amar in Annaba; it is the oldest glass processing plant in Algeria. The glass was supplied as debris of about 5 cm in size, partially freed of its impurities. The preparation of aggregates was carried out in accordance with the standard (*NF P18-594*). The delivered glass was washed with water and then put in an oven at 80 °C to dry (Fig. 1). After cooling, the dry material was introduced into a ball mill with a capacity of 10 kg and crushed to obtain the following granulometries: 5–2.5–1.25 mm, 630–315–160 μm then dried for 24 h in an oven at 80 °C. The fines smaller than 160 μm have been eliminated to avoid any interaction with the mineral additive particles in accordance with the (*NF EN 196-1*) standard. Figure 1 shows scanning electron microscope (*SEM*) image of glass particles. Indeed, the morphology of the particles is rounded facies without edges.

Demineralized water was used in all the mixes and curing of the specimens. The granulated slag ($L_a$) used in this work comes from the elaboration of the cast iron at the steel plant of El-Hadjar, Annaba, Algeria. It is defined by the standard *NF P 18-506*. It is a slag melted in the water basins, which leads to the formation of a large quantity of the vitreous phase.

The granulated slag ($L_a$) used in this work comes from the elaboration of the cast iron at the steel plant of El-Hadjar, Annaba, Algeria. It is defined by the standard *NF P 18-506*. It is a slag melted in the water basins, which leads to the formation of a large quantity of the vitreous phase. The natural pozzolan ($P_z$) used in this work is defined by the standard *NF P 18-308*. It is obtained by grinding of a siliceous volcanic rock extracted from the deposit of BENI-SAF in western Algeria. The physical properties, chemical and mineralogical compositions of cement, aggregate, granulated slag and natural pozzolan are shown in Table 1.

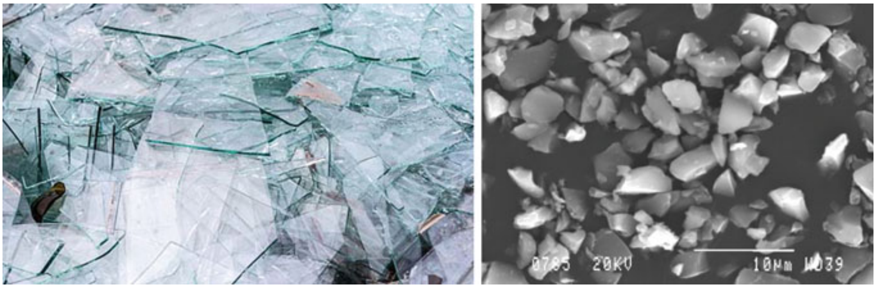

**Fig. 1** Left, glass waste freed from its impurities and right, Scanning electron microscope of glass grains

**Table 1** Physical properties, chemical and mineralogical compositions of cement, aggregate, granulated slag and natural pozzolan

| | CEM II/A 42.5 M'Sila | Glass waste aggregate | Granulated slag | Natural pouzzolan |
|---|---|---|---|---|
| *Chemical compositions (%)* | | | | |
| $SiO_2$ | 23.2 | 72.1 | 33.0 | 46.8 |
| $Al_2O_3$ | 4.9 | 1.0 | 11.8 | 18.8 |
| $Fe_2O_3$ | 3.3 | 0.1 | 1.6 | 10.5 |
| CaO | 64.2 | 6.3 | 41.3 | 9.2 |
| MgO | 0.2 | 3.7 | 9.0 | 3.8 |
| $SO_3$ | 2.5 | 0.1 | 0.13 | 0.2 |
| $K_2O$ | 0.1 | 0.1 | 0.51 | 0.5 |
| $Na_2O$ | 0.1 | 12.7 | 0.32 | 0.8 |
| *Composition (Bogue) (%)* | | | | |
| $C_3S$ | 56.0 | / | / | / |
| $C_2S$ | 16.0 | / | / | / |
| $C_3A$ | 5.5 | / | / | / |
| $C_4AF$ | 12.1 | / | / | / |
| *Physical properties* | | | | |
| Specific surface blaine ($m^2/kg$) | 320 | / | 300 | 300 |
| Specific weight ($kg/m^3$) | 3090 | 2310 | 2400 | 2670 |

## 3 Experimental Methods

The mortars were made with a replacement of 10, 20 and 30% cement volume by one of the supplementary cementations materials. The combination of all these experimental mixtures led to the manufacture of seven mortar mixtures made according to the same protocol so as to ensure repeatability in handling. Table 2 lists the mortars mixtures studied. To achieve the objective of the study, we made a mortar whose composition is inspired by that of the mortar defined by standard *NF P 18-594*. The preparation of mortars was carried out using a mixer with a capacity of *2* L consisting of a container and a stainless steel mixer able to operate at two speeds slow and fast according to the prescriptions of the standard *EN 196-1*. Water and cement with or without additions is introduced into the container at a standstill, then the mixer is started at a slow speed for 60 s and then at a fast speed for 30 s; the sand being introduced during the first 30 s. While the mixer is stopped for 90 s, manual scraping of the container walls is performed for the first 15 s of stopping and then the mixer is restarted at a faster speed for 60 s.

**Table 2** Mortar mixtures design and density

| Mortar | | Composition | | | | | Density |
|---|---|---|---|---|---|---|---|
| SCMs | % | Cement (kg/m$^3$) | Water ($l$/m$^3$) | W/C | Sand (kg/m$^3$) | SCMs (kg/m$^3$) | (kg/m$^3$) |
| V | 0 | 585 | 254 | 0.43 | 1760 | 0 | 2100 |
| V – $L_a$ | 10 | 525 | 266 | 0.46 | | 57 | 2204 |
| | 20 | 470 | 260 | 0.45 | | 115 | 2266 |
| | 30 | 410 | 259 | 0.45 | | 170 | 2218 |
| V – $P_z$ | 10 | 525 | 247 | 0.44 | | 52 | 2285 |
| | 20 | 470 | 254 | 0.44 | | 105 | 2260 |
| | 30 | 410 | 234 | 0.45 | | 155 | 2245 |

The mixing is performed with a standard laboratory mixer with a quantity of water adjusted to obtain a reference consistency. The reference consistency was evaluated by measuring the fresh mortar spread on a flow table ($l = 115$ mm). The fresh mortar placed in two layers compacted with a metal rod, in a truncated cone, with a small diameter of 100 mm, and upper diameter of 70 mm and height of 60 mm. After removal of the cone, the table is shaken 30 s and the value of the spread considered is the average of the measurement of the spread of the mixture along two perpendicular directions.

For each mortar having acquired the reference consistency, 40 × 40 × 160 mm specimens were prepared. The setting up of the mortars in the molds is carried out in two layers which undergo on a shock table 60 shakes in 60 s per layers, and then the density of the fresh mortars is measured by difference of weighing of the empty and solid mold according to standard *NF EN 196-1*. The test specimens are unmolded at one day and kept immersed in water at a temperature of 20 ± 2°C until testing time. For each mixture, we made 03 test pieces 40 × 40 × 160 mm, which was tested in bending, using a total of 21 bending tests. Two half-test specimens of each specimen were tested in flexion, with a total of 42 compressive tests. To achieve the study objective at 28 days curing time, the Zwick/Roe II Z020 universal machine was used for bending and compressive strength test (Fig. 2), a very low strain rate was used. The control and the acquisition of the results are done by computer from the software testXpert II, the results are the stress-strain curves, the strengths, the strains, the energy and the module of elasticity ($E$).

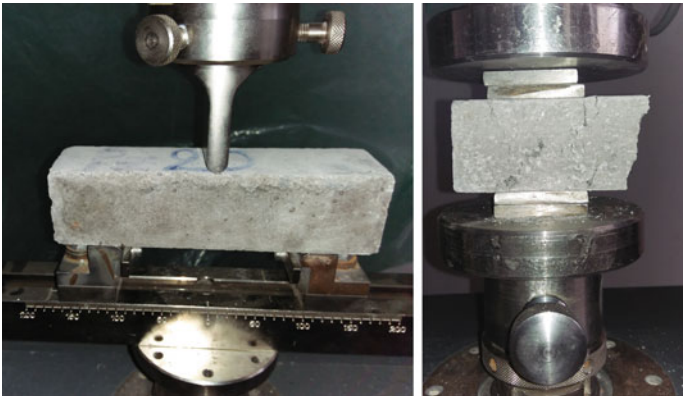

**Fig. 2** Bending and compressive strength tests

## 4 Results and Discussion

### *4.1 Bending Strength Test Results*

The analysis of the tests then consists in transforming the force-displacement curves obtained into stress-strain curves. Figure 3 give the stress-strain curves in bending obtained for different types of mortars at 28 days curing time.

From these curves it is noted that the behavior of *V* mortar without *SCMs* is elastic until the rupture so no plastic domain, this is due to the internal porosity which constitutes local concentration zones of constraints. It can be classified as a fragile material.

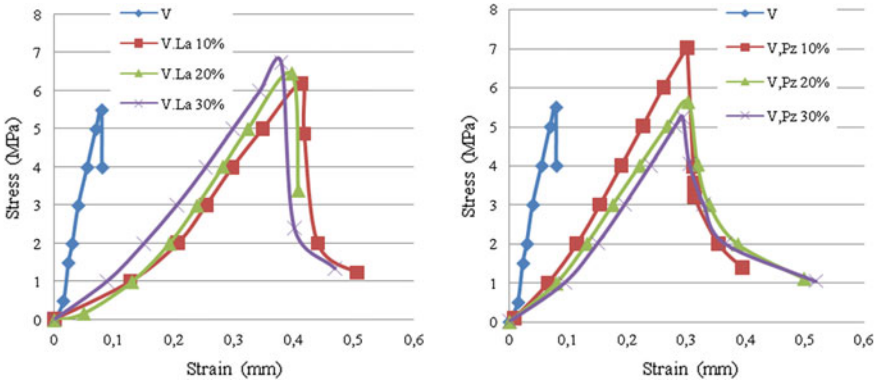

**Fig. 3** Respectively, $V \cdot L_a$ and $V \cdot L_z$ mortars stress-strain curves at 28 days

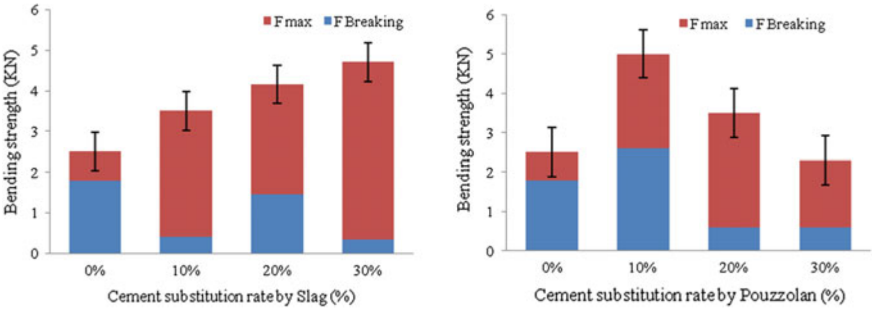

**Fig. 4** V · $L_a$ and V · $L_z$ mortars bending strengths variations at 28 days

The partial replacement of 10–30% of the cement volume by granulated slag or natural pozzolan considerably improves the ductility of a fragile material such as recycled glass mortar. In particular, the progressive substitution of the cement by the slag does not improve the ductility; unlike the progressive substitution of cement with pozzolan improves ductility.

At the end of each test, data collection allowed to record in Table 3 the values of the maximum strengths ($F_{max}$) and the breaking strengths ($F_{Breaking}$) and for each strength the strains ($\Delta L$) and the corresponding energy ($U_e$) is recorded.

The variations of bending strength values at 28 days of the mortars without and with SCMs are represented as a function of the degree of substitution of the cement in Fig. 4. The bending strength ($F_{max}$) is the maximum strength reached during the bending test, it is the elastic limit; the bending strength ($F_{Breaking}$) is the final strength reached during Breaking of the specimen. We observe ($\Delta F$) the difference between $F_{max}$ and $F_{Breaking}$, the higher $\Delta F$ is the more ductile the material is.

For mortar $V$, we note that $\Delta F$ is the weakest that interprets the fragility of this mortar. This difference is more important for mortars with SCMs ($L_a$ and $P_z$) that are considered more ductile. The bending strength at 28 days improves with increase of the substitution rates of cement by slags and reaches its maximum value at 30%. Which corresponds well with the results obtained by Memon et al. (2002) and Demirboga (2003). For mortars with natural pozzolan it is noted that the strength decreases with increase of cement substitution rates by natural pozzolan. The highest strength is measured for the rate of 10%, as has been shown in a number of studies (Çolak 2003).

The variations of bending strain at 28 days of mortars without and with *SCMs* are represented as a function of the degree of substitution of the cement in Fig. 5. The strains measured during the bending test are those corresponding to the tensile strength ($F_{max}$) noted ($\Delta L - F_{max}$), and those correspond to the final tensile strength ($F$-$_{Breaking}$) noted ($\Delta L - F_{Breaking}$) and more than these elongations are closer than the material is fragile (case of mortar *V)* and more than these elongations are discarded more than the material is ductile (Case of mortars with substitution of cement by the slag and natural pozzolan).

**Table 3** Mortar bending and compressive test results at 28 days

| Mortar | | Bending test results | | | | | | | Compressive test results |
|---|---|---|---|---|---|---|---|---|---|
| | | Strength (F) | | $\Delta L$ | | $U_e$ | | | |
| | | Max | Breaking | $F_{max}$ | $F_{Breaking}$ | $U_{e\ max}$ | $U_{e\ Breaing}$ | Stress | E |
| SCMs | % | KN | KN | mm | mm | KN.mm | KN.mm | MPa | GPa |
| V | 0 | 0.70 | 1.80 | 0.05 | 0.07 | 0.047 | 0.080 | 23.9 | 38.7 |
| $V \cdot L_a$ | 10 | 3.10 | 0.4 | 0.42 | 0.55 | 0.478 | 0.569 | 24.3 | 38.8 |
| | 20 | 2.70 | 1.45 | 0.38 | 0.40 | 0.440 | 0.460 | 22.1 | 37.2 |
| | 30 | 4.35 | 0.35 | 0.35 | 0.47 | 0.436 | 0.520 | 17.2 | 36.1 |
| $V \cdot P_z$ | 10 | 2.40 | 2.60 | 0.29 | 0.40 | 0.394 | 0.398 | 26.4 | 40.3 |
| | 20 | 2.90 | 0.60 | 0.31 | 0.50 | 0.403 | 0.467 | 23.0 | 37.9 |
| | 30 | 1.70 | 0.60 | 0.28 | 0.52 | 0.275 | 0.501 | 21.8 | 36.6 |

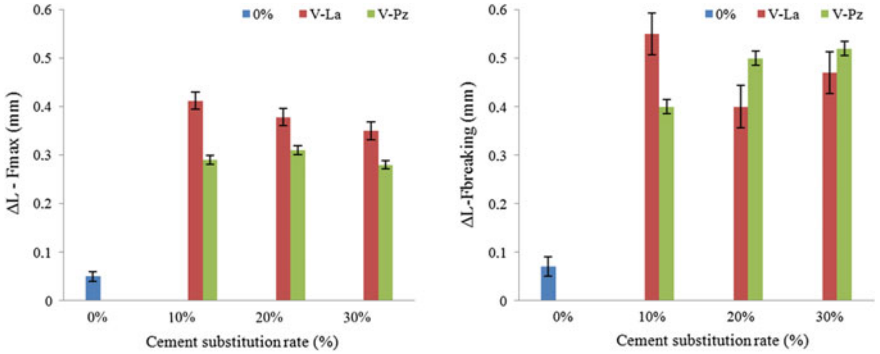

**Fig. 5** $V \cdot L_a$ and $V \cdot P_z$ mortars bending strain variations at 28 days respectively for $F_{max}$ and $F_{Breaking}$

For the $(V - L_a)$ mortars the variations of $(\Delta L - F_{max})$ are decreasing with cement substitution rate by slag and mortar with 10% has the lowest bending strength and the most important value of elongation for $(F_{max})$ and $(F_{Breaking})$.

The variations of $(\Delta L - F_{max})$ for $(V - P_z)$ mortars are very close to *0.33 mm* and lower than those of $(V - L_a)$ mortars. However the variations of $(\Delta L - F_{Breaking})$ are similar to those of $(V - L_a)$ mortars except for the $(V\text{-}Pz\ 10\%)$ mortar or the values recorded for $(\Delta L - F_{max})$ and $(\Delta L - F_{Breaking})$ are the lowest.

The bending energy's at 28 days of mortars with and without mineral additions is represented as a function of the degree of substitution of the cement in Fig. 6. The elastic strain energy per unit volume is the area under the bending curve; it is expressed by Eq. (1):

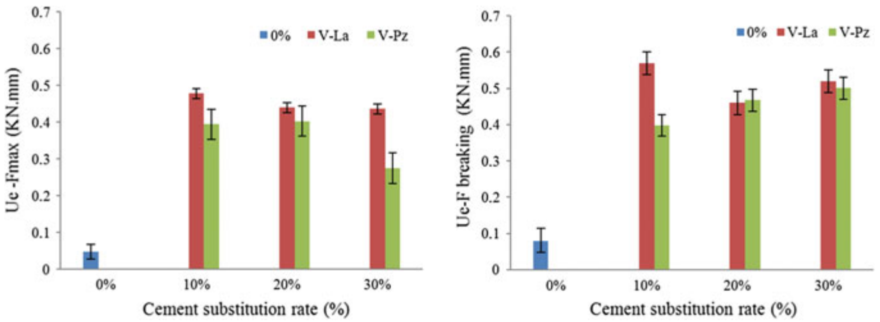

**Fig. 6** $V \cdot L_a$ and $V \cdot P_z$ mortars bending energy variations at 28 days respectively for $F_{max}$ and $F_{Breaking}$

$$U_e = \int_0^{\varepsilon} \sigma_n d\varepsilon_n = \int_0^{\varepsilon} E \cdot \varepsilon_n d\varepsilon_n = E \cdot \left[ \frac{\varepsilon_n^2}{n} \right]_0^{\varepsilon} = \frac{E\varepsilon^2}{2} = \frac{\sigma^2}{2E} \tag{1}$$

The elastic strain energy measured during the bending test is the energy corresponding to the bending strength ($F_{max}$) noted ($U_e - F_{max}$) and the final energy that corresponds to the final bending strength ($F_{Breaking}$) reached during the breaking of the noted specimen ($U_e - F_{Breaking}$) which is the energy necessary to break the specimen. In general, the value of ($U_e - F_{max}$) is very low at the value of ($U_e - F_{rupt}$) for ductile materials (Case of mortars with substitution of cement by slag and pozzolan), the values of two energies are close for fragile materials (case of mortar $V$).

For all types of mortar the recorded energy values are low which confirms the fragile fracture and the elastic behavior of the mortars. The variations of the energy ($U_e - F_{rupt}$) of the $V - L_a$ mortars are opposed to the variations of the strength. It can be noticed that they are increasing with the rate of substitution of cement by slag and that the *10%* mortar has the highest energy and the lowest strength.

The energy values measured for the $V - P_z$ mortars are very similar and weak compared to those measured for the $V - L_a$ mortars either for ($F_{\mathrm{max}}$) or for ($F_{\mathrm{Breaking}}$) with the exception of the 30% mortar. The difference between the energy values measured at ($F_{max}$) and ($F_{Breaking}$) is high so this mortar is considered ductile.

## *4.2 Compressive Strength Test Results*

The variation in the compressive strength values of the mortar at 28 days to various mixtures is given in Fig. 7. The strength decreases considerably with the increase in the *SCMs* content. For a composition ranging from 0 to 30%, the compressive strength varies from 24 MPa. For the reference mortar without *SCMs* to 17 and 21.8 MPa a reduction of the order of 30 and 10% for mortars with granulated slag and mortars with natural pozzolan respectively. The loss of strength is linked on the one hand to the mineralogical nature of the *SCMs* and on the other hand to the increase in porosity because of the greater quantity of water used. This excess water is characterized by the increase in the spread of fresh mortar by the flow table test. The evaporation of this water during curing generates additional porosity in the matrix. The results show that despite the reduction in the compressive strength the value obtained for a 30% addition composition remains compatible with the use of the material in the field of application of construction concretes.

The elasticity modules results given in Fig. 8 show that the addition of granulated slag and natural pozzolan in the cementations matrix slightly reduces the elasticity modules from 39 GPa (mortar at 0% *SCMs*) to 35 and 36 GPa for a content of 30% granulated slag and natural pozzolan respectively. This decrease is due to the dilution effect. The natural pozzolan by its beneficial pozzolanic reaction decreases the elasticity modules. These results correspond well with the results of compressive strength.

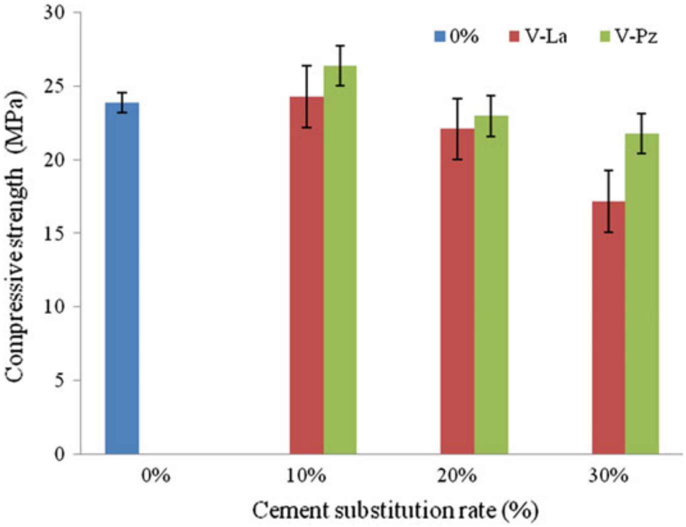

**Fig. 7** V · $L_a$ and V · $P_z$ mortars compressive strengths variations at 28 days as a function of cement substitution rate by SCMs

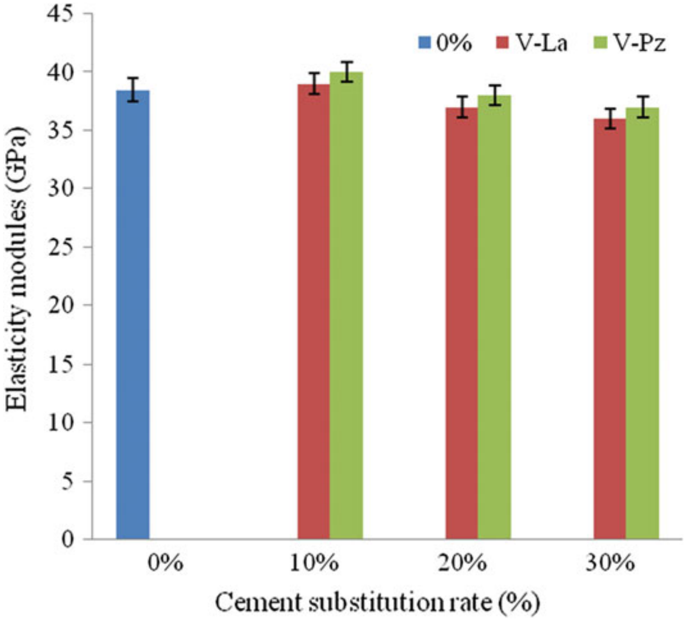

**Fig. 8** V · $L_a$ and V · $P_z$ mortars mortars elasticity modules variations at 28 days, as a function of cement substitution rate by SCMs

## 5 Conclusion

The present study concerns the verification of the effect of *SCMs* on the mechanical properties of mortars when recycled glass is used as an aggregate. Bending and compressive tests showed that:

1. According to the stress-strain curves the ductility of the mortars with *SMCs* improves with increase of cement substitution rate by natural pozzolan and decreases with increase of the substitution rates of cement by granulated slag.
2. Bending strength decreases with increasing natural pozzolan content, but improves with increase in the granulated slag content.
3. The variations of the strains with the rate of substitution of cement by the SCMs are decreasing for $(V - L_a)$ mortars and increasing for $(V - P_z)$ mortars.
4. The recorded energy values are low for all types of mortar.

Despite a decrease in the compressive strength the value obtained for mixtures with 30% of *SCMs* remains compatible with the use of the material in field construction applications. In addition the elasticity module measurements correspond well with the results of the compressive strength.

## References

Boudchicha A, Cheikh Zouaoui M, Gallias J-L, Mezghiche B (2007) Analysis of the effects of mineral admixtures on the strength of mortars: application of the predictive model of Feret. J Civil Eng Manag 13(2):87–96. https://doi.org/10.1080/13923730.2007.9636424

Carles-Gibergues A, Cyr M, Moisson M, Ringot E (2008) A simple way to mitigate alkali-silica reaction. Mater Struct 41:73–83. https://doi.org/10.1617/s11527-006-9220-y

Çolak A (2003) Characteristics of pastes from a Portland cement containing different amounts of natural pouzzolan. Cem Concr Res 33(4):585–593. https://doi.org/10.1016/S0008-8846(02)01027-X

Demirboga R (2003) Influence of mineral admixtures on thermal conductivity and compressive strength of mortar. Energy Build 35(2):189–192. https://doi.org/10.1016/S0378-7788(02)00052-X

Douaissia Z, Merzoud M (2018) Effect of mineral admixtures on the rheological and mechanical properties of mortars, MATEC Web of conferences 149. https://doi.org/10.1051/matecconf/201814901066

Idir R, Cyr M, Tagnit-Hamou A (2011) Pozzolanic properties of fine and coarse color-mixed glass cullet. Cem Concr Compos 33(1):19–29. https://doi.org/10.1016/j.cemconcomp.2010.09.013

Idir R, Cyr M, Tagnit-Hamou A (2010) Use of fine glass as ASR inhibitor in glass aggregate mortars. Constr Build Mater 24(7):1309–1312. https://doi.org/10.1016/j.conbuildmat.2009.12.030

Jin C, Meyer C, Baxter S (2000) Glascrete-concrete with glass aggregate, American concrete institute. Mat J 97:208–213. http://www.columbia.edu/cu/civileng/meyer/publications/publications/56.pdf

Manjit S, Mridul G (1999) Cementitious binder from fly ash and other industrial wastes. Cem Concr Res 29(3):309–314. https://doi.org/10.1016/S0008-8846(98)00210-5

Memon AH, Radin SS, Zain MFM, Trottier JF (2002) Effect of mineral and chemical admixtures on high-strength concrete in seawater. Cem Concr Res 32(3):373–377. https://doi.org/10.1016/S0008-8846(01)00687-1

Meyer C, Baxter S (1997) Use of recycled glass for concrete masonry blocks, final report to New York state energy research and development authority, Report no. 97–15, Albany, New York. https://www.osti.gov/biblio/649568

Yixin S, Thibaut L, Shylesh M, Damian R (2000) Studies on concrete containing ground waste glass. Cem Concr Res 30(1):91–100. https://doi.org/10.1016/S0008-8846(99)00213-6

Zhu H, Chen W, Zhou W et al (2009) Expansion behaviour of glass aggregates in different testing for alkali-silica reactivity. Mater Struct 42:485. https://doi.org/10.1617/s11527-008-9396-4

# Buckling Analysis of Isotropic and Composite Laminated Plates: New Finite Element Formulation

**Khmissi Belkaid**

## 1 Introduction

Nowadays, the multilayer composite materials are found increasingly wide applications essentially in all industrial sectors. This considerable use is probably due to the notable benefits of this type of materials namely; an excellent rigidity weight ratio, good corrosion resistance, fatigue resistance. The multilayer composite structures analysis is still questionable and soliciting accurate theories to describe their complicated mechanical behavior. Several higher order shear deformation theories (HSDT) have been proposed in the literature (Reddy and Robbins 1994; Ghugal and Shimpi 2002), in accurately assessing the deformation and stress of transverse shear multilayer plates without to need factors correction. Moreover, Reddy's theory (*TSDT*) is the higher order theory most frequent for multilayer plates analysis when it is able to assess the stresses and transverse shear deformations with a small number unknown and don't depend on the layer number (Reddy 1984a, b). Recently, Belkaid and Tati (2015), Belkaid et al., (2016) developed a four node finite element $C_1$ with five degrees of freedom in each node based on Reddy's theory for the bending behavior analysis of isotropic and laminated composites plates. The first buckling analysis of orthotropic and isotropic plates was undertaken by (Gerard and Becker 1957). Thereafter, it was followed by Leissa's general work (Leissa 1987a, b) for the buckling of laminated composite plates. Furthermore, a review is recently published by (Xu et al. 2013) on the analysis of buckling behavior and post-buckling of composite structural elements.

---

K. Belkaid (✉)
Research Center in Industrial Technologies CRTI, P.O. Box 64, 16014 Cheraga, Algiers, Algeria
e-mail: khmissi.belkaid85@gmail.com

T. Boukharouba et al. (eds.), *Computational Methods and Experimental Testing In Mechanical Engineering*, Lecture Notes in Mechanical Engineering,
https://doi.org/10.1007/978-3-030-11827-3_8

Moreover, some studies have been presented in literature on the thin and thick buckling laminated plates structures based on higher order theories using two-dimensional finite element models by calculating the stiffness and geometry matrix (Putcha and Reddy 1986; Chakrabarti and Sheikh 2003; Averill and Reddy 1992; Singh and Chakrabarti 2012; Ghosh abd Dey 1994; Singh and Rao 1996; Moita et al. 1996, 1999).

The objective of this paper is to propose a simple finite element less expensive in terms of accuracy and stability on the basis of Reddy's third order theory (*TSDT*) by adopting the approach of equivalent single layer, and able to analyze the mechanical buckling behavior of isotropic and laminated composite plates by ensuring the right compromise between the cost and precision.

## 2 Kinematic

The displacement field according to the Reddy's third order shear deformation theory *TSDT* (Reddy 1984a) can be expressed as follows:

$$u_1 = u + z\psi_x - \frac{4z^3}{3h}(\psi_x + \frac{\partial w}{\partial x}),\ u_2 = v + z\psi_y - \frac{4z^3}{3h}(\psi_y + \frac{\partial w}{\partial y}),\ u_3 = w \tag{1}$$

where $u$, $v$, $w$ are the displacements to the median plane of the plate and $\psi_x$, $\psi_y$ are rotations about the axes $y$ and $x$ respectively, and $h$ is the thickness of the plate. The deformations associated with displacement field (1), given as follows:

$$\begin{aligned}
\varepsilon_{11} &= \frac{\partial u_1}{\partial x} + \frac{1}{2}\left[\left(\frac{\partial u_3}{\partial x}\right)^2\right] = \varepsilon_1^0 + z\left(\kappa_1^0 + z^2\kappa_1^2\right);\\
\varepsilon_{22} &= \frac{\partial u_2}{\partial y} + \frac{1}{2}\left[\left(\frac{\partial u_3}{\partial y}\right)^2\right] = \varepsilon_2^0 + z\left(\kappa_2^0 + z^2\kappa_2^2\right);\\
\varepsilon_{23} &= \left(\frac{\partial u_2}{\partial z} + \frac{\partial u_3}{\partial y} + \frac{\partial u_3}{\partial y}\frac{\partial u_3}{\partial z}\right) = \varepsilon_4^0 + z^2\kappa_4^2;\\
\varepsilon_{13} &= \left(\frac{\partial u_1}{\partial z} + \frac{\partial u_3}{\partial x} + \frac{\partial u_3}{\partial x}\frac{\partial u_3}{\partial z}\right) = \varepsilon_5^0 + z^2\kappa_5^2;\\
\varepsilon_{12} &= \left(\frac{\partial u_1}{\partial y} + \frac{\partial u_2}{\partial x} + \frac{\partial u_3}{\partial x}\frac{\partial u_3}{\partial y}\right) = \varepsilon_6^0 + z\left(\kappa_6^0 + z^2\kappa_6^2\right);
\end{aligned} \tag{2}$$

## 3 Constitutive Equations

The stress-strain relationships laminated to the $k^{\text{ième}}$ layer after the global coordinate $x, y, z$ transformation (Reddy 2004) and according the transformation matrix and the stress-strain relationships, it is given by (Fig. 1):

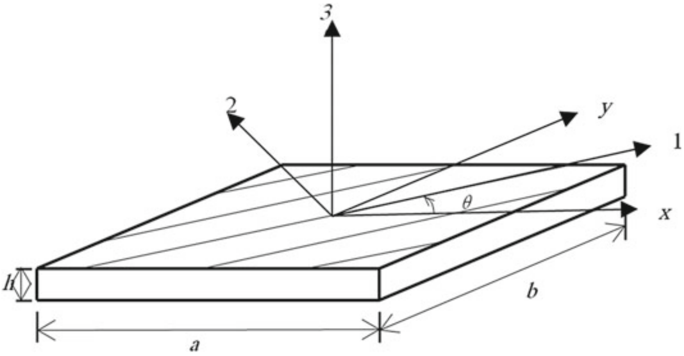

**Fig. 1** Geometry and coordinate system of the laminated composite plate

$$\begin{Bmatrix} \sigma_{xx} \\ \sigma_{yy} \\ \sigma_{xy} \end{Bmatrix}_k = \begin{bmatrix} \overline{C}_{11} & \overline{C}_{12} & \overline{C}_{16} \\ \overline{C}_{12} & \overline{C}_{22} & \overline{C}_{26} \\ \overline{C}_{16} & \overline{C}_{26} & \overline{C}_{66} \end{bmatrix}_k \begin{Bmatrix} \varepsilon_{xx} \\ \varepsilon_{yy} \\ \gamma_{xy} \end{Bmatrix}; \begin{Bmatrix} \sigma_{yz} \\ \sigma_{xz} \end{Bmatrix}_k = \begin{bmatrix} \overline{C}_{44} & \overline{C}_{45} \\ \overline{C}_{45} & \overline{C}_{55} \end{bmatrix}_k \begin{Bmatrix} \gamma_{yz} \\ \gamma_{xz} \end{Bmatrix} \tag{3}$$

## 4 Virtual Work Principle

The static equations of the theory can be derived from the virtual work principle (Reddy 1984a) by expressing the strain variation energy as follows:

$$\int\limits_{-h/2}^{h/2} \int\limits_{A} (\sigma_1 \delta\varepsilon_1 + \sigma_2 \delta\varepsilon_2 + \sigma_6 \delta\varepsilon_6 + \sigma_5 \delta\varepsilon_5 + \sigma_4 \delta\varepsilon_4)\, dA dz + \int\limits_{A} q \delta W dA = 0 \tag{4}$$

According to the substitution of Eq. (2) in the static Eq. (4) we obtain:

$$\begin{aligned} &\int\limits_{A} [N_1 \frac{\partial \delta u}{\partial x} + M_1 \frac{\partial \delta \psi_x}{\partial x} + P_1(-\frac{4}{3h^2}(\frac{\partial \delta \psi_x}{\partial x} + \frac{\partial^2 \delta w}{\partial x^2})) + N_2 \frac{\partial \delta v}{\partial y} + M_2 \frac{\partial \delta \psi_y}{\partial y} \\ &+ P_2(-\frac{4}{3h^2}(\frac{\partial \delta \psi_y}{\partial y} + \frac{\partial^2 \delta w}{\partial y^2})) + N_6(\frac{\partial \delta u}{\partial y} + \frac{\partial \delta v}{\partial x}) + M_6(\frac{\partial \delta \psi_x}{\partial y} + \frac{\partial \delta \psi_y}{\partial x}) \\ &+ P_6(-\frac{4}{3h^2}(\frac{\partial \delta \psi_x}{\partial y} + \frac{\partial \delta \psi_y}{\partial x} + 2\frac{\partial^2 \delta w}{\partial x \partial y})) + Q_2(\delta \psi_y + \frac{\partial \delta w}{\partial y}) + R_2(-\frac{4}{h^2}(\delta \psi_y + \frac{\partial \delta w}{\partial y})) \\ &+ Q_1(\delta \psi_x + \frac{\partial \delta w}{\partial x}) + R_2(-\frac{4}{h^2}(\delta \psi_x + \frac{\partial \delta w}{\partial x})) + \varepsilon_{NL}^{\circ T}\{N\} + q \delta w] dA = 0 \end{aligned} \tag{5}$$

where $N_i$, $M_i$, $P_i$, $Q_1$, $Q_2$ and $R_1$, $R_2$ are the resulting forces to define:

$$(N_i, M_i, P_i) = \sum_{k=1}^{n} \int_{h_{k-1}}^{h_k} \sigma_i\left(1, z, z^3\right) dz; (i = 1, 2, 6);\ (Q_2, R_2) = \sum_{k=1}^{n} \int_{h_{k-1}}^{h_k} \sigma_4\left(1, z^2\right) dz;$$

$$(Q_1, R_1) = \sum_{k=1}^{n} \int_{h_{k-1}}^{h_k} \sigma_5\left(1, z^2\right) dz;\ \varepsilon_{NL}^{0T} = \left[\ \left(\tfrac{\partial w}{\partial x}\right)^2\ \left(\frac{\partial w}{\partial y}\right)^2\ 2\tfrac{\partial w}{\partial x}\tfrac{\partial w}{\partial y}\ \right];$$

$$\{N\}^T = \left[\, N_1\ N_2\ N_6 \,\right]$$

$\varepsilon_{NL}^{0T}$ is the large strain of Von Karman theory, $\{N\}^T$ is the vector of membrane resulting forces. Therefore, the generalized relations resulting forces can be given as follows (Reddy 1984a):

$$\begin{Bmatrix} \{N_i\} \\ \{M_i\} \\ \{P_i\} \end{Bmatrix} = \begin{bmatrix} [A_{ij}] & [B_{ij}] & [E_{ij}] \\ & [D_{ij}] & [F_{ij}] \\ sym & & [H_{ij}] \end{bmatrix} \begin{Bmatrix} \varepsilon^0 \\ \kappa^0 \\ \kappa^2 \end{Bmatrix}; \begin{Bmatrix} \begin{Bmatrix} Q_2 \\ Q_1 \end{Bmatrix} \\ \begin{Bmatrix} R_2 \\ R_1 \end{Bmatrix} \end{Bmatrix} = \begin{bmatrix} A_{44} & A_{45} & D_{44} & D_{45} \\ & A_{55} & D_{45} & D_{55} \\ & & F_{44} & F_{45} \\ sym & & & F_{55} \end{bmatrix} \begin{Bmatrix} \varepsilon_4^0 \\ \varepsilon_5^0 \\ \kappa_4^2 \\ \kappa_5^2 \end{Bmatrix} \quad (6)$$

where:

$$\left[\ \underbrace{\varepsilon_1^0\ \varepsilon_2^0\ \varepsilon_6^0}_{}\ \underbrace{\kappa_1^0\ \kappa_2^0\ \kappa_6^0}_{}\ \underbrace{\kappa_1^2\ \kappa_2^2\ \kappa_6^2}_{}\ \right]^T = \left[\, \varepsilon^0\ \kappa^0\ \kappa^2 \,\right]^T; \left[\ \underbrace{\varepsilon_4^0\ \varepsilon_5^0}_{}\ \underbrace{\kappa_4^2\ \kappa_5^2}_{}\ \right]^T = \left[\, \gamma^s\ \kappa^s \,\right]^T$$

where:

$$(A_{ij}, B_{ij}, D_{ij}, E_{ij}, F_{ij}, H_{ij}) = \sum_{k=1}^{n} \int_{h_{k-1}}^{h_k} \overline{C}_{ij}(1, z, z^2, z^3, z^4, z^6)\, dz, \quad (i, j = 1, 2, 6)$$

$$(A_{ij}, D_{ij}, F_{ij}) = \sum_{k=1}^{n} \int_{h_{k-1}}^{h_k} \overline{C}_{ij}(1, z^2, z^4)\, dz, \quad (i, j = 4, 5)$$

Substituting the resulting forces defined in Eq. (5), we obtain:

$$\begin{aligned} \int_A & (\delta\varepsilon^{0T}[A]\varepsilon^0 + \delta\varepsilon^{0T}[B]\kappa^0 + \delta\varepsilon^{0T}[E]\kappa^2 + \delta\kappa^{0T}[B]\varepsilon^0 + \delta\kappa^{0T}[D]\kappa^0 \\ & + \delta\kappa^{0T}[F]\kappa^2 + \delta\kappa^{2T}[E]\varepsilon^0 + \delta\kappa^{2T}[F]\kappa^0 + \delta\kappa^{2T}[H]\kappa^2 + \delta\gamma^{sT}\left[A^s\right]\gamma^s \\ & + \delta\gamma^{sT}\left[D^s\right]\kappa^s + \delta\kappa^{sT}\left[D^s\right]\gamma^s + \delta\kappa^{sT}\left[F^s\right]\kappa^s + \varepsilon_{NL}^{0T}\{N\} + q\delta w)\, dA = 0 \end{aligned} \quad (7)$$

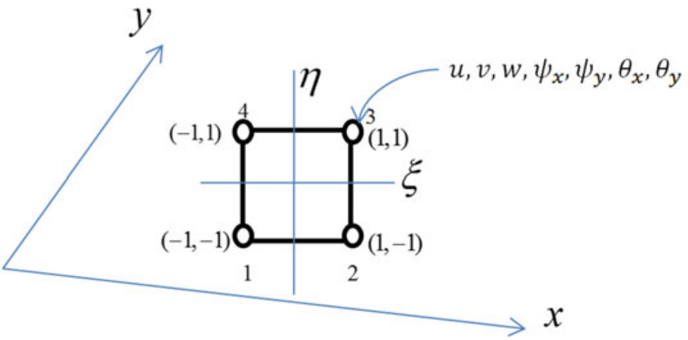

**Fig. 2** Description of the normalized isoparametric element

# 5 Finite Element Formulation

The present finite element is a $C_0$ four nodes isoparametric having seven DOF for each node (Fig. 2). Three displacements *u, v, w*, two rotations $\psi_x$, $\psi_y$ and two higher order rotations $\theta_x$, $\theta_y$ where $\theta_x = (\psi_x + \partial w/\partial x)$, $\theta_y = (\psi_y + \partial w/\partial y)$. The analytical integration can be converted to Gauss's numerical integration (Hughes et al. 1978). For more model performance in terms of accuracy and stability and to avoid shear locking problem, the technical selective numerical integration is used from Gauss points (2 × 2) for membrane and flexional contribution and (1 × 1) point for the transverse shear contribution.

## 5.1 Nodal Approximation

The nodal approximation is expressed from the Lagrange interpolation concerning the considered degrees of freedom in each node and the element geometry through all coordinates $(\zeta, \eta)$, the field variables may be expressed as follows:

$$u(\xi,\eta) = \sum_{i=1}^{4} \bar{N}_i(\xi,\eta)u_i;\ v(\xi,\eta) = \sum_{i=1}^{4} \bar{N}_i(\xi,\eta)v_i;\ w(\xi,\eta) = \sum_{i=1}^{4} \bar{N}_i(\xi,\eta)w_i;$$

$$\psi_x(\xi,\eta) = \sum_{i=1}^{4} \bar{N}_i(\xi,\eta)\psi_{xi};\ \psi_y(\xi,\eta) = \sum_{i=1}^{4} \bar{N}_i(\xi,\eta)\psi_{yi};$$

$$\theta_x(\xi,\eta) = \sum_{i=1}^{4} \bar{N}_i(\xi,\eta)\theta_{xi};\ \theta_y(\xi,\eta) = \sum_{i=1}^{4} \bar{N}_i(\xi,\eta)\theta_{xi};\ x = \sum_{i=1}^{4} \bar{N}_i(\xi,\eta)x_i;$$

$$y = \sum_{i=1}^{4} \bar{N}_i(\xi,\eta)y_i,\ Where: \bar{N}_i(\xi,\eta) = \frac{1}{4}(1+\xi\xi_i)(1+\eta\eta_i)$$

$N_i(\zeta, \eta)$ are the bi linear interpolation functions of Lagrange type corresponding to node $i = 1{,}2{,}3{,}4$ (Zienkiewicz and Cheung 1964).

## 5.2 Deformations and Nodal Displacements Relations

The deformation vectors and the nodal unknowns can be taken as the elementary nodal matrix forms as follows:

$$\varepsilon^0 = \left[B_\varepsilon^0\right]^r \{\delta\} = \begin{bmatrix} \frac{\partial \overline{N}_i}{\partial x} & 0 & 0\,0\,0\,0\,0 \\ 0 & \frac{\partial \overline{N}_i}{\partial y} & 0\,0\,0\,0\,0 \\ \frac{\partial \overline{N}_i}{\partial y} & \frac{\partial \overline{N}_i}{\partial x} & 0\,0\,0\,0\,0 \end{bmatrix} \begin{Bmatrix} u_i \\ v_i \\ w_i \\ \psi_{x_i} \\ \psi_{y\,\mathrm{i}} \\ \theta_{x\,\mathrm{i}} \\ \theta_{y\,\mathrm{i}} \end{Bmatrix} \quad \kappa^0 = \left[B_\kappa^0\right]^r \{\delta\} = \begin{bmatrix} 0\,0\,0 & \frac{\partial \overline{N}_i}{\partial x} & 0 & 0\,0 \\ 0\,0\,0 & 0 & \frac{\partial \overline{N}_i}{\partial y} & 0\,0 \\ 0\,0\,0 & \frac{\partial \overline{N}_i}{\partial y} & \frac{\partial \overline{N}_i}{\partial x} & 0\,0 \end{bmatrix} \begin{Bmatrix} u_i \\ v_i \\ w_i \\ \psi_{x_i} \\ \psi_{y\,\mathrm{i}} \\ \theta_{x\,\mathrm{i}} \\ \theta_{y\,\mathrm{i}} \end{Bmatrix}$$

$$\kappa^2 = \left[B_\kappa^2\right]^r \{\delta\} = c_1 \begin{bmatrix} 0\,0\,0\,0\,0 & \frac{\partial \overline{N}_i}{\partial x} & 0 \\ 0\,0\,0\,0\,0 & 0 & \frac{\partial \overline{N}_i}{\partial y} \\ 0\,0\,0\,0\,0 & \frac{\partial \overline{N}_i}{\partial y} & \frac{\partial \overline{N}_i}{\partial x} \end{bmatrix} \begin{Bmatrix} u_i \\ v_i \\ w_i \\ \psi_{x_i} \\ \psi_{y\,\mathrm{i}} \\ \theta_{x\,\mathrm{i}} \\ \theta_{y\,\mathrm{i}} \end{Bmatrix} \quad \gamma^s = \left[B_\varepsilon^s\right]^r \{\delta\} = \begin{bmatrix} 0\,0 & \frac{\partial \overline{N}_i}{\partial y} & 0 & \overline{N}_i & 0\,0 \\ 0\,0 & \frac{\partial \overline{N}_i}{\partial x} & \overline{N}_i & 0 & 0\,0 \end{bmatrix} \begin{Bmatrix} u_i \\ v_i \\ w_i \\ \psi_{x_i} \\ \psi_{y\,\mathrm{i}} \\ \theta_{x\,\mathrm{i}} \\ \theta_{y\,\mathrm{i}} \end{Bmatrix}$$

$$\kappa^s = \left[B_\kappa^s\right]^r \{\delta\} = c_2 \begin{bmatrix} 0\,0\,0\,0\,0 & 0 & \overline{N}_i \\ 0\,0\,0\,0\,0 & \overline{N}_i & 0 \end{bmatrix} \begin{Bmatrix} u_i \\ v_i \\ w_i \\ \psi_{x_i} \\ \psi_{y\,\mathrm{i}} \\ \theta_{x\,\mathrm{i}} \\ \theta_{y\,\mathrm{i}} \end{Bmatrix} \qquad \text{With : } c_1 = -4/3h^2,\ c_2 = -4/h^2$$

According to the substitution of deformation and nodal displacements relations in the equilibrium Eq. (7) and from the static system $[K]_e\{\delta\} = \{F\}$ we can conclude the elementary stiffness matrix $[K]_\mathrm{e}$ as follow:

$$\begin{aligned} [K]_e = \int_{-1}^{1}\int_{-1}^{1} \Big( & \left[B_\varepsilon^0\right]^T [A] \left[B_\varepsilon^0\right] + \left[B_\varepsilon^0\right]^T [B] \left[B_\kappa^0\right] + \left[B_\varepsilon^0\right]^T [E] \left[B_\kappa^2\right] + \left[B_\kappa^0\right]^T [B] \left[B_\varepsilon^0\right] \\ & + \left[B_\kappa^0\right]^T [D] \left[B_\kappa^0\right] + \left[B_\kappa^0\right]^T [F] \left[B_\kappa^2\right] + \left[B_\kappa^2\right]^T [E] \left[B_\varepsilon^0\right] + \left[B_\kappa^2\right]^T [F] \left[B_\kappa^0\right] + \left[B_\kappa^2\right]^T [H] \left[B_\kappa^2\right] \\ & + \left[B_\varepsilon^s\right]^T \left[A^s\right]\left[B_\varepsilon^s\right] + \left[B_\varepsilon^s\right]^T \left[D^s\right]\left[B_\kappa^s\right] + \left[B_\kappa^s\right]^T \left[D^s\right]\left[B_\varepsilon^s\right] + \left[B_\kappa^s\right]^T \left[F^s\right]\left[B_\kappa^s\right] \Big) \det[J] d\xi d\eta \end{aligned} \tag{8}$$

where: $\{F\}$, $\{\delta\}$ are the elementary nodal vectors of forces and unknowns displacement, respectively.

The elementary geometric matrix is given as follows:

$$\left[K_g\right]_e = \int_{-1}^{1}\int_{-1}^{1} [G]^T [N_0][G] \det[J] d\xi d\eta \tag{9}$$

The linear analysis of a finite element buckling problem is expressed as follows (Xu et al. 2013):

$$[K] + \lambda\left[K_g\right] = 0 \tag{10}$$

## 6 Results and Discussion

Some of the best known numerical tests in the literature have been taken in order to validate and to investigate the accuracy and reliability of the newly developed laminated plate finite element on the buckling behavior.

– The boundary conditions used in this study is given as follow:

$$x = \overset{+}{-}a/2 \rightarrow w = \psi_y = \theta_y = 0; y = \overset{+}{-}b/2 \rightarrow w = \psi_x = \theta_x = 0$$

### 6.1 *Convergence Study*

In the first example, the convergence of the developed quadrilateral element is studied for a simply supported isotropic square plate. Different thickness ratios ($a/h = 5$, 10, 100) are considered for this analysis. The non-dimensional results of critical uniaxial load for different mesh sizes are displayed on Table 1. The comparison was made with the analytical solutions given by (Reddy and Phan 1985), and the finite element solution given by (Chakrabarti and Sheikh 2003). The comparison results show the performances and convergence of the present formulation. It can be noticed that the present model is appropriate in both thick and thin isotropic plates. Moreover, in this study a demonstration has been considered on the two buckling modes for isotropic plate (Fig. 3).

### 6.2 *The Orthotropic Effect on Cross-Ply Square Plates (0/90)*

In this example, we consider different simply supported cross-ply laminated plates with $a/h = 10$ ratio, in order to determine the uniaxial critical load along the $x$ axis for different orthotropic ratio $E_1/E_2 = open$, $G_{12} = G_{13} = 0.5E_2$, $G_{23} = 0.2E_2$, $\nu = 0.25$. Satisfactory results are obtained from the present element (Table 2) comparing to those obtained analytically by Noor Elasticity 3D (Noor 1975; Putcha and Reddy 1986) and with numerical models by Ferreira et al. (2011).

**Table 1** Convergence test of the uniaxial critical load of a simply supported isotropic square plate, $N_{cr} = \overline{N}_{cr} a^2/\pi^2 D$, $D = Eh^3/12(1 - \nu^2)$, $\nu = 0.3$

| Reference | Theory | $N_{cr}$ (critical load) | | |
|---|---|---|---|---|
| | | a/h = 5 | a/h = 10 | a/h = 100 |
| Present (4 × 4) | TSDT | 3.3426 | 3.9992 | 4.1550 |
| Present (8 × 8) | | 3.2511 | 3.8085 | 4.0874 |
| Present (12 × 12) | | 3.2510 | 3.7852 | 4.0371 |
| Present (16 × 16) | | 3.2551 | 3.7810 | 4.0190 |
| Present (18 × 18) | | 3.2561 | 3.7811 | 4.0143 |
| Chakrabarti and Sheikh (2003) | HSDT (FE) | 3.2600 | 3.7820 | 3.9960 |
| Reddy and Phan (1985) | TSDT | 3.2650 | 3.7870 | 3.9980 |

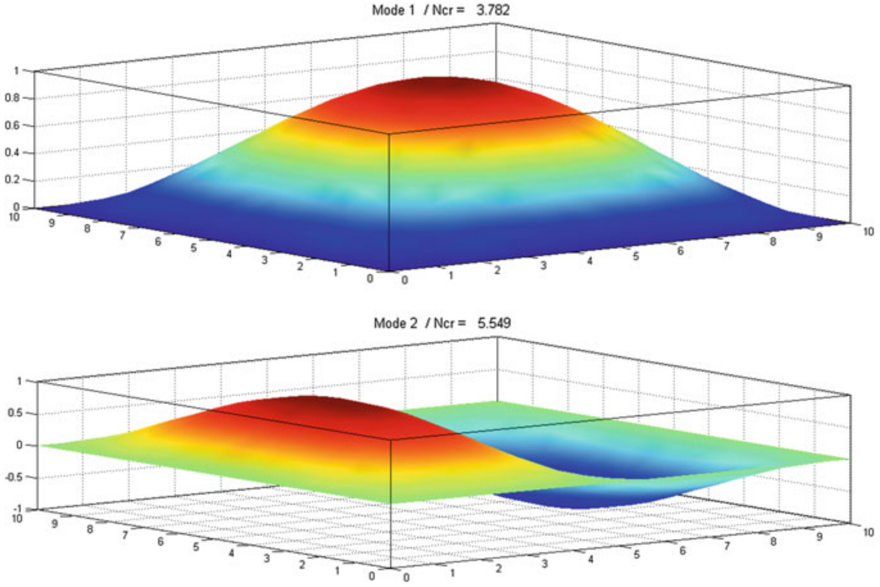
Mode 1 / Ncr = 3.782

Mode 2 / Ncr = 5.549

**Fig. 3** First 2 buckling modes uniaxial buckling load of simply supported isotropic square plate a/h = 10

## 7 Conclusion

In this paper, a developed four nodes isoparametric finite element is proposed on the basis on Reddy's third order shear deformation theory by adopting the equivalent single-layer approach. The present element has seven degrees of freedom for each node, three displacements, two rotations and two higher order rotations. The formulation is able to take into account the transverse shear effect in order to analyze the buckling behavior of isotropic and laminated composite thin and thick plates

**Table 2** Orthotropic ratio effect on the uniaxial critical load $N_{cr} = \overline{N}_{cr} a^2/E_2 h^3$ of different simply supported square cross-ply laminated plates (a/h = 10)

| Reference | Layers | $E_1/E_2$ | | | | |
|---|---|---|---|---|---|---|
| | | 3 | 10 | 20 | 30 | 40 |
| Elaticity-Noor (1975) | 2 | 4.6948 | 6.1181 | 7.8196 | 9.3746 | 10.817 |
| Putcha and Reddy (1986) | | 4.7149 | 6.2721 | 8.1151 | 9.8695 | 11.563 |
| Present (16 × 16) | | 3.7633 | 5.1543 | 7.3472 | 9.4666 | 11.435 |
| Putcha and Reddy (1986) | 3 | 5.3933 | 9.9406 | 15.298 | 19.674 | 23.340 |
| Ferreira et al. (2011) | | 5.3872 | 9.8331 | 14.895 | 18.892 | 22.153 |
| Present (16 × 16) | | 5.4088 | 9.8833 | 14.965 | 18.965 | 22.213 |
| Ferreira et al. (2011) | 4 (symetrical) | 5.3933 | 9.9406 | 15.298 | – | 23.340 |
| Present (16 × 16) | | 5.3870 | 9.969 | 15.348 | 19.729 | 23.389 |
| Putcha and Reddy (1986) | 5 | 5.4096 | 10.15 | 16.008 | 20.999 | 25.080 |
| Ferreira et al. (2011) | | 5.4041 | 10.088 | 15.793 | 20.594 | 24.691 |
| Present (16 × 16) | | 5.4265 | 10.138 | 15.842 | 20.615 | 24.680 |
| Putcha and Reddy (1986) | 9 | 5.4313 | 10.197 | 16.172 | 21.315 | 25.790 |
| Ferreira et al. (2011) | | 5.4092 | 10.177 | 16.103 | 21.198 | 25.608 |
| Present (16 × 16) | | 5.4325 | 10.231 | 16.172 | 21.248 | 25.643 |

without to need correction factors. Furthermore, the selective numerical integration technique is conducted in order to get accurate results without including numerical locking problem.

## References

Averill R, Reddy JN (1992) An assessment of four-noded plate finite elements based on a generalized third-order theory. Int J Numer Meth Eng 33(8):1553–1572

Belkaid K, Tati A (2015) Analysis of laminated composite plates bending using a new simple finite element based on Reddy's third order theory. Revue Des Composites et des Materiaux Avancés 25(1):89–106

Belkaid K, Tati A et al (2016) A simple finite element with five degrees of freedom based on Reddy's third-order shear deformation theory. Mech Compos Mater 52(2):257–270

Chakrabarti A, Sheikh AH (2003) Buckling of laminated composite plates by a new element based on higher order shear deformation theory. Mech Adv Mater Struct 10(4):303–317

Ferreira AJM, Roque CMC et al (2011) Buckling analysis of isotropic and laminated plates by radial basis functions according to a higher-order shear deformation theory. Thin-Walled Structures 49(7):804–811. https://doi.org/10.1016/j.tws.2011.02.005

Gerard G, Becker H (1957) Handbook of structural stability part III: buckling of curved plates and shells

Ghosh AK, Dey SS (1994) Buckling of laminated plates-A simple finite element based on higher-order theory. Finite Elem Anal Des 15(4):289–302

Ghugal Y, Shimpi R (2002) A review of refined shear deformation theories of isotropic and anisotropic laminated plates. J Reinf Plast Compos 21(9):775–813

Hughes TJ, Cohen M et al (1978) Reduced and selective integration techniques in the finite element analysis of plates. Nucl Eng Des 46(1):203–222

Leissa AW (1987a) An overview of composite plate buckling. Compos Struct 4:1–29. (Springer)

Leissa AW (1987b) A review of laminated composite plate buckling. Appl Mech Rev 40(5):575–591

Moita J, Soares CMM et al (1996) Buckling behaviour of laminated composite structures using a discrete higher-order displacement model. Compos Struct 35(1):75–92

Moita JS, Soares CMM et al (1999) Buckling and dynamic behaviour of laminated composite structures using a discrete higher-order displacement model. Comput Struct 73(1):407–423

Noor AK (1975) Stability of multilayered composite plates. Fibre Sci Technol 8(2):81–89. https://doi.org/10.1016/0015-0568(75)90005-6

Putcha N, Reddy JN (1986) Stability and natural vibration analysis of laminated plates by using a mixed element based on a refined plate theory. J Sound Vib 104(2):285–300

Reddy JN (1984a) A simple higher-order theory for laminated composite plates. J Appl Mech 51(4):745–752

Reddy JN (1984b) A refined nonlinear theory of plates with transverse shear deformation. Int J Solids Struct 20(9):881–896

Reddy JN (2004) Mechanics of laminated composite plates and shells: theory and analysis. CRC Press, Boca Raton, FL

Reddy JN, Phan N (1985) Stability and vibration of isotropic, orthotropic and laminated plates according to a higher-order shear deformation theory. J Sound Vib 98(2):157–170

Reddy JN, Robbins D (1994) Theories and computational models for composite laminates. Appl Mech Rev 47(6):147–169

Singh SK, Chakrabarti A (2012) Buckling analysis of laminated composite plates using an efficient $C_0$ FE model. Latin Am J Solids Struct 9:1–13

Singh SNLG, Rao GV (1996) Stability of laminated composite plates subjected to various types of in-plane loadings. Int J Mech Sci 38(2):191–202

Xu J, Zhao Q, et al (2013) A critical review on buckling and post-buckling analysis of composite structures

Zienkiewicz OC, Cheung YK (1964) The finite element method for analysis of elastic isotropic and orthotropic slabs, ICE proceedings, Thomas Telford

# Prediction of Optimal Lifetime of the Tool's Wear in Turning Operation of AISI D3 Steel Based on the a New Spectral Indicator SCG

**Mohamed Khemissi Babouri, Nouredine Ouelaa, Mohamed Cherif Djamaa, Abderrazek Djebala, Septi Boucherit and Nacer Hamzaoui**

## 1 Introduction

The vibratory analysis aims to identify the evolution of the state of cutting tool during its lifetime, in particular the transition from the stabilization phase to the acceleration phase of wear. Thus, direct control of the flank wear (*VB*) of the cutting insert studied revealed a differentiated behavior with respect to the lifetime as a function of the cutting speed. Indeed, the quality of the machined workpieces depends directly on the degree of cutting tool wear. Several authors have concentrated their efforts on detecting the rupture of the cutting tool which is usually indicated by a changes abrupt the trends of the measured parameters whose values exceed a predefined threshold (Ravindra et al. 1997; Dimla 1998; Babouri et al. 2012; Babouri et al. 2017a). Previous work on the development of an efficient system, have focused

---

M. K. Babouri (✉)
USTHB, P.O. Box. 32, El-Alia, Bab-Ezzouar, 16111 Algiers, Algeria
e-mail: babouri_bmk@yahoo.fr

M. K. Babouri · N. Ouelaa · M. C. Djamaa · A. Djebala · S. Boucherit
Mechanics and Structures Laboratory (LMS), 8 May University of Guelma, 24000 Guelma, Algeria
e-mail: n_ouelaa@yahoo.fr

M. C. Djamaa
e-mail: mc_djamaa@yahoo.fr

A. Djebala
e-mail: djebala_abderrazek@yahoo.fr

S. Boucherit
e-mail: boucherit_sebti@yahoo.fr

N. Hamzaoui
Laboratory of Vibration-Acoustics, INSA of Lyon, 69621 Villeurbanne Cedex, France
e-mail: nacer.hamzaoui@insa-lyon.fr

T. Boukharouba et al. (eds.), *Computational Methods and Experimental Testing In Mechanical Engineering*, Lecture Notes in Mechanical Engineering,
https://doi.org/10.1007/978-3-030-11827-3_9

mainly on mathematical models using large quantities of experimental data. Indeed, the design of a surveillance system has become necessary through the use of highly reliable online supervision and monitoring methods. These methods are based most often on the measurement of several indicators such as cutting forces, acoustic emission, cutting temperature and vibration signatures ‘acceleration signals’ from which correlated parameters that are related to the cutting tool wear must be extracted to give a measure of the extent of tool wear.

In the literature, Rmili (2007) proposed a joint analysis in time and frequency of the vibratory signals generated in machining in order to determine of the cutting tools wear. The results of the spectrograms show two frequency bands corresponding to the natural frequencies of the cutting tool and tool holder. On the other hand, the vibratory level at the characteristic frequencies mentioned increases progressively with deterioration of the cutting insert used.

Babouri et al. (2016, 2017b) focused on the application of several approaches, namely time and frequency analysis, wavelet analysis (*WMRA*), empirical mode decomposition (*EMD*), or a hybrid approach. The results obtained made it possible to locate the transition of the lifetime of the cutting tools. Gradisek et al. (1998), in their attempt to study the chattering phenomenon that occurs due to the cyclic variation of the cutting effort, proposed a new method based on the different properties of the dynamic cutting and that accompanied of chattering. The analysis shows that a high value of the entropy rate is typical of the free chattering cutting, so a significant decrease in this value indicates the beginning of the chattering.

In the present work we propose the application of a new spectral indicator called the spectral center of gravity, which is calculated from the autospectrums of the measured accelerations to characterize the three phases of the cutting tool life.

## 2 Lifetime Theory

All cutting tools wear out as they are used until the end of their lifetime. The service lifetime of the cutting tool can be terminated when the cutting edge is no longer able to form a chip or when the wear profile reaches a critical stage such as a the cutting edge rupture. Indeed, it is necessary to identify the evolution of the state of cutting tool during its lifetime, in particular the transition from the stabilization phase to the accelerated wear phase synonymous of catastrophic wear.

Several authors have concentrated their efforts on establishing mathematical models such as Taylor, Koning-Depiereux and Colding, which allow calculation of the lifetime of cutting tools according to the cutting parameters. Gilbert, in 1950, proposed the generalization of the Taylor model taking into account the cutting conditions. This model sufficiently used to evaluate the lifetime of cutting tools. The cutting tool wear develops in five distinct stages, namely: initial wear, regular wear, micro-rupture the cutting insert, rapid wear and breakage of the cutting insert. However, most authors identify three stages of wear: initial ‘break-in’ (*A*), regular ‘normal wear’ (*B*) and rapid ‘accelerated wear’ (*C*) with their monitoring strategy, see Fig. 1.

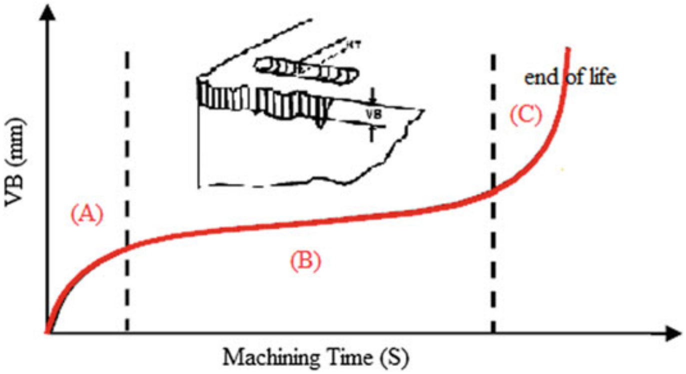

**Fig. 1** Lifetime theory of the cutting tools

Several researchers have also shown that the stages of initial wear and rapid wear (before tool failure) occur faster than regular wear. That is, rapid wear occurs briefly after a normal working period of the cutting insert. Hence, the difficulty of detecting this transition at the appropriate time.

## 3 Spectral Center of Gravity—SCG

In this work, the use of the *SCG*, calculated from the autospectrum of the signals measured around the most dominant natural frequencies of the machining system, is proposed for monitoring of the cutting tools wear. The *SCG* is widely used to reveal a perspective dimension of sound on the timbre of musical instruments as well as for analysis of vehicle sounds and traffic noise. It is therefore considered the most reliable factor for judging the dissimilarity between two sounds of corpus, corresponding to two defects of different gravity. Since *SCG* depends mainly on the change in the amplitudes of the natural frequencies of the cutting tool, the idea is to find a relationship between this indicator and cutting wear. The expression of the spectral center of gravity is given by the following expression (Krimphoff et al. 1994; Babouri et al. 2017c):

$$SCG = \sum_{i=1}^{N} f_i L_i / \sum_{i=1}^{N} L_i \tag{1}$$

The value of the SCG varies inversely with the severity of the defect (Younes et al. 2015). For the detection of rolling defects, Younes et al. (2015) and Kenzari (2009) show that the *SCG* value decreases with the worsening of the fault. This explains the dissimilarity judgments for rolling sensors in the case of a simulated and true fault.

This criterion is valid until the end of the stabilization phase. The appearance of wear in the accelerated stage leads to an increase in the vibratory energy which results in a disturbance of the spectral balance.

## 4 Experimental Validation and Data Acquisition

The machining tests were carried out without lubrication using a conventional lathe '*TOS TRENCIN*' model *SN 40C* with a power on the spindle of 6.6 Kw. The material used in this study is steel *AISI D3* high chromium steel. Its chemical composition is given as follows: 2% C, 11.5% Cr, 0.3% Mn and 0.25% Si. The test specimens used are round bars with a diameter of 80 mm and a length of 400 mm. The Sandvik *GC2015* square cutting insert with eight cutting edges, designated *SNMG 432-MF 2015*, was coated with TiCN/$Al_2O_3$/TiN. The basic carbide, itself, is sufficiently hard to manufacture the *D3*. The three coating layers offer some specific characteristics to the basic substrate. The TiN assures a good thermal resistance and providing low friction coefficient, the TiCN permits to improve the wear resistance and the thermal stability. However, the $Al_2O_3$ is required to improve the toughness to high temperature and the resistance to crater wear. The cutting insert are mounted on a reference tool holder *PSDNN 25×25 M12* with the following geometrical specifications: rake angle $\gamma = -6°$, major cutting edge angle $\chi_r = 75°$, inclination angle $\lambda = -6°$ and relief angle $\alpha = -6°$(Sandvik 2009).

In this study, acquisition of vibratory signals was performed during machining using a Brüel & Kjaer type *4524B* triaxial piezoelectric accelerometer placed in the area closest to the cutting sector to record the intensity of the accelerations in real time in the three main directions (x, y, z). The frequency band selected varies between (0–12, 800 Hz) where each signal contains 16,384 points. The measurement results were stored directly on the PC using the analyzer acquisition system, driven by Brüel & Kjaer's Pulse Lab shop® software (Fig. 2).

The development of the flank wear on the cutting insert is measured after each test; the cutting insert is removed from the tool holder, cleaned and then placed on the table of the optical microscope Standard Gage type Visual 250. Having an optical enlargement from 0.7× to 4.5× the actual size. The Visual Gage software allows any operator as well as the metrologist to measure quickly and accurately most geometric elements.

Three experimental companions of 25 trials have taken several values of the flank wear and tear of the three plates studied, from the new state to the end of the lifetime (see Table 1). After each machining pass, the surface state of the workpiece is characterized by measuring the various roughness criteria ($R_a$, $R_t$, $R_z$) using a *2D* rugosimeter of the type surftest 301 Mitutoyo (Fig. 3).

The measurements are repeated three times on the surface of the work piece with three reference lines placed at 120° at the level of the three jaws and in the direction parallel to the advance of the cutting tool and the average of these values is taken as final result.

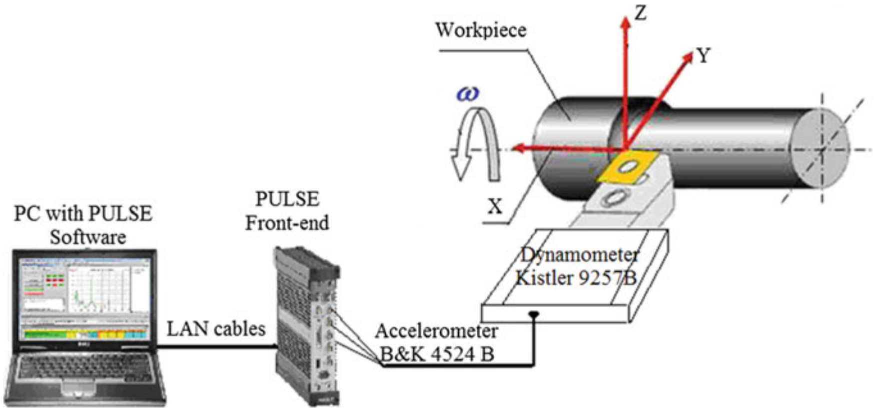

**Fig. 2** General sight of the experimental installation

# 5 Results and Discussion

## *5.1 Vibration Signals and Characterization of Cutting Wear*

Such an experimental protocol makes it possible to always retain the same conditions for generating the vibratory responses and to detect in a specific manner any variation in the characteristics of the signal supposed to be closely related to the change in the state of the cutting insert. In a first step, the concatenation of the vibratory signals of accelerations acquired in the directions: radial ($Y$), tangential ($Z$) and axial ($X$) during a trial companion is shown in Fig. 4.

Figure 4 shows, by way of example, a concatenation of the vibratory acceleration signals over the entire lifetime of the cutting tool. Five sets of vibratory responses were measured. Each series consists of a number of records corresponding to the lifetime of the cutting insert used. According to the example of these responses, we observe that we have three main phases of tool lifetime: break-in, wear stabilization and acceleration wear of cutting tool where the rate of wear increases until rapid tool aging occurs. We note that the evolution of the acceleration signals as a function of the cutting time is very significant in the radial direction ($Y$) than in the other directions ($X$, $Z$). This finding has been the same on all acquisitions. From these results, it is concluded that the analysis of the vibratory signals, particularly in the radial direction, provides effective monitoring of the cutting tool wear in different states.

**Table 1** Experimental result for AISI D3

| Run N° | Machining time | Flank wear | Crater wear | Roughness | | |
|---|---|---|---|---|---|---|
| | t (s) | $V_B$ (mm) | $K_T$ (mm) | $R_a$ (µm) | $R_t$ (µm) | $R_z$ (µm) |
| $V_c = 120$ m/min, $a_p = 0.2$ mm, $f = 0.12$ mm/tr | | | | | | |
| 1 | 240 | 0.041 | 0.010 | 0.50 | 5.15 | 4.87 |
| 2 | 480 | 0.090 | 0.012 | 0.66 | 5.66 | 5.42 |
| 3 | 720 | 0.118 | 0.016 | 0.87 | 5.67 | 5.33 |
| 4 | 1200 | 0.154 | 0.021 | 1.08 | 6.66 | 5.67 |
| 5 | 1440 | 0.180 | 0.026 | 1.25 | 6.35 | 5.87 |
| 6 | 1680 | 0.202 | 0.030 | 1.56 | 6.79 | 6.70 |
| 7 | 1920 | 0.215 | 0.035 | 1.87 | 9.14 | 8.73 |
| 8 | 2400 | 0.257 | 0.039 | 2.20 | 11.3 | 10.34 |
| 9 | 2640 | 0.280 | 0.044 | 2.27 | 10.4 | 10.04 |
| 10 | 2880 | 0.292 | 0.049 | 2.55 | 11.1 | 10.62 |
| 11 | 3360 | 0.323 | 0.053 | 2.97 | 14.18 | 13.62 |
| 12 | 3600 | 0.345 | 0.057 | 2.99 | 15.09 | 14.59 |
| 13 | 3840 | 0.360 | 0.066 | 3.20 | 15.40 | 14.61 |
| 14 | 4080 | 0.377 | 0.070 | 3.26 | 16.09 | 14.67 |
| 15 | 4320 | 0.396 | 0.077 | 3.51 | 16.81 | 16.12 |
| 16 | 4560 | 0.403 | 0.091 | 3.62 | 17.01 | 16.15 |
| $V_c = 175$ m/min, $a_p = 0.2$ mm, $f = 0.12$ mm/tr | | | | | | |
| 1 | 169 | 0.077 | 0.013 | 0.48 | 4.12 | 3.52 |
| 2 | 507 | 0.289 | 0.060 | 1.54 | 7.96 | 7.82 |
| 3 | 676 | 0.373 | 0.078 | 2.49 | 11.2 | 10.53 |
| 4 | 845 | 0.488 | 0.103 | 2.76 | 12.61 | 11.46 |
| 5 | 1014 | 0.628 | 0.161 | 5.23 | 20.19 | 19.63 |

## 5.2 *Spectral Analysis of Characteristic Frequencies*

Before performing the machining tests, we first determined the Eigen modes of the cutting tool in the main directions using an instrumented impact hammer (Fig. 5). In order to obtain the Eigen frequencies of the system, the cutting tool is mounted on the machine under the experimental conditions associated with machining. In order to obtain the Eigen frequencies of the system, the cutting tool is mounted on the machine under the experimental conditions associated with machining. The excitation impacts were carried out in directions perpendicular to the surfaces of the cutting tool. The spectral behavior of the measured signals has been studied throughout the lifetime of the cutting inserts by frequency analysis. In Fig. 6, we distinguish the Eigen frequencies of the cutting tool represented in the frequency band [4000–5100 Hz].

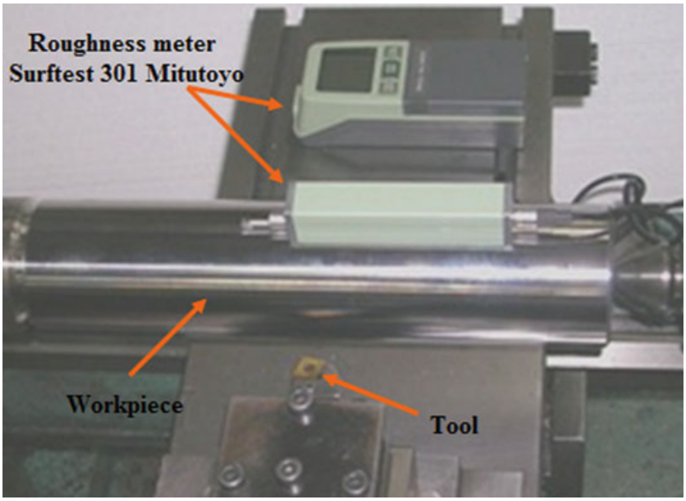

**Fig. 3** Measurement of the roughness without disassembling the workpiece

**Fig. 4** Concatenation of measured signals of the cutting tool for $V_c$ = 175 m/min

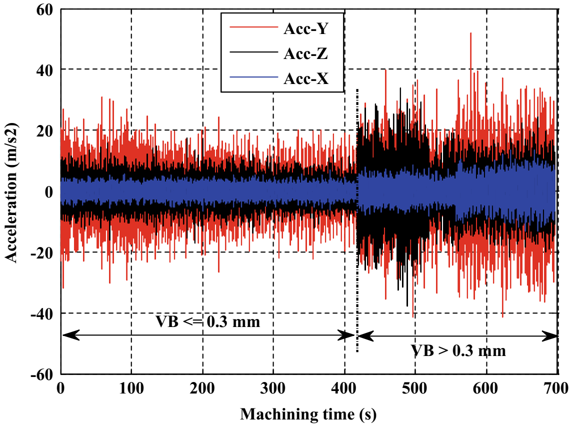

According to these measurements, it is noted that the torsion mode appears between 4700 Hz and 4800 Hz and the bending mode appears at 5032 Hz. The results of this approach allow us to identify the most significant Eigen modes of the cutting tool which subsequently intervene in the interpretation of the results.

Figure 7 shows the Eigen modes of the cutting tool which appear in the [3500–5500 Hz] frequency band identical to that identified by the modal analysis according to Fig. 6. Furthermore, after the running-in period, a stability of the amplitudes of the tool natural frequency is observed, with a progressive increase in cutting wear. When the wear exceeds its permissible value, the amplitudes of the natural frequencies increase sharply. These spectra cover the entire lifetime of the cutting tool from the first test to the last.

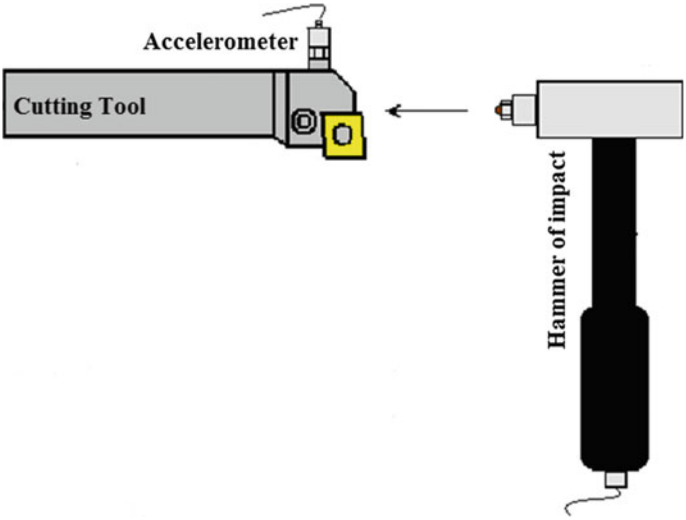

**Fig. 5** Device used for modal analysis

**Fig. 6** Natural frequencies of the cutting tool

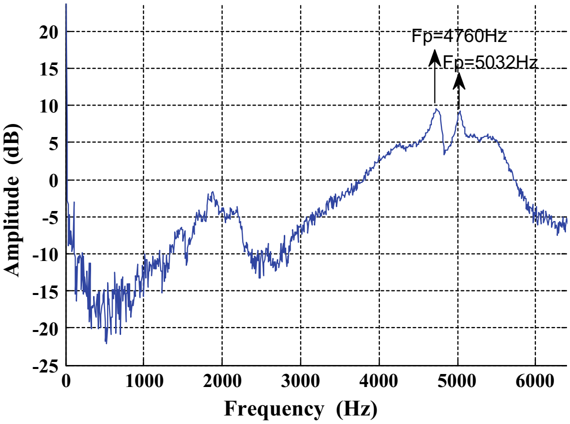

The characterization of the evolution of this vibratory level as a function of cutting wear depends directly on the frequency band 3500–5500 Hz which can be considered as a good frequency indicator the state of the cutting tool. Indeed, the potential failure modes are characterized by the specific frequencies, and these are detected by the amplitude variation of the vibratory signals at these frequencies. In this context, the vibratory signals measured from the first test to the end of the tool lifetime are shown as narrow peaks at specific frequencies.

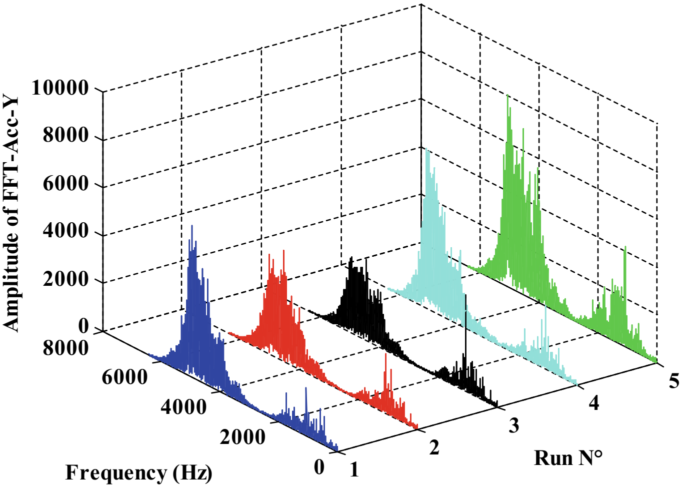

**Fig. 7** Spectrum obtained from radial direction

### *5.3 Proposed Spectrum Indicators*

In order to facilitate the industrial application of the monitoring of the state of the cutting tool, the use of the *SCG*, calculated from the autospectrums of the measured accelerations, is proposed to characterize the three phases of tool's wear. The autospectrums corresponding to the evolution of tool's wear in the series of experiments (Figs. 8 and 9) comprise two characteristic frequency bands. The first appears between 1500 and 2500 Hz which describes the natural frequencies of the Kistler platform and the second appears between 3500 and 5500 Hz which describes the natural frequencies of the cutting tool. The autospectrum clearly show the variation in the amplitudes of the measured signals from one wear phase to another around the natural frequencies of the cutting tool. The wear phases are clearly explained by this variation in amplitude, in the break-in phase, where the contact surface of the tool-workpiece is very small, almost punctual, so the amplitudes of vibrations are important. In the second phase of wear stabilization, the tool-workpiece contact surface becomes larger and regular, which dampens the vibrations of the cutting tools where the stiffness of the tool increases and causes a decrease in the amplitudes of the natural frequencies of the cutting tool, then it increases again in the last phase.

We show in Fig. 10 the evolution of the *SCG* as a function of the cutting time. During the wear stabilization phase, the *SCG* decreases significantly and reaches a minimum value of 3729 Hz after 2640 s of cutting time corresponding to a *VB* flank wear of 0.28 mm. As soon as wear begins to worsen, the *SCG* changes direction and starts to take larger values. After a cutting time of 2880 s corresponding to $VB = 0.292$ mm, the *SCG* reaches 4152 Hz and then a maximum of 4209 Hz to fall back to values lower than the end of the tests.

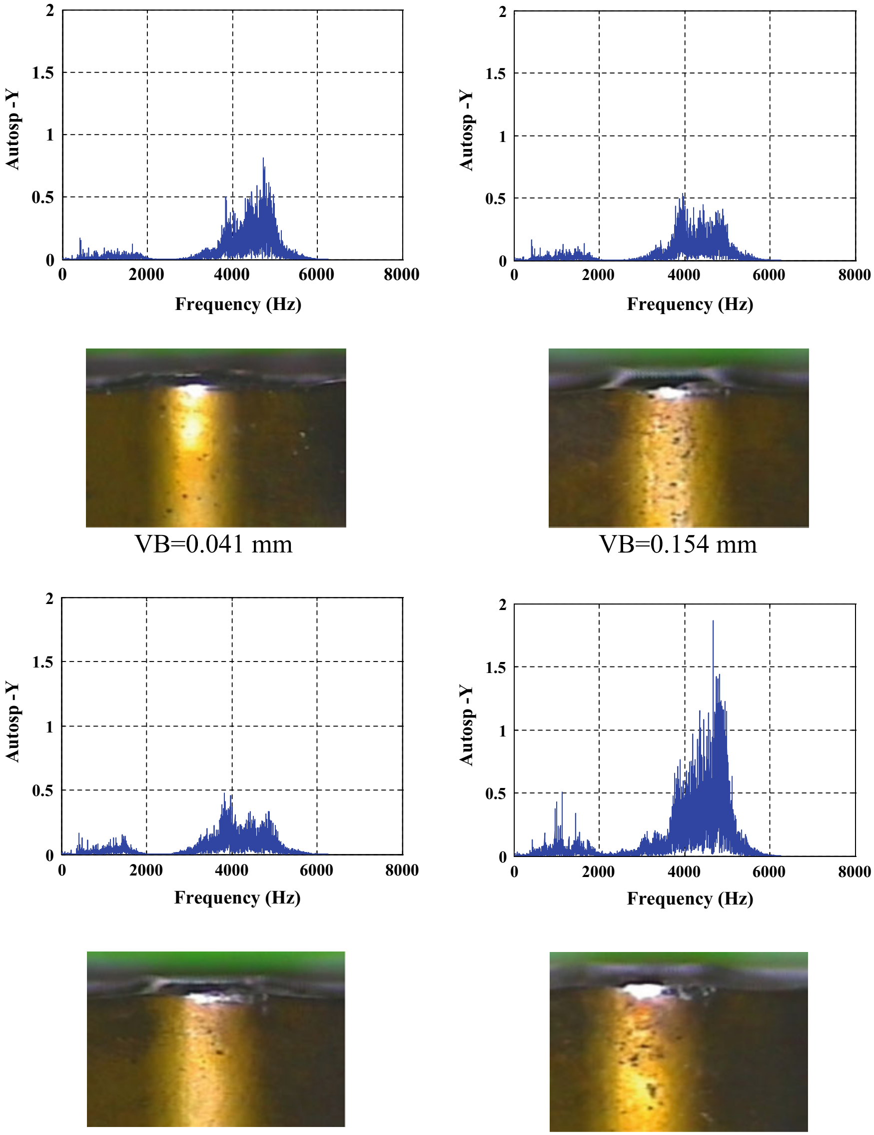

VB=0.041 mm

VB=0.154 mm

VB=0.257 mm

VB=0.323 mm

**Fig. 8** Autospectrums of the signals measured in the radial direction for various flank wear (VB), $V_c = 120$ m/min

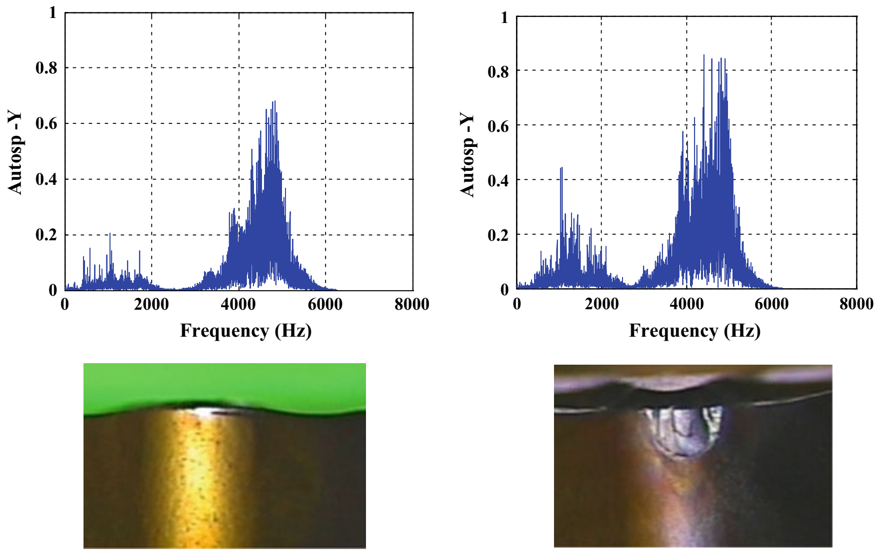

VB=0.077 mm

VB=0.628 mm

**Fig. 9** Autospectrums of the signals measured in the radial direction for various flank wear (VB), $V_c = 175$ m/min

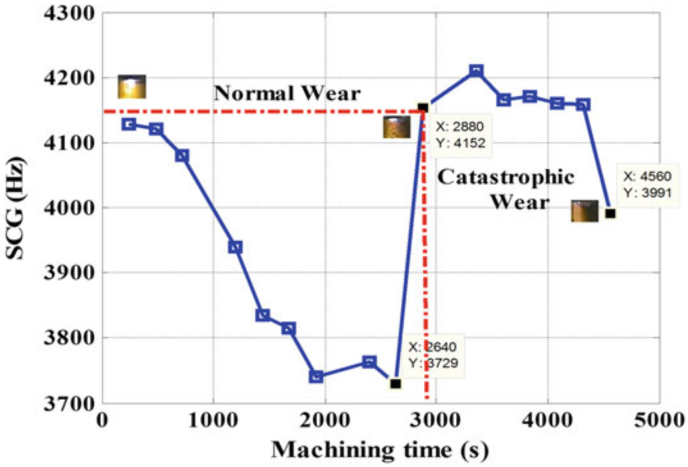

**Fig. 10** SCG of the auto spectrum of the Fig. 8

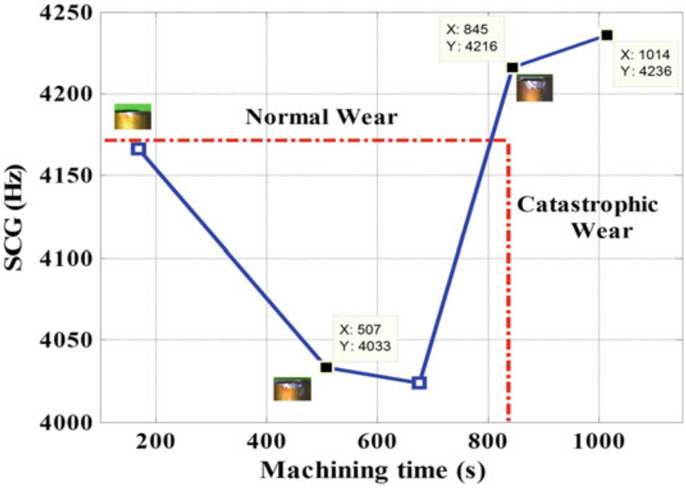

**Fig. 11** SCG of the autospectrum of the Fig. 9

The result of the calculation of the *SCG* presented in Fig. 11 is similar to the previous result. The change in direction of the SCG at the end of the wear stabilization phase is clear. The *SCG* values cover the frequency band [3700–4200 Hz] which is that of the natural frequencies of the cutting tool mentioned above. The decrease in *SCG* results from the stable appearance of the vibrations produced by the regular evolution of wear. The appearance of wear in the accelerated stage leads to an increase in the vibratory energy which results in a disturbance of the spectral balance. As the value of the *SCG* varies inversely with the severity of the defect.

Starting from the behavior of the *SCG*, which has shown its ability to predict the transition from the normal wear phase to that corresponding to the catastrophic wear of the cutting tool, this indicator can be integrated into an industrial monitoring system to alert the end of the tool life of the cutting tool.

Since the transition between the two phases does not occur in too short a period, we propose as a criterion for decommissioning the cutting tool, a value of *SCG* just above that of the first calculated *SCG* when the cutting tool is in new condition. This criterion is only valid for machining speeds recommended for machining where the wear evolution takes place over a wider period allowing the calculation of the *SCG* in close intervals. This is the case for the cutting speed of 120 m/min where the tool life is approximately 50 min.

## 6 Conclusion

This article has been devoted to monitoring the evolution of the cutting tool wear by processing the signals measured during the cutting process. We also proposed the application of a new spectral indicator *SCG* to monitor the evolution of tool's wear. The first conclusions that can be drawn are as follows:

1. The evolution of the amplitudes of the natural frequencies of the cutting tool perfectly describes the state of its degradation and the band containing these frequencies is the best qualified to monitor tool's wear.
2. The spectral indicator *SCG*, calculated from the acceleration autospectrum, has also shown its effectiveness in a surveillance system capable of providing the moment of transition to accelerated wear.
3. Finally, we can say that the results presented in this study come from an off-line test. That is, after processing the signals collected during machining. This approach makes it possible to test and verify the validity of the proposed approach. This approach, once validated on off-line tests, could be integrated into of an online tool wear monitoring system. It is in a sense the use of feedback derived from off-line tests for setting up an on-line system.

In our future works, we intend to validate the obtained results by widening the study for tool carrier stiffness in different cutting conditions and why not for milling operations.

## References

Babouri MK, Ouelaa N, Djebala A (2012) Identification de l'évolution de l'usure d'un outil de tournage basée sur l'analyse des efforts de coupe et des vibrations. Revue Sci Technol Synthèse 24:123–134

Babouri MK, Ouelaa N, Djebala A (2016) Experimental study of tool life transition and wear monitoring in turning operation using a hybrid method based on wavelet multi-resolution analysis and empirical mode decomposition. Int J Adv Manuf Technol 82:2017–2028

Babouri MK, Ouelaa N, Djebala A (2017a) Application of the empirical mode decomposition method for the prediction of the tool wear in turning operation. Mechanika 23(2):315–320

Babouri MK, Ouelaa N, Djebala A, Djamaa MC, Boucherit S (2017b) Prediction of cutting tool's optimal lifespan based on the scalar indicators and the wavelet multi-resolution analysis. In: Applied mechanics, behavior of materials, and engineering systems. Springer International Publishing, pp 299–310

Babouri MK, Ouelaa N, Djamaa MC, Djebala A, Hamzaoui N (2017c) Prediction of tool wear in the turning process using the spectral center of gravity. J Fail Anal Prev 17:905–913. https://doi.org/10.1007/s11668-017-0319-y

Dimla DE (1998) Multivariate tool condition monitoring in a metal cutting operation using neural networks. Ph.D. thesis, School of Engineering and Built Environment, University of Wolverhampton

Gradisek J, Govekar E, Grabec I (1998) Using coarse-grained entropy rate to detect chatter in cutting. J Sound Vib 214(5):941–952

Kenzari M., (2009) Vibroacoustic diagnosis of gears defects: sound perception approach analysis. Thesis, INSA of Lyon, France

Krimphoff J, Mcadams S, Winsberg S (1994) Caractérisation du timbre des sons complexes. II. Analyses acoustiques et quantification psychophysique. Journal de Physique IV 4(C5):625–628

Ravindra HV, Srinivasa YG, Krishnamurthy R (1997) Acoustic emission for tool condition monitoring in metal cutting. Wear 212(1):78–84

Rmili W (2007) Analyse vibratoire pour l'étude de l'usure des outils de coupe en tournage. Thesis, University François Rabelais Tours, France

Sandvik (2009) Coromant: Catalogue Général Outils de coupe Sandvik Coromant, Tournage –Fraisage – Perçage – Alésage – Attachements

Younes R, Hamzaoui N, Ouelaa N, Djebala A (2015) Perceptual study of the evolution of gear defects. Appl Acoust 99:60–67

# The Evaluation of the Dynamic Response of the Moving Exciter Due to the Irregularities of the Slab

**Moussa Guebailia and Nouredine Ouelaa**

## 1 Introduction

Many important parameters can be extracted and evaluated from the dynamic analysis of path surfaces. Moreover, the interaction path surface–mobile exciter can be amplified by other factors. In the references Zhu and Law (2002) and Marchesiello et al. (1999), the mobile exciter was modeled by a three-dimensional dynamic model with two axles and seven degrees-of-freedom degrees of freedom compliant with the standard H20-44 (2005). The natural frequencies and modes shapes were calculated by the Rayleigh-Ritz method, and the dynamic response was obtained by the modal superposition method (Zhu and Law 2002; Marchesiello et al. 1999). Zhu and Law (2002) and Marchesiello et al. (1999) used the variational method of Rayleigh-Ritz to determine the natural frequencies and mode shapes of the path surfaces using the Eigen modes of the beams as approximation functions. These authors decomposed into a product the two admissible functions, which are the Eigen modes of a continuous beam simply supported and a free beam mode.

The dynamic behaviour of path surfaces subjected to road traffic was studied by Broquet (1999), in which a two-stage evaluation of the path surface slab was proposed. In Stage 1, for situations similar to those analysed in that study, a simplified evaluation was applied. This employed a static analysis using an increased load based on a dynamic amplification factor. If the simplified evaluation could not be applied, a second stage (stage 2) was adopted to evaluate the deck slab using a dynamic analysis, which took the form of either a numerical or an experimental approach (Broquet 1999). That work evaluated the influence of roadway flatness and

---

M. Guebailia (✉)
Mechanical Department of FST, Kasdi Merbah University, Ouargla, Algeria
e-mail: guebailiamoussa2@hotmail.com

M. Guebailia · N. Ouelaa
Laboratory of Mechanics and Structures, 8 May 1945 University, Guelma, Algeria
e-mail: n_ouelaa@yahoo.fr

T. Boukharouba et al. (eds.), *Computational Methods and Experimental Testing In Mechanical Engineering*, Lecture Notes in Mechanical Engineering,
https://doi.org/10.1007/978-3-030-11827-3_10

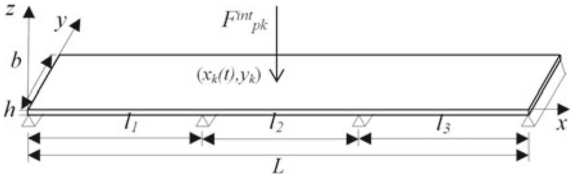

**Fig. 1** Path surface model

the load and speed of trucks on the dynamic response of the deck slab (Broquet 1999). Chompooming and Yener (1995) present an analysis of the bridge-vehicle interaction problem taking into account the dynamic effects due to the bouncing of vehicles caused by the irregularity of the road surface and the variation of the rolling speed.

In a vibro-acoustic study on a railway path surface excited by the passage of train, Ouelaa et al. (2006) modeled the deck rail system including the train weight, the viscoelastic mobile exciter suspension, and the track irregularities.

To resolving the equations of coupled motion, the modal superposition and Newmark methods were used. They show that the track irregularities disturb significantly the transverse movement of the mobile exciters, whereas they have a very small influence on the dynamic behaviour of the path surface (Ouelaa et al. 2006). An analytical solution presented in reference Gao and Zhang (2016) to resolve the motion equation by taking into account the state of the path surface and its irregularities.

## 2 Path Surface Model

The assumptions proposed by Zhu and Law (2002) and Marchesiello et al. (1999) to model the path surface vibrations are the modeling basis of this work. The path surface is modeled by an orthotropic, thin plate with three spans (Fig. 1). The free vibration part is presented in Guebailia et al. (2013). The equation of the path surface motion is written in Eq. 1:

$$\bar{m}\frac{\partial^2 w}{\partial t^2} + c\frac{\partial w}{\partial t} + D_x\frac{\partial^4 w}{\partial x^4} + 2H\frac{\partial^4 w}{\partial x^2 \partial y^2} + D_y\frac{\partial^4 w}{\partial y^4} = -\sum_{k=1}^{rf} F_{pk}^{\mathrm{int}}\delta\big(x - x_k(t), \mathrm{y} - \mathrm{y_k}\big) \tag{1}$$

where:

- $\bar{m} = \rho h$ is the mass density of the plate,
- $D_x = \frac{E_x h^3}{12(1-\upsilon_{xy}\upsilon_{yx})}$ and $D_y = \frac{E_y h^3}{12(1-\upsilon_{xy}\upsilon_{yx})}$ are flexural rigidities, according to the $x$ and $y$ directions,
- $H = \upsilon_{xy} D_y + 2D_{xy}$ is the equivalent rigidity,
- $c$ is the damping ratio of the path surface,
- $F_{pk}^{\mathrm{int}}$ is the interaction force between the $k$th mobile exciter wheel and the path surface,

- $\left(x_k(t),\ \mathrm{y_k}\right)$ is the position of the *k*th interaction force,
- $\upsilon_{xy}$ and $\upsilon_{yx}$ are the Poisson's coefficients according to the *x*- and *y*-directions, respectively,
- $D_{xy} = \frac{G_{xy}h^3}{12}$ is the flexural rigidity for the *x*–*y* plane,
- $G_{xy}$ is the shear modulus in bending in the *x*–*y* plane,
- $E_x$ and $E_y$ are the Young's moduli in the *x*- and *y*-directions.

The mobile exciters are assumed to move along the path surface in linear direction meaning that $y_k$ is constant. The mobile exciters speeds are considered constant. Thus, $x_{k(t)} = v_x \cdot t_k$ (where $v_x$ is the linear speed of the mobile exciter and $t_k$ is the time at the point *k*). The equation of motion (1) is solved using modal superposition and Newmark's method. The vertical displacement of the path surface presented in Eq. (2).

$$w(x, y, t) = \sum_{i=1}^{n} \sum_{j=1}^{m} \phi_{ij}(x, y)\mathrm{q_{ij}}(t) \tag{2}$$

where: $\phi_{ij}(x, y)$ are the mode shapes of a thin, multi-span orthotropic plate, which are associated with the natural angular frequencies $\omega_{ij}$ and $q_{ij}(t)$ are the generalized coordinates.

Substituting expression (2) into the equation of motion (1) and multiplying both sides by $\phi_u(x, y)$, Eq. (3) is generated when the equation is integrated over the entire surface of the path surface.

$$\begin{aligned}&\iint_s \bar{m} \sum_{i,j=1}^{n,m} \phi_{ij}(x, y)\, \ddot{\mathrm{q}}_{\mathrm{ij}}(t)\phi_{kl}(x, y)dxdy + \iint_s c \sum_{i,j=1}^{n,m} \phi_{ij}(x, y)\dot{\mathrm{q}}_{\mathrm{ij}}(t)\, \phi_{kl}(x, y)dxdy\\ &+ \iint_s D_x \sum_{i,j=1}^{n,m} \frac{\partial^4\phi_{ij}}{\partial x^4}\mathrm{q_{ij}}(t)\, \phi_{kl}(x, y)dxdy + 2\iint_s H\frac{\partial^2\phi_{ij}}{\partial x^2}\frac{\partial^2\phi_{ij}}{\partial y^2}\mathrm{q_{ij}}(t)\, \phi_{kl}(x, y)dxdy\\ &+ \iint_s D_y \sum_{i,j=1}^{n,m} \frac{\partial^4\phi_{ij}}{\partial y^4}\mathrm{q_{ij}}(t)\phi_{kl}(x, y)dxdy = -\iint_s \sum_{k=1}^{nf} F_{pk}^{\mathrm{int}}\, \phi_{kl}\delta(x - x_k, y - y_k)\end{aligned} \tag{3}$$

The orthogonally of natural modes guarantees the decoupling of modal responses and gives the relations in Eq. (4):

$$\begin{aligned}&\iint_s \bar{m}\phi_{ij}(x, y)\phi_{kl}(x, y)dxdy = \begin{cases}0, & \mathrm{ij} \neq \mathrm{kl}\\ \mathrm{M_{ij}}, & \mathrm{ij} = \mathrm{k}\end{cases}\\ &\iint_s C\phi_{ij}(x, y)\, \phi_{kl}(x, y)dxdy = D_x\frac{\partial^4\phi_{ij}}{\partial x^4}D_x\begin{cases}0, & \mathrm{ij} \neq \mathrm{kl}\\ \mathrm{C_{ij}} = 2\xi_{ij}\omega_{ij}M_{ij}, & \mathrm{ij} = \mathrm{kl}\end{cases}\\ &\iint_s \left(D_x\frac{\partial^4\phi_{ij}}{\partial x^4} + 2H\frac{\partial^4\phi_{ij}}{\partial x^2\partial y^2} + D_y\frac{\partial^4\phi_{ij}}{\partial y^4}\right)\phi_{kl}(x, y)dxdy = \begin{cases}0, & \mathrm{ij} \neq \mathrm{kl}\\ \omega_{ij}M_{ij} = K_{ij}, & \mathrm{ij} = \mathrm{kl}\end{cases}\end{aligned} \tag{4}$$

where: $\xi_{ij} = \frac{c}{2\bar{m}\omega_{ij}}$, the modal damping coefficients of the path surface.

By applying orthogonally conditions (4), the terms that satisfy $ij \neq kl$ disappear and the modal equations $(i, \mathrm{j})$ are decoupled from Eq. 3, as shown in Eq. (5):

$$M_{ij} q_{ij}(t) + C_{ij} q_{ij}(t) + K_{ij} q_{ij}(t) = F_{ij}(t) \tag{5}$$

where:

$$\begin{aligned}
M_{ij} &= \iint\limits_{s} \bar{m} \phi_{ij}^{2}(x, \mathrm{y}) dx dy \\
C_{ij} &= \iint\limits_{s} c \phi_{ij}^{2}(x, \mathrm{y}) dx dy = 2\xi_{ij} \omega_{ij} M_{ij} \\
K_{ij} &= \iint\limits_{s} \left( D_x \frac{\partial^4 \phi_{ij}}{\partial x^4} + 2H \frac{\partial^4 \phi_{ij}}{\partial x^2 \partial y^2} + D_y \frac{\partial^4 \phi_{ij}}{\partial y^4} dx dy \right) \cdot \phi_{ij} dx dy = M_{ij} \omega_{ij}^{2} \\
F_{ij} &= -\iint\limits_{s} \sum_{k=1}^{nf} F_{pk}^{\text{int}} \cdot \delta(x - x_k(t),\ \mathrm{y} - \mathrm{y_k}) \cdot \phi_{ij}(x, \mathrm{y}) ds \\
&= -\sum_{k=1}^{nf} F_{pk}^{\text{int}}(x_k, \mathrm{y_k}) \cdot \phi_{ij}(x_k, \mathrm{y_k})
\end{aligned} \tag{6}$$

where: $M_{ij}$, $C_{ij}$, $K_{ij}$ and $F_{ij}$ are the modal masses, damping, stiffness and forces respectively. The determination of the natural frequencies and mode shapes are presented in Guebailia et al. (2013).

## 3 Mobile Exciter-Path Surface Coupled Equation of Motion

The equations of motion of the mobile exciter model with seven degrees of freedom in accordance with the *H20-44 AASHTO* norm (2005) were obtained by applying the law of dynamic equilibrium of forces and moments to each degree of freedom. After simplifying Eq. (7) was obtained:

$$[M_v]\{Z_v\} + [C_v]\{Z_v\} + [K_v]\{Z_v\} = \{F_v^{\text{int}}\} \tag{7}$$

where: $[M_v]$, $[C_v]$ and $[K_v]$ are matrices of mass, damping and stiffness of the mobile exciter.

To solve the equations of coupled path surface-mobile exciter motion, Newmark's numerical integration method was applied.

### 3.1 Solving Method Algorithm

To solve the coupled equations of motion involved the following steps:

- input the data from the path surface, mobile exciter and roadway,
- calculate $D_x$, $D_y$, $H$, $D_{xy}$, $G_{xy}$ and $\bar{m}$,
- choose the number of Eigenmodes $n \; and \; m$,
- determine the natural frequencies $\omega_{ij}$ and calculate the mode shapes $\phi_{ij}$,
- select the passage speed,
- choose the time step $\Delta t$, parameters $(\gamma, \beta)$ and the precision $\varepsilon$,
- calculate the matrixes of mass, stiffness and damping of the path surface and mobile exciter,
- specify the initial conditions for the path surface and the mobile exciter.
- Path surface $\{q\}_0$, $\{\dot{q}\}_0$, $\{\ddot{q}\}_0$, Displacements, velocities and accelerations generalized (modal coordinates).
- Mobile exciter $\{Z_v\}_0$, $\{\dot{Z}_v\}_0$, $\{\ddot{Z}_v\}_0$, mobile exciter' *DOFs*,
- Choose the mobile exciter trajectory on the path surface,
- for each time step $t = t + \Delta t$. Determine the $x$ position of the mobile exciter on the path surface,
- calculate the profile of the road at each point of contact,
- for each iteration $\bar{k} = \bar{k}+1$, solve this by Newmark's method $[M_v]\{Z_v\}+[C_v]\{\dot{Z}_v\}+K\{\ddot{Z}_v\}_0 = \{F_v^{\mathrm{int}}\}$,
- calculate the interaction forces on the path surface to mobile exciter by the following expression $\{F_v^{\mathrm{int}}\} = \{F_g\} + \{F_p\}$, where $\{F_g\}$ = force vector due to the effects of gravity and $\{F_p\}$ = force vector exerted by the path surface.

$$\ddot{q}_{ij} + 2\xi_{ij}\omega_{ij}\dot{q}_{ij} + \omega_{ij}^2 q_{ij} = \frac{1}{M} F_{ij} \tag{8}$$

with: $F_{ij} = -\sum_{k=1}^{4} F_{pk}^{\mathrm{int}}(x_k, \mathrm{y_k}) \cdot \varphi_{ij}(x_k, \mathrm{y_k})$ Calculate the path surface's vertical displacement: $w(x, y, z) = \sum_{i=1}^{n} \sum_{j=1}^{m} \phi_{ij}(x_k, \mathrm{y_k}) \cdot q_{ij}(t)$ and verify the convergence $\left| w^{(\bar{k}+1)}(x, y, t) - w^{(\bar{k})}(x, y, t) \le \varepsilon \right| l_1$.

### 3.2 Validation Exemple

In order to validate the proposed model and, the path surface and mobile exciter used by Zhu and Law (2002) were employed. The necessary path surface data are given into Tables 1 and 2.

Stability parameters of Newmark's method in all calculation steps were as follows ($\gamma = 0.5, \beta = 0.25$).

**Table 1** Path surface data

| | |
|---|---|
| Path surface’s length $L$ | 78 m |
| Width $b$ | 13.715 m |
| Span’s lengths $l_1$, $l_2$ and $l_3$ | 24, 30, 24 m |
| Path surface’s thickness $h$ | 0.21157 m |
| Mass per unit of length $\rho$ | 3265.295 kg/m$^3$ |
| The flexural rigidity according to $x$ $D_x$ | $2.415 \times 10^9$ Nm |
| The flexural rigidity according to $y$ $D_y$ | $2.1807 \times 10^7$ Nm |
| The flexural rigidity for the $x$–$y$ plane $D_{xy}$ | $1.1424 \times 10^8$ Nm |
| The Poisson’s ratio $\nu_{xy}$ | 0.3 |
| Young moduli $E_x$ | $3.0576 \times 10^{12}$ N/m$^2$ |
| Young moduli $E_y$ | $2.7607 \times 10^{10}$ N/m$^2$ |
| The shear modulus in bending for the $x$–$y$ plane $G_{xy}$ | $1.4475 \times 10^{11}$ N/m$^2$ |

**Table 2** Mobile exciter data

| | |
|---|---|
| Masses of the wheel with axles front and rear, respectively | $\mathrm{m}_1 = 600$ kg, $\mathrm{m}_2 = 1000$ kg |
| Masses and moments of inertia of the mobile exciter block | $\mathrm{m}_\mathrm{v} = 17{,}000$ kg, $\mathrm{I}_{\theta\mathrm{v}} = 9 \times 10^4$kg, $\mathrm{I}_{\alpha\mathrm{v}} = 1.3 \times 10^{4\ \mathrm{kg}}$ |
| Moments of inertia of the axles of the front and rear respectively | $\mathrm{I}_{\theta 1} = 550$ kg m$^2$, $\mathrm{I}_{\theta 2} = 600$ kg m$^2$ |
| Tires’ rigidities | $K_{p1} = K_{p2} = 7.85 \times 10^5$ N/m<br>$K_{p3} = K_{p4} = 5.7 \times 10\ ^5$N/m |
| *S*uspensions’ rigidities | $K_{s1} = K_{s2} = 1.16 \times 10^5$ N/m<br>$K_{s3} = K_{s4} = 3.73 \times 10^5$ N/m |
| Tires’ damping | $C_{p1} = C_{p2} = 2.5 \times 10^4$ Ns/m<br>$C_{p3} = C_{p4} = 3.5 \times 10^4$ Ns/m |
| *S*uspensions’ damping | $C_{s1} = C_{s2} = 1.0 \times 10^2$ Ns/m<br>$C_{s3} = C_{s4} = 2.0 \times 10^2$ Ns/m |
| Tires spacing of the mobile exciter front and rear axles, respectively | $S_{p1} = S_{p2} = 2.05$ m |
| Legs spacing of the mobile exciter front and rear axles, respectively | $S_1 = S_2 = 1.41$ m |
| Spacing between the mobile exciter front and rear axles | $S_x = 4.73$ m |
| Eccentricities | $a_1 = 0.67$ m, $a_2 = 0.33$ m |

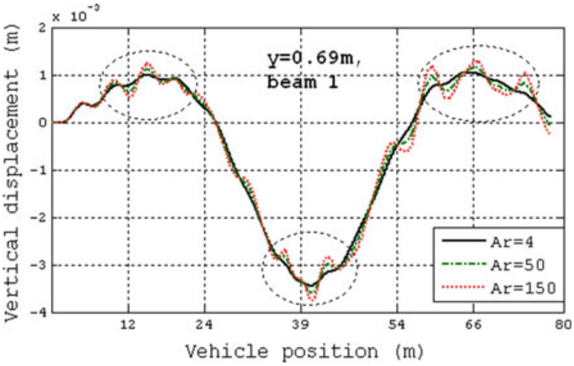

**Fig. 2** Roadway influence on the path surface dynamic displacement

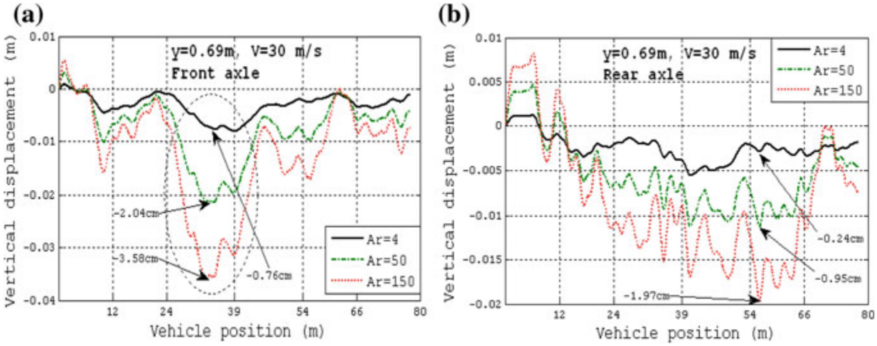

**Fig. 3** Roadway conditions influence on the dynamic displacement (left) of the front mobile exciter axle and (right) of the rear mobile exciter axle

### 3.3 Stability Roadway Irregularities Influence

Figure 2 presents the influence of the roadway conditions on the dynamic displacement of the path surface obtained by applying the presented method with a 30 m/s vehicle speed.

The roughness has a minor effect on the dynamic displacement of the path surface (Fig. 2).

Figure 3 left and right present also the dynamic displacements of the mobile exciter's axles, respectively, obtained by presented work with a 30 m/s mobile exciter speed at different roadway irregularities. We can note that the roughness has a major effect on the dynamic displacement of the mobile exciter axles (Fig. 3 left, right) greatly increasing displacement with higher levels of affiliated roughness.

The influence of roughness was also observable at the middle of the second span (measure point). At that location, the dynamic displacements from the front mobile exciter axle was 7 times that of good roadway conditions. The rear mobile exciter axle was also influenced but not as strongly (only 3 times compared to the good roadway conditions).

## 4 Conclusion

Only small differences in the minima and maxima of the dynamic response obtained in the presented work were observed and were likely due to the exclusion of the torsional modes (intermodal coupling).

The roughness did not have a major effect on the dynamic displacement of the path surface but did strongly influence to the mobile exciter axles.

The method proposed herein uses a local estimate method for the position, thereby drastically reducing the number of differential equations of the free motion of the path surface to be solved and enables it to be incorporated into a structural analysis software, as there is no required integration.

This is a major advantage over approaches that rely upon a Rayleigh-Ritz method.

## References

AASHTO (2005) LRFD bridge design specifications, SI Units 3rd edition. By American Association of State Highway and Transportation officials

Broquet C (1999) Comportement dynamique des dalles de roulement des ponts en béton sol-licités par le trafic routier. Thèse de Doctorat 1999, Ecole Polytechnique Fédérale de Lausanne

Chompooming K, Yener M (1995) The influence of roadway surface irregularities and mobile exciter deceleration on path surface dynamics using the method of lines. J Sound Vib 183(4):567–586

Gao Q, Zhang J (2016) Analytical solutions for a mass moving along a finite stretched string with random surface irregularities. J Sound Vib 371(9):305–320

Guebailia M, Ouelaa N, Guyader JL (2013) Solution of the free vibration equation of a multi span path surface deck by local estimation method. Eng Struct 48:695–703

Marchesiello S, Fasana A, Garibaldi L, Piombo BAD (1999) Dynamics of multi-span continuous straight Path surfaces subject to multi-degrees of freedom Moving mobile exciter excitation. J Sound Vib 224(3):541–561

Ouelaa N, Rezaiguia A, Laulagnet B (2006) Vibro-acoustic modelling of a railway path surface crossed by a train. Appl Acoust 67:461–475

Zhu XQ, Law SS (2002) Dynamic load on continuous multi-lane path surface deck from moving mobile exciters. J Sound Vib 251(4):697–716

# Rolling Bearing Local Fault Detection During a Run-Up Test Using Wavelet-Filtered CEEMDAN Envelopes

**Mohamed Lamine Bouhalais, Abderrazek Djebala and Nouredine Ouelaa**

## 1 Introduction

Bearings have a major role in most rotating machines as parts that guarantee a desired motion and minimize friction. Bearings surveillance is thus essential for a normal and continuous operating. For this purpose, many techniques have been established on the base of lubricant analysis, infrared imaging, vibration and acoustic analysis.

Vibration analysis is often favored over other techniques due to its proficiency. The undesired mechanical motion of machines can now be measured and used to reveal its condition. A vibration signal representing this shaking motion is habitually treated with several mathematical tools in order to extract abnormal operating signs. For bearings, Fourier transform has been utilized for a long period of time as a successful tool that decomposes signals on the frequency base which allows the recognition of unusual repeated phenomena like bearing faults (McFadden and Smith 1984). Empirical decompositions appeared later and successfully used for signal modes separation and bearing response extraction (Mohanty et al. 2016). For optimal filtration and noise reduction, Wavelet transform has been implemented in many techniques that let researchers extract signal components that have a particular structure through the convolution principle, which also helps in isolating the bearing fault vibration representation (Djebala et al. 2008). In the search for an optimal technique that is able to detect bearing faults in different conditions faced in the industries on the base of vibration analysis, researchers have been looking for solutions that allow the surveillance of bearings under variable speed condition, since the most of the designed signal processing techniques have been able to do the task under normal conditions but had a common shortcoming. Indeed, they all have been made to work with stationary signals measured from constant speed machines. The obligations of

---

M. L. Bouhalais (✉) · A. Djebala · N. Ouelaa
Mechanics and Structures Laboratory (LMS), May 8th 1945 University, 401, 24000 Guelma, Algeria
e-mail: mouhamed_mars@hotmail.com

T. Boukharouba et al. (eds.), *Computational Methods and Experimental Testing In Mechanical Engineering*, Lecture Notes in Mechanical Engineering,
https://doi.org/10.1007/978-3-030-11827-3_11

industrial maintenance management had put the researchers between two choices: Develop new diagnostic tools specifically for variable speed machines, or simply adjust the classical tools to make them useful in this special case.

In a previous work the authors (Djebala et al. 2015) have successfully extracted the bearing state under constant speed using a hybrid technique based on *EMD* and *WMRA*. A new method named *CEEMDAN* has been used in this paper together with *WMRA* for rolling bearing local fault diagnosis under variable speed condition. A vibration signal has been decomposed with *CEEMDAN* which provided a number of *IMFs* that have been analysed and classified according to their frequencies contents and Kurtosis values. An optimal mode is then selected. The two famous techniques have been assisted with an order tracking algorithm that helps redressing the variable speed issue. An envelope order spectrum applied after using the hybrid technique has successfully revealed the presence of a local ball fault found in a rolling bearing mounted on a test rig.

## 2 Tools and Methodology

The study proposes the decomposition of the non-stationary vibration signals with *CEEMDAN* that uses an operator $E_j(\cdot)$ which, given a signal, produces the $j$th *IMF* obtained by *EMD*, adding at each operation a white noise signal that respects a proposed Signal to Noise Ratio $\varepsilon_i$ as the following (Colominas et al. 2012):

1. Use the original *EMD* to obtain the first $\overline{IMF}$,
2. Calculate the first residue as:

$$r_1(t) = x(t) - \overline{IMF}_1(t) \tag{1}$$

3. Decompose $I$ realizations of $r_1(t) + \varepsilon_1 E_1\left(n^i(t)\right)$ until their first *EMD* mode and calculate the second mode:

$$\overline{IMF}_2(t) = \frac{1}{I}\sum_{i=1}^{I} E_1(r_1(t)) + \varepsilon_1 E_1\left(n^i(t)\right) \tag{2}$$

4. For $k = 2, \ldots k$, calculate the $k - th$ residue:

$$r_k(t) = r_{k-1}(t) - \overline{IMF}_k(t) \tag{3}$$

5. For $k = 2, \ldots k$, define the $k + 1 - th$ mode as:

$$\overline{IMF}_{k+1}(t) = \frac{1}{I} \sum_{i=1}^{I} E_1(r_k(t)) + \varepsilon_k E_k\left(n^i(t)\right) \tag{4}$$

6. Go for step 4 for next $k$.

Steps from 4 to 6 are repeated until the obtained residue in no longer feasible to be decomposed.

An ideal mode that represents the bearing response, is then picked from the gotten *IMFs* to be analyzed with *WMRA* filters: a low-pass ($L$) and a high-pass ($H$) filters, this would give two vectors representing the low frequencies and the high frequencies of the chosen *IMF* respectively, allowing the selection of the best filtered detail that represents the impulse train generated by the fault. For an *IMF* of length $N$, the proposed technique consists of:

- Calculating the Discrete Wavelet Transform (*DWT*) over the chosen signal envelope with $\log_2 N$ stages at most.
- Produces two sets of coefficients: approximation coefficients $cA_1$ and detail coefficients $cD_1$. These vectors are obtained by convolving s with the low-pass filter for approximations, and with the high-pass filter for details.
- Splits the approximation coefficients $cA_1$ in two parts using the same scheme, replacing the chosen signal by $cA_1$ and producing $cA_2$ and $cD_2$.
- Repeat the same procedure to obtain the approximations and details of level $j$.
- Reversely, starting from $cA_j$ and $cD_j$, the Inverse *DWT* reconstructs $cA_{j-1}$, inverting the decomposition step by inserting zeros and convolving the results with the reconstruction filters.

An envelope order spectrum is finally executed with the purpose of confirming the presence of the fault as follow:

- The mean of the chosen detail is initially removed.
- The upper and lower envelopes of the reconstructed signal are calculated using the Discrete Fourier Transform.
- The removed mean is added back to the calculated envelopes.
- The upper envelope is angularly resampled on the base of the arriving time of the tachometer pulses.
- An envelope order spectrum is calculated using a Short-time Fourier Transform with a hanning window applied on the resampled envelope signal.

Order analysis is used due to the fact that, when the speed is variable, the majority of signal components follow the speed variation, which makes FT incapable of detecting anything useful since it only detects oscillatory functions whose frequencies are constant. To avoid such a problem, it is often preferred to have a spectrum with *X-axis* based on Orders instead of frequencies, where orders are just harmonics

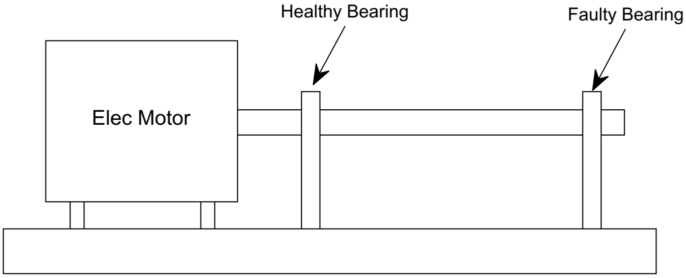

**Fig. 1** Test rig

**Fig. 2** Speed variation

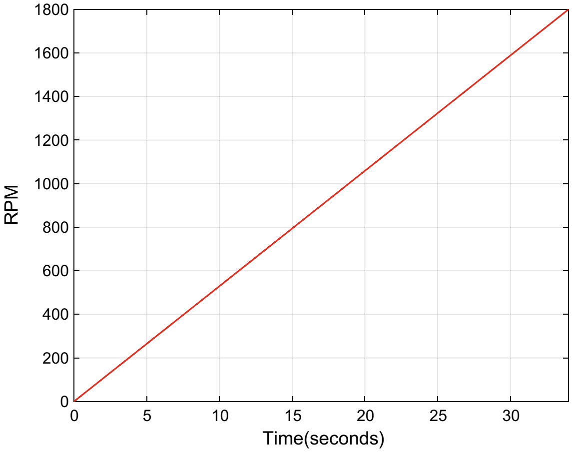

of shaft speed, the process of diagnosis is then performed by calculating the characteristic orders of machine elements and looking for the corresponding pics in the obtained order spectrum.

The selection of both optimal mode and optimal detail is based on Kurtosis values and bearing resonance frequency coverage.

## 3 Application

In order to prove the efficiency of the proposed method, it has been tested in the field. For that, a number of signals have been measured in the laboratory using a bearing having a local ball defect of small size characterized by a fault order equal to 1.9, mounted on the test rig represented in Fig. 1. The speed has been linearly varied from 0 to 1800 RPM within 34.13 s as shown in Fig. 2, and measured simultaneously with the vibration signal.

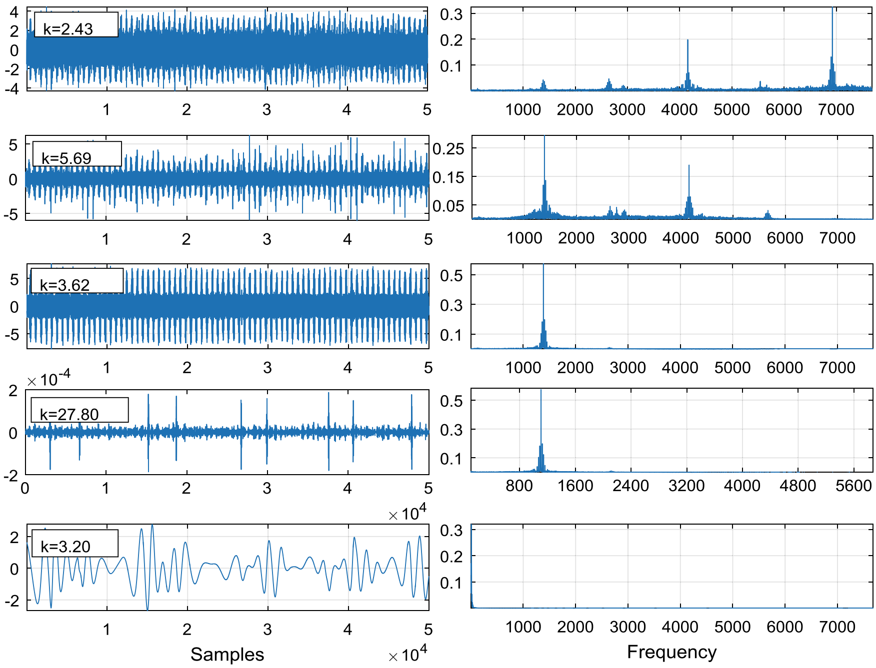

**Fig. 3** IMFs with their spectrum and kurtosis values

The *CEEMDAN* decomposition has given the modes represented in Fig. 3. The analysis of the spectrums shows that the first three modes have almost the same frequency components, including the bearing resonance frequency, but with different magnitudes, the second *IMF* seems to have the clearest representation of the resonance frequency and its harmonics, however, its kurtosis is significantly low. On the other hand, the third mode contains the resonance frequency in its spectrum with no harmonics, but with higher kurtosis value. It is also noticeable that its time domain representation shows a clear impulse train that may represent the shocks generated whenever the faulty ball makes contact with the inner or the outer race. The optimal mode that should be used in the next procedure should thus be the third one, since it covers the bearing resonance frequency and has the most valuable kurtosis.

For the next step, the envelope of the chosen mode has been calculated as described before, and then passed through *WMRA* filters to obtain the details sown in Fig. 4. The detail that has been chosen according to the previously mentioned criteria has given a clearer view of the shocks resulted from the fault, as represented in Fig. 4. The envelope order spectrum is finally performed over the signal; the fault order has been successfully highlighted with the proposed method as shown in Fig. 5, which proves its efficiency (Fig. 6).

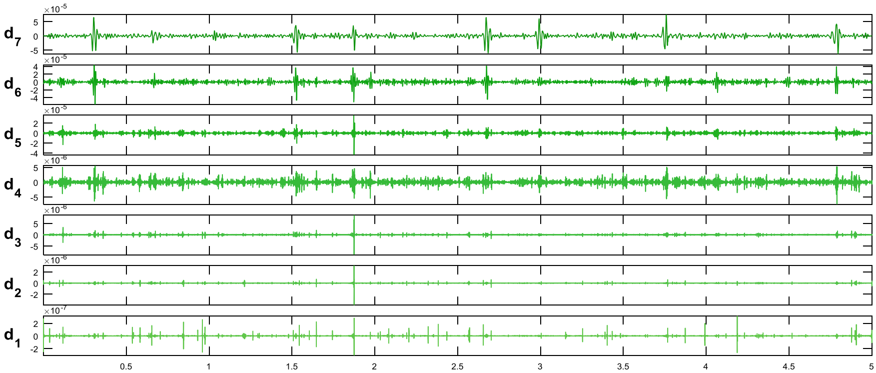

**Fig. 4** Details given by WAMRA

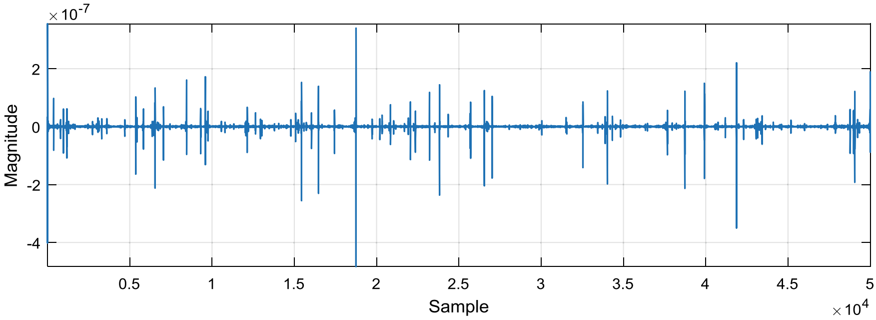

**Fig. 5** Details of the third IMF

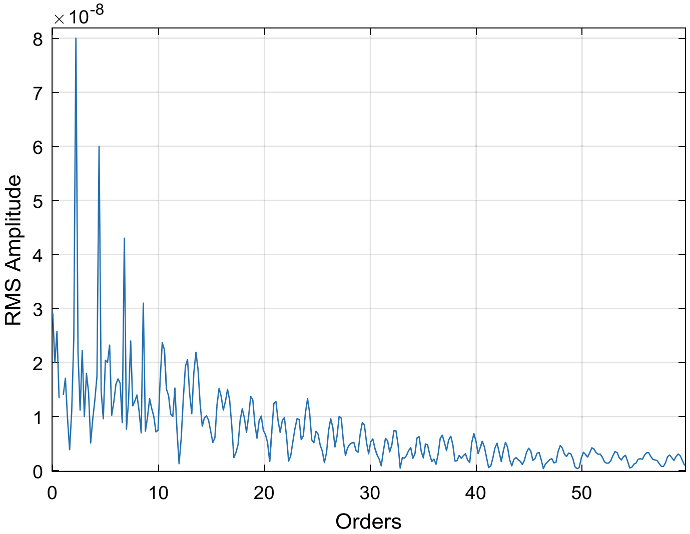

**Fig. 6** Envelope order spectrum

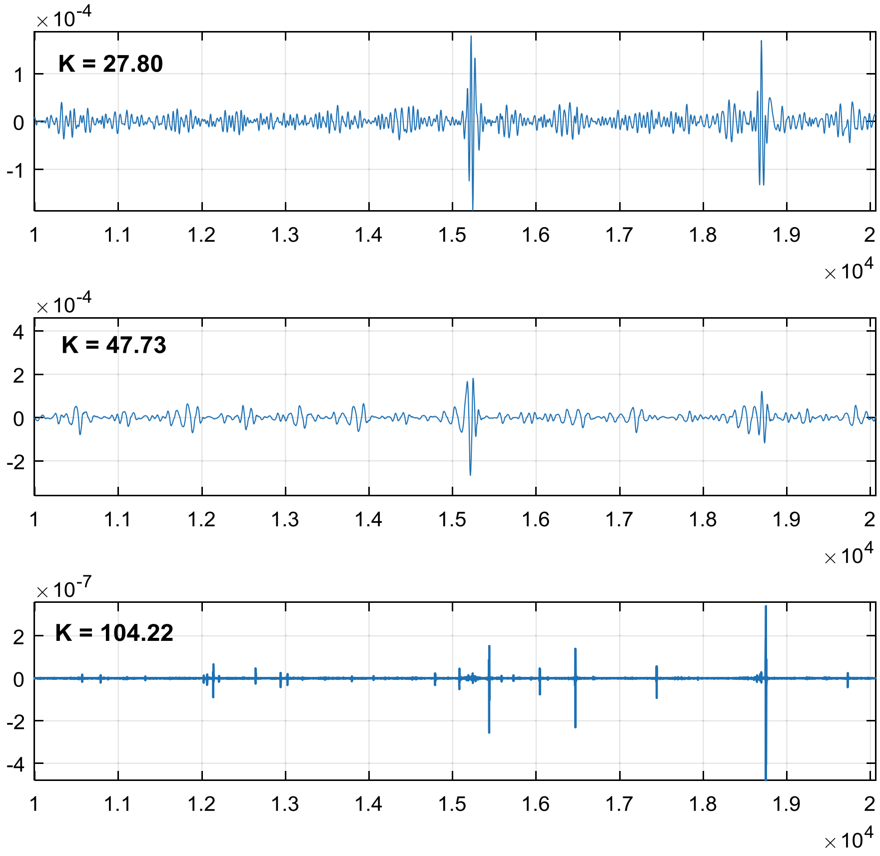

**Fig. 7** CEEMDAN (top), WMRA (Middle) and hybrid (bottom)

The obtained results show that the *CEEMDAN* and *WMRA* techniques complete each other to form a powerful tool able to isolate the faults time representation and pre-process the signals for a frequency or order domain tool such as order analysis. Figure 7 represents a comparison between the time domain results obtained after applying the *CEEMDAN* and *WMRA* separately and those obtained with the proposed hybrid technique. It is clear that the proposed tool gives better and clearer representation, as confirmed by kurtosis values.

Moreover, the envelope order spectrum performed after applying only *CEEMDAN* or *WMRA*, represent a less accurate result when compared with the one obtained after using the proposed approach, this can be noticed on Fig. 8.

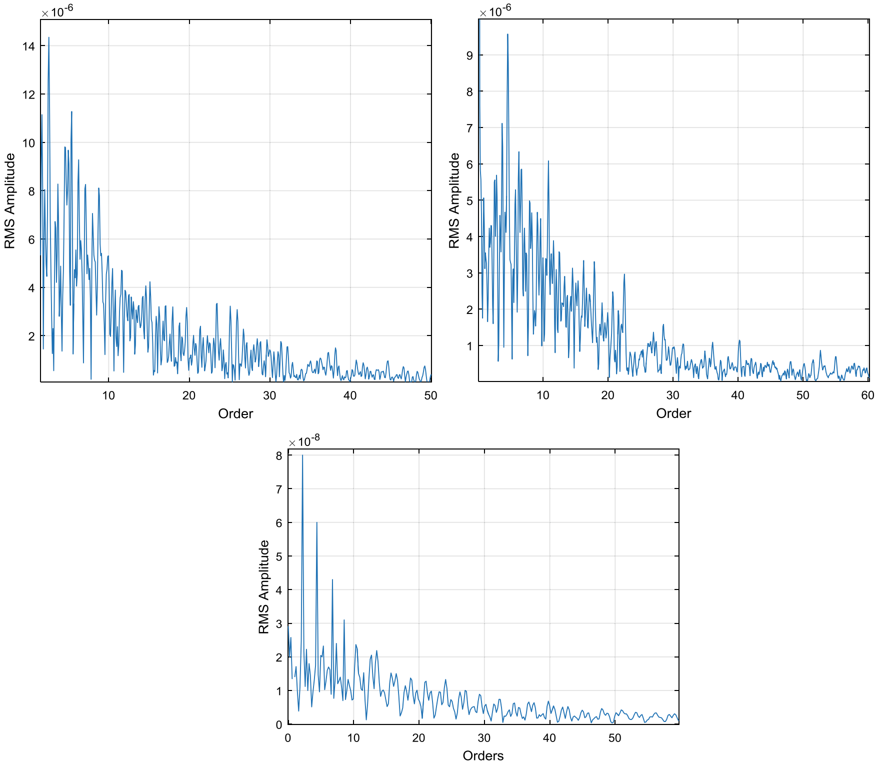

**Fig. 8** Envelope Order Spectrum, CEEMDAN (top Right), WMRA (Top Left) and CEEMDAN + WMRA (Bottom)

## 4 Conclusion

A hybrid method designed for local fault detection of rolling bearings working under variable speed is proposed in this article. The Complete Empirical Mode Decomposition with Adaptive noise has been successfully used to extract the bearing vibration response from the raw captured signal. The *WMRA* has been then used as a filter that isolates the impulse train generated by bearing fault. An Order Tracking Algorithm has been also used to remove the effects of the speed variation. The proposed method has been proven to be effective with real measured signals from a rolling bearing having a ball defect.

## References

Colominas MA, Schlotthauer G, Torres ME, Flandrin P (2012) Noise-assisted EMD methods in action. Adv Adapt Data Anal, **4**(04), 1250025

Djebala A, Babouri MK, Ouelaa N (2015) Rolling bearing fault detection using a hybrid method based on empirical mode decomposition and optimized wavelet multi-resolution analysis. Int J Adv Manuf Technol 79(9–12):2093–2105

Djebala A, Ouelaa N, Hamzaoui N (2008) Detection of rolling bearing defects using discrete wavelet analysis. Meccanica 43(3):339–348

McFadden PD, Smith JD (1984) Model for the vibration produced by a single point defect in a rolling element bearing. J Sound Vib 96(1):69–82

Mohanty S, Gupta KK, Raju KS (2016) Vibro-acoustic fault analysis of bearing using FFT, EMD, EEMD and CEEMDAN and their implications. In: Advances in machine learning and signal processing (pp. 281–292). Springer, Cham

# Industrial Reproduction of Objects with Freeform Surfaces Using Reverse Engineering Process

**Sahla Ferhat, Mohamed Bey and Hassène Bendifallah**

## 1 Introduction

Freeform surfaces used in several domains such as aeronautics, automotive, medical etc. *CAD* models are an interface between designer and *CAD* software. These models can be obtained using Forward Engineering or Reverse Engineering approach (Raja and Fernandes 2008). The former one consists in using *CAD* functionalities to design object surfaces with low geometric complexity. The later one is used if objects *CAD* models are unavailable or surfaces geometries are of high complexity. Reverse Engineering approach is widely used in mechanical engineering, electrical, medical, etc. Its main objective is the analysis of a physical object in order to reproduce or to improve the *CAD* model (Ali 2015).

The Reverse Engineering process is based on the acquired *3D* clouds of points obtained in object digitalization. These clouds undergo a series of treatments in software in order to reconstruct object *CAD* model which can be exported to dedicated software for other studies such as stress analysis, manufacturing, etc. (Creaform 2014).

In this work, Reverse Engineering process is used for industrial reproduction of physical object with freeform surfaces defined by *3D* clouds of points until object prototyping. The principal stages of Reverse Engineering process are depicted in Fig. 1.

---

S. Ferhat (✉) · M. Bey · H. Bendifallah
Centre de Développement des Technologies Avancées, CDTA, Algiers, Baba Hassen, Algeria
e-mail: ferhatsahla@gmail.com

T. Boukharouba et al. (eds.), *Computational Methods and Experimental Testing In Mechanical Engineering*, Lecture Notes in Mechanical Engineering,
https://doi.org/10.1007/978-3-030-11827-3_12

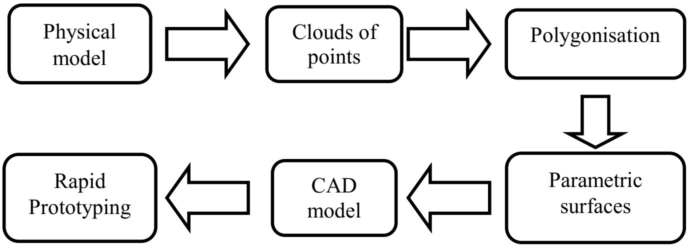

**Fig. 1** Reverse engineering process (Krivoš et al. 2014; Nartz et al. 2003)

## 2 Exploited Equipments

The presented work has an experimental character. Consequently, it is necessary to select the most appropriate equipments. For object digitalization, a Coordinate Measuring Machine—*CMM*—of Hexagon Metrology equipped with a Laser Scanner *HP-L-10.6* is used for its high precision (Fig. 2).

This Laser scanner is chosen for these reasons (Chevrot III/03):

- High density of clouds of points.
- Rapid scan of freeform surfaces.
- Non-contact scans suitable for fragile, flexible and tender parts.
- High productivity due to scanning speed.

These clouds of points are treated using "*3D* Reshaper" software or "Scan to *3D*" module of SolidWorks software.

For object prototyping, a *3D* Printer is used (Fig. 3).

**Fig. 2** Coordinate measuring machine and laser scanner

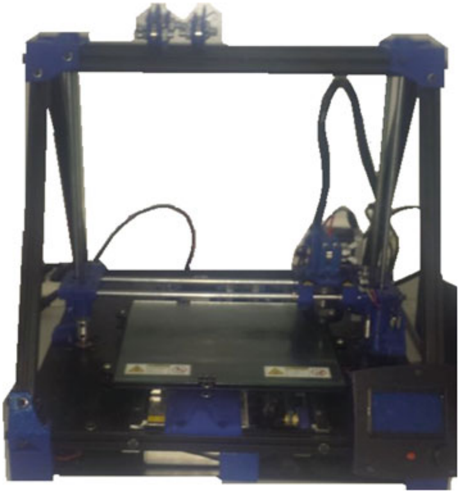

**Fig. 3** 3D printer

## 3 Reproduction Procedure

The first step of the approach is object digitalization using *CMM* machine to recover *3D* clouds of points representing faithfully object shape. The considered object is a freeform mold cavity of dimensions 92 mm × 50 mm × 36 mm (Fig. 4). To ensure continuity between surfaces, very dense clouds of points must be acquired.

The digitalization is performed according to the following strategy:

- Positioning the object on a support.
- Setting the Laser advance speed to 2 mm/s to obtain dense clouds of points.
- Orienting the object so that its faces are parallel to machine axes X and Y.
- Positioning the Laser at a height equal to 170 mm to scan the upper face of the object (Fig. 5 left).

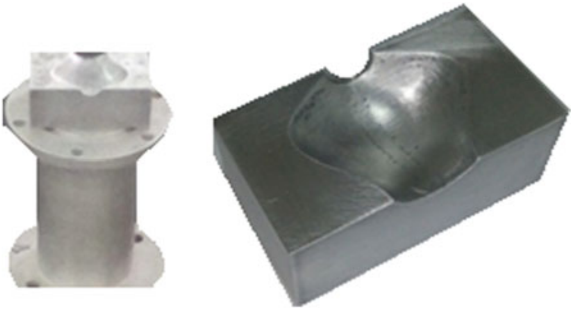

**Fig. 4** Freeform mold cavity

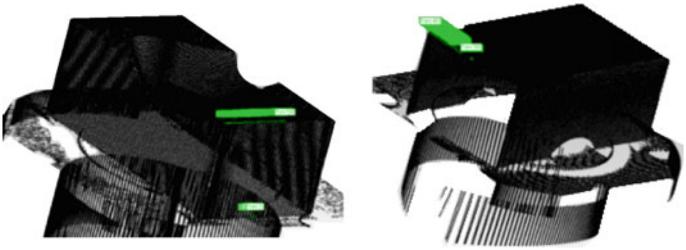

**Fig. 5** Clouds of points for the two positions: left upper part and right lower part

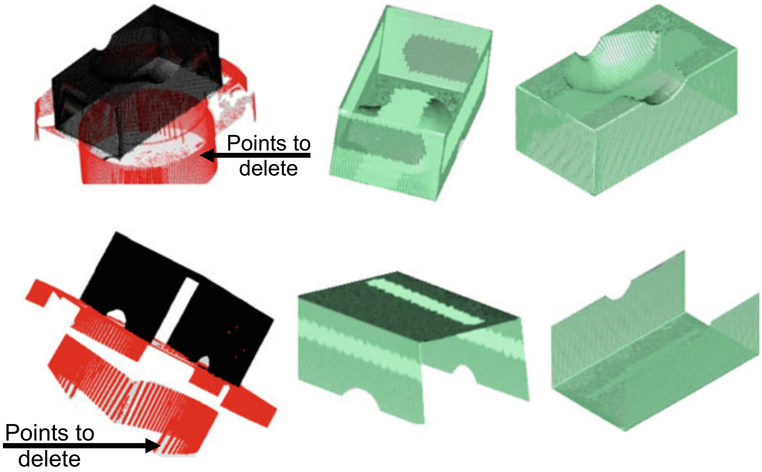

**Fig. 6** Cleaning of the two clouds of points, left upper part before and after cleaning and right lower part before and after cleaning

- For the same object positioning, orientation of the Laser to an angle equal to 90° to scan the four vertical faces (Fig. 5 left). The resulted cloud of points is composed of 704,373 points.
- Turning the object to scan its bottom face (Fig. 5 right). It must be noted that areas of vertical faces are also scanned to create overlapping clouds of points. The resulted cloud of points is composed of 409,517 points.

After object digitalization, the two acquired clouds of points must undergo several treatments to retrieve the mold cavity *CAD* model. Points do not belonging to the mold cavity are deleted for the two clouds of points (Fig. 6). Deleted points belong to the support. After cleaning, the two clouds of points become composed of 677,925 points.

The next step consists in grouping the two clouds of points in the same referential. The objective is the search of solids geometric transformations (three translations and three rotations) allowing alignment of these clouds. It is done in two steps:

1. **Manual alignment**: based on visual aspects of the two clouds of points, specific points are manually selected for the first alignment (Fig. 7 top-left and Fig. 7 top-right). Its objective is to accelerate global alignment process especially for clouds of high density. It must be noted that the two clouds of points are not perfectly aligned and it results alignment errors (Fig. 7 low).
2. **Global alignment**: to minimize alignment errors, a global alignment is performed on the resultant clouds of points in manual alignment. Figure 8 shows clearly that errors are minimized. Thereafter, the two clouds of points are merged to form a single cloud of points representing the freeform mold cavity.

To minimize the number of manipulated points and consequently to reduce the processing times, the resulted cloud of points must be decimated. For this, the minimum distance between two points is set equal to 0.5 mm (Fig. 9). The final cloud of points becomes composed of 119,215 points. So, a reduction of 82.40%.

The reconstruction of the *CAD* model is based on a defined mesh. For this, the resulted cloud of points is converted to a 3D polygonal mesh model. It is created by

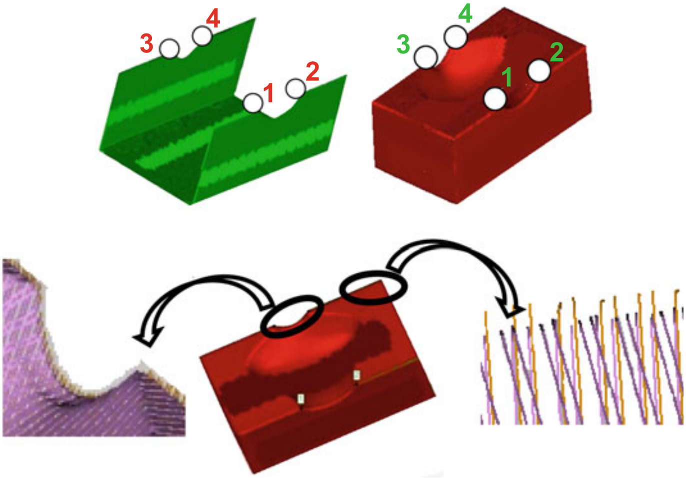

**Fig. 7** Manual alignment of the clouds of points, top-left upper part, top-right lower part, low cloud aligned manually with errors

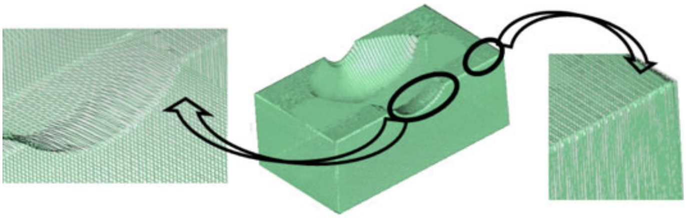

**Fig. 8** Global alignment of the clouds of points

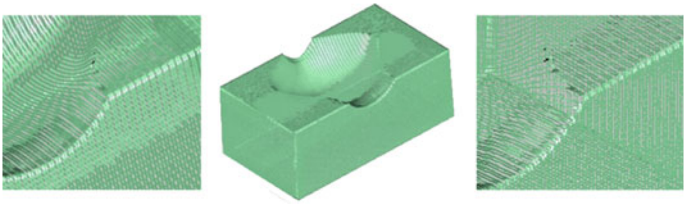

**Fig. 9** Decimation of the cloud of points left, before and right, after

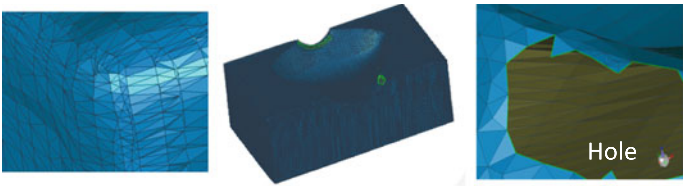

**Fig. 10** Mesh creation

**Fig. 11** Correction of the mesh size

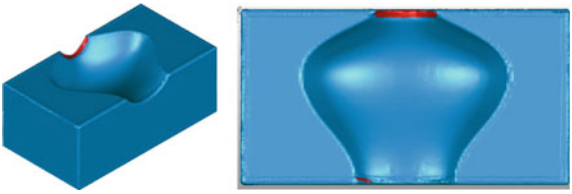

setting the mesh size equal to 0.2 mm with maximum reduction of noise (Fig. 10). The created mesh contains holes and errors that must be corrected.

The next step is based on visual aspects of the object. It consists in remeshing particular areas where the mesh size is not correct (continuity problems) by filling holes with triangles (Fig. 11).

Based on the generated mesh, the object *CAD* model is generated from these steps (Fig. 12):

- Automatic identification of regions from geometric characteristics (Fig. 12 top left).
- Adjustment of identified surfaces by automatic recognition of surfaces types (plane, cylinder, cone, and sphere), surfaces based on contours (extrusions and revolutions) and material removal (Fig. 12 top right).
- Joining surfaces (Fig. 12 low left).
- Object CAD model generation (Fig. 12 low right).

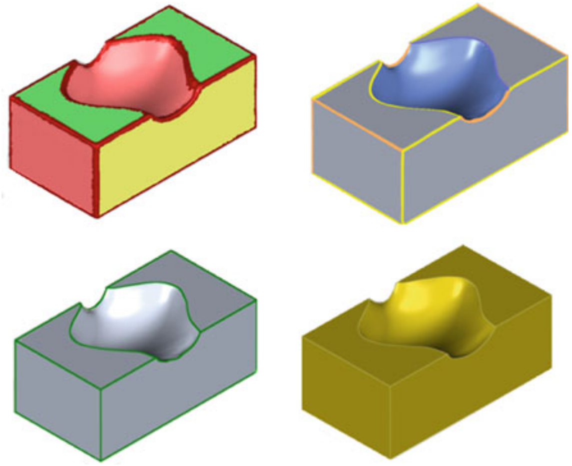

**Fig. 12** CAD model reconstruction, top left and right, regions identification and surfaces adjustment, low left and right, surfaces joining and CAD model

## 4 Variances Analysis

To verify the accuracy of the generated *CAD* model compared to the original cloud of points, it is indispensable to quantify the deviation between them. For this, variances spectral analysis is conducted (Fig. 13). Table 1 gives the critical values of maximum and minimum errors while Table 2 represents real differences. Figure 13 shows that the majority of the part is in the interval [−0.0324, 0.0324] (68.262%). Nevertheless, less than 3% of small areas present an important deviation of 0.05 mm. The appearance of these areas is explained by the fact that the clouds of points are not very dense in these regions. These results demonstrate that the *CAD* model representing the cavity mold is reconstructed faithfully.

To minimize errors between object *CAD* model and the cloud of points, the minimum distance between two points is reduced from 0.5 to 0.2 mm. The spectrum of the differences between the new *CAD* model and the new cloud of points is shown by Fig. 14. This figure shows that the maximum discrepancies are reduced to 0.3974 mm

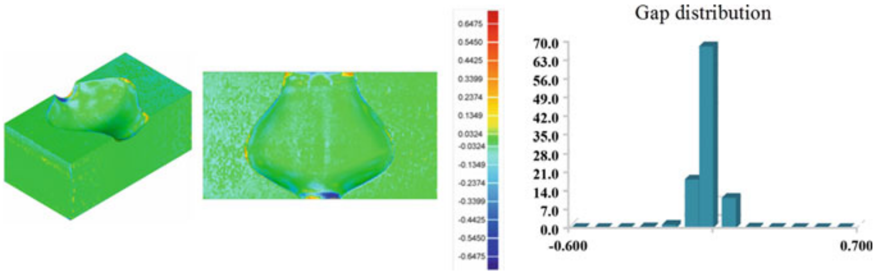

**Fig. 13** Comparison of results, left variances spectrum and right discrepancies distribution

**Table 1** CAD model errors relative to the cloud of points

| Type of tolerance | 3D gap (mm) |
|---|---|
| Critical maximum error | 0.6475 |
| Nominal maximum error | 0.0324 |
| Nominal minimum error | −0.0324 |
| Critical minimum error | −0.6475 |

**Table 2** Gaps in the CAD model relative to the cloud of points

| Type | Gap (mm) |
|---|---|
| Maximum upper gap | 0.5704 |
| Maximum lower gap | −0.6475 |
| Average gap | 0.0267/−0.0322 |

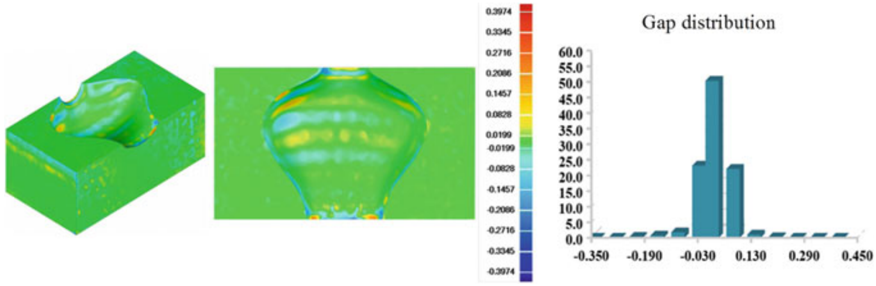

**Fig. 14** Results of the comparison, left variances spectrum and right discrepancies distribution

instead of 0.6475 mm. At the same time, the majority of the gap belongs to the interval [−0.0199, 0.0199].

These results show that the reconstruction of the object *CAD* model with freeform surfaces with a good precision requires dense clouds of points particularly in areas of high curvature variation. In the same time, it must have clouds of points with an optimal density to facilitate its handling and to reduce processing times.

## 5 Cavity Mold Prototype Realization

For the experimental validation, from the *STL* model generated based on the generated *CAD* model, a prototype is produced using a *3D* printer. This process is chosen due to its simplicity. The rapid prototyping process is shown in Fig. 15 (Aragon and Patrice).

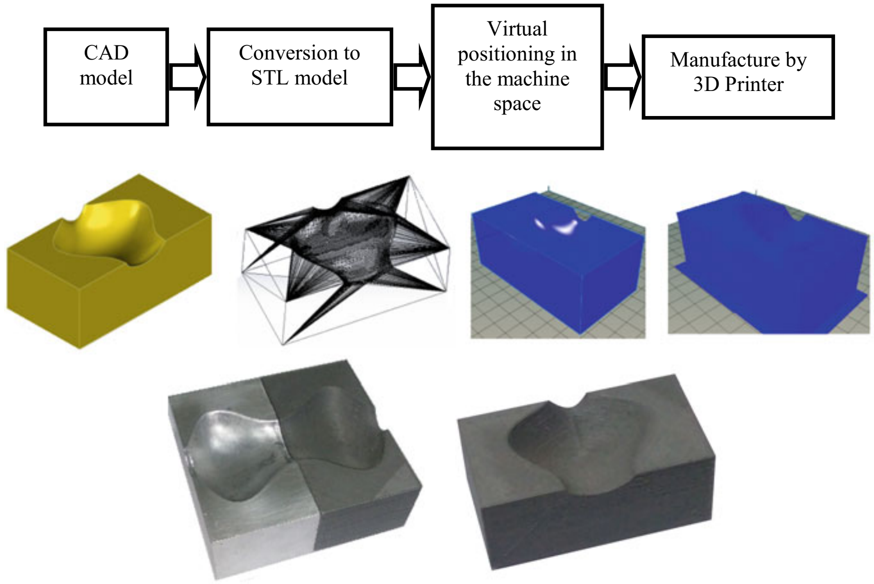

**Fig. 15** Rapid prototyping of the freeform mold cavity

## 6 Conclusions

In this work, an experimental-based approach is adopted to duplicate objects with free form surfaces. From clouds of points acquired using *CMM* machine, a single cloud of points is produced to represent the object geometry. Subsequently, the *CAD* model is reconstructed and a spectral analysis is conducted to validate the model.

The conducted analysis highlighted the fact that the reconstruction of the *CAD* model with a good accuracy depends on the density of the clouds of points and more particularly in the zones of high curvature variations. Consequently, the analysis of object surfaces to duplicate is a critical operation before object scanning. In the same time, clouds of points must have optimal densities to facilitate their treatment and to minimize the processing times.

## References

Ali S (2015) La Rétro-Conception de Composants Mécaniques par une Approche Concevoir pour Fabriquer. Dissertation, University of Technology Troyes, UTT, France

CREAFORM (2014) Reverse engineering of physical objects teaching manual, Version 1.0, 1–60. www.creaform3d.com |© 2014 Creaform Inc. Accessed 24 Sept 2017

Krivoš E, Pastirčák R, Lehocký P (2014) Using of the reverse engineering method for the production of prototype molds by patternless process technology. Arch Foundry Eng 14(2):115–118

Nartz O, Bernard A, Ris G, Remy S (2003) Rétro-conception d'un Bouchon de Radiateur de Delahaye 135. WorkShop Integration Numérique en Dévelopement de Produits, Nancy, France
Raja V, Fernandes Kj (2008) Reverse engineering, an industrial perspective. Springer Series in Advanced Manufacturing, Edition Springer

# Effect of Boundary Conditions and Damping on Critical Speeds of a Flexible Mono Rotor

**Saliha Belahrache and Brahim Necib**

## 1 Introduction

Playing an important role in a very wide range of applications in the industry, rotating machines such as turbines, pumps, generators and propellers are considered among the masterpieces in the mechanisms. Rotating machines, and more particularly those mounted on Hydrodynamics bearings, possess all sorts of particular vibratory phenomena: Critical velocities, direct and inverse precession, whirling, gyroscopic effects, etc. The prediction of the dynamic behavior of rotors is therefore necessary in the design of rotating machineries. This is made by rotor dynamics which is the study of these systems that comes to precisely understand and predict their vibratory behavior (Rao 1983; Lee 1993; Vance 1988). There are phenomena that are particularly dangerous and can lead to unacceptable vibratory levels and the consequences are often catastrophic. Indeed, critical speeds are a function of the dynamic rigidity of rotating systems and the presence of gyroscopic forces creates dependence between the speed of rotation and the pulsations of such structures: This implies that the correct determination of the critical velocities is one of the essential elements when dimensioning such dynamic systems. The model chosen for this work is similar to that of Lalanne and Ferraris who just considered the supported-supported case (Lalanne and Ferraris 1998). In previous analyses the study of the same rotor was made when it is undamped symmetrical and undamped asymmetrical (Belahrache and Necib 2013, 2014). Here we treated a more general condition that

---

S. Belahrache (✉) · B. Necib
Mechanical Engineering Department, Mentouri Frères University
Constantine 1, Constantine, Algeria
e-mail: sbelahrache@hotmail.com

B. Necib
e-mail: necibbrahim2004@yahoo.fr

T. Boukharouba et al. (eds.), *Computational Methods and Experimental Testing In Mechanical Engineering*, Lecture Notes in Mechanical Engineering,
https://doi.org/10.1007/978-3-030-11827-3_13

consists of a damped asymmetrical rotor where the damping comes from bearings whose friction is of the viscous type. The vibratory analysis and then the comparison are made for the rotor when it is simply-simply supported, free-simply supported and free-free.

## 2 Model Equations Implementation

In this work, we considered the model of rotor represented in Fig. 1 which has been treated by Lalanne and Ferraris on two fixed supports. But here it is treated with two other boundary conditions to see the effects on the results of the rotor dynamic analysis. The specifications of the rotor are given in Tables 1, 2, 3 and 4.

The rotor flexural vibrations analysis is carried out by a modeling which is based on the Rayleigh-Ritz method that is characterized by the substitution of the displacements u and w in the *x* and *z* directions respectively by approximation functions:

$$u(y,t) = f(y) \cdot q_1(t) = f(y) \cdot q_1 \tag{1}$$

$$w(y,t) = f(y) \cdot q_2(t) = f(y) \cdot q_2 \tag{2}$$

where *u* and *w* are the displacements considered respectively along x and z, $q_1$ and $q_2$ are the generalized independent coordinates and *f(y)* is the displacement function which is taken for the first mode of a beam in flexion with a constant cross-section and. It is given by:

- For simply-simply supported case:

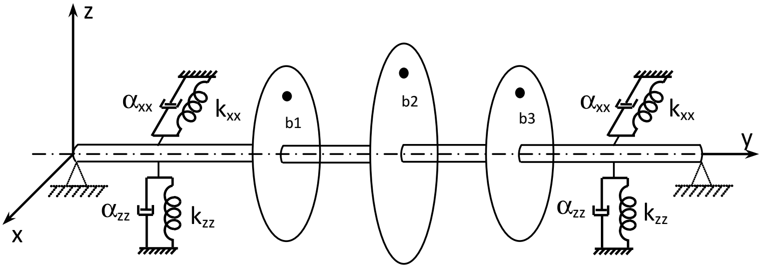

**Fig. 1** Considered rotor model

**Table 1** Shaft characteristics

| Length (m) | Cross-section radius (m) | Young modulus (N/m$^2$) | Poisson coefficient | Density (kg/m$^{3)}$ | Diametric moment of inertia (m$^4$) | Cross-section (m$^2$) |
|---|---|---|---|---|---|---|
| L = 1.3 | r = 0.05 | E = 2.10$^{11}$ | $\upsilon = 0.3$ | $\rho = 7800$ | I = 4.906.10$^{-6}$ | s = 7.85.10$^{-3}$ |

**Table 2** Rigid disks characteristics

| | Density (kg/m$^3$) | Internal radius (m) | External radius (m) | Thick-ness (m) | Position (m) | Mass (kg) | Moments of inertia (kgm$^2$) |
|---|---|---|---|---|---|---|---|
| $D_1$ | $\rho = 7800$ | $R_{i1} = 0.05$ | $R_{e1} = 0.12$ | $h_1 = 0.05$ | $l_2 = 0.45$ | $M_{d1} = 14.57$ | $I_{dx1} = I_{dz1} = 0.0645$<br>$I_{dy1} = 0.123$ |
| $D_2$ | $\rho = 7800$ | $R_{i2} = 0.05$ | $R_{e2} = 0.2$ | $h_2 = 0.05$ | $l_3 = 0.65$ | $M_{d2} = 45.92$ | $I_{dx2} = I_{dz2} = 0.497$<br>$I_{dy2} = 0.9758$ |
| $D_3$ | $\rho = 7800$ | $R_{i3} = 0.05$ | $R_{e3} = 0.2$ | $h_3 = 0.06$ | $l_4 = 0.85$ | $M_{d3} = 55.11$ | $I_{dx3} = I_{dz3} = 0.602$<br>$I_{dy3} = 1.171$ |

**Table 3** Unbalances characteristics

| Unbalance | Mass of the unbalance (kg) | Position of unbalance from the axis of the shaft (m) |
|---|---|---|
| $b_1$ | $m_{b1} = 0.88\ 10^{-4}$ | $d_1 = 0.12$ |
| $b_2$ | $m_{b2} = 2.785\ 10^{-4}$ | $d_2 = 0.20$ |
| $b_3$ | $m_{b3} = 3.34\ 10^{-4}$ | $d_3 = 0.20$ |

**Table 4** Bearings characteristics

| Bearing | Position (m) | Stiffness $k_{xx}$ (N/m) | Damping $C_{xx}$ (Ns/m) | Stiffness $k_{zz}$ (N/m) | Damping $C_{zz}$(Ns/m) |
|---|---|---|---|---|---|
| 1 | $l_1 = 0.2$ | $k_{xx} = 5 \times 10^7$ | $C_{xx} = 5 \times 10^2\ \beta$ | $k_{zz} = 7 \times 10^7$ | $C_{zz} = 7 \times 10^2\ \beta$ |
| 2 | $l_5 = 1.1$ | $k_{xx} = 5 \times 10^7$ | $C_{xx} = 5 \times 10^2\ \beta$ | $k_{zz} = 7 \times 10^7$ | $C_{zz} = 7 \times 10^2\ \beta$ |

With: $k_{xz}$, $k_{zx}$, $C_{xz}$ and $C_{zx} = 0$ are taken equal to zero and β is constant whose value defines the magnitude of damping

$$f(y) = B[\sin \beta_n y] \tag{3}$$

where: $\beta_n = \pi$.

- For simply-free supported case:

$$f(y) = B[\sin \beta_n y + \alpha_n \, sh \, \beta_n y] \tag{4}$$

where: $\alpha_n = \frac{\sin \beta_n L}{sh \beta_n L}$ and $\beta_n L = 3.9266$.

- For free-free supported case:

$$f(y) = B[\sin \beta_n y + sh\beta_n y] + \alpha_n[\cos \beta_n y + ch\beta_n y] \tag{5}$$

where: $\alpha_n = \frac{\sin \beta_n L - sh\beta_n L}{ch\beta_n L - \cos \beta_n L}$, $\beta_n L = 4.730041$, $B$ is a constant (taken equal to 1).

The expressions of the kinetic and stain energies (T and U) can therefore be obtained. The total kinetic energy of the system is:

$$T = T_s + T_d + T_b \tag{6}$$

where: $T_s$, $T_d$ and $T_b$ are the kinetic energies of the shaft, the unbalances and the discs respectively. They are given by:

$$T_s = \frac{1}{2}\rho \mathrm{s}(\dot{\mathrm{q}}_1^2 + \dot{\mathrm{q}}_2^2)\int_0^L f^2(y)\,dy + \frac{1}{2}\rho \mathrm{I}(\dot{\mathrm{q}}_1^2 + \dot{\mathrm{q}}_2^2)\int_0^L g^2(y)\,dy - 2\,\rho \mathrm{I}\Omega\dot{\mathrm{q}}_1\,\mathrm{q}_2)\int_0^L g^2(y)\,dy \tag{7}$$

$$T_d = T_{d1} + T_{d2} + T_{d3} \tag{8}$$

With:

$$\begin{aligned}
T_{d1} &= T_{d1}^{tra} + T_{d1}^{rot} = \frac{1}{2}\mathrm{M}_{\mathrm{d}1} f^2(l_2)(\dot{\mathrm{q}}_1^2 + \dot{\mathrm{q}}_2^2) + \frac{1}{2}\mathrm{Id}_{\mathrm{x}1}\mathrm{g}^2(\mathrm{l}_2)(\dot{\mathrm{q}}_1^2 + \dot{\mathrm{q}}_2^2)\\
&\quad + \frac{1}{2}\,\mathrm{Id}_{\mathrm{y}1}\Omega^2 - \mathrm{Id}_{\mathrm{y}1} g^2(l_2)\dot{\mathrm{q}}_1\,\mathrm{q}_2\Omega\\
T_{d2} &= T_{d2}^{tra} + T_{d2}^{rot} = \frac{1}{2}\mathrm{M}_{\mathrm{d}2} f^2(l_3)(\dot{\mathrm{q}}_1^2 + \dot{\mathrm{q}}_2^2) + \frac{1}{2}\mathrm{Id}_{\mathrm{x}2}\mathrm{g}^2(\mathrm{l}_3)(\dot{\mathrm{q}}_1^2 + \dot{\mathrm{q}}_2^2)\\
&\quad + \frac{1}{2}\mathrm{Id}_{\mathrm{y}2}\Omega^2 - \mathrm{Id}_{\mathrm{y}2} g^2(l_3)\dot{\mathrm{q}}_1\,\mathrm{q}_2\Omega\\
T_{d3} &= T_{d3}^{tra} + T_{d3}^{rot} = \frac{1}{2}\mathrm{M}_{\mathrm{d}3} f^2(l_4)(\dot{\mathrm{q}}_1^2 + \dot{\mathrm{q}}_2^2) + \frac{1}{2}\mathrm{Id}_{\mathrm{x}3}\mathrm{g}^2(\mathrm{l}_4)(\dot{\mathrm{q}}_1^2 + \dot{\mathrm{q}}_2^2)\\
&\quad + \frac{1}{2}\mathrm{Id}_{\mathrm{y}3}\Omega^2 - \mathrm{Id}_{\mathrm{y}3} g^2(l_4)\dot{\mathrm{q}}_1\,\mathrm{q}_2\Omega
\end{aligned}$$

And:

$$T_b = T_{b1} + T_{b2} + T_{b3} \tag{9}$$

With:

$$\begin{aligned}
T_{b1} &= \mathrm{m}_{\mathrm{b}1} d_1 \Omega f(l_2)(\dot{\mathrm{q}}_1 \cos \Omega \mathrm{t} - \dot{\mathrm{q}}_2 \sin \Omega t)\\
T_{b2} &= \mathrm{m}_{\mathrm{b}2} d_2 \Omega f(l_3)(\dot{\mathrm{q}}_1 \cos \Omega \mathrm{t} - \dot{\mathrm{q}}_2 \sin \Omega t)\\
T_{b3} &= \mathrm{m}_{\mathrm{b}3} d_3 \Omega f(l_4)(\dot{\mathrm{q}}_1 \cos \Omega \mathrm{t} - \dot{\mathrm{q}}_2 \sin \Omega t)
\end{aligned}$$

The total strain energy is that of the shaft and it is given by:

$$U_a = \frac{EI}{2}(q_1^2 + q_2^2)\int_0^L h^2(y)\,dy \tag{10}$$

where: $h(y) = \frac{d^2 f(y)}{dy^2}$

The total virtual work due to the stiffness of the bearings is:

$$\delta \mathrm{W} = -\mathrm{k_{xx}f^2(l_1)q_1}\delta\mathrm{q_1} - \mathrm{k_{zz}}f^2(l_1)\mathrm{q_2}\delta\mathrm{q_2} - \mathrm{k_{xx}f^2(l_5)q_1}\delta\mathrm{q_1} - \mathrm{k_{zz}}f^2(l_5)\mathrm{q_2}\delta\mathrm{q_2} \quad (11)$$

This gives:

$$F.q_1 + F.\dot{q}_1 = [-k_{xx}f^2(l_1) - k_{xx}f^2(l_5)]q_1 + [-C_{xx}f^2(l_1) - C_{xx}f^2(l_5)]\dot{q}_1 \quad (12)$$

$$F.q_2 + F.\dot{q}_2 = [-k_{zz}f^2(l_1) - k_{zz}f^2(l_5)]q_2 + [-C_{zz}f^2(l_1) - C_{zz}f^2(l_5)]\dot{q}_2 \quad (13)$$

Introduction of these relations in Lagrange equations lead to the movement equations:

$$\begin{cases} m\ddot{q}_1 - a\,\Omega\,\dot{q}_2 + k\,q_1 = -\left[k_{xx}f^2(l_1) + k_{xx}f^2(l_5)\right]q_1 - \left[C_{xx}f^2(l_1) + C_{xx}f^2(l_5)\right]\dot{q}_1 + m * d\Omega^2 \sin\Omega t \\ m\ddot{q}_2 + a\,\Omega\,\dot{q}_1 + k\,q_2 = -\left[k_{zz}f^2(l_1) + k_{zz}f^2(l_5)\right]q_2 - \left[C_{zz}f^2(l_1) + C_{zz}f^2(l_5)\right]\dot{q}_2 + m * d\Omega^2 \cos\Omega t \end{cases} \quad (14)$$

With: $c_1 = c_{xx}f^2(l_1) + c_{xx}f^2(l_5),\ c_2 = c_{zz}f^2(l_1) + c_{zz}f^2(l_5)\ and\ C = m * d.$

Considering the characteristics of the rotor and the boundary conditions the calculations yield:

- In the simply-simply supported case,

$$\begin{cases} 155.0624\ \mathrm{\ddot{q}_1} - 37.0897\ \Omega\ \mathrm{\dot{q}_2} + 216.422\ \beta\ \dot{q}_1 + 43.358\ 10^6\ \mathrm{q_1} = 124.35610^{-6}\Omega^2 \sin\Omega\mathrm{t} \\ 155.0624\ \mathrm{\ddot{q}_2} + 37.0897\ \Omega\ \mathrm{\dot{q}_1} + 302.990\,\beta\ \dot{q}_2 + 52.015\ 10^6\ \mathrm{q_2} = 124.356\ 10^{-6}\Omega^2 \cos\Omega\mathrm{t} \end{cases} \quad (15)$$

- In the free-simply supported case,

$$\begin{cases} 98.126\ \mathrm{\ddot{q}_1} - 14.076\,\Omega\mathrm{\dot{q}_2} + 331.76\ \beta\dot{q}_1 + 86.21610^6\mathrm{q_1} = 80.12310^{-6}\Omega^2 \sin\Omega\mathrm{t} \\ 98.126\ \mathrm{\ddot{q}_2} + 14.076\ \Omega\mathrm{\dot{q}_1} + 464.4677\ \beta\dot{q}_2 + 99.486710^6\mathrm{q_2} = 80.12310^6\Omega^2 \cos\Omega\mathrm{t} \end{cases} \quad (16)$$

- In the free-free supported case,

$$\begin{cases} 2202.417\ \mathrm{\ddot{q}_1} - 181.992\ \Omega\mathrm{\dot{q}_2} + 2333.73\ \beta\dot{q}_1 + 89.50610^7\mathrm{q_1} = 13.2510^{-5}\ \Omega^2 \sin\Omega\mathrm{t} \\ 2202.417\ \mathrm{\ddot{q}_2} + 181.992\ \Omega\mathrm{\dot{q}_1} + 3267.22\ \beta\dot{q}_2 + 98.841210^7\mathrm{q_2} = 13.2510^{-5}\Omega^2 \cos\Omega\mathrm{t} \end{cases} \quad (17)$$

Any of the above systems of equations can be put in the form:

$$\begin{cases} m\ddot{q}_1 - a\,\Omega\,\dot{q}_2 + c_1\dot{q}_1 + k_1 q_1 = C\,\Omega^2 \sin \Omega t \\ m\ddot{q}_2 + a\,\Omega\,\dot{q}_1 + c_2\dot{q}_2 + k_2 q_2 = C\,\Omega^2 \cos \Omega t \end{cases} \tag{18}$$

## 3 Natural Frequencies and Campbell Diagrams

The study of the homogeneous solutions makes it possible to have the frequencies which make it possible to locate the critical speeds using the Campbell diagram. To do this we seek the solutions of the homogeneous system (without a second member), that is to say:

$$\begin{cases} m\,\ddot{q}_{h1} - a\,\Omega\,\dot{q}_{h2} + c_1\dot{q}_{h1} + k_1\,q_{h1} = 0 \\ m\,\ddot{q}_{h2} + a\,\Omega\,\dot{q}_{h1} + c_2\dot{q}_{h2} + k_2\,q_{h2} = 0 \end{cases} \tag{19}$$

Since it is a damped system we look for solutions of the form:

$$\begin{cases} q_{1h} = A_1 \exp\, rt \\ q_{2h} = A_1 \exp\, rt \end{cases} \tag{20}$$

After substitution of (19) in (20) we have equations that can be put in matrix form:

$$\begin{bmatrix} mr^2 + c_1 r + k_1 & -a\Omega r \\ a\Omega r & mr^2 + c_2 r + k_2 \end{bmatrix} \begin{Bmatrix} A_1 \\ A_2 \end{Bmatrix} = \begin{Bmatrix} 0 \\ 0 \end{Bmatrix} \tag{21}$$

The trivial solutions $A_1 = A_2 = 0$ are of no interest; we are therefore interested in non-trivial solutions which make the determinant equal to zero. To do this, we seek the values of r which cancel the determinant, namely:

$$m^2 r^4 + m(c_1 + c_2)r^3 + (k_1 m + k_2 m + a^2\Omega^2 + c_1 c_2)r^2 + (k_1 c_2 + k_2 c_1)r + k_1 k_2 = 0 \tag{22}$$

The roots of this equation are pairs of conjugate complex quantities of the form:

$$r_i = -\lambda_i \pm j\omega_i \tag{23}$$

where: $\omega_i$ and $\lambda_i$ are the ith frequency and the corresponding damping factor. The eigenvalue equations (det = 0) are then:

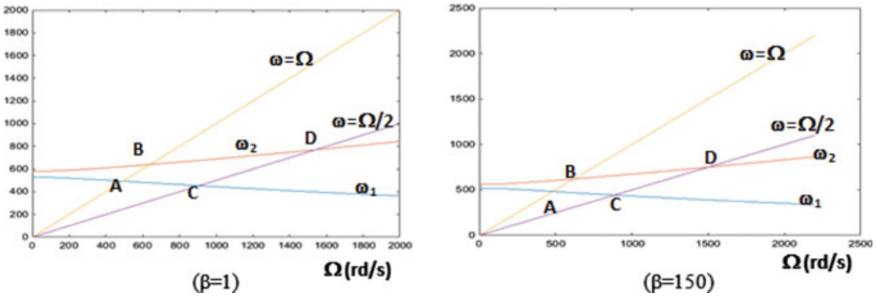

(β=1)

(β=150)

**Fig. 2** Simply-simply supported case

– In the simply-simply supported case:

$$24044.347r^4 + 80541.2713\beta r^3 + (1.478876.10^{10} + 1375.64\Omega^2 + 65573.70\,\beta^2)r^2 + 2.439.10^{10}\beta r + 2.255.10^{15} = 0$$

In the free-simply supported case:

$$9628.711876\,r^4 + 78130.63929\,\beta r^3 + (1.822.10^{10} + 198.1337\,\Omega^2 + 154091.804\,\beta^2)r^2 + 7.305.10^{10}\,\beta\,r + 8.5773.10^{15} = 0$$

In the free-free supported case:

$$48.506\,r^4 + 136.571.10^5\beta\,r^3 + (4.1482.10^{12} + 926.3318\;\Omega^2 + 90.25.10^5\beta^2)\,r^2 + 5.7680.10^{12}\beta\,r + 8.8468.10^{117} = 0$$

The roots of each equation have been determined numerically for values of β corresponding to different dampings. From these, the values of the frequencies which correspond to the imaginary parts are represented as a function of the rotation speed by the Campbell diagram (Figs. 2, 3 and 4).

## 4 Response to the Synchronous Force (Unbalance)

When we consider the presence of the force of excitation from the unbalances, the study of the particular solution is made by considering the system with the second member. It corresponds to the harmonic steady state with frequency Ω. It has the complex form:

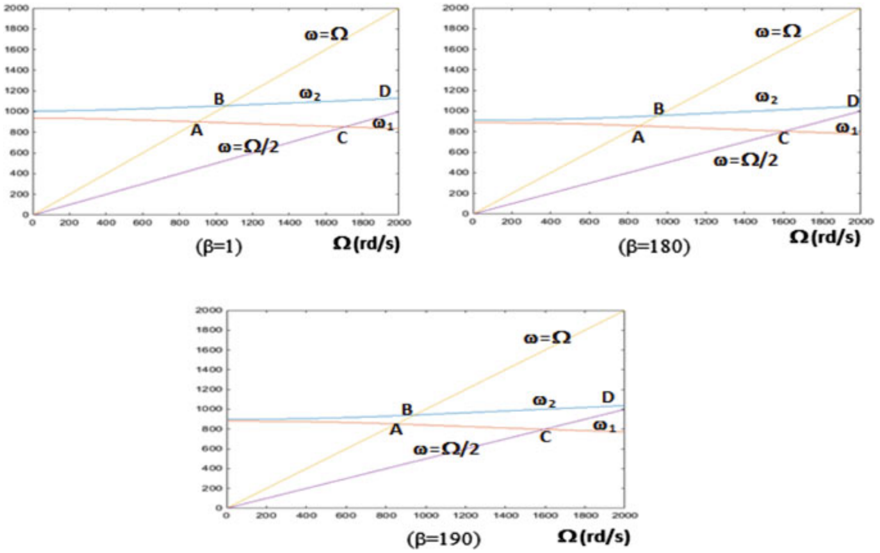

**Fig. 3** Free-simply supported case for different values of $\beta$

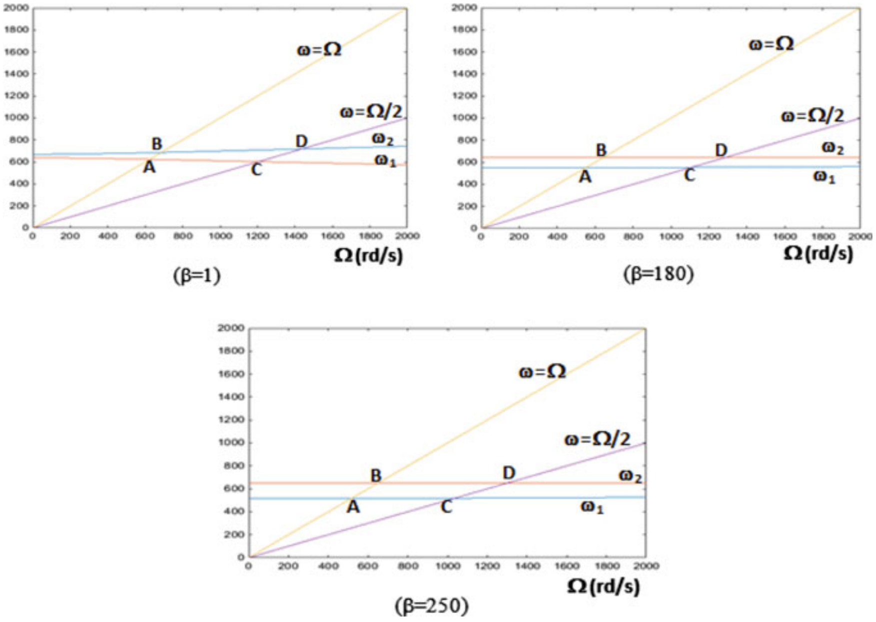

**Fig. 4** Free-free supported case for different values of $\beta$

$$\begin{cases} \underline{q}_{1p} = \underline{A}_{e1} \exp j\Omega t \\ \underline{q}_{2p} = \underline{A}_{e2} \exp j\Omega t \end{cases} \tag{24}$$

With: $\underline{A}_{e1} = A_{e1} \exp j\phi_{e1}$ and $\underline{A}_{e2} = A_{e2} \exp j\phi_{e2}$.
Its introduction in the complex inhomogeneous system:

$$\begin{cases} m\ddot{\underline{q}}_{1p} - a\Omega\dot{\underline{q}}_{2p} + c_1\dot{\underline{q}}_{1p} + k_1\underline{q}_{1p} = C\Omega^2 \exp j(\Omega t - \pi/2) \\ m\ddot{\underline{q}}_{2p} + a\Omega\dot{\underline{q}}_{1p} + c_2\dot{\underline{q}}_{2p} + k_2\underline{q}_{2p} = C\Omega^2 \exp j(\Omega t) \end{cases} \tag{25}$$

Yields:

$$\begin{bmatrix} k_1 - m\Omega^2 + jc_1\Omega & -ja\Omega^2 \\ ja\Omega^2 & k_2 - m\Omega^2 + jc_2\Omega \end{bmatrix} \begin{bmatrix} \underline{A}_{e1} \\ \underline{A}_{e2} \end{bmatrix} = \begin{bmatrix} C\Omega^2 \exp(-j\pi/2) \\ C\Omega^2 \end{bmatrix} \tag{26}$$

This last equation represents a linear system of two equations with two unknowns which are $\underline{\mathrm{A}}_{\mathrm{e1}}$ and $\underline{\mathrm{A}}_{\mathrm{e2}}$ with a parameter which is $\Omega$. The solutions depend on the latter and the determinant method gives:

$$\underline{A}_{e1} = \frac{-jC\Omega^2(k_2 - m\Omega^2 + jc_2\Omega) + jaC\Omega^4}{(k_1 - m\Omega^2 + jc_1\Omega)(k_2 - m\Omega^2 + jc_2\Omega) - a^2\Omega^4} \tag{27}$$

$$\underline{A}_{e2} = \frac{C\Omega^2(k_1 - m\Omega^2 + jc_1\Omega) - aC\Omega^4}{(k_1 - m\Omega^2 + jc_1\Omega)(k_2 - m\Omega^2 + jc_2\Omega) - a^2\Omega_4^4} \tag{28}$$

- In the simply-simply supported cas,

$$\underline{A}_{e1} = \frac{-j124.356.10^{-6}\Omega^2(52.015.10^6 - 155.0624\,\Omega^2 + j302.990\,\beta\Omega) + j24.14.10^{-4}\Omega^4}{(43.36.10^6 - 155.06\,\Omega^2 + j216.42\,\beta\,\Omega)(52.02.10^6 - 155.06\,\Omega^2 + j302.99\,\beta\,\Omega) - 1375.64\,\Omega^4}$$

$$\underline{A}_{e2} = \frac{124,356.10^{-6}\Omega^2(43,358.10^6 - 155,0624\,\Omega^2 + j216.422\,\beta\Omega) - 24.14.10^{-4}\Omega^4}{(43.35810^6 - 155.0624\,\Omega^2 + j216.42\,\beta\Omega)(52.01.10^6 - 155.06\,\Omega^2 + j302.99\,\beta\Omega) - 1375.64\Omega^4}$$

In the free-simply supported case:

$$\underline{A}_{e1} = \frac{-j80.12\ 10^{-6}\Omega^2(99.4867\,10^6 - 98.126\Omega^2 + j464.4677\beta\Omega) + j122.78.10^{-5}\Omega^4}{(86.22\,10^6 - 98.126\Omega^2 + j331.76\,\beta\Omega)(99.49\ 10^6 - 98.126\Omega^2 + j464.468\,\beta\Omega) - 198.14\Omega^4}$$

$$\underline{A}_{e2} = \frac{80,123.10^{-6}\Omega^2(86,216.10^6 - 98,126\Omega^2 + j331.76\,\beta\Omega) - 122.78.10^{-5}\Omega^4}{(86.216.10^6 - 98.126\Omega^2 + j331.76\,\beta\,\Omega)(99.4867.10^6 - 98.126\Omega^2 + j464.4677\,\beta\Omega) - 198.135\Omega^4}$$

- Free-free supported case:

$$\underline{A}_{e1} = \frac{-j13,27.10^{-5}\Omega^2(98.8412.10^7 - 2202.417\Omega^2 + j3867.22\,\beta\Omega) + j16.9.10^{-3}\Omega^4}{(89.81.10^6 - 2202.417\Omega^2 + j2333.73\beta\,\Omega)(98.84.10^7 - 2202.417\Omega^2 + j3867.22\,\beta\,\Omega) - 33121.69\,\Omega^4}$$

$$\underline{A}_{e2} = \frac{-j13.27\ 10^{-5}\Omega^2(89.5062\ 10^7 - 2202.42\Omega^2 + j2333.22\,\beta\,\Omega) - 16.9.10^{-3}\Omega^4}{(89.81.10^6 - 2202042\,\Omega^2 + j2333.73\,\beta\,\Omega)(98.84\ 10^7 - 2202.42\,\Omega^2 + j3867.22\,\beta\,\Omega) - 33121.69\,\Omega^4}$$

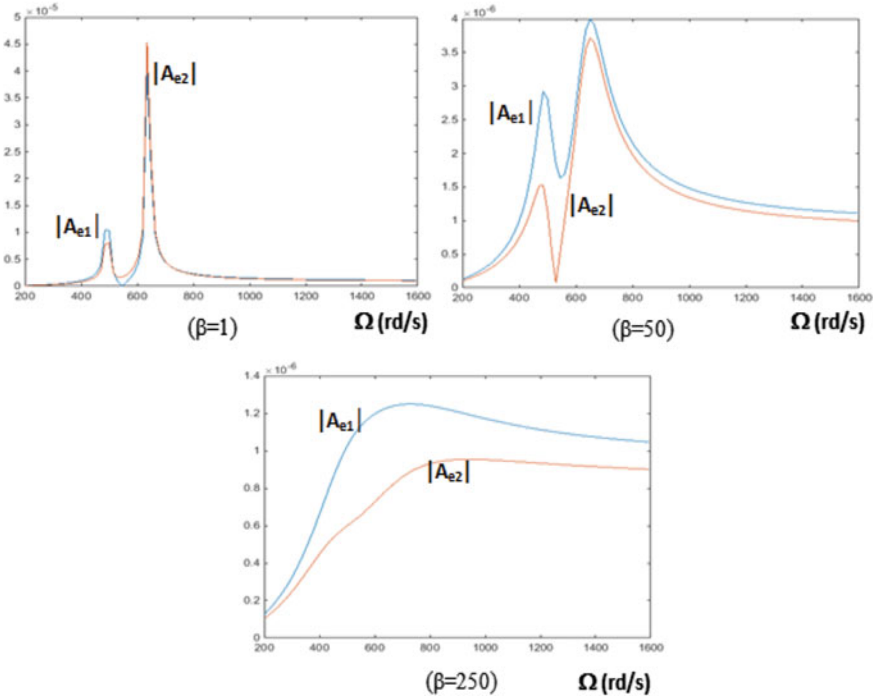

**Fig. 5** Simply-simply supported case

The modules of the complex amplitudes $\underline{A}_{e1}$ and $\underline{A}_{e2}$ are represented in Figs. 5, 6 and 7 for different values of the damping. It is clear that the peak of resonance decreases until it disappears with the increase in damping.

## 5 Response to an Asynchronous Force

The rotor can also be excited by an asynchronous force during its operation. Let us suppose a force that is acting on the rotor in $l_3$. It has a constant amplitude $F_0$ and speed $s\Omega$ different from that of the rotor. The equations to be solved are then:

$$\begin{cases} m\ddot{q}_1 - a\,\Omega\,\dot{q}_2 + k_1 q_1 + c_1\,\dot{q}_1 = F\sin s\Omega t \\ m\ddot{q}_2 + a\,\Omega\,\dot{q}_1 + k_2 q_2 + c_2\,\dot{q}_2 = F\cos s\Omega t \end{cases} \tag{29}$$

As for the synchronous force the particular solution corresponds to a harmonic steady state but with frequency $s\Omega$. It has than the complex form:

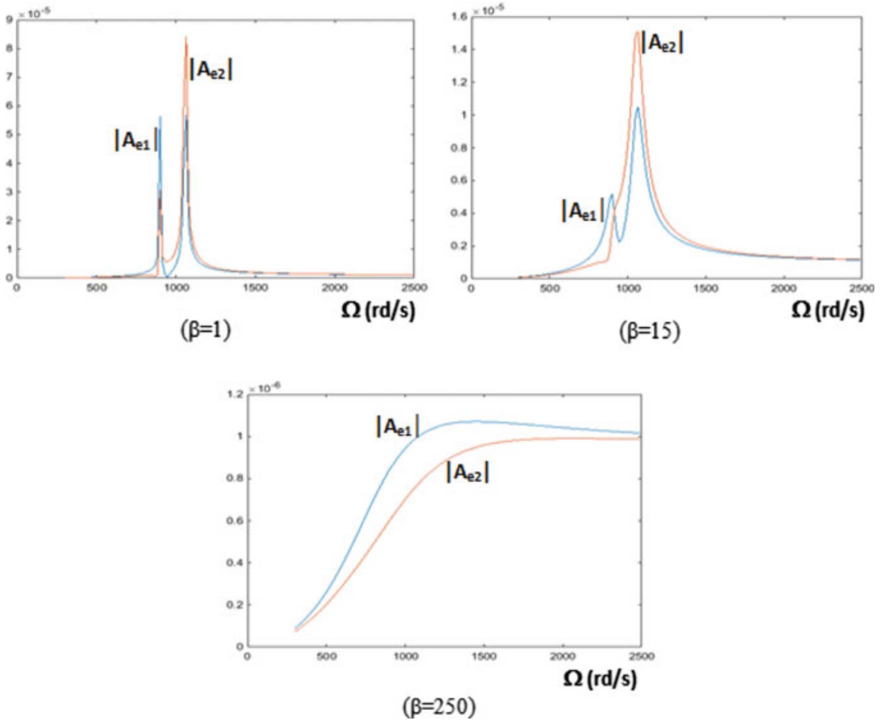

(β=1)

(β=15)

(β=250)

**Fig. 6** Free-simply supported case

$$\begin{cases} \underline{\mathrm{q}}_{1\mathrm{p}} = \underline{\mathrm{A}}_{\mathrm{e}1} \exp \mathrm{js}\Omega \mathrm{t} \\ \underline{\mathrm{q}}_{2\mathrm{p}} = \underline{\mathrm{A}}_{\mathrm{e}2} \exp \mathrm{js}\Omega \mathrm{t} \end{cases} \tag{30}$$

With: $\underline{A}_{e1} = A_{e1} \exp j\phi_{e1}$ and $\underline{A}_{e2} = A_{e2} \exp j\phi_{e2}$ and in the complex inhomogeneous system:

$$\begin{cases} m\ddot{\underline{q}}_{1p} - a\Omega\dot{\underline{q}}_{2p} + c_1\dot{\underline{q}}_{1p} + k_1\underline{q}_{1p} = F \exp j(s\Omega t - \pi/2) \\ m\ddot{\underline{q}}_{2p} + a\Omega\dot{\underline{q}}_{1p} + c_2\dot{\underline{q}}_{2p} + k_2\underline{q}_{2p} = F \exp j(s\Omega t) \end{cases} \tag{31}$$

To get:

$$\begin{bmatrix} k_1 - ms^2\Omega^2 + jc_1 s\,\Omega & -jas\Omega^2 \\ jas\,\Omega^2 & k_2 - ms^2\Omega^2 + jc_2 s\Omega \end{bmatrix} \begin{bmatrix} \underline{A}_{e1} \\ \underline{A}_{e2} \end{bmatrix} = \begin{bmatrix} F \exp(-j\pi/2) \\ F \end{bmatrix} \tag{32}$$

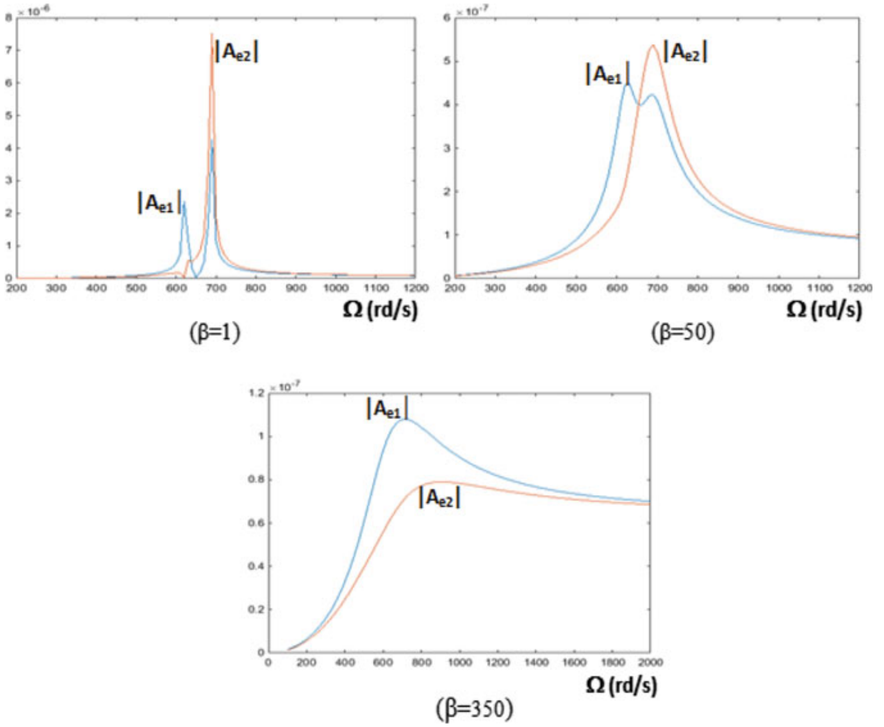

(β=1) (β=50)

(β=350)

**Fig. 7** Free-free supporte case

This last equation represents a linear system of two equations with two unknowns which are $\underline{A}_{e1}$ and $\underline{A}_{e2}$ with a parameter which is $\Omega$. The solutions depend on the latter and the determinant method which give us:

$$\underline{A}_{e1} = \frac{-jF(k_2 - ms^2\Omega^2 + jc_2s\Omega) + jasF\Omega^2}{(k_1 - ms^2\Omega^2 + jc_1s\Omega)(k_2 - ms^2\Omega^2 + jc_2s\Omega) - a^2s^2\Omega^4} \tag{33}$$

$$\underline{A}_{e2} = \frac{F(k_1 - ms^2\Omega^2 + jc_1s\Omega) - asF\Omega^2}{(k_1 - ms^2\Omega^2 + jc_1s\Omega)\cdot(k_2 - ms^2\Omega^2 + jc_2s\Omega) - a^2s^2\Omega^4} \tag{34}$$

And in function of the limit conditions, we get:

- In the simply-simply supported case

$$\underline{A}_{e1} = \frac{-jF(52.015\ 10^6 - 38.765\Omega^2 + j151.495\beta\Omega) + jF.18.81\Omega^2}{(43.39.10^6 - 38.765\Omega^2 + j108.21\beta\Omega)\cdot(52.02\ 10^6 - 38.765\Omega^2 + j151.49\beta\Omega) - 343.91\Omega^4}$$

$$\underline{A}_{e2} = \frac{F(43.36.10^6 - 38.76\Omega^2 + j108.21\beta\Omega) - F.18.81\Omega^2}{(43.36.10^6 - 38.76\Omega^2 + j108.21\beta\Omega)\cdot(52.015\ 10^6 - 38.765\Omega^2 + j151.495\beta\Omega) - 343.91\Omega^4}$$

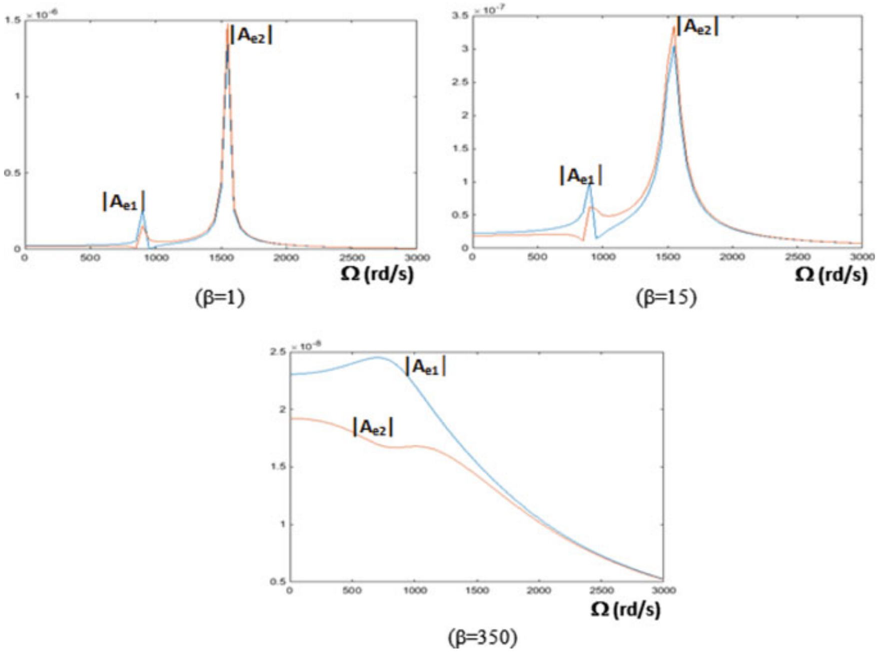

(β=1)

(β=15)

(β=350)

**Fig. 8** Simply-simply supported case

- In the free-simply supported case:

$$\underline{A}_{e1} = \frac{-jF(99,4867.10^6 - 24,5315\Omega^2 + j232.2338\,\beta\Omega) + jF.7.038\Omega^2}{(86.216.10^6 - 24.5315\Omega^2 + j165,88\beta\Omega)\cdot(99.4867\ 10^6 - 24.5315\Omega^2 + j232.2338\,\beta\Omega) - 49.5334\Omega^4}$$

$$\underline{A}_{e2} = \frac{F(86,216.10^6 - 24,5315\Omega^2 + j165.88\,\beta\Omega) - F.7.038\Omega^2}{(86.216.10^6 - 24.5315\Omega^2 + j165.88\,\beta\Omega)\cdot(99.4867.10^6 - 24.5315\Omega^2 + j232.2338\,\beta\Omega) - 49.5334\Omega^4}$$

In the free-free supported case:

$$\underline{A}_{e1} = \frac{-jF(98.8412\ 10^7 - 550.604\Omega^2 + j1933.61\beta\Omega) + jF.90.996\Omega^2}{(89.506.10^7 - 550.604\Omega^2 + j1166.865\beta\Omega)\cdot(98.8412.10^7 - 550.604\Omega^2 + j1933.61\beta\Omega) - 8280.27\Omega^4}$$

$$\underline{A}_{e2} = \frac{F(89,506.10^7 - 550,604\Omega^2 + j1166.865\beta\Omega) - F.90.996\Omega^2}{(89.506\ 10^7 - 550.604\Omega^2 + j1166.865\beta\Omega)\cdot(98.8412\ 10^7 - 550.604\Omega^2 + j1933.61\beta\Omega) - 8280.27\Omega^4}$$

The modules of the complex amplitudes $\underline{A}_{e1}$ and $\underline{A}_{e2}$ for $F = 1\,N$ are represented in Figs. 8, 9 and 10 for different damping values done for the synchronous case.

## 6 Conclusion

The purpose of the work presented by this paper is an investigation into the effect of boundary conditions as well as damping on the flexural vibrations behavior of a multidisc mono-rotor that we considered asymmetrical and damped. The modal

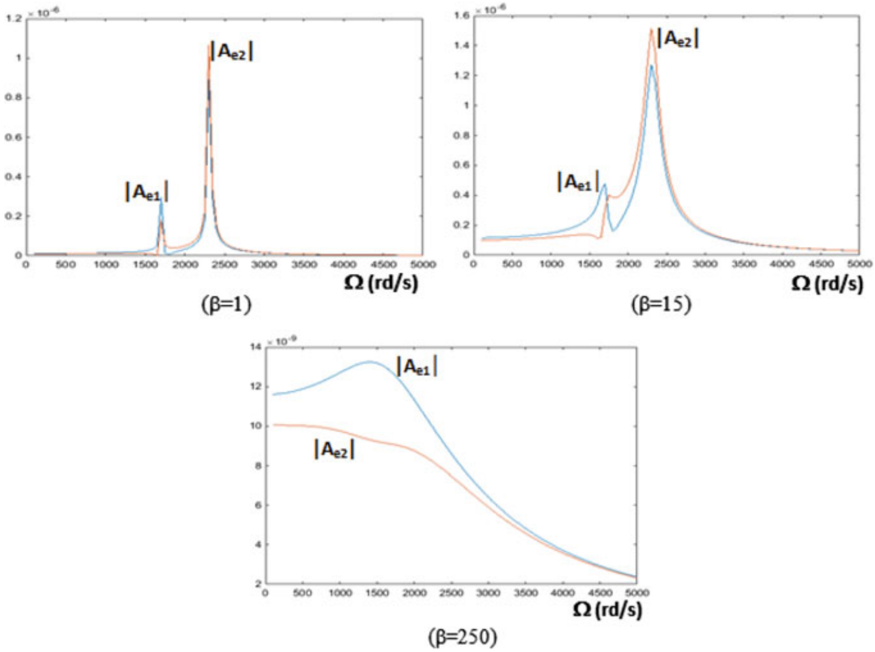

(β=1) (β=15)

(β=250)

**Fig. 9** Free-simply supported case

chosen is that of Lalanne and Ferraris which is chosen by a large number of people who use it in their research work. However, it happens that most of them consider the simplest displacement function taken by Lalanne and Ferraris that corresponds to the simply-simply supported boundary condition. Considering it as a questionable choice we examined for comparison the flexible rotor with the boundary conditions simply-simply supported as well as free -simply supported and free-free. As it was expected, the damping affects the amplitudes of the responses to the synchronous and asynchronous excitations. This means that we have to pay attention to the change of this one as for instance the degradation of oil viscosity in hydrodynamic bearings. But more importantly is the effect due the boundary conditions where the results obtained by the Campbell diagram as well as the responses to the synchronous and asynchronous forced show for the three cases a net difference of critical speeds where the resonance phenomenon may occurs. Therefore it is very important to put the right conditions and parameters in the dimensioning of rotating systems to improve their safety and their performance. Such as, for rotor on magnetic bearings we may choose the free-free boundary condition.

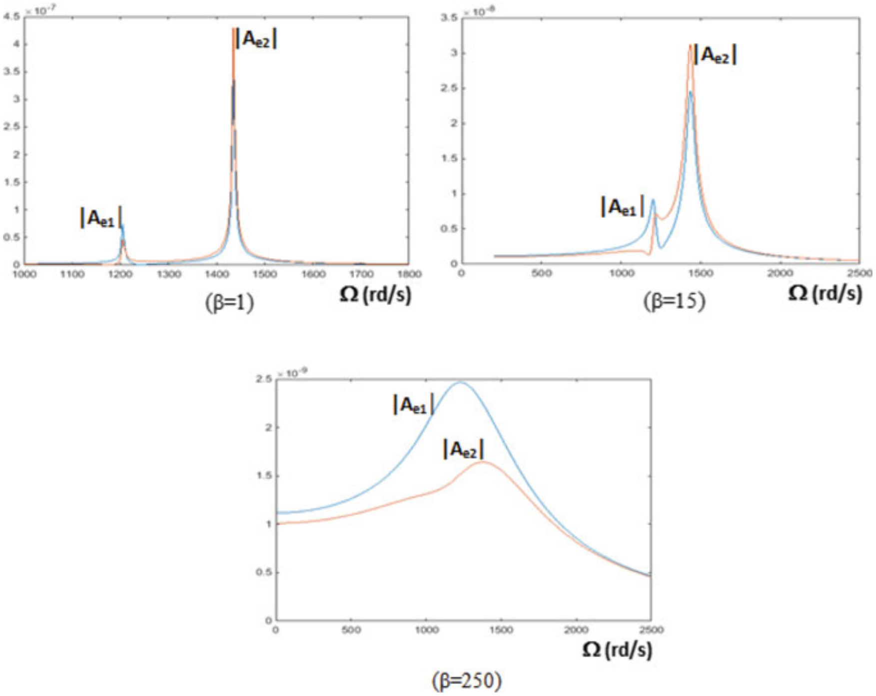

**Fig. 10** Free-free supported case

## References

Belahrache S, Necib B (2013) Flexural vibration of a multi disk rotor with different boundary conditions, Revue de l'Université de Constantine 1, Sciences & Technologie B—N°38, pp 15–24

Belahrache S, Necib B (2014) 5th international symposium on aircraft materials, ACMA

Lalanne M, Ferraris G (1998) Rotor dynamics prediction in engineering. Wiley

Lee C (1993) Vibration analysis of rotors. Kluwer Academic Publishers

Rao JS (1983) Rotor dynamics. Wiley, New York

Vance JM (1988) Rotordynamics of turbomachinery. Wiley, New York

# Remaining Life Estimation of the High Strength Low Alloy Steel Pipelines by Using Response Surface Methodology

**Djamel Zelmati, Oualid Ghelloudj, Mohamed Hassani and Abdelaziz Amirat**

## 1 Introduction

The finite element method has been used with great success in deterministic problems, but it is little used with once the uncertainties are taken into account, due to the relatively long computational time required to solve the problems. In most cases, the problem treated presents several difficulties such as a three-dimensional structure, non-linearity, singularity …, so the objective function is not explicit and a combination of finite element and reliability methods has been conducted through a response surface, where the finite element code is controlled by the probabilistic model. The quadratic response surface is the most used as the basis of approximation of the objective function because it is considered the most efficient in the coupling with the finite element method. The quadratic form of the response surface does not allow the resulting anomaly of the oscillation of the approximations, which limits the number of trials (Wong 1985; Ditlevsen and Madsen 1996; Lemaire 2013).

---

D. Zelmati (✉) · O. Ghelloudj · M. Hassani
Research Center in Industrial Technologies (CRTI), P.O. Box 64,
16014 Cheraga, Algiers, Algeria
e-mail: Zelmati_djamel@yahoo.fr

O. Ghelloudj
e-mail: Oualid.ghelloudj@gmail.com

D. Zelmati · O. Ghelloudj · A. Amirat
LRTAPM: Research Laboratory of Advanced Technology in Mechanical Production, Department of Mechanical Engineering, Faculty of Engineering Science,
Badji Mokhtar University Annaba, BP 12, 23000 Annaba, Algeria

T. Boukharouba et al. (eds.), *Computational Methods and Experimental Testing In Mechanical Engineering*, Lecture Notes in Mechanical Engineering,
https://doi.org/10.1007/978-3-030-11827-3_14

## 2 Theory

The reliability analysis is based on five steps (Amirat et al. 2009; Zelmati et al. 2017a, b):

- define the geometrical model,
- define the probabilistic model,
- define the objective function,
- assess the reliability index and variables sensitivities.

The approximation of the implicit limit state function by a polynomial representing a response surface will transform the limit state function from its implicit to explicit form, and reduced their calls number.

The general form of the approximation of the objective function $G(X)$ in the space of n random factors $x_i$ can be expressed by the polynomial (1) (Wong 1985).

$$g(x) = c_0 + \sum_{i=1}^{n} c_i x_i + \sum_{i=1}^{n} c_{ii} x_i^2 \tag{1}$$

where $c_0$, $c_i$ and $c_{ii}$ are constants to be determined and n is the number of the random variables of the mechanical model.

The polynomial $G(X)$ is defined by at least a number of points $N_p$ in order to determining the constants as expressed by Eq. (2):

$$N_p = \frac{(n+1)(n+2)}{2}. \tag{2}$$

## 3 Experimental Procedure

Fifteen specimens for tensile tests have been prepared from an *X70* steel pipe in the longitudinal direction of the base metal according to the *API 5L* standards. Tensile tests were carried out at room temperature in order to determine the mechanical material properties. Statistical analysis is done in order to sort out the probabilistic distribution of the mechanical properties that will be used in reliability estimation (Zelmati et al. 2017a, b).

## 4 Results and Discussion

The *HSLA* steel pipe used in this work is an *API X70* steel grade, produced and provided by THYSSEN Company in the form of coils obtained by rolling, and the pipe will be fabricated in a forming cage. It is very interesting to model this

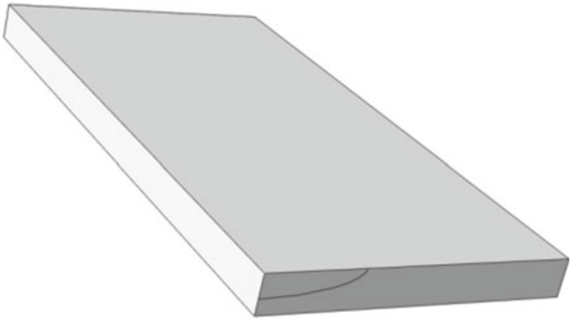

**Fig. 1** Semi elliptical crack in a rectangular plate

rectangular plate under a crack or notch defect. In this paper, the flat specimen is subjected to uniform tensile stress and has a semi-elliptic crack with a defect depth to wall thickness ratio, $a/t = 60\%$ and a defect depth to defect length ratio, $a/L = 0.12$ (Fig. 1).

## *4.1 Meshing of the Rectangular Plate*

For symmetry reasons, only one quarter of the plate has been modeled and the boundary conditions are shown in Fig. 2. The semi elliptical defect in the rectangular plate is modeled and meshed as illustrated in Fig. 3 and the commercial code used is ABAQUS software *Vs11*. The shape of the element used is bloc, the meshing is *HEX*, the meshing technique is structured and the element type of linear brick with 8 nodes is adopted.

For the crack meshing, the shape Wedge is attributed and the technique Sweep is used. The partition on the crack tip is modeled with the HEX shape and the technique is structured.

As illustrated in Fig. 4, the evolution of the stress intensity factor $K_I$ as a function of the applied stress to yield stress ratio, is assessed by finite element method, are compared to the results obtained by Raju and Newman (1979), Toshio and Parks (1992), the average relative error is within 5%.

Figure 5 illustrates the effect of the normalized applied stress on the J integral, for the *API X70* steel plate with a semi-elliptical surface crack. The elastics values of J integral are deducted directly from the stress intensity factor values as expressed by Eq. (3):

$$J_I = \frac{K_I^2}{E} \tag{3}$$

The relative error for the assessment of *J* integral by using finite element method comparing to Raju Newman is multiplied by factor 2, when comparing to the *J* integral, estimated from the stress intensity factor values, so the relative error is about 10%.

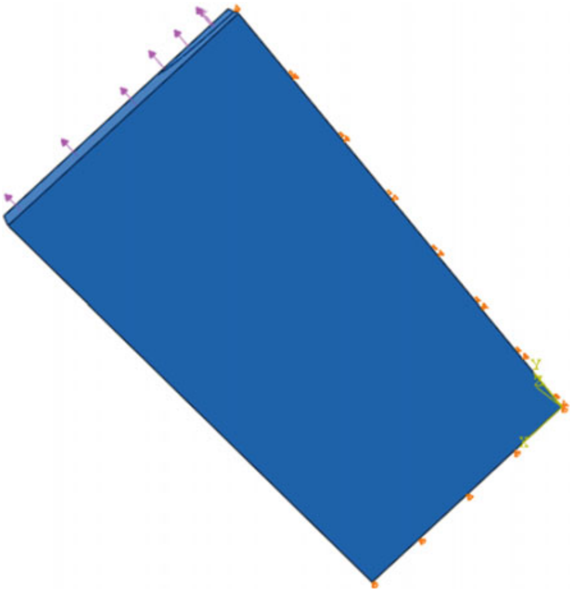

**Fig. 2** Boundary conditions of the cracked plate

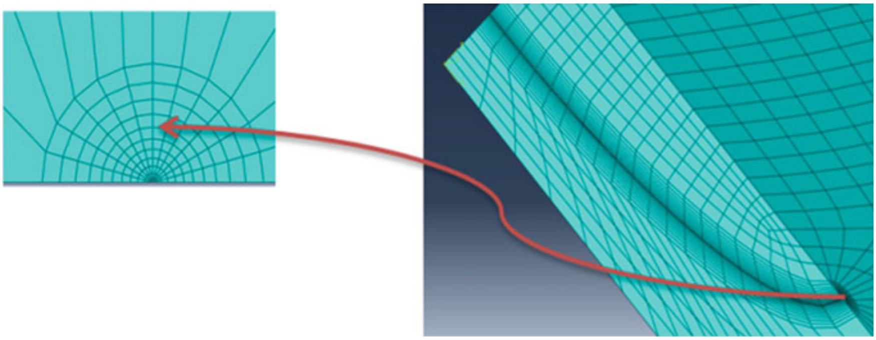

**Fig. 3** Meshes of the FEM model using ABAQUS Software

## 4.2 *T Stress Along the Ligament*

The effect of the applied tensile stress, on the *T stress*, is illustrated in Fig. 6, for the same defect configuration shown in Fig. 1 ($a/t = 60\%$). The values of the second Williams term are significant within the ligament length near of the crack tip. The assessment of *T stress* en mode I is illustrated in Fig. 7, for an applied tensile stress to yield stress ratio of 10%, shown a pic of the confinement of the plasticity on the crack tip. After, this maximum value decrease and stabilize on the outside of the ligament (Raju and Newman 1979; Toshio and Parks 1992; Wang 2003; Bouledroua et al. 2016, 2017).

**Fig. 4** Stress intensity factor $K_I$ as a function of applied stress to yield stress ratio

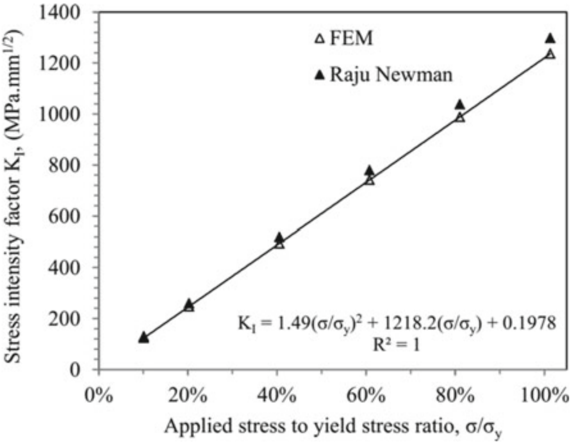

**Fig. 5** Effect of the applied stress to yield stress ratio on the J integral

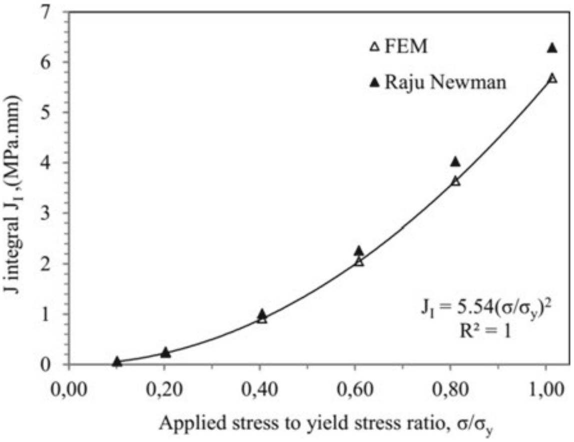

**Fig. 6** T-stress evolution as a function of the applied stress to yield stress ratio

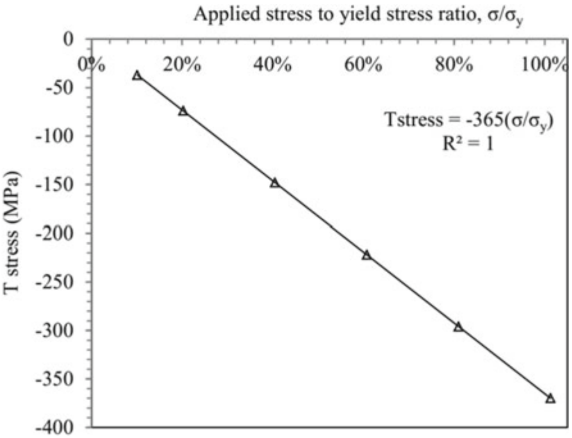

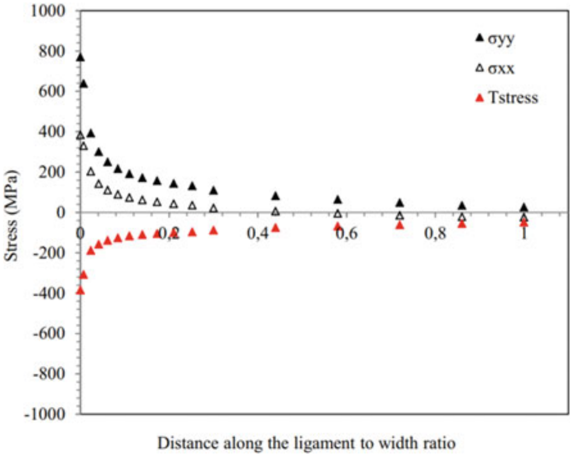

**Fig. 7** Stress distribution within the ligament

As shown in Fig. 6, for the *API X70* steel plate, in the semi elliptical crack tip zone (*a/t* = 60%), the T stress within the ligament is a compressive stress (negative stress). Therefore, the crack propagation direction is considered stable, and the fracture mode is the opening mode.

A *3D* finite element method analysis is carried out by authors of references (Raju and Newman 1979; Toshio and Parks 1992; Wang 2003) in order to assess the T stress, in plate with a semi elliptical crack under tensile or bending stress within the ligament for a crack depth to wall thickness ratio from 20 to 80%, and for different crack length. Therefore, the coupling of the *T stress* and stress intensity factor or the *J* integral results, could be considered as a constraint parameter during the fracture analysis.

## 4.3 Limit State Function for Reliability Analysis

The limit state function which separates the safe region $G(X_j) > 0$, from the failure region $G(X_j) < 0$, is considered to estimate the reliability of semi elliptical cracked plate, where $X_j$ are the random variables in the system. The limit state function is expressed by the implicit Eq. (4):

$$G = J_{Ic} - J_I \tag{4}$$

$J_{Ic}$ is the tenacity of the material *API X7*0 is estimated to be 44.5 MPa.mm basing on the Charpy V notch tests (Zelmati et al. 2017a) and $J_I$ is estimated by finite element method.

According to above Eq. (5), the material is considered on security if the *J* integral $J_I$, estimated by finite element method, for all applied tensile stress to yield stress

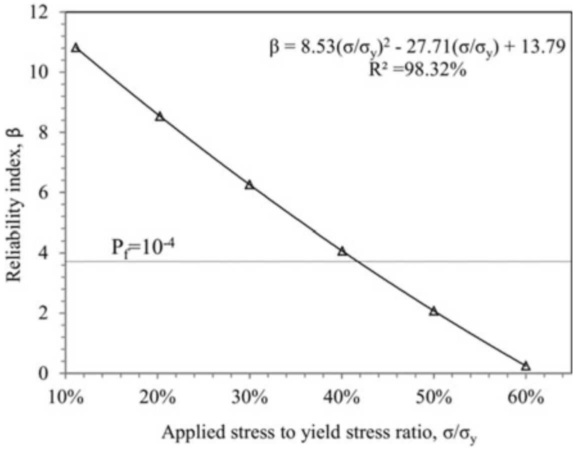

**Fig. 8** Effect of the applied stress to yield stress ratio on the reliability index β

ratio of the *API X70* is less than the tenacity $J_{IC}$ of the steel plate. The *J* integral is a function of the random variables: elastic modulus E, the charge factor *K*, the hardening coefficient n and the yield stress $\sigma_y$ as expressed in Eq. (5):

$$G = J_{Ic} - J_I\big(E, \sigma_{\mathrm{y}}, \mathrm{K}, \mathrm{n}\big). \tag{5}$$

Figure 8 illustrates the effect of the normalized applied tensile stress to yield stress ratio, of the semi elliptical cracked plate, on the reliability index β. The results were assessed by the indirect combination of the finite element method and the probabilistic model, basing on a quadratic response surface. The steel plate is considered reliable if the applied tensile stress to yield stress ratio is lower than 39%, that's to say, the applied stress is lower than 195 MPa and the security factor is estimated to be 2.5 higher than the conventional value 2. This curve could be considered as a power decision tool for maintenance program.

## 5 Conclusion

In this paper, the response surface methodology is developed by coupling the finite element method with a reliability model. The stress intensity factor and the *J* integral were estimated within the remaining ligament of the steel plate in order to estimate a quadratic response surface. The assessment of the reliability index and the probability of failure were carried out by the indirect coupling of the finite element method and the probabilistic model. This estimation may be considered as a power tool for decision and maintenance program.

**Acknowledgements** This work is partially supported by ALFAPIPE ANNABA Company for the furniture of the materials and experimental tests. The authors also gratefully acknowledge the helpful comments and suggestions of the reviewers, which have improved the presentation.

## References

Amirat A, Benmoussat A, Chaoui K (2009) Reliability assessment of underground pipelines under active corrosion defects. Damage and fracture mechanics. Springer, Netherlands, pp 83–92

Bouledroua O, Meliani MH, Pluvinage G (2016) A review of T-stress calculation methods in fracture mechanics computation. Nat Tech 15:20

Bouledroua O, Meliani MH, Azari Z, Sorour A, Merah N, Pluvinage G (2017) Effect of sandblasting on tensile properties, hardness and fracture resistance of a line pipe steel used in Algeria for oil transport. J Fail Anal Prev 17(5):890–904

Ditlevsen O, Madsen HO (1996) Structural reliability methods, vol 178. Wiley, New York

Lemaire M (2013) Structural reliability. Wiley, New York

Raju IS, Newman JC (1979) Stress-intensity factors for a wide range of semi-elliptical surface cracks in finite thickness plates. Eng Fract Mech 11(4):817–829

Toshio N, Parks DM (1992) Determination of elastic T-stress along three-dimensional crack fronts using an interaction integral. Int J Sol Struct 29(13):1597–1611

Wang X (2003) Elastic T-stress solutions for semi-elliptical surface cracks in finite thickness plates. Eng Fract Mech 70(6):731–756

Wong FS (1985) Slope reliability and response surface method. J Geot Eng 111(1):32–53

Zelmati D, Ghelloudj O, Amirat A (2017a) Correlation between defect depth and defect length through a reliability index when evaluating of the remaining life of steel pipeline under corrosion and crack defects. Eng Fail Anal 79:171–185

Zelmati D, Ghelloudj O, Amirat A (2017b) Reliability estimation of pressurized API 5L X70 pipeline steel under longitudinal elliptical corrosion defect. Int J Adv Manfact Tech 90(9–12):2777–2783

# Implementation and Experimentation of (VSI) Applied for a Photovoltaic System

**K. Baali, S. Saad, Y. Menasriya and F. Zaamouche**

## 1 Introduction

Actually, energy sources and the increase of the greenhouse effect are the present issues. Many research works are carried out on the use of renewable energies to overcome these problems. Among these energies, photovoltaic (*PV*) energy produced by photovoltaic panels.

The main concern is the production of electrical energy by this technique and panels (*PV*) optimum operation. This has lead to the elaboration of electronic devices enabling to use efficiently these alternative sources. Devices such as inverters designed to convert a $d_c$ voltage to a desired $a_c$ voltage and current with variable frequency become a very important element of energy conversion system a general overview of different types of *PV* inverter is given (Messenger and Ventre 2004; Daher et al. 2008; Selvaraj and Rahim 2009). The efficiency of these converters depends on the control strategy of the switches used to generate the desired output voltage and current with less harmonic distortion.

There are various electronic controllers used to control the inverters switches, such as analogue and digital controllers, microcontrollers and microcomputers (El-Hefnawi 1997; Rodrigues et al. 1979; Melkhilef et al. 2002; Selvaraj and Rahim 2009; Chouder et al. 2008). These controllers can be used to improve inverter performances to avoid photovoltaic (*PV*) system failure. A *dSPACE* system is recently applied to control the inverter switches and can be extended to photovoltaic systems (Li et al. 2006; Sefa et al. 2008; Gonzalez et al. 2008; Zamre et al. 2010; Hannan et al. 2010; Vijayalakshmi et al. 2012).

---

K. Baali (✉) · S. Saad · Y. Menasriya · F. Zaamouche
Laboratoire Systèmes Electromécaniques (LSELM), Badji Mokhtar University Annaba, Annaba, Algeria
e-mail: baalikheira23@yahoo.fr

S. Saad
e-mail: saadsalah2006@yahoo.fr

T. Boukharouba et al. (eds.), *Computational Methods and Experimental Testing In Mechanical Engineering*, Lecture Notes in Mechanical Engineering,
https://doi.org/10.1007/978-3-030-11827-3_15

In this paper, the *PV* system mathematical model describing the operation of each element is given. The developed model of photovoltaic panels, dc-dc converter and dc-ac inverter along with *MPPT* control algorithm are simulated. Moreover, the simulation and real time implementation of a space vector pulse-width modulation (*SVPWM*) control scheme is performed to demonstrate the high performance of the photovoltaic inverter when *dSPACE* is used as controller. The simulations and experiments are carried out in Simulink/MATLAB environment and *dSACE1104* in real time implementation, respectively.

In this work SVPWM inverter is used, replacing the conventional two-level sinusoidal pulse width-modulation (*SPWM*) inverter because it offers great advantages, such as improved output waveforms, lower electromagnetic interference, less harmonic distortion (*THD*). The results of the open loop operation have showed that *SVPWM* technique has high performances in harmonics current reduction, torque and speed time response. The experimental waveforms such as ac output voltages, current and total harmonic distortion are presented and analyzed.

# 2 Theory

## 2.1 Photovoltaic Generator Model

The so-called photovoltaic generator is the energetic sub-system located at the beginning of the system producing a $d_c$ electrical energy by photovoltaic conversion of illumination. The conventional equivalent circuit of the solar cell represented by a courant source in parallel to one or two diodes is shown in Fig. 1. The model is developed on the basis of a circuit composed from a photo-current source, a diode in parallel to the source, a series resistor $R_s$ and a shunt resistor $R_p$ and additional diode for better adjustment of the curves. This model requires the knowledge of four parameters at standard conditions of illumination and temperature. These parameters are given usually by the manufacturer or obtained by tests.

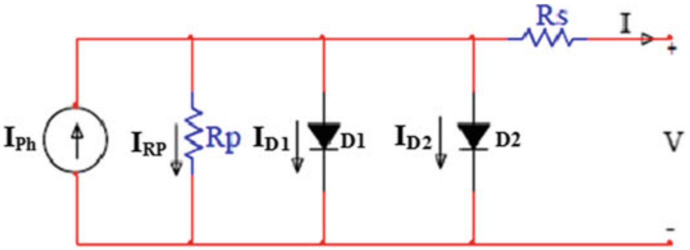

**Fig. 1** Cell equivalent circuit of two diodes circuits

Solar cell equivalent circuit used in this study is simplified by neglecting the shunt resistor. The relation of the current in function of voltage can be expressed approximately by Eqs. 1 and 2.

$$I = I_{CC}\left[1 - C_1\left(\exp\left(\frac{v}{C_2 v_{CO}}\right) - 1\right)\right] \tag{1}$$

where:

$$C_1 = \left(1 - \frac{I_{mp}}{I_{CC}}\right)\exp\left(\frac{-v_{mp}}{c_2 v_{CO}}\right) \tag{2}$$

$$C_2 = \frac{\frac{v_{mp}}{v_{co}} - 1}{\ln\left(1 - \frac{I_{mp}}{I_{CC}}\right)} \tag{3}$$

For other illuminations intensity $G$ (W/m$^2$) and temperatures $T$ (°C), the model shifts any point ($V_{ref}, I_{ref}$) of the curves of (Rodrigues et al. 1979; El-Hefnawi 1997; Messenger and Ventre 2004; Daher et al. 2008; Selvaraj and Rahim 2009) to a new point ($V$-$I$) (*V: Voltage*, *I: Current*) on the basis of Eqs. 4 and 8.

$$\Delta T = T - T_{ref} \tag{4}$$

$$\Delta I = \alpha\left(\frac{G}{G_{ref}}\right)\Delta T + \left(\frac{G}{G_{ref}} - 1\right)\mathrm{I_{CC}} \tag{5}$$

$$\Delta V = -\beta\,\Delta T - R_S I \tag{6}$$

$$I_{new} = I_{ref} + \Delta I \tag{7}$$

The effect of illumination on current-voltage and power—voltage characteristics of $PV$ panel at $T = 25$ °C are presented respectively in Figs. 2 and 3.

$$V_{new} = V_{ref} - \Delta V \tag{8}$$

## 2.2 Modeling and Control of Dc-Dc Converter

The $d_c$-$d_c$ converter is used to elevate the voltage produced by $PV$ cells for the application requiring high voltages. Thus, this converter is called Boost converter and is illustrated in Fig. 4a. The operation of the $\mathrm{d_c}$-$\mathrm{d_c}$ boost converter is as follows:

$$\text{If, } S = 0 \text{ the diode is on and the IGBT is off}$$

$$S = 1 \text{ the diode is off and the IGBT is on}$$

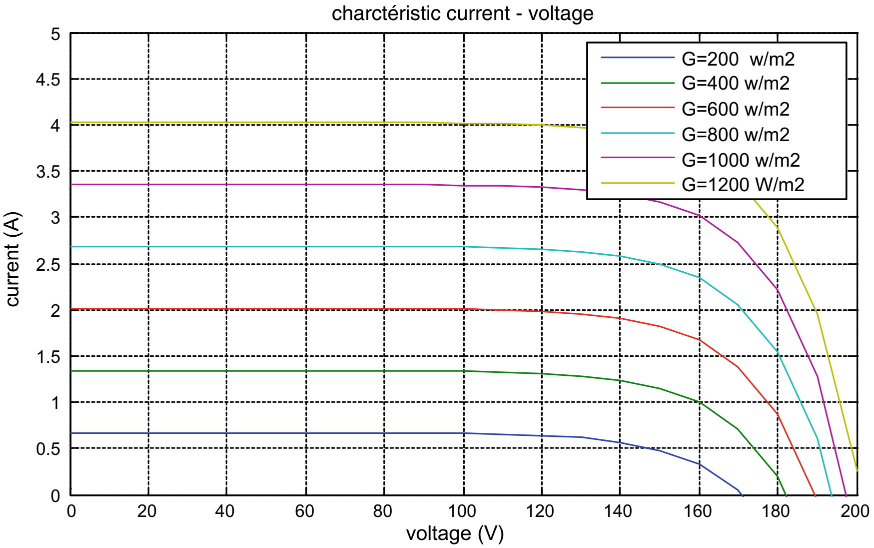

**Fig. 2** Effect of illumination on current-voltage (I-V) characteristic of PV panel at T = 25 °C

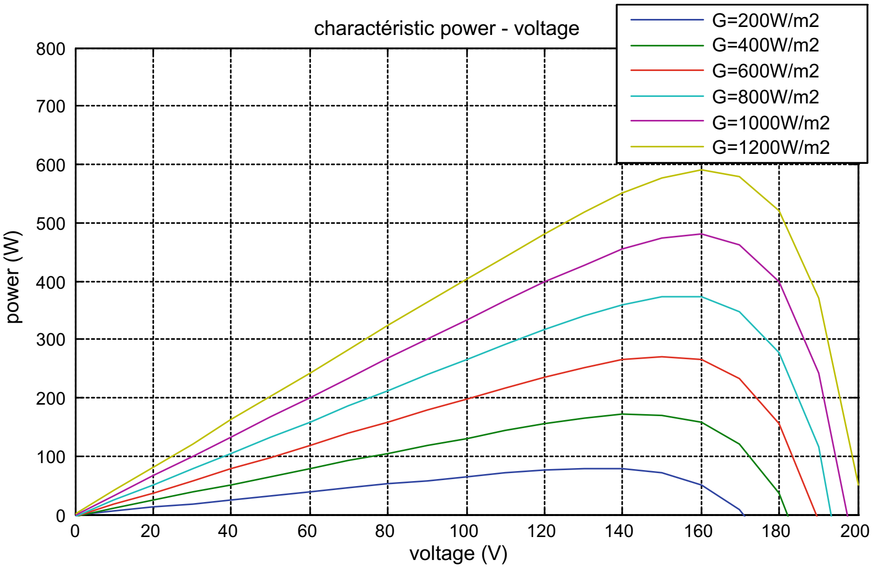

**Fig. 3** Effect of illumination on power-voltage (P-V) characteristic of PV panel at T = 25 °C (power produced by a panel)

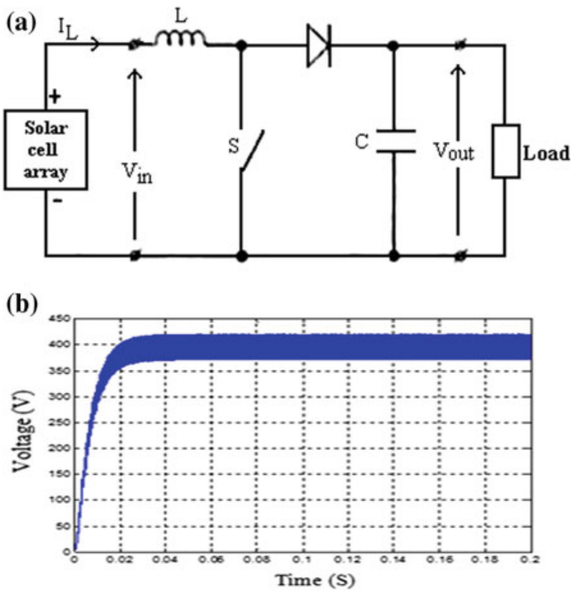

**Fig. 4** **a** Synoptic diagram of $d_c$-$d_c$ boost converter, **b** voltage output of the converter

The following equations can be derived:

$$V_{pv} t_{on} = \left(V_{out} - V_{pv}\right) \mathrm{t}_{\mathrm{off}} \tag{9}$$

$$V_{out} = \frac{t_{on} + t_{off}}{t_{off}} V_{pv} \tag{10}$$

$$T = t_{on} + t_{off} \tag{11}$$

$$V_{out} = \frac{V_{pv}}{1 - \alpha} \tag{12}$$

$$\alpha = \frac{t_{on}}{T} \tag{13}$$

The obtained output voltage $V_{out}$ of the boost converter is shown in Fig. 4b.

The input voltage is 150 V representing the *PV* output voltage ($V_{out}$). This voltage is elevated to 400 V by $d_c$-$d_c$ converter as illustrated in Fig. 4b and is composed from an inductance ($L_1$), (*IGBT*) commutation circuit and their *MPP*T control and a diode. It appears at capacitor terminals *C* and acts as inverter input voltage. The voltage calculation is explained by the expressions presented below:

$$V_{out} = \frac{V_{in}}{1 - K}, V_{out} = \frac{150}{1 - 0.86}, V_{out} = 400\,\mathrm{V}.$$

Then, the inverter converts to ac voltage waveform using space vector pulse width modulation as control strategy.

## 2.3 Inverter Model

The inverter is the most important part of this work therefore, it is necessary to present a description of the inverter and the development of its model. Figure 5 illustrates the topology of a conventional three phase inverter used in this work. The switches of the same arm must not be on at the same time to avoid the source to be short circuited.

Its operation is based on *SVPWM* control technique to control the switches in order to obtain a waveform with a desired frequency. The *PWM* voltage source inverter with six *IGBTs* shown in Fig. 5 is often used for this kind of application. The load is modeled from the line to neutral voltages $V_{an}$, $V_{bn}$ and $V_{cnand}$ the inverter switches are controlled as follows:

Considering $K_{i1}$ and $K_{i2}$ as transistors of each arm with $i = a$, $b$ and $c$ defining the phases.

If $K_{i1} = 1$, thus $K_{i1}$ is on and $K_{i2}$ is off
If $K_{i2} = 0$, thus $T_{i1}$ is off and $T_{i2}$ is on.

The line to line voltages are obtained from the inverter output and can be expressed as follows:

$$\begin{bmatrix} V_{ab} = V_{an0} - V_{bn0} \\ V_{bc} = V_{bn0} - V_{cn0} \\ V_{ca} = V_{cn0} - V_{an0} \end{bmatrix} \tag{14}$$

Lines to neutral voltages of the load derived from the line to line voltages have a sum equal to zero thus:

$$\begin{bmatrix} V_{an} = (1/3)\ [V_{ab} - V_{ca}] \\ V_{bn} = (1/3)\ [V_{bc} - V_{ab}] \\ V_{cn} = (1/3)\ [V_{ca} - V_{bc}] \end{bmatrix} \tag{15}$$

**Fig. 5** Inverter topology

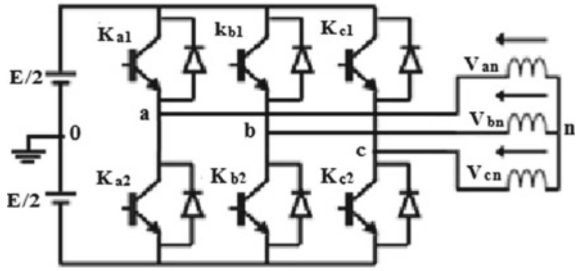

They can be obtained from the inverter output voltages by introducing the neutral to line voltage of the load in relation to reference point no (Melkhilef et al. 2002; Chouder et al. 2008).

$$\begin{bmatrix} V_{an} + V_{nn0} = V_{an0} \\ V_{bn} + V_{nn0} = V_{bn0} \\ V_{cn} + V_{nn0} = V_{cn0} \end{bmatrix} \tag{16}$$

Therefore, it can be concluded:

$$V_{nn0} = \left(\frac{1}{3}\right)[V_{an0} + V_{bn0} + V_{cn0}] \tag{17}$$

The switches are considered as ideal then if ($i = a$, $b$ and $c$) thus:

$$V_{in0} = KiE - \frac{E}{2} \tag{18}$$

The following matrix is obtained:

$$\begin{bmatrix} V_{an0} = (S_a - 0.5)E \\ V_{bn0} = (S_b - 0.5)E \\ V_{cn0} = (S_c - 0.5)E \end{bmatrix} \tag{19}$$

Substituting (17) in (19) the equation below is obtained:

$$\begin{bmatrix} V_{an} = \frac{2}{3}V_{an0} - \frac{1}{3}V_{bn0} - \frac{1}{3}V_{cn0} \\ V_{bn} = -\frac{2}{3}V_{an0} + \frac{1}{3}V_{bn0} - \frac{1}{3}V_{cn0} \\ V_{cn} = -\frac{2}{3}V_{an0} - \frac{1}{3}V_{bn0} + \frac{1}{3}V_{cn0} \end{bmatrix} \tag{20}$$

Substituting (6) in (7) the following expression is obtained:

$$\begin{bmatrix} V_{an} \\ V_{bn} \\ V_{cn} \end{bmatrix} = \frac{1}{3}E \begin{bmatrix} 2 & -1 & -1 \\ -1 & 2 & -1 \\ -1 & -1 & 2 \end{bmatrix} \begin{bmatrix} S_a \\ S_b \\ S_c \end{bmatrix} \tag{21}$$

In recent years, several pulse width modulation (*PWM*) techniques were developed and studied. Two techniques were given a great interest mainly; sinusoidal pulse width modulation (*SPWM*) and space vector modulation (*SVPWM*) in this work a *SVPWM* is used for its efficiency and simplicity.

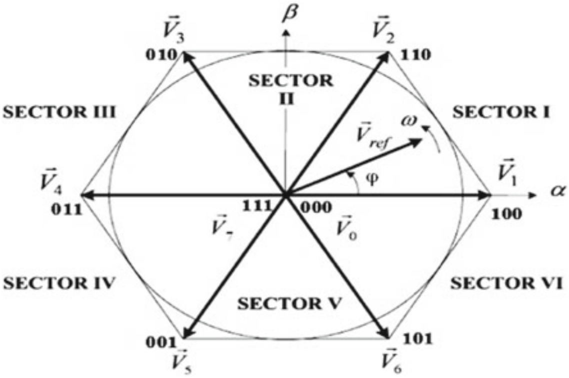

**Fig. 6** Inverter voltage vectors representation

## 2.4 Theory of SVPWM Technique

The *SVM* technique was developed for space vector electrical machines control. Its principle is to rebuild the reference vector $\vec{V}_{ref}$ from different voltage vectors (El-Hefnawi 1997; Rodrigues et al. 1979; Daher et al. 2008). Each vector corresponds to a combination of a three phase inverter switches states. The *SVPWM* technique processes the signals directly on the diphase frame of the Concordia transformer. Thus, the line to neutral voltages $v_{an}$, $v_{bn}$ and $v_{cn}$ at the inverter output is represented in the $(\alpha, )$ frame by the following equations:

$$\begin{bmatrix} v_\alpha \\ v_\beta \end{bmatrix} = \sqrt{\frac{2}{3}} \begin{bmatrix} 1 & -\frac{1}{2} & -\frac{1}{2} \\ 0 & \frac{\sqrt{3}}{2} & -\frac{\sqrt{3}}{2} \end{bmatrix} \begin{bmatrix} v_{an} \\ v_{bn} \\ v_{cn} \end{bmatrix} \tag{22}$$

From the combination of the three state variables ($C_a$, $C_b$ and $C_c$), the inverter has eight switching states. It can generate eight different vectors of voltage output. These eight space vectors define the limits of the six sectors in the $(\alpha, \beta)$ frame as illustrated in Fig. 6. Two of these vectors equal to zero $\vec{V}_0(000)$ and $\vec{V}_7(111)$. Recalling that:

- $C_i = 1$: Upper switch is on and the lower is off,
- $C_i = 0$: Upper switch is off and the lower is on.

Reference voltage vector $\vec{V}_{ref}$ can be defined in the $(\alpha, \ \beta)$ frame by:

$$\vec{V}_{ref} = \vec{v}_\alpha + j\vec{v}_\beta \tag{23}$$

$$\varphi = 2\pi f$$

$\varphi$: The instantaneous angle of the reference vector
$f$: Fundamental frequency of inverter output parameters

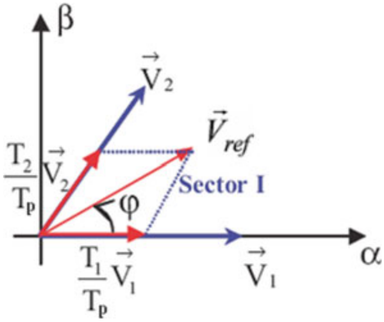

**Fig. 7** Projection of reference vector in sector I

Then, the reference vector $\vec{V}_{ref}$ is approximated during one sampling period by adjacent vectors $\vec{V}_j$, $\vec{V}_{j+1}$ and $\vec{V}_0$, or $\vec{V}_7$ ($j = 1, \ldots, 5$) corresponding to the eight possible inverter switches states. The symmetrical three phase system enables to limit the study to a general case where the reference vector $\vec{V}_{ref}$ is located in the sector 1 of $\pi/3$ radians as shown in Fig. 7.

Thus, the following equation is obtained:

$$T\vec{V}_{ref} = T_1\vec{V}_1 + T_2\vec{V}_2 + T_0\vec{V}_0\left(\text{or } \vec{V}_7\right) \tag{24}$$

- $\vec{V}_0$ and $\vec{V}_7$ are the zero vectors: $\vec{V}_0 = \vec{V}_7 = \vec{0}$,
- $T_p$: Modulation period, $T_p = 1/f_p, f_p$: Modulation frequency, $T_1$: Time attributed to vector $\vec{V}_1$, $T_2$: Time attributed to vector $\vec{V}_2$, $T_0$: time shared by $\vec{V}_0$ and $\vec{V}_7$.

Solving Eq. (24), after the decomposition on two axes of complex frame ($\alpha$, $\beta$) gives the equations presented below:

$$T_1 = \sqrt{2}\frac{T_p V_{ref}}{E}\sin\left(\frac{\pi}{3} - \varphi\right) \tag{25}$$

$$T_2 = \sqrt{2}\frac{T_p V_{ref}}{E}\sin(\varphi) \tag{26}$$

$$T_0 = \frac{1}{2}\left(T_p - T_1 - T_2\right) \tag{27}$$

$$0 \le \varphi \le \frac{\pi}{3}$$

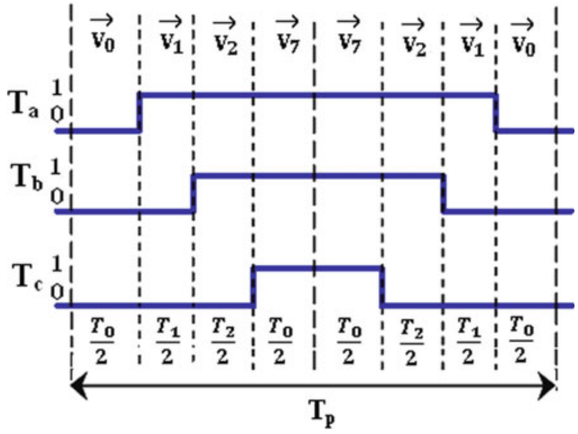

**Fig. 8** Chronogram of pulses of sector I

The same rules were applied for others sectors from *II* to *VI* (Fig. 6), the following relations are obtained:

$$\begin{cases} T_1 = \sqrt{2}\frac{T_P V_{ref}}{E}\sin\left(\left(\frac{\pi}{3}-\varphi\right)+\left(\frac{k-1}{3}\right)\pi\right) \\ T_2 = \sqrt{2}\frac{T_P V_{ref}}{E}\sin\left(\left(\frac{\pi}{3}-\varphi\right)+\left(\frac{k-1}{3}\right)\pi\right) \\ T_0 = \frac{1}{2}(T_P - T_K - T_{k+1}) \end{cases} \quad (28)$$

$k$: the sector number ($k = 1, \ldots, 6$).

Figure 8 shows a chronogram of pulses when the reference vector $\vec{V}_{ref}$ is located in the first sector. Thus, the sequence (or mode) of commutations during a period of modulation $T_p$ is represented as follows:

$$\vec{V}_0 \Rightarrow \vec{V}_1 \Rightarrow \vec{V}_2 \Rightarrow \vec{V}_7 \Rightarrow \vec{V}_7 \Rightarrow \vec{V}_2 \Rightarrow \vec{V}_1 \Rightarrow \vec{V}_0$$

Thus:

$$\begin{cases} T_a = T_1 + T_2 + T_0 \\ T_b = T_2 + T_0 \\ T_c = T_0 \end{cases} \quad (29)$$

$T_a$, $T_b$ and $T_c$ are commutation times of upper switches of inverter arms $a$, $b$ and $c$ respectively. Therefore, the duty cycles to generate the signal of space vector modulation are given by:

$$\begin{cases} d_a = \frac{T_a}{T_p} \\ d_b = \frac{T_b}{T_p} \\ d_c = \frac{T_c}{T_p} \end{cases} \quad (30)$$

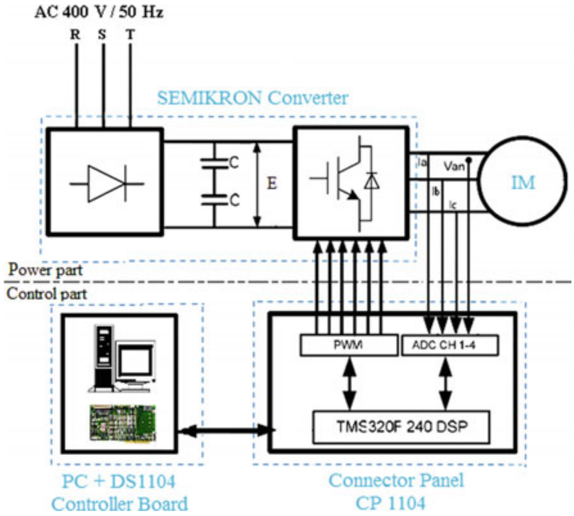

**Fig. 9** Synoptic scheme of the experimental setup

## 3 Implementation and Experiments

The experimental test rig designed to validate and confirm the theoretical developments and evaluate at the same time the performances of *SVPWM* control technique is illustrated in Fig. 9. The real-time applications on the *dSPACE DS1104* are carried out using Real-Time Interface in MATLAB/Simulink environment. This test rig is composed from the following elements:

- *IGBTs* voltage source inverter commercialized by SEMIKRON with a DC source of 400 V.
- A 1.5 kW three phase induction motor.
- Powder brake used to provide accurate load torque.
- A *dSPACE* 1104 *card* (controller Board) was integrated in a *PC* enabling to generate the required pulses to control the inverter switches.
- Current and voltage sensors to measure the output voltages and currents.

The visualization of system waveforms is realized through *CONTROL DESK* software, enabling to control the signals from SimulinkdSPACE schemes. The modulation frequency is 5 kHz and the torque applied to the motor shaft is 4 Nm.

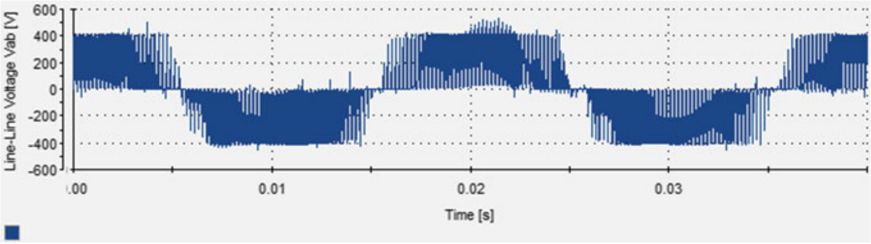

**Fig. 10** Inverter line to line output voltage

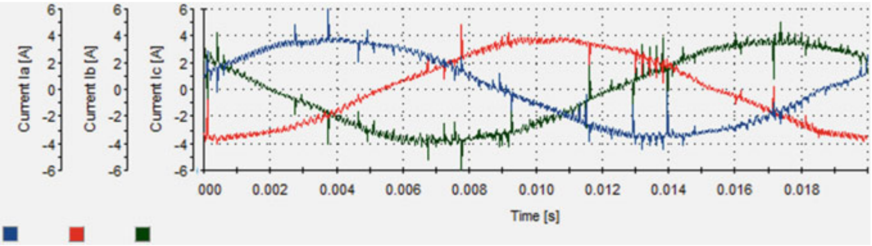

**Fig. 11** The three phase currents waveforms at the inverter output

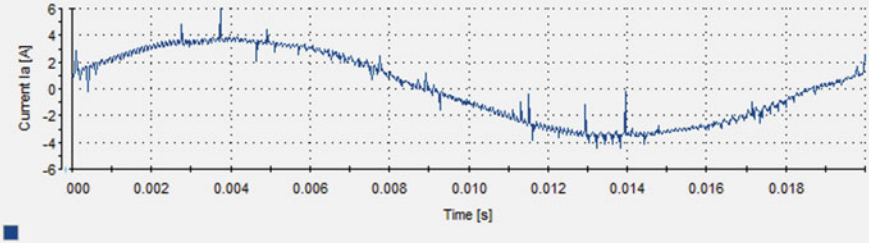

**Fig. 12** Phase current waveform at the inverter output

## 3.1 Results and Discussion

The waveforms obtained by experimental tests are presented below: (Fig. 10).

Figure 11 illustrates the line to line voltage vabat the inverter output. It can be observed that the shape of these waves is similar to those obtained by simulation. However, Fig. 12 presents motor stator currents $I_a$, $I_b$ and $I_c$ shifted from each other by $2\pi/3$ radians.

Figure 13 shows the inverter phase current $I_a$ waveform, it can be remarked from its frequency spectrum illustrated in Fig. 13 that the waveform obtained by *SVPWM* technique has high quality spectrum as it has been demonstrated by simulation with a total harmonic distortion (*THD*) $= 5.58\%$.

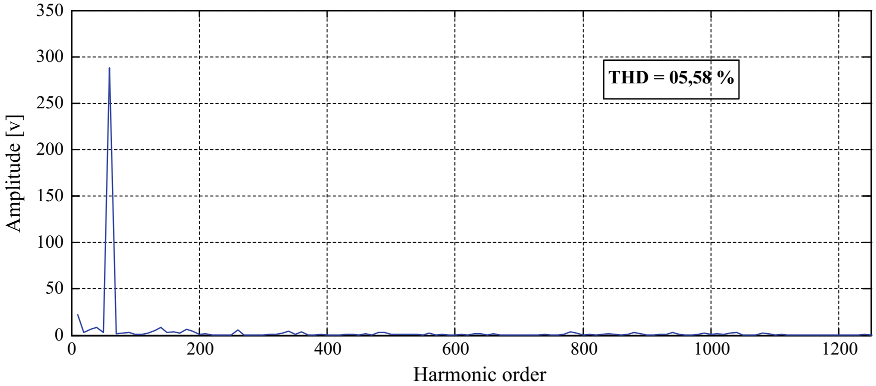

**Fig. 13** Harmonic current frequency spectrum

# 4 Conclusion

In this paper the main characteristics of *PV* system enabling to supply a system in an isolating area where no energy source is available are presented. A *PV* generator delivering a dc voltage to static power converter tracking the operating optimum point is discussed. The electric model of the system is simulated in Matlab environment for different temperatures and solar illumination and their influence on ($I$-$V$) and ($P$-$V$) characteristics. This model showed that the optimization is very important at low illumination. Inversely with temperature which lowers the optimal operating point.

As the inverter is the most important device of the system an investigation was carried out to improve inverter performances. The *SVPWM* control strategy is one of the means to develop in order to improve inverter performances to avoid photovoltaic *PV* system malfunction.

The space vector pulse width modulation implementation has been developed in MATLAB/Simulink programming environment and in *dSPACE* 1104 kit system. The performance analysis of this control technique from the point of view of output voltage and currents has been presented in this paper. The results of the open loop operation have showed that *SVPWM* technique has high performances in harmonics current reduction, torque and speed time response. Therefore, this technique as inverter control strategy is more suitable for *PV* System.

**Acknowledgements** The authors gratefully acknowledge the Algerian General Directorate of Research for providing the facilities and the financial funding of this project.

## References

Chouder A, Guijoan F, Silvestre S (2008) Simulation of fuzzy-based MPP tracker and performance comparison with perturb and observe method. Revue des Energies Renouvelables 11(4):577–586

Daher S, Schmid J, Antunes FLM, Member IEEE (2008) Multilevel inverter topologies for stand-alone PV systems. IEEE Trans Ind Electron 55(7):2703–2712

El-Hefnawi SH (1997) Digital firing and digital control of a photovoltaic inverter. Renew Energy 12(3):315–320

Gonzalez R, Gubia E, Lopez J, Marroyo L (2008) Transformerless single-phase multilevel-based photovoltaic inverter. IEEE Trans Ind Electron 55(7):2694–2702

Hannan MA, Zamer AG, Azah M (2010) An enhanced inverter controller for PV applications using the dSPACE Platform. Int J Photoenergy Volume, Article ID 457562, 10 pages (Hindawi Publishing Corporation)

Li HL, Hu AP, Gao J, Dai X (2006) Development of a direct ac-ac converter based on a dSPACE platform. In: International conference on power system technology, Chongqing (China), pp 1–6

Melkhilef S, Rahim NA, Xilin X (2002) FPGA based three-phase PWM inverter and its application for utility connected system. In: Proceeding of IEEE TENCON, pp 2079–2082

Messenger R, Ventre J (2004) Photovoltaic system engineering, 2nd edn. CRC Press LLC, Boca Raton

Rodrigues F, Thomas HB, McMurray A (1979) Inverter controller. IEEE Trans Indust Electron Control Instrum (IECI) 26(3):156–160

Sefa I, Altin NS, Ozdemir S, Demirtas M (2008) dSPACE based control of voltage source utility interactive inverter. In: International symposium on power electronics, electrical drives, automation and motion (SPEEDAM), pp 662–666

Selvaraj J, Rahim NA (2009) Multilevel inverter for grid-connected PV system employing digital PI controller. IEEE Trans Ind Electron 56(1):149–158

Vijayalakshmi C, Latha R (2012) Implementation of new single phase multilevel inverter for PV power conditioning system. Int J Adv Sci Res Technol 2(2)

Zamre AG, Hannan MA, Azah M (2010) Renewable energy inverter development using dSPACE DS1104 controller board. In: IEEE international conference on power and energy, Nov 29–Dec 1, Kuala Lumpur, Malaysia

# CFD Study About an Archimed Wind Mill

**Nassereddine Hamdi**

## 1 Introduction

Although the choice of solar energy is predominant, wind energy represents the second axis of production of this program Wind energy is a non-degraded "renewable" energy, geographically diffuse, and especially seasonally correlated (electric power is much more demanded in winter and it is often at this period that the average wind speed is the most high). In addition, it is an energy that produces no atmospheric or radioactive waste. It is, however, random over time and its catchment remains rather complex, requiring large masts and blades (up to 60 m for wind turbines of several megawatts) in geographically clear areas to avoid turbulence phenomena.

Despite the impacts of the current financial crisis, which make short-term forecasts difficult, it can be expected that, in the medium term, wind energy will attract investors because of its low risk and the need for clean energy and reliable. More and more governments are understanding the multiple benefits of wind power and are putting in place favorable policies, including promoting decentralized investment by independent, small, medium or community-based producers, all paving the way for a system production of more renewable energies for the future (Gorban et al. 2001).

By rigorously calculating and taking into account factors of insecurity, it is estimated that wind energy will be able to contribute to at least 12% of global electricity consumption by 2020. In 2015, a total capacity of 600,000 MW is possible. By the end of 2020 (Kasbadji 2006), at least 1,500,000 MW may be expected, (see Fig. 1)

By 2030, Algeria expects to achieve nearly 40% of national electricity production from renewable sources (Boudia 2013). This work represents an examined application of a revolutionary wind turbine, it is called "Archimede Wind Mill, *AWM*", and it is very different from the other known wind turbines especially in its conception.

---

N. Hamdi (✉)
Laboratoire de Génie de Procédés, Amar Telidji University, 03000 Laghouat, Algeria
e-mail: n.hamdi@mail.lagh-univ.dz

T. Boukharouba et al. (eds.), *Computational Methods and Experimental Testing In Mechanical Engineering*, Lecture Notes in Mechanical Engineering,
https://doi.org/10.1007/978-3-030-11827-3_16

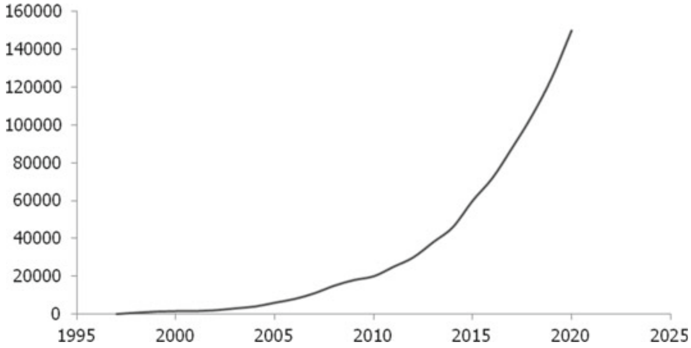

**Fig. 1** World wind energy

## 2 Archimede WIND MILL ‘AWM’

The story began in 2003. The inventor Marinus Mieremet civil engineer (Netherlands) began working on a new type of wind turbine. This new design is based on the works of the great Archimedes.

In 2006, the first patent for the wind turbine of Archimedes *AWM* (Archimede Wind Mill) was filed. Several patents would follow were approved. The shape of this wind turbine is not only beautiful, but also its mathematical properties are magnificent. In 2012, Marinus Mieremet moved to South Korea and started working with Esco *RTS*, a Korean company. Testing and development have all taken place in Korea, with Esco *RTS*, National University of Busan, Borim and other Korean partners. Among the tests were numerous wind blow tests, wind force tests up to 50 m/s and numerous field trials in South Korea, the Netherlands, Germany, Spain, Poland, Czech Republic, Netherlands Antilles and India. The *AWM* is tested in almost all climatic conditions. In 2016, all activities were transferred to South Korea. The sale and research of local distributors and manufacturers have started. Local production will further reduce the carbon footprint and help the state and popular economy.

When used in combination with solar panels on the roof, a house could be powered off the urban electrical grid. When there is wind, the energy produced by the wind turbine is used, when the sun is shining, photovoltaic cells are used to generate energy. The wind turbine Archimedes has the shape of a shell ‘Nautilus’ (see Fig. 2). Its design allows it to point to the wind to capture the greatest amount of energy, while producing very little noise. The inventor of the turbine Marinus Mieremet says that the power produced can reach 80% of the theoretical maximum energy that could be exploited by the wind.

The symbol of this wind turbine is that it is domestic; it can be used to power a house, a boat, or an administration. The aim of this work is to apply our modest knowledge in mechanics by realizing a prototype of the *AWM* on all levels, on geometry design, *CFD* calculation and rigid dynamics software’s. Its geometrical shape which resembles a marine shell ‘Nautilus’ repeated allows it to catch the

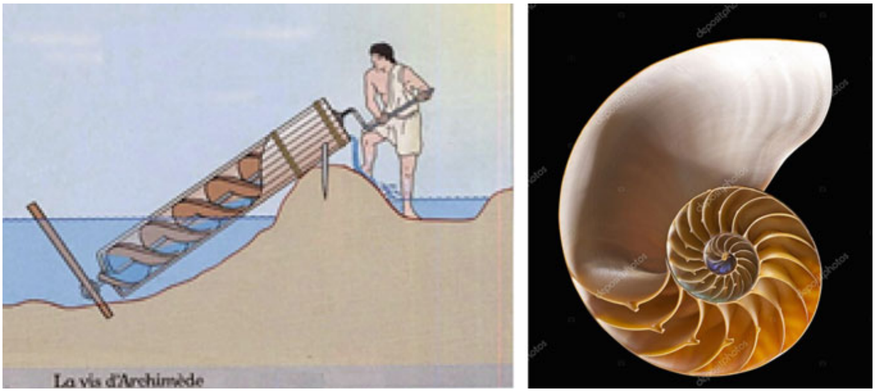

**Fig. 2** left, Archimed pump and right, AWM

maximum kinetic energy of the wind, which gives it a good performance compared to those colleagues of the wind turbines.

## 3 Theory

The study of this *AWM* is starting first with the design by SolidWorks software, and then the import of the geometry towards ANSYS-CFX is assured by *IGES* format files. The implementation of the boundary conditions is done in *CFX-Pre* and then the simulation is launched by the *CFX* solver. The results obtained are commented as a pressure, total pressure, and velocity around the wind turbine; we present also the field of velocity vectors and the streamlines which inform us the behavior of the flow of the wind. Air flow around the *AWM* in the compression and depression zones is evoked when we remark the vortices (secondary flow) in the wake upstream. Also we will determine the force and torque exerted on the wind turbine by using the numerical option in the *post-CFX* module. The application of Rigid-dynamics software from *CFX* will predict the speed of rotation of the wind turbine, and finally the calculation of the power.

The study is carried out by *ANSYS CFX* in steady state with the scalable *K-E* turbulence model. The design is provided by SolidWorks software *CAD* software is now widely used in industry (see Fig. 3). Among these codes one has the SolidWorks which a 3D modeler using the parametric design. It generates 3 types of files related to three basic concepts: the part, the assembly and the drawing. These files are related, any changes at any level will be reflected to all affected files. A complete record containing all the data relating to the same system constitutes a digital mock-up.

Many software packages complete the SolidWorks editor. Utilities oriented business (sheet metal, wood, construction), but also applications of mechanical simulation or synthetic image work from the elements of the virtual mock-up. The dimensions

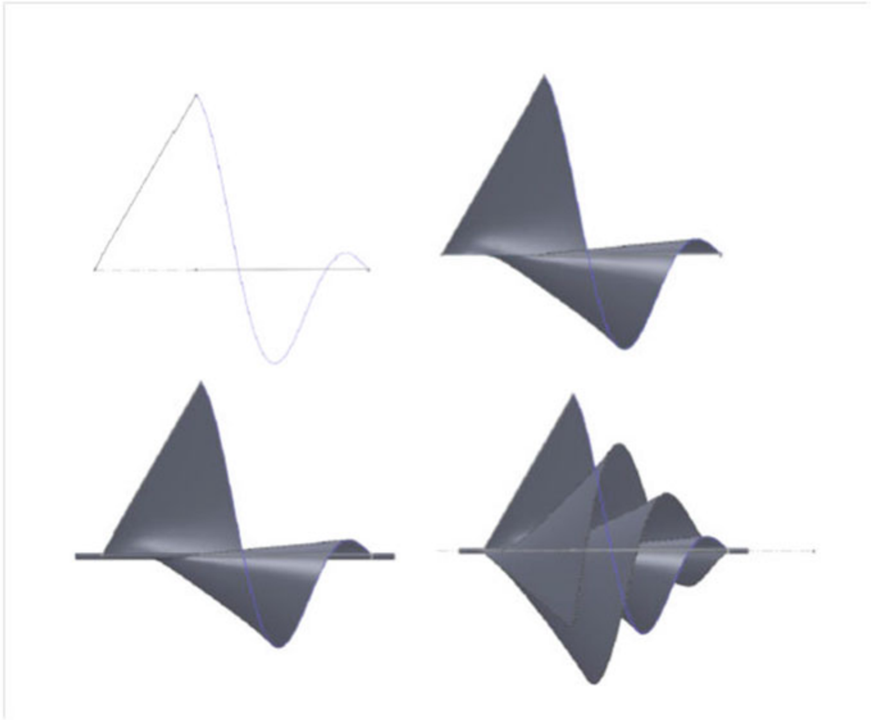

**Fig. 3** Main steps of design by Solidwork

of the *AWM* are not taken from an industrial reference or previous work, the radius; diameter of the axis of rotation, thickness of the blades, pitch and number of repetitions is taken freely from such that the size of the wind turbine responds to the need for domestic consumption in energy.

For steady flows the following assumptions are made in the system analysis:

1. The mass flow through the system remains constant.
2. Fluid is uniform in composition.
3. The only interaction between the system and surroundings are work and heat.
4. The state of fluid at any point remains constant with time.
5. In the analysis only potential, kinetic and flow energies are considered.

For steady flow process, net quantity of energy contained within the system will never change with respect to time. Therefore according to the principle of conservation of energy, we will have following statement and energy equation for a steady flow process.

Net quantity of energy entering to the control volume = Net quantity of energy leaving the control volume Hartwanger (2008).

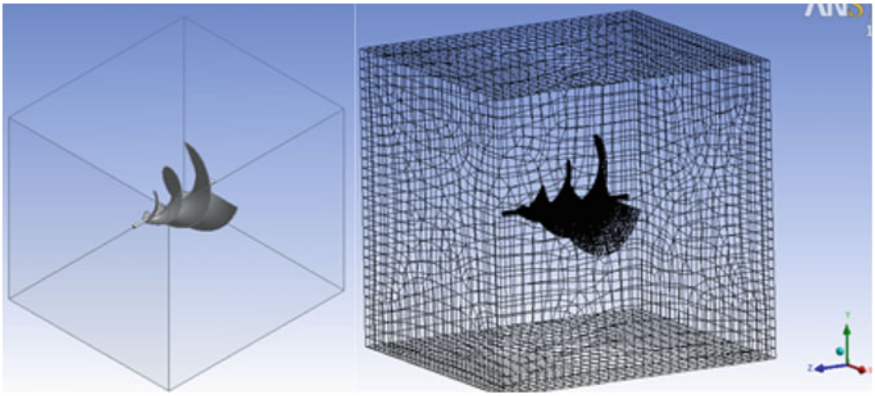

**Fig. 4** left, box of calculation and right, mesh generation

## 4 Results and Discussion

The Design Modler has a very interesting feature called in French “Englober” that allow us to choose the shape of the box and its dimensions (cylinder, box, …) to cover the device to study. A box parallelepiped is proposed and it has been chosen sufficiently distant to neutralize the aerodynamic disturbances; one renames the box “Fluid” and the windMill “Solid” (see Fig. 4 left) which shows the calculation domain in the form of a cubic box.

The mesh is generated by the Ansys-ICEM module. Generation can be automatic, as can be controlled by the user where we can demand according to our need methods or functions such as refinement, dimensioning, pinching, inflation, etc. … For example in our case a degree 1 surface refinement was carried out on the walls of the wind turbine, a dimensioning on the 12 edges of the cube where an element number of 30 was fixed on each edge. The software has been forced to proceed with a hexahedral dominant mesh generation. The mesh after generation comprises 588,062 elements and 183,308 nodes (see Fig. 4 Right) which shows the mesh generated by *ICEM-CFD*.

The fluid is taken at 25 °C, the flow is in the steady isothermal regime with the morphology of a continuous medium under a reference pressure of 1 atm and in the non-buoyancy condition, and the turbulence model used in the simulation is k-epsilon scalable.

1/Domain Fluid (parallelepiped box):

- Input condition: a constant velocity of 8 m/s is fixed; the flow is subsonic, with an input turbulence intensity of 5%.
- Output condition: the condition OPNING is set with the relative pressure “0 Pa” with a perpendicular direction of the flow on the output face with an output turbulence intensity of 5%.

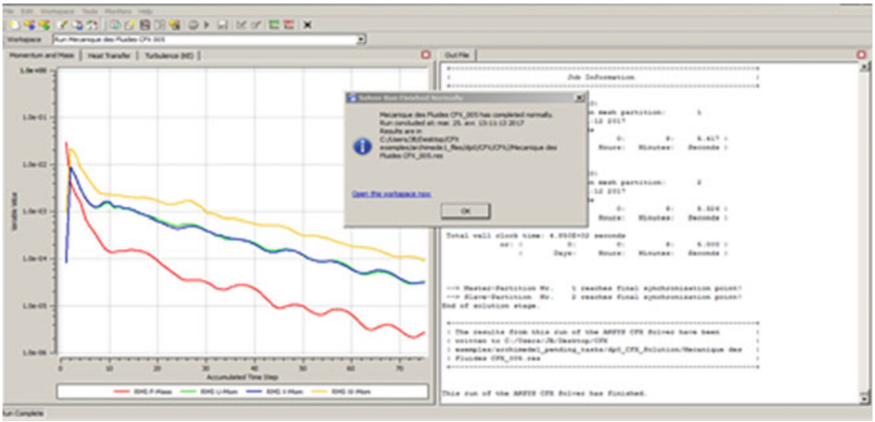

Fig. 5 Convergence of simulation

- Wall condition: the non-slip condition is applied to the wind turbine walls, i.e., with the “smooth wall” roughness hypothesis.

2/Solid domain (helical wind turbine):

Aluminum was taken as the metal of the wind turbine with the morphology of a continuous medium with stationary mobility (the wind turbine is stationary in advance) in an adiabatic heat transfer with a zero deformation of the mesh. The adventive numerical scheme is taken with the high resolution option; the computing of the turbulence is taken with the option of order 1. The iterations of the convergence is taken between 1 and 100 iteration, the control of the time increments is taken automatically, and the residual digital is taken up to $10^{-4}$. After the installation of all boundary conditions and the configuration of the resolution method, the simulation is started in the CFX-Solver-Manager module. The calculation can be started with a single processor or with several processors by applying the Message Passing Interface (*MPI*) function if it is installed with Ansys-CFX. It can be seen that the solution is converged after 75 iterations (see Fig. 5).

**Pressure on the AWM**: The static and total pressure fields are respectively shown (see Fig. 6 left and right) on the wind turbine. It is clear that there is a compression on the curved faces of the turbine exposed to the wind indicated by the red colors, on the other hand a depression is observed downstream (behind) of each blade indicated by the blue colors.

**Velocity Vectors**: The direction of velocity vectors which tangent on the streamlines rotating around the wind turbine can be observed. With the no slip wall condition, the air flow is totally adhered to the wall, and therefore the air velocity take zero value on the walls which represented by the blue color (see Fig. 7 left).

**Stream lines**: About the volumetric flow lines around the wind turbine, it is clear how the air streams revolve around the wind turbine through the 3 big blades flowing the flow air (see Fig. 7 right).

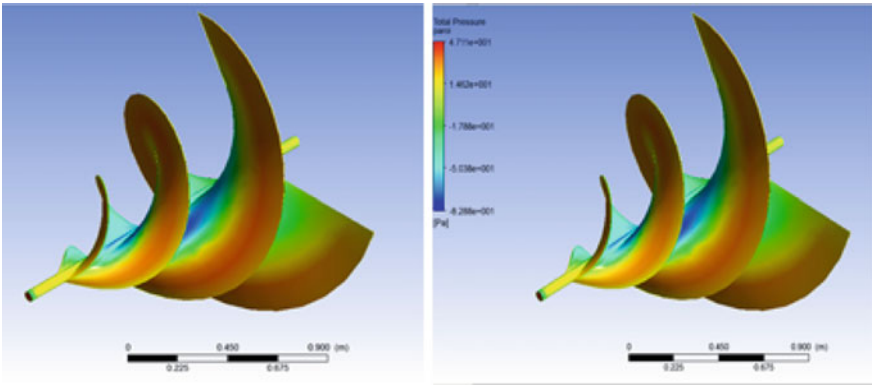

**Fig. 6** Left, Satic pressure and right, total pressure on the AWM

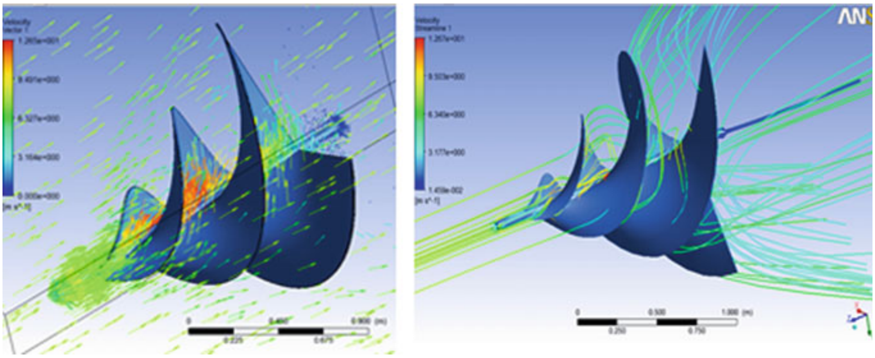

**Fig. 7** left, Velocity vectors and right, streamlines around the AWM

**Force and torque**: The module *CFX-CFD*-Post gives us the possibility to calculate the force exerted by the wind on the wind turbine, the result will be = −40.2552 [N], the sign '−'indicates that the force is the inverse of the positive of Z axis. The same applies to calculating the torque exerted on the wind turbine, in this case we choose the axis of rotation around the *Z* axis, which gives a torque of −6.47359 [Nm], The sign '−'indicates that the torque follows a direction against the direction of a clock hand.

**Power Calculation**: The power can be calculated in two ways: the Betz formula by knowing the incident wind speed, or by the mechanical formula linking the torque *C* with the angular velocity *w* of the wind turbine.

$$P = w \, . \, C \tag{1}$$

$$p = (25) \, . \, (6.474) \tag{2}$$

$$P = 162\,w \tag{3}$$

By the Betz limit:

$$P_{incidence} = \frac{16}{17} \cdot \frac{1}{2} \,.\, \rho \,.\, s \,.\, v^2 \tag{4}$$

$$P_{incidence} = \frac{16}{17} \cdot \frac{1}{2} \,.\, (1.2) \,.\, \pi(0.65^2) \,.\, 8^2 = 241.6\,w \tag{5}$$

It is clear that the power calculated by the Betz limit is greater than that calculated by the torque formula because the maximum power of Beltz is then assigned the coefficient of performance specific to the wind turbine type, model, and installation. This coefficient is generally between 0.2 and 0.7.

## 5 Conclusion

In the World, the production of electric power from wind turbines has increased from 3.9 Twh in 1990 to 100 Twh in 2014 which is worth 3% of the overall electric power produced. In this work, a test application of a revolutionary wind turbine is examined; it is called “Archimedes Wind Mill AWM”. It is very different from the other windmills by its geometric shape and functions. Its blades takes the form of a repeated nautilus shell, this shape will give it the ability to catch the maximum of momentum and energy of the airflow. in this work the dimensions of the *AWM* are not taken by a reference or an industrial design, but they are taken in such a way to have a domestic windmill of diameter and length between 0.5 and 2 m in maximum; the goal of this work is reached; the behavior of the airflow was observed, the torque and power generated by this proposed *AWM* are calculated.

## References

Boudia SM (2013) Optimisation de l’Évaluation Temporelle du Gisement Énergétique Éolien par Simulation Numérique et Contribution à la Réactualisation de l’Atlas des Vents en Algérie. Université de Tlemcen, Thèse de Doctorat

Gorban AN, Gorlov AM, Silantyev VM (2001) Limits of the Turbine Efficiency for Free Fluid Flow. J Energy Res Technol 123(4):311–317

Hartwanger D, Horvat A (2008) 3D, Modelling of A Wind Turbine Using CFD, NAFEMS UK Conference 2008 “Engineering Simulation: Effective Use and Best Practice”, Cheltenham, UK, June 10–11, Proceedings 2008

Kasbadji MN (2006) Evaluation du gisement énergétique éolien. Contribution à la détermination du profil vertical de la vitesse du vent en Algérie. Thèse de Doctorat. Université de Tlemcen, 2006 http://www.ren21.net/wp-content/uploads/2015/06/2012KFfr.pdf

# Periodic Inspection Policy for a System with Two Levels of Degradation

**Bachir Cherfaoui and Radouane Laggoune**

## 1 Introduction

The complexity of Technological systems increases the occurrence of a catastrophic failure, which can have significant consequences for businesses. To overcome the random occurrence of failures we are forced to develop mathematical models that allow us to predict the date of such occurrence in order to avoid it by preventive maintenance.

A simple review of the literature allows us to conclude that the models proposed in this context can be classified into two categories. The first consists of purely reliability models. In this category, the modeling of the systems is carried out according to the binary configuration where only two states are allowed: normal operation and complete failure (Wang and Tsai 2012; Barlow and Proschan 1965). In addition, it is assumed that the performances of the system studied are of the same level throughout the operating phase of the system. Although the such modeling has many applications in practice, it is considered insufficient to describe the various situations that arise in the life of the system and which may affect its performance. For this reason, a second category of models, which take into account the degradation of the system, are constructed. Laggoune et al. (2016) modeled the degradation process using the power law process. Alternatively, the use of Gamma processes for the modeling of systems undergoing perfect preventive maintenance "*as good as new*" (Huynh et al. 2013) and the Gaussian process for the modeling of systems undergoing imperfect preventive maintenance "*as bad as old*" (Deloux et al. 2009) are also used.

B. Cherfaoui (✉) · R. Laggoune
Research Unit LaMOS (Modeling and Optimization of Systems), Faculty of Technology,
University of Bejaia, 06000 Bejaia, Algeria
e-mail: bachircherfaoui2015@gmail.com

R. Laggoune
e-mail: r_laggoune@yahoo.fr

T. Boukharouba et al. (eds.), *Computational Methods and Experimental Testing In Mechanical Engineering*, Lecture Notes in Mechanical Engineering,
https://doi.org/10.1007/978-3-030-11827-3_17

Note that, such approaches, suppose that systems can operate in degraded mode. Indeed, to know the level of degradation of the system we must carry out at each time inspections in order to determine the exact level of the system. It should be noted that the dates of inspections, checks, and maintenance must be chosen in a judicious and optimal manner within the meaning of a certain criterion set by the decision maker. Indeed, the actions to be performed and their dates can be set, for example, to maximize the availability of the system (Laggoune et al. 2016; Ait Mokhtar et al. 2016; Cui and Xie 2005) or to minimize maintenance costs (Huynh et al. 2013; Deloux et al. 2009; Chouikhi et al. 2012), etc.

In this work, we propose to analyze, based on the real data, the influence of the various parameters of the degradation model on the performances of a system modeled by the homogeneous gamma process (Abdel-Hameed 1975). More precisely, our interest concerns the influence of the parameters on the optimal policy in the economic sense. The paper is organized as follows: First, we give in Sect. 2 a brief presentation of the mathematical model of degradation called *DT* (*degradation threshold*) modeled by an homogeneous Gamma process. Then, in Sect. 3, the inspection/replacement model called and noted ($\Delta T$, $B$) is provided. It permits to find the optimal inspection dates $\Delta T$ and the preventive replacement level $B$ minimizing the total maintenance cost. The effects of various parameters on the pair ($\Delta T$, $B$) is examined numerically in Sect. 4.

# 2 Reliability of the DT Model (Degradation Threshold Model)

## 2.1 *System Description*

Let's consider a system that, undergoes an increasing continuous degradation with two important levels. The first level, denoted $L$, is the critical degradation threshold, which is considered as a total breakdown. While the second, level denoted $B$, lies between the new state of the system and the failure threshold $L$ (see Fig. 1).

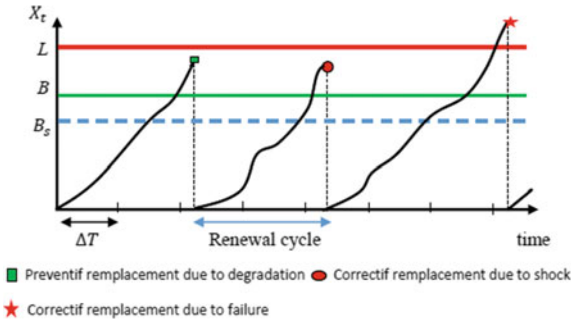

**Fig. 1** Illustration of the policy decision rule *($\Delta T$, B)*

The objective is to model the degradation process using the threshold model *DT* (Degradation Threshold). In this paper, we opt for the homogeneous gamma model proposed by Van Noortwijk (2009). For this, let's consider a random variable $x_t$ representing the degradation's level of the system at time $t$, and $\{x_t\}_{t\ge 0}$ the degradation process. Moreover, $\{x_t\}_{t\ge 0}$ is a gamma process with a form parameter $\alpha > 0$, and a scale parameter $\beta > 0$.

## 2.2 Degradation Threshold Model (DT)

**Survival time function $\tau_B$**

Let $\tau_B$ be the time of reaching the degradation level $B$, its survival function $R_{\tau B}(t)$ at instant $t > 0$, is obtained by:

$$R_{\tau B}(t) = 1 - F_{\tau B}(t) = 1 - P(\tau_B \le t) = P(x_t \ge B) = 1 - \frac{\Gamma(\alpha t,\ \mathrm{B}\beta)}{\Gamma(\alpha \mathrm{t})} \tag{1}$$

where $\Gamma(\alpha,\ x) = \int_x^\infty z^{\alpha-1}\mathrm{e}^{-z}dz$ corresponds to the incomplete gamma function for $x \ge 0$ and $\alpha \ge 0$ and $F_{\tau B}$ is its distribution function having as density:

$$f_{\tau B}(t) = \frac{\partial}{\partial t}F_{\tau B}(t) = \frac{\alpha}{\Gamma(\alpha t)} \cdot \int\limits_{B\beta}^{\infty} \{\log(z) - \psi(\alpha t)\}\ \mathrm{z}^{\alpha \mathrm{t}}\mathrm{e}^{-z}dz \tag{2}$$

**Survival time function $\tau_L - \tau_B$**

Given a second level of degradation $L$ ($\mathrm{B} < \mathrm{L}$), we seek to determine the survival function of the reaching time $R_{\tau L - \tau_B}(t),\ \mathrm{t} > 0$.

$$R_{\tau L}(t) = R_{\tau_L,\,\tau_B}(t, x, y)\, 1_{\{y > x > 0\}} + R_d(t, x, y)\, 1_{\{y = x > 0\}} \tag{3}$$

where:

$$R_{\tau_B,\tau_L}(t, x, y) = -\int\int_{B<x<L,\, 0<x+y<L,\, 0<y} \left(\int\limits_0^\infty f_{\alpha u,\beta}(x)du\right)\frac{\partial f_{\alpha t,\beta}(y)}{\partial t}dxdy \tag{4}$$

$$R_d(t, x, y) = \int\limits_t^\infty \int\limits_0^{y-t} \alpha \int\limits_0^B f_{\alpha x,\beta}(w)dw\left(\int\limits_{L-y}^\infty \frac{\mathrm{e}^{-\beta z}}{z}dz\right)dxdy \tag{5}$$

In practice, the failure of a system is not always caused by degradation only. However, it can also be caused by a shock event. In addition, the degradation process may depend on shock processes. For this purpose, it is essential to include the shock process in the model.

One of the most frequent assumptions about the shock process is that shocks occur according to a homogeneous Poisson process of intensity $r$, when it depend on time, it is noted $r(t)$, $t > 0$ and called a non-homogeneous Poisson process (Huynh et al. 2013). Since, as the system is degraded, it is more vulnerable to shocks, then this dependence can be modeled by representing the intensity of shock as a function of the degradation level $x_t$ and the operational time $(t)$ by:

$$r(t, x_t) = r_1(t)1_{\{x_t < B_S\}} + r_2(t)1_{\{x_t \geq B_S\}} \tag{6}$$

where $1_{\{.\}}$ correspond to the indicator function, $r_1(t)$ and $r_2(t)$ are continuous non-time-decreasing functions that represent the intensity of a Poisson shock at time $t$ with $r_1(t) \geq r_2(t)$ and $B_S$ corresponds to a degradation level previously set. The purpose of this part is to give the system reliability model associated to the shock process.

Let $R_1(t)$ (respectively $R_2(t)$) be the survival function at time $t > 0$ associated to the intensity $r_1(t)$(respectively intensity $r_2(t)$ of the shock. Thus, we obtain the reliability of the system at time $t > 0$, as follows:

$$R_s(t) = R_1(t)R_{\tau_{B_s}}(t) + R_2(t)\int_0^t \frac{R_1(u)}{R_2(u)} f_{\tau_{B_s}}(u)du \tag{7}$$

where the quantities $R_{\tau_{B_s}}$ and $f_{\tau_{B_s}}$ correspond to the survival function and to the density of the reaching time $\tau_{B_S}$ of the degradation level $B_S$, calculated respectively by (1) and (2), and the reliability function $R_i$ $(i = 1, 2)$ is given by:

$$R_i(t) = \mathrm{e}^{-\int_0^t r_i(udu)}, \qquad \mathrm{i} = 1, 2. \tag{8}$$

## 3 Inspection Policy (ΔT, B) for a System with Two Levels of Degradation

The policy ($\Delta T$, $B$) is a periodic conditional inspection/replacement policy. The structure of this policy in a renewal cycle is interpreted in the following way. The system is inspected periodically (the inter-inspection period is denoted $\Delta T$) and the decision rule at an inspection $T_i = i\,\Delta T$ $(i = 1, 2, \ldots, n)$ is conditioned by the system state and the inspected degradation level $x_{T_i}$. Finally, the details of this policy is schematized in Fig. 1.

Let us remember that the fundamental aim of optimization in reliability models is to find a compromise between the operation time of the system and the maintenance cost. In this work, we propose to minimize the overall cost per unit of time generated by not only maintenance, but also the production losses caused by the unavailability of the system, and this when the policy ($\Delta T$,$B$) is adopted.

This cost is defined as follows:

$$C_{\infty}^{\Delta T,B}(\Delta T, B) = \lim_{t\to\infty} \frac{C^{\Delta T,B}(t)}{t} \tag{9}$$

where:

$$C^{\Delta T,B}(t) = C_{id}N_i^{\Delta T,B}(t) + C_p N_p^{\Delta T,B}(t) + C_c N_c^{\Delta T,B}(t) + C_d W_d^{\Delta T,B}(t) \tag{10}$$

With $C_{id}$: inspection cost, $C_p$: preventive replacement cost, $C_c$: corrective replacement cost, $C_d$: cost of system unavailability and $N_i^{\Delta T,B}(t)$, $N_p^{\Delta T,B}(t)$, $N_c^{\Delta T,B}(t)$ and are respectively the number of inspections, the number of preventive replacements, the number of the corrective replacements and the acc umulated unavailability time on $[0, t]$.

Since the system maintained is a regenerative process and the instants of replacement of the system constitute renewal points, then the knowledge of a single renewal cycle makes it possible to describe the overall evolution of the maintained system. Thus, the average asymptotic cost $C_{\infty}^{\Delta T,B}(\Delta T, B)$ can be estimated as the quotient of the average cost over a renewal cycle divided by the mean cycle length, i.e.:

$$C_{\infty}^{\Delta T,B}(\Delta T, B) = \frac{C_{id}E\left[N_i^{\Delta T,B}\right] + C_p P_p^{\Delta T,B}(\Delta T, B)}{E\left[S^{\Delta T,B}(\Delta T, B)\right]} + \frac{C_c\left(1 - P_p^{\Delta T,B}(\Delta T, B)\right) + C_d E\left[W S_d^{\Delta T,B}(\Delta T, B)\right]}{E\left[S^{\Delta T,B}(\Delta T, B)\right]} \tag{11}$$

where $P_p^{\Delta T,B}(\Delta T, B)$ is the probability of preventive replacement on a cycle $S^{\Delta T,B}(\Delta T, B)$.

At this stage all the difficulty lies in the calculation of the four quantities $E\left[N_i^{\Delta T,B}(\Delta T, B)\right]$, $P_p^{\Delta T,B}(\Delta T, B)$, $E\left[S^{\Delta T,B}(\Delta T, B)\right]$ and $E\left[W S_d^{\Delta T,B}(\Delta T, B)\right]$ involved in the expression (11), whose evaluations are relatively complex. In the following, we provide only the final formulas of the previous quantities (for more details the reader can refer to Huynh et al. 2013).

**Average length of a renewal cycle**

$$E\left[S^{\Delta T,B}(\Delta T, B)\right] = \sum_{k=0}^{\infty} (k+1)\Delta T \left(P_{s,1}^{\Delta T,B}(k) 1_{\{B_s \le B\}} + P_{s,2}^{\Delta T,B}(k) 1_{\{B_s \ge B\}}\right) \tag{12}$$

The quantities $P_{s,1}^{\Delta T,B}(k)$ and $P_{s,2}^{\Delta T,B}(k)$ corresponding to the probability of a replacement on the date $(k+1)\Delta T$ when $B_S \le B$ and $B_S > B$ respectively.

**Average length of unavailability on the renewal cycle**

$$E\left[WS_d^{\Delta T,B}(\Delta T, B)\right] = \sum_{k=0}^{\infty} \int\limits_{k\Delta T}^{(k+1)\Delta T} \left(P_{d,1}(t,k)1_{\{B_s \le B\}} + P_{d,2}(t,k)1_{\{B_s > B\}}\right)dt \quad (13)$$

where $\tau_f$ the date of the first failure in a renewal is cycle, $P_{d,1}(t,k)$ and $P_{d,2}(t,k)$ is the probability that the system break down at $t \in [K\Delta T, (K+1)\Delta T]$ when $B_S \le B$ and $B_S > B$ respectively.

**Probability of preventive replacement**

$$\begin{aligned} P_p^{\Delta T,B}(\Delta T, B) &= \sum_{k=1}^{\infty} P\left(k\Delta T < \tau_{\mathrm{B}} \le (k+1)\Delta T < \tau_L, N_{(k+1)\Delta T} = 0\right) \\ &= \sum_{k=1}^{\infty} P_{p,1}^{\Delta T,B}(k)1_{\{B_S \le B\}} + P_{p,2}^{\Delta T,B}(k)1_{\{B_S > B\}} \quad (14) \end{aligned}$$

The probabilities $P_{p,1}^{\Delta T,B}(k)$ and $P_{p,2}^{\Delta T,B}(k)$ correspond to the probability of a preventive replacement on $(k+1)\Delta T$ when $B_S \le B$ and $B_S > B$ respectively.

**Average number of inspections on a renewal cycle**

$$E\left[N_i^{\Delta T,B}(\Delta T, B)\right] = \frac{E\left[S^{\Delta T,B}(\Delta T, B)\right]}{\Delta T} \quad (15)$$

where $E\left[S^{\Delta T,B}(\Delta T, B)\right]$ is given by (12).

## 4 Numerical Example

In order to highlight the optimal policy $(\Delta T, B)$ in the economic sense according to the parameters governing the system in question, we will present in this section two numerical applications realized on real data. First we will mainly present the collected data as well as the cost estimates of different maintenance, then we will consider the case of variation of the system parameters in order to analyse their impact on the optimal policy $(\Delta T, B)$.

## 4.1 Presentation of Data

The data available are collected from the company ***CEVITAL*** and it range from January 2012 to December 2014. The analysis allowed us to estimate the average costs of preventive maintenance and corrective maintenance in monetary unit (*MU*) and which are given by: $C_p = 44279.91\,MU$ and $C_c = 17173.93\,MU$. In order to quantify the different characteristics associated with the system as well as the optimal policy $\left(\Delta T_{opt}, B_{opt}\right)$ we have implemented a program under Matlab environment. This latest involves several numerical computational techniques such as the trapezoid method and the rectangles method to calculates the integrals, the method of the interior points to determine the optimum (minimal) of the objective function (the total cost of maintenance).

The results show that the inspections must be separated by a 57 days duration and we conduct a preventive maintenance when the degradation threshold is equal to or greater than 60% and this in order to minimize the maintenance and unavailability costs.

## 4.2 Influence of Model Parameters on $\left(DT_{opt}, B_{opt}\right)$

In this section, the idea is to analyze the influence of the different parameters on the model with two-levels of degradation describing the production system, on the optimal policy $\left(\Delta T_{opt}, B_{opt}\right)$ according to the economic criterion. For this, we considered the following six (06) situations:

**Case 1**: $\alpha \in \{0.1, 0.2, 0.3\}$ **&** $\beta = 0.1$, $B_S = 20$, $L = 30$, $r_1 = 0.01$, $r_2 = 0.1$.
**Case 2**: $\beta \in \{0.1, 0.2, 0.3\}$ **&** $\alpha = 0.1$, $B_S = 20$, $L = 30$, $r_1 = 0.01$ and $r_2 = 0.1$.
**Case 3**: $r_1 \in \{0.02, 0.03, 0.04\}$. **&** $\alpha = 0.1$, $\beta = 0.1$, $B_S = 20$, $L = 30$, $r_2 = 0.1$.
**Case 4**: $r_2 \in \{0.2, 0.3, 0.4\}\}$ **&** $\alpha = 0.1$, $\beta = 0.1$, $B_S = 20$, $L = 30$, $r_1 = 0.01$.
**Case 5**: $B_S$: 0, 5, 25 and 30. **&** $\alpha = 0.1$, $\beta = 0.1$, $L = 30$, $r_1 = 0.01$, $r_2 = 0.1$.
**Case 6**: $L$, namely: 30, 50 and 100. **&**$\alpha = 0.1$, $\beta = 0.1$, $B_S = 20$, $r_1 = 0.01$, $r_2 = 0.1$.

For a preventive maintenance cost $C_p = 50\,MU$, a corrective maintenance cost $C_c = 100\,MU$, an unavailability cost $C_d = 25\,MU$ and an inspection cost $C_{id} = 2\,MU$, the results obtained for the six situations considered, are presented in Tables 1, 2, 3, 4, 5, 6.

**Table 1** Case of variation of $\alpha$

| $\alpha$ | $\Delta T_{opt}$ | $B_{opt}$ | Cost |
|---|---|---|---|
| 0.1 | 13.00 | 16.93 | 0.17 |
| 0.2 | 19.01 | 19.99 | 21.60 |
| 0.3 | 19.41 | 25.39 | 24.33 |

**Table 2** Case of variation of $\beta$

| $B$ | $\Delta T_{opt}$ | $B_{opt}$ | Cost |
|---|---|---|---|
| 0.1 | 13.00 | 16.93 | 0.17 |
| 0.2 | 19.01 | 19.99 | 21.60 |
| 0.3 | 19.41 | 25.39 | 24.33 |

**Table 3** case of variation of $r_1$

| $r_1$ | $\Delta T_{opt}$ | $B_{opt}$ | Cost |
|---|---|---|---|
| 0.02 | 19.99 | 19.99 | 04.46 |
| 0.03 | 19.70 | 19.99 | 05.10 |
| 0.04 | 19.74 | 19.99 | 06.06 |

**Table 4** Case of variation of $r_2$

| $r_2$ | $\Delta T_{opt}$ | $B_{opt}$ | Cost |
|---|---|---|---|
| 0.2 | 13.50 | 19.99 | 03.54 |
| 0.3 | 19.99 | 24.09 | 21.03 |
| 0.4 | 19.99 | 24.46 | 23.61 |

**Table 5** Case of variation of $L$

| $L$ | $\Delta T_{opt}$ | $B_{opt}$ | Cost |
|---|---|---|---|
| 30 | 13.00 | 16.93 | 0.17 |
| 50 | 19.07 | 14.99 | 03.82 |
| 100 | 19.88 | 23.83 | 21.25 |

## 5 Discussion of Results

From the numerical results, we see that:

- All the parameters have an impact on the optimal policy inspection/replacement $\left(\Delta T_{opt}, B_{opt}\right)$ and of course on the total cost associated with it.
- The increase of the parameters $\alpha$, $\beta$ and $r_2$ leads to a considerable increase in the maintenance cost, the optimal inter-inspection time $\Delta T_{opt}$ and the optimal preventive replacement threshold $B_{opt}$. On the other hand, the increase in $r_1$ generates

**Table 6** Case of variation of $B_S$

| $B_S$ | $\Delta T_{opt}$ | $B_{opt}$ | Cost |
|---|---|---|---|
| 0 | 15.10 | 29.99 | 11.54 |
| 5 | 15.30 | 29.99 | 14.30 |
| 25 | 19.98 | 24.33 | 0.89 |
| 30 | 15.50 | 21.33 | 0.65 |

only a slight increase in the maintenance cost and the couple $\left(\Delta T_{opt}, B_{opt}\right)$ tends to be a constant. This may be explained by the fact that the increase in $\alpha$ means a faster degradation of the system. Consequently, we have a tendency to carry out corrective maintenance, although it is very costly, that preventive maintenance which is less expensive but which serves no purpose, this corresponds to the case of a system in its wear-out period.

- The increase in $B_S$ leads to a monotonic decrease in maintenance costs as well as the preventive replacement threshold. On the other hand, the cost has no monotonic variation.
- The increase in $L$ generates the increase in inspection interval length and the critical threshold of preventive replacement. While the optimal cost is not a monotonous variation. This can be explained by the negligible probability of the realization of a breakdown. For this purpose, it is only necessary to put a preventive replacement level $B_{opt}$ near $L$, in order to avoid a breakdown and the unavailability of the system.

## 6 Conclusion

The idea of this work is to clarify the influence of the parameters of a monotonous continuous degradation system on an inspection/replacement policy when its degradation, is modeled by a homogeneous gamma process.

Although the numerical application realized on real data has yielded realistic results and it has highlighted the link between the different parameters of the system with its characteristics, the tedious calculations, in the sense of the calculation time, remains the big handicap to determine the pair $\left(\Delta T_{opt}, B_{opt}\right)$. In view of the complexity and the delay of the algorithm's response, the need to elaborate a less complex and fast algorithm remains a primordial perspective.

## References

Abdel-Hameed M (1975) A Gamma wear process. IEEE Trans Reliab 2(24):152–153

Ait Mokhtar EH, Laggoune R, Chateauneuf A (2016) Utility-based maintenance optimization for complex water-distribution systems using Bayesian networks. Water Resour Manage 30(12):4153–4170

Barlow R, Proschan F (1965) Mathematical theory of reliability. Wiley, New York

Chouikhi H, Khatab A, Rezg N, (2012) Condition-based maintenance for availability optimization of production system under environment constraints. In: The 9th international conference on modeling, optimization & simulation, Bordeaux, France

Cui L, Xie M (2005) Availability of a periodically inspected system with random repair or replacement times. J Stat Plan Inference 131(1):89–100

Deloux E, Castanier B, Berenguer C (2009) Predictive maintenance policy for a gradually deteriorating system subject to stress. Reliab Eng Syst Saf 94:418–431

Huynh KT, Barros A, Bérenguer C, Castro I (2013) A periodic inspection and replacement policy for systems subject to competing failure modes due to degradation and traumatic events. Reliab Eng Syst Saf 96(4):497–508

Laggoune R, Cherfaoui B, Abbas S, Ablaoui F (2016) Preventive maintenance optimization for multi-state deteriorating systems. Maintenance and life cycle assessment of structures and industrial systems. In: proceeding of the 51st ESReDA Seminar, Clermont-Ferrand, France

Van Noortwijk J (2009) A survey of the application of gamma processes in maintenance. Reliab Eng Syst Saf 94(1):2–21

Wang CH, Tsai (2012) Optimizing bi-objective imperfect preventive maintenance model for series-parallel system using established hybrid genetic algorithm. J Intell Manuf 25(3):603–616

# Modeling of Elastic and Mechanical Properties of ZnS Using Mehl Method

**R. Nouri, R. Belkacemi, S. Ghemid, H. Meradji and R. Chemam**

## 1 Introduction

Semiconducting materials from infrared (Nouri 2010) to ultraviolet (Nouri et al. 2017a) applications have attracted tremendous attention in electronics. Among the various types of semiconductors, Zinc sulfide which has been extensively studied due to its unique electronic and optical characteristics (Nouri et al. 2017a). Anyhow, ZnS is a wide band gap semiconductor and an attractive material due to its use in various advanced technological applications in blue or green luminescence, optics, ultraviolet laser devices and electronic image displays etc. (Bilge et al. 2008a, b). Thermoluminescence (TL) is among the types of luminescence which caused by Detrapping process caused by heating or thermostimulation (Fang et al. 2011). The first who reported the (TL) of ZnS nanoparticle is (Chen et al. 1997). Also, the luminescence induced by any mechanical action on solids is known as mechanoluminescence (ML). The light emissions induced by the elastic deformation, plastic deformation, and fracture of solids are called elasto-mechanoluminescence (EML), plasto-mechanoluminescence (PML) and fracto-mechanoluminescence (FML), respectively, and the light induced by rubbing of solids or separation of two solids in contact is known as tribo- mechanoluminescence or triboluminescence (Sharma et al. 2011a, b). These applications are well known in II–VI semiconductors and several effects such as: traps, defects,

---

This paper was arranged by the recommendations of Senior Editor Dr: Leontina Di Cecco.

---

R. Nouri (✉)
Department of Physics, Faculty of Exact Sciences, Brothers Mentouri Constantine 1 University, Ain El Bye, 25000 Constantine, Algeria
e-mail: rachida.nouri@yahoo.fr; rachimecheri.nour110@gmail.com; nouri.physics@hotmail.com

R. Belkacemi · S. Ghemid · H. Meradji · R. Chemam
Badji Mokhtar Annaba University, 23000 Annaba, Algeria

R. Nouri
Chadli Ben Djedid University, 36000 El Tarf, Algeria

T. Boukharouba et al. (eds.), *Computational Methods and Experimental Testing In Mechanical Engineering*, Lecture Notes in Mechanical Engineering,
https://doi.org/10.1007/978-3-030-11827-3_18

piezoelectric and dislocations can influence on their behaviors (Sharma et al. 2011a, b). So, before beginning to study these novel applications, basic and fundamental researches are required to more comprehend the physical aspects of materials in atomic scale. On the other hand, elastic properties of solids are important due to fundamental solid-state phenomena such as equation of state, phonon spectra and atomic potentials. Elastic stiffness coefficients are essential for many applications related to mechanical properties of a solid such as internal strain, thermoelastic stress and load deflection. Measure of the deformations is depending on elastic constants that is a very important property of the materials under the change of pressure. Moreover, the elastic constants of the crystals at high pressures are essential in order to predict and understand material response, strength, mechanical stability and phase transformations (Bilge et al. 2008a, b). Until now, a few academic studies as regards to the elastic and mechanical properties of ZnS are carried out. The Researches on the elastic and mechanical properties within local density approximation LDA potential and via Mehl method have not been reported to the best of our knowledge. This is may be due to the difficulty and complexity of Mehl method.

## 2 Theoretical Section

The methodology of calculation followed here is well described in our earlier work (Nouri et al. 2017a). As regards to the graphs of Fig. 1, the paces of these curves demonstrate the high accuracy of the computational method. The calculations of the elastic constants from the total energy are based on the method developed by Mehl detailed in these references (Mehl et al. 1994; Osburn et al. 1991; Chami 2009; Ouahrani 2011; Zerarga 2008; Kanoun 2004), which consists to impose the conservation of the volume of the sample under the effect of the pressure. Clearly, that the Mehl method is iterative and irksome. So, the use of numerical model based on any office automation programs such as: Excel or Origin together with any a-b initio code to simplify the task-work and to ensure the accuracy of our calculations is necessary. The knowledge of complete elastic stiffness matrix is essential for modeling, estimation and evaluation of the mechanical behavior of materials under severe loading conditions which is here the pressure. The mechanical quantities are estimated through the mathematical equations described in the following Algerian works (Zerarga 2008; Zerarga et al. 2011; Khenata et al. 2006). Unlike to the other structures where the anisotropy effect must be included (Baste 1999; Abell et al. 2014), this method is valid only with the cubic phases.

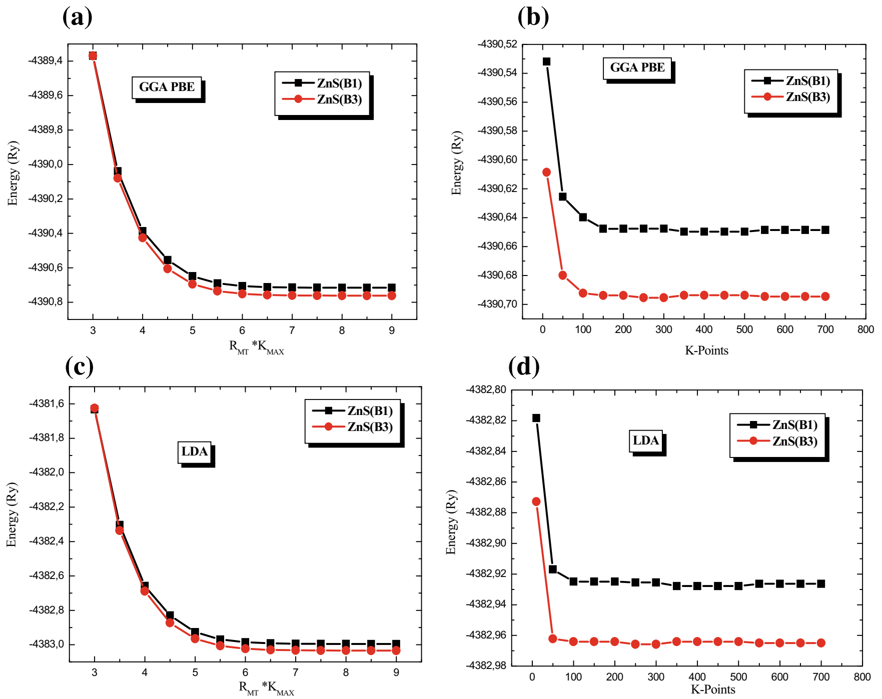

**Fig. 1** The test of convergency of both cubic phases of ZnS at different computational parameters within GGAPBE and LDA. **a**, **c** $R_{MT}*K_{MAX}$, **b**, **d** k-point sampling

# 3 Results and Discussions

## 3.1 *Elastic and Mechanical Properties Under Ambient Conditions at P = 0 GPa*

The structural properties and the pressures transitions between the both cubic phases (B1) and (B3) of ZnS are well explained in our earlier works (Nouri et al. 2017a, b). For the Mehl method, in the Fig. 2, the curves represent the variation of total energies as a function of orthorhombic and monoclinic constraints for both structures of ZnS. With iterative manner, it is necessary to ensure the linearity of these curves because the investigation of slopes guides us to induce the values of $C_{ij}$. The values of elastic constants at $P = 0$ GPa for both phases of ZnS with the using of LDA are enumerated in Table 1, along with previous theoretical and experimental data. Our results are in good agreement with the previous quoted in this table.

Also, after the complete determination of elastic coefficients, the mechanical properties are calculated at equilibrium condition $P = 0$ for zinc-blende phase of ZnS (B3). After the application of different criteria and the laws of mechanics, the

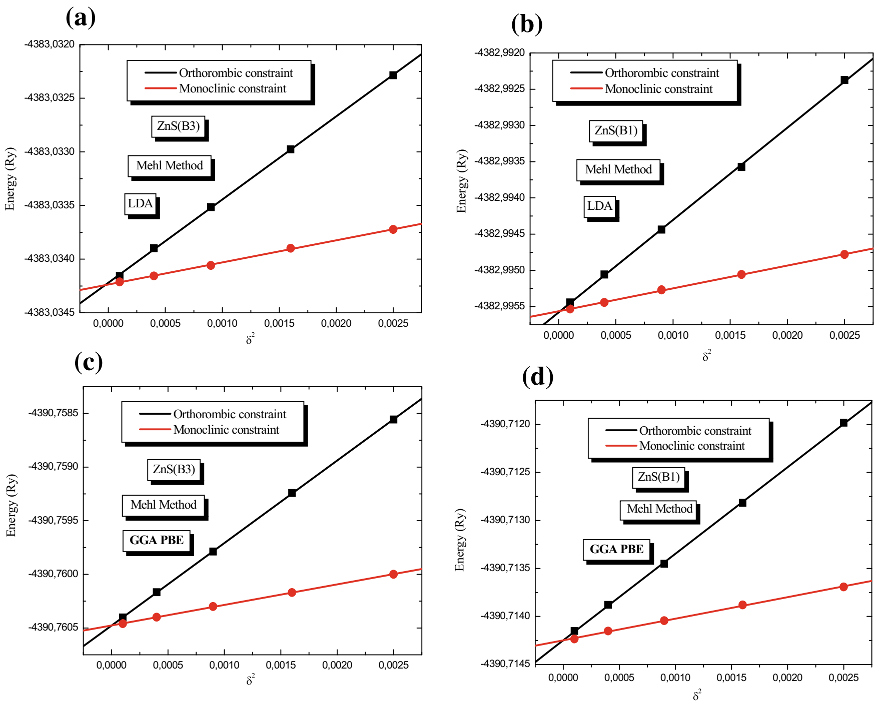

**Fig. 2** The variation of total energy as a function of orthorhombic and monoclinic constraints for both structures of ZnS within LDA and GGA

**Table 1** Calculated elastic constants $C_{ij}$ (in GPa) of ZnS phases in comparison with the available data

| | Ours | | Others | | Exp |
|---|---|---|---|---|---|
| | ZnS (B1) | ZnS (B3) | ZnS (B1) | ZnS (B3) | ZnS (B3) |
| $C_{11}$ (GPa) | 117.43[a]<br>157.63[b] | 95.93[a]<br>116.07[b] | 133.075[c]<br>136.1[d] | 96.283[c],<br>99.6[d],<br>123.7[e],<br>118[f], 122[g] | 104.0[h]<br>101 ± 5[i] |
| $C_{12}$ (GPa) | 62.97[a]<br>74.07[b] | 54.95[a]<br>70.32[b] | 61.124[c]<br>65.0[d] | 55.555[c],<br>57.0[d], 62.1[e],<br>72[f], 68[g] | 65.0[h]<br>64 ± 5[i] |
| $C_{44}$ (GPa) | 63.66[a]<br>92.19[b] | 43.76[a]<br>46.87[b] | 47.10[c]<br>54.1[f] | 62.497[c],<br>50.5[d], 59.7[e],<br>75[f], 57[g] | 46.2[h]<br>42 ± 4[i] |

[a] Calculated with Mehl method GGAPBE 96; [b] Calculated with Mehl method LDA; [c] Bilge et al. (2008a, b) Calculated with GGA PBE 96; [d] Chen et al. (2006) Calculated with GGA 91; [e] Casali and Christensen (1998) Calculated with LDA; [f] Khenata et al. (2006) Calculated with LDA; [g] Wang et al. (2012) Calculated with LDA; [h] Xu and Ching (1993); [i] Wang and Isshiki (2006)

**Table 2** Computed mechanical quantities and the most important induced mechanical information (at P = 0 GPa and T = 0 K): shear (G) and Young (E) moduli, Lame's coefficients (λ and μ), Kleinman parameter (ζ), Poisson ratio (υ) and anisotropy constant (A) for zinc–blende (B3) phase of ZnS. Also, calculated longitudinal $V_L$, transverse $V_T$, average $V_m$ sound velocities, Debye temperatures ($\Theta_D$) concluded from mechanical parameters for (B3) structure of ZnS

| Mehl method for ZnS (B3) | | | Mechanical behaviors | Literature data |
|---|---|---|---|---|
| Potential | GGA | LDA | Mechanical information | |
| G (GPa) | 32.271 | 35.144 | Strong | 40.590[a], 31.2[b] |
| E (GPa) | 83.68 | 92.737 | Stiff | 102.1[a], 105[c] |
| λ (GPa) | 46.843 | 62.146 | To simplify the Hook's law | |
| μ (GPa) | 32.283 | 35.144 | The same value of G | |
| ζ | 0.685 | 0.712 | Large resistance against bond-angle distortions | 0.692[a], 0.715[d] |
| υ | 0.296 | 0.31939 | Brittle | 0.257[a], 0.32[b], 0.27 |
| A | 2.135 | 2.04896 | Anisotrope | 0.901[a] |
| $V_T$ (m/s) | 2871.04 | 2882.033 | Classical mechanics | 3300.00[e] at (T = 300 K) |
| $V_L$ (m/s) | 5338.551 | 5594.658 | Classical mechanics | 5000.00[e] at (T = 300 K) |
| $V_m$ (m/s) | 3205.48 | 3227.165 | Classical mechanics | |
| $\Theta_D$ (K) | 347.687 | 359.268 | Quantum mechanics | 340[e] at (T = 0 K) |

[a] Bilge et al. (2008a, b) Cal; [b] Tropf et al. (1995) Exp; [c] Chen et al. (2009) from the bulk nanowires of ZnS; [d] Khenata et al. (2006) Cal; [e] Adachi (2004) The sound velocities calculated along [100] propagation direction

values of these quantities and the mechanical informations are collected in Table 2. Our results of mechanical quantities obtained in this work are in close agreement with those obtained experimentally and are better than results obtained using other methods.

## 3.2 Elastic and Mechanical Properties Under Pressure

The variations versus pressure of the elastic stiffness coefficients ($C_{11}$, $C_{12}$, $C_{44}$), the bulk modulus B and the shear wave modulus $C_S$ in both phases of ZnS are shown in Fig. 3 a, b. One can note for the zinc-blende structure that the variation of all the elastic stiffness coefficients is linear with pressure except of $C_{44}$. Similar variations were obtained in the rocksalt structure. The same behavior of elastic constants is indicated in this reference (Ali Sahraoui et al. 2007).

We are also interested to investigate the pressure dependence of mechanical quantities of the (B3) structure of ZnS. The variations of mechanical quantities as a function of pressure are given in Fig. 3c, d, respectively. Generally, the behaviors

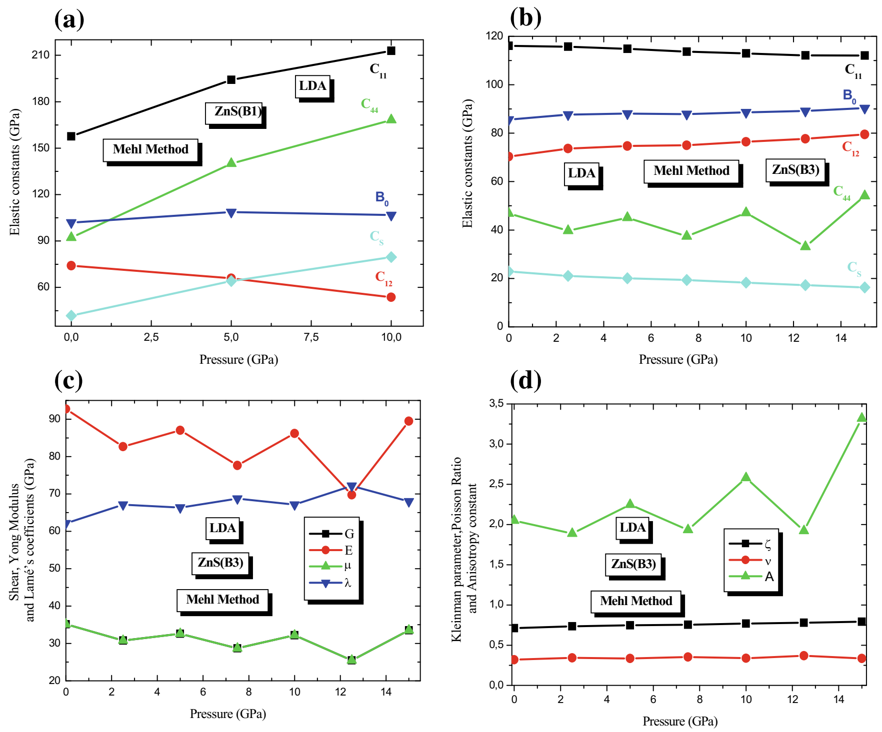

**Fig. 3** **a**, **b** Calculated pressure dependences of elastic coefficients $C_{ij}$, $C_S$ and bulk modulus B for both cubic phases of ZnS, **c** mechanical quantities: shear modulus G, Young modulus E, Lame's coefficients λ and μ under pressure for Zinc-blende ZnS, **d** mechanical quantities: Kleinman parameter ζ, Poisson ratio υ and anisotropy constant A, as a function of pressure for Zinc-blende ZnS

of mechanical properties are resembling to those reported in reference (Bilge et al. 2008a, b) where the Vienna Ab initio Simulation Package (VASP) is applied. Commonly, the zigzag behaviors of elastic and mechanical constants of ZnS are similar to the changes reported in the references (Bilge et al. 2008a, b) where the VASP code is used and the work of Chen et al. (2006) within Cambridge Serial total Energy Package (CASTEP) code. It is obvious seen that the poison ratio (υ) is independent to the temperature which consistent well with the experimental work reported in this reference (Harris et al. 2008). Generally, this investigations is considered as a complimentary study to the earlier works of the first author of this paper (Nouri et al. 2017a, b).

## 4 Conclusion

We have presented some results of the cubic phases of ZnS, which are based on the first-principle calculations. The elastic properties of ZnS are estimated via Mehl method. The variation of mechanical properties and behaviors of zinc-blende ZnS under pressure are determined through the mathematical equations. Our results are in good agreement with the values reported in the literature.

**Acknowledgements** Dr: A. Bendjedid and Pr: Dj. Miroud are gratefully acknowledged.

## References

Abell BC, Shao S, Pyrak-Nolte LJ (2014) Measurements of elastic constants in anisotropic media. Geophysics 79(5):D349–D362

Adachi S (2004) Handbook on physical properties of semiconductors, vol 2. Springer, Berlin

Ali Sahraoui F, Zerroug S, Louail L, Maouche D (2007) Effect of pressure on the structural and elastic properties of ZnS and MgS alloys in the B3 and B1 phases. Mater Lett 61(10):1978–1981. https://doi.org/10.1016/j.matlet.2006.07.170

Baste S (1999) Determination of elastic properties by an ultrasonic technique. In: Paper read at proceedings of the 12th international conference on composite materials, Paris

Bilge M, Özdemir Kart S, Kart HH, Cagin T (2008a) Mechanical and electronical properties of ZnS under pressure. J Achievements Mater Manufact Eng 31(1):29–34

Bilge M, Özdemir Kart S, Kart HH, Çağın T (2008b) B3–B1 phase transition and pressure dependence of elastic properties of ZnS. Mater Chem Phys 111(2–3):559–564. https://doi.org/10.1016/j.matchemphys.2008.05.012

Casali RA, Christensen NE (1998) Elastic constants and deformation potentials of ZnS and ZnSe under pressure. Solid State Commun 108(10):793–798. https://doi.org/10.1016/S0038-1098(98)00303-2

Chen W, Wang Z, Lin Z, Lin L (1997) Thermoluminescence of ZnS nanoparticles. Appl Phys Lett 70(11):1465–1467. https://doi.org/10.1063/1.118563

Chen X-R, Li X-F, Cai L-C, Zhu J (2006) Pressure induced phase transition in ZnS. Solid State Commun 139(5):246–249. https://doi.org/10.1016/j.ssc.2006.05.043

Chen H, Shi D, Shi, Qi J, Wang B (2009) Electronic and mechanical properties of ZnS nanowires with different surface adsorptions. Phys E 42:32–37

Fang X, Zhai T, Gautam UK, Li L, Limin W, Bando Y, Golberg D (2011) ZnS nanostructures: from synthesis to applications. Prog Mater Sci 56(2):175–287

Harris DC, Baronowski M, Henneman L, LaCroix L, Wilson C, Kurzius S, Burns B, Kitagawa K, Gembarovic J, Goodrich SM (2008) Thermal, structural, and optical properties of Cleartran® multispectral zinc sulfide. Opt Eng 47(11):114001–1140015

Kanoun MB (2004) First-principles study of structural, elastic and electronic properties of AlN and GaN semiconductors under pressure effect and magnetism in AlN. Doctor's thesis. Option: Materials Science. Abou-Bakr Belkaid University-Tlemcen

Khenata R, Bouhemadou A, Sahnoun M, Reshak AH, Baltache H, Rabah M (2006) Elastic, electronic and optical properties of ZnS, ZnSe and ZnTe under pressure. Comput Mater Sci 38(1):29–38. https://doi.org/10.1016/j.commatsci.2006.01.013

Mehl MJ, Klein BM, Papaconstantopoulos DA (1994) First principles calculations of elastic properties of metals, vol 1. Wiley, London

Nouri R (2010) Etude par spectroscopie de rétrodiffusion Rutherford de l'implantation ionique de $Sb^+$ dans Si. Effet de l'orientation du détecteur sur les spectres obtenus. Mémoire de Magister en Physique, Spécialité: Sciences des Matériaux, Option: Semi-conducteurs, Université Mentouri de Constantine

Nouri R et al (2017a) Investigation of opto-é"electronic properties of ZnS polymorphs through modified Becke-Johnson exchange potential. Optik—Int J Light Electron Opt 130:1004–1013. doi:http://dx.doi.org/10.1016/j.ijleo.2016.11.116

Nouri R et al (2017b) Structural, elastic and mechanical properties of ZnS. In: 6th Algerian congress of mechanics, CAM2017

Osburn JE, Mehl MJ, Klein BM (1991) First-principles calculation of the elastic moduli of $Ni_3Al$. Phys Rev B 43(2):1805

Ouahrani T (2011) Calcul des propriétés structurales, thermiques et optiques des composés chalcopyrites par la méthode FP-(L)APW, Thèse de Doctorat en Physique, Spécialité: Matière condensée et Semi-conducteur, Université Abou Bakr Bel-Kaïd -Tlemcen, Algérie

Sabah C (2009) Etude Théorique des Propriétés Electroniques, Structurales et Elastiques des Semi-Conducteurs et leurs Super-réseaux Mémoire de Magister. Spécialité: physique, Option: Sciences des matériaux, Université de Mouhamed Boudiaf de M'sila, Algérie

Sharma R, Bisen DP, Brahme N, Chandra BP (2011a) Mechanoluminescence glow curve of ZnS: Mn nanocrystals prepared by chemical route. Digest J Nanomater Biostruct 6:499–506

Sharma Ravi, Bisen DP, Dhoble SJ, Brahme N, Chandra BP (2011b) Mechanoluminescence and thermoluminescence of Mn doped ZnS nanocrystals. J Lumin 131(10):2089–2092

Tropf WJ, Thomas ME, Harris TJ (1995) Properties of crystals and glasses. Handb Opt 2(33):61

Wang J, Isshiki M (2006) Wide-bandgap II–VI semiconductors: growth and properties. In: Springer handbook of electronic and photonic materials. Springer, Berlin, pp 325–342

Wang HY, Cao J, Huang XY, Huang JM (2012) Pressure dependence of elastic and dynamical properties of zinc-blende ZnS and ZnSe from first principle calculation. arXiv preprint arXiv:1204.6102 15:1–10. https://doi.org/10.5488/cmp.15.13705

Xu Y-N, Ching WY (1993) Electronic, optical, and structural properties of some wurtzite crystals. Phys Rev B 48(7):4335–4351

Zerarga F (2008) Contribution à l'étude des propriétés structurales, électroniques et élastiques de quelques spinelles $A^{II}$ $B_2$ $^{III}$ $O_4$, Mémoire de Magister. Spécialité: physique, Option: Sciences des matériaux, Université de Mouhamed Boudiaf de M'sila, Algérie

Zerarga F, Bouhemadou A, Khenata R, Binomran S (2011) FP-LAPW study of the structural, elastic and thermodynamic properties of spinel oxides $ZnX_2O_4$ (X=Al, Ga, In). Comput Mater Sci 50(9):2651–2657